Advanced Materials

ADVANCED MATERIALS
www.advmat.de

REVIEW

Exploring the Potential of Ni-Based Hydrogen Evolution Catalysts in Anion Exchange Membrane Water Electrolyzer

Defa Miao | Jingyao Li | Jintao Ren | Zhongwei Chen

Power Battery & System Research Center, State Key Laboratory of Catalysis, Dalian Institute of Chemical Physics, Chinese Academy of Sciences, Dalian, China

Correspondence: Jintao Ren (renjintao@dicp.ac.cn) | Zhongwei Chen (zwchen@dicp.ac.cn)

Received: 17 October 2025 | **Revised:** 17 December 2025 | **Accepted:** 23 December 2025

Keywords: alkaline electrolyte | anion exchange membrane water electrolyzer | hydrogen energy | hydrogen evolution reaction | nickel-based catalysts

ABSTRACT

The pressing need for sustainable hydrogen production has spotlighted anion exchange membrane water electrolyzer (AEMWE) as a promising technology, due to its potential for cost-effective and efficient hydrogen evolution. Nickel (Ni)-based catalysts have emerged as pivotal players in this domain, offering a compelling alternative to noble metal catalysts for the hydrogen evolution reaction (HER) in AEMWE. Despite their widespread use, challenges such as insufficient activity, conductivity, and long-term stability under alkaline conditions hinder their commercial scalability. This review provides a systematic exploration of Ni-based catalysts for HER in AEMWE, beginning with an in-depth analysis of design principles, including reaction mechanisms, key performance descriptors, and their interrelationships. Subsequently, we categorize advanced regulation strategies for Ni-based HER catalysts into distinct approaches, offering a critical evaluation of catalyst design, synthesis methods, electrocatalytic performance, and representative examples alongside current limitations. The diverse types of Ni-based HER catalysts, including metals/alloys, oxides/hydroxides, and Ni-based composites, are examined, highlighting their respective advantages and drawbacks. We also review the latest research progress on Ni-based catalysts in practical AEMWE devices. Finally, this review concludes with a discussion of challenges and future prospects, aiming to guide the development of Ni-based HER catalysts for industrial-scale hydrogen production via AEMWE.

1 | Introduction

The global transition to a low-carbon economy has elevated hydrogen as a pivotal energy carrier, owing to its carbon-neutral potential and versatility across transportation, power generation, and industrial applications. Water electrolysis powered by renewable energy enables the production of green hydrogen with zero lifecycle carbon emissions, positioning it as a cornerstone of sustainable energy systems. Compared to a conventional alkaline water electrolyzer (AWE), an anion exchange membrane water electrolyzer (AEMWE) offers superior ionic conductivity, operational flexibility, and the potential to utilize cost-effective, earth-abundant materials, making it a promising technology for scalable hydrogen production (Figure 1) [1–3]. However, AEMWE efficiency is constrained by the performance of electrocatalysts, particularly for the hydrogen evolution reaction (HER) at the cathode. Although noble metal catalysts, such as platinum (Pt), exhibit exceptional HER activity across pH ranges, their scarcity and high cost (~\$33 000 kg^{-1} in 2025) necessitate alternatives. Nickel (Ni)-based catalysts, leveraging abundant reserves (~\$22 kg^{-1}), robust corrosion resistance, and favorable electrocatalytic properties, have emerged as viable candidates [4–6]. For instance, Raney Ni and Ni mesh are employed as cathode and anode, respectively, in industrial electrolyzers, capitalizing on Ni's intrinsic activity and compatibility with alkaline environments.

Despite their promise, Ni-based catalysts face significant challenges in AEMWE systems, driven by stringent operational

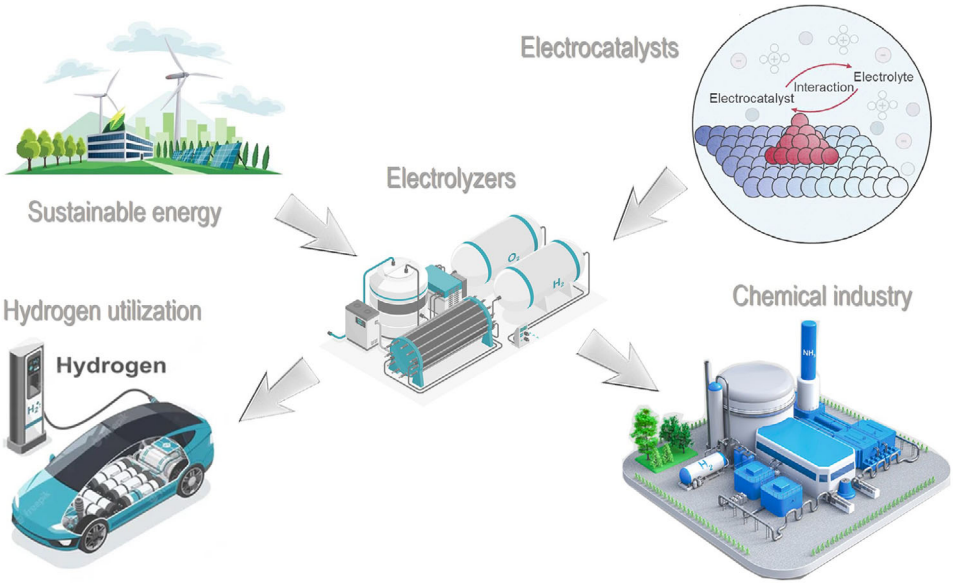

FIGURE 1 | Illustration of the modern sustainability energy economy with green hydrogen as the core.

requirements, including high current density, long-term stability, and compatibility with anion exchange membranes (AEMs) [7, 8]. Compared to Pt, Ni-based catalysts exhibit inferior HER performance, necessitating improvements in activity, conductivity, and durability [9–11]. Key obstacles include: (i) In alkaline media, HER involves an additional water dissociation step, which increases the energy barrier and slows kinetics, requiring catalysts that efficiently promote water dissociation and hydrogen recombination. (ii) Poor stability during continuous operation reduces catalytic efficiency. (iii) At high current density, hydrogen bubble accumulation on catalyst surfaces impedes electrolyte diffusion and blocks active sites, increasing ohmic losses. (iv) Industrial electrolyzers often contain contaminant ions (e.g., Fe) from bipolar plates, piping, or electrolytes, which can poison active sites and compromise catalyst activity. To address these limitations, a diverse array of Ni-based catalysts has been explored, including pure Ni, alloys, oxides, hydroxides, and composite structures (e.g., sulfides, phosphides) [12–14]. These materials exhibit varied electronic and physical properties, enabling tailored optimization for HER performance. For instance, Ni alloys leverage synergistic effects from alloying elements to enhance charge transfer and hydrogen adsorption, while $Ni(OH)_2$ outperforms in water dissociation due to its hydroxyl-rich surfaces. However, oxides and hydroxides often suffer from poor conductivity and structural instability at high current densities, necessitating innovative design approaches. To overcome these challenges, researchers have proposed several regulation strategies, including heteroatom doping, interface engineering, and morphological engineering [15–17]. Heteroatom doping with elements such as Fe, Co, or P modulates Ni's electronic structure, optimizing hydrogen binding energy and facilitating water dissociation. Interface engineering, such as Ni/NiO or Ni/MoO_2 composites, enhances charge transfer and catalytic synergy [18–21]. Morphological engineering, employing structures like nanosheets or nanowires, increases specific surface area and exposes more active sites. Each strategy offers distinct advantages, yet challenges persist, including dopant leaching, synthesis complexity, and interface stability, which require further investigation to fully realize their potential in AEMWE applications. These efforts collectively aim to bridge the performance gap with noble metal catalysts, positioning Ni-based materials as a cornerstone for scalable, sustainable hydrogen production.

In recent years, research on optimizing Ni-based catalysts for the HER in AEMWE has surged, driven by the primary objectives of enhancing reaction kinetics, reducing overpotentials, and improving durability under industrially relevant conditions [22, 23]. Over the past decade, the number of publications on Ni-based catalysts in alkaline HER has risen sharply, a clear indicator of the growing academic and industrial interest, as well as the steady technological advancements in this field. These studies have delved into the reaction mechanisms of alkaline HER, identified critical performance metrics, such as activity, conductivity, and stability, and employed sophisticated catalyst design strategies to precisely tune the electronic structure, electrical conductivity, and long-term robustness of Ni-based catalysts [24, 25]. While numerous reviews have addressed non-precious metal catalysts or Pt-based HER catalysts, a systematic analysis specifically targeting Ni-based catalysts for AEMWE remains scarce [26–28]. Existing literature often focuses on catalysts in alkaline or neutral environments or provides broad overviews of non-precious metal properties, yet it rarely examines the unique behavior of Ni-based catalysts in AEMWE's alkaline conditions, such as the specific demands of the water dissociation step, the influence of OH^- adsorption, and their interplay with AEMs. As AEMWE progresses toward industrial adoption, heightened expectations for Ni-based catalysts in real-world applications, such as stability at current densities exceeding 1 A cm^{-2}, integration with membrane electrode assemblies (MEAs), and cost-effectiveness, demonstrate the urgent need for a comprehensive synthesis of this field [29, 30]. This gap highlights the necessity for a focused review that systematically evaluates the current state of Ni-based catalysts in AEMWE, offering insights into their design principles, performance optimization, and future prospects in sustainable hydrogen production.

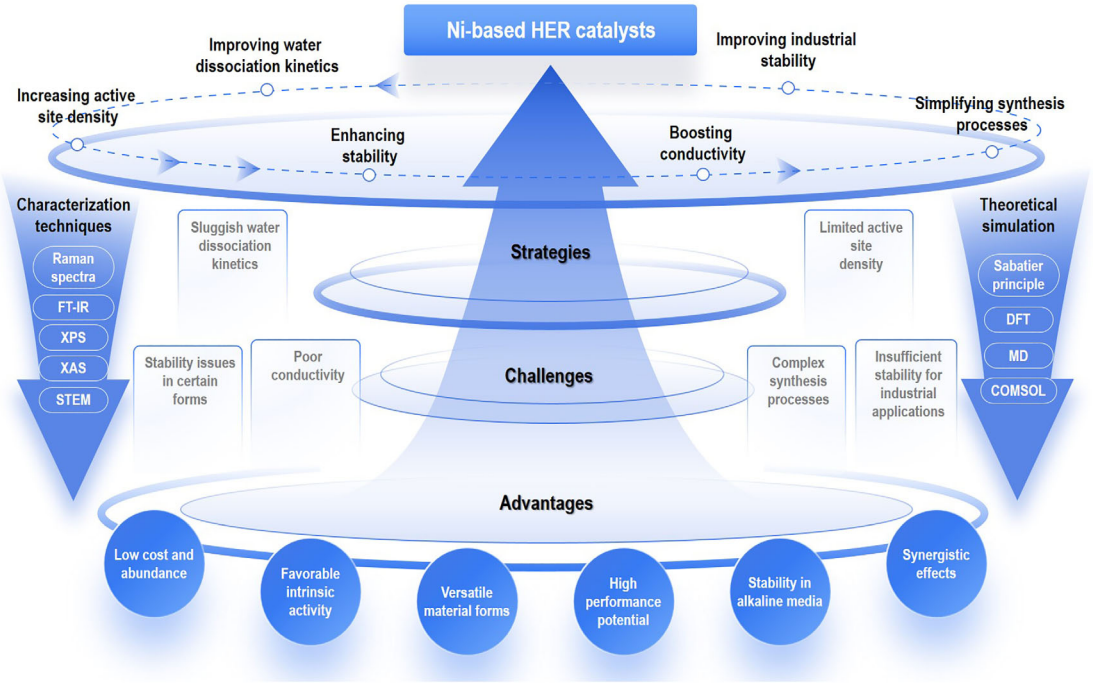

FIGURE 2 | Overview of the unique design criteria of Ni-based HER electrocatalysts.

Given the pivotal role of the HER in AEMWE and the remarkable advancements in Ni-based electrocatalysts, this review provides a comprehensive examination of the latest research developments in this field to guide future studies and industrial applications (Figure 2). Initially, we outline the significance of AEMWE as a hydrogen production technology and highlight the critical role of Ni-based catalysts in alkaline HER. Subsequently, we delve into the design principles of Ni-based HER catalysts, encompassing reaction mechanisms, key performance metrics (activity, electrical conductivity, and structural stability), and their degradation pathways. Next, we systematically summarize and evaluate strategies for modulating Ni-based catalysts, including heteroatom doping, morphological control, and interface engineering, discussing their synthesis methods, electrocatalytic performance, advantages, and limitations, with analyses supported by representative examples. Furthermore, we systematically assess the strengths and weaknesses of different categories of HER catalysts, such as Ni metal, alloys, and compounds. Finally, we review the latest progress in the application of Ni-based HER catalysts in practical AEMWE devices, analyzing their performance under real-world conditions and the challenges encountered, while offering perspectives on future research directions to accelerate the transition of Ni-based catalysts toward commercial hydrogen production.

2 | The Necessity for Studying Ni-Based Alkaline HRE Catalysts

The pressing demand for sustainable hydrogen production has catalyzed extensive research into water electrolysis technologies, with a particular focus on developing cost-effective and efficient electrocatalysts for the HER. Among these technologies, AEMWE has emerged as a promising candidate due to its potential to bridge the gap between high-performance systems and economic viability [31, 32]. Within this framework, Ni-based catalysts have garnered significant interest as alternatives to precious-metal catalysts for the HER in alkaline environments, driven by their abundance, affordability, and intrinsic electrocatalytic properties. This section elucidates the necessity of studying Ni-based HER catalysts by comparing water electrolysis technologies and highlighting their unique potential in advancing AEMWE toward commercial scalability.

2.1 | Comparative Analysis of Water Electrolysis Technologies

Water electrolysis technologies can be broadly classified into three categories: AWE, proton exchange membrane water electrolyzer (PEMWE), and AEMWE (Figure 3). Each system offers distinct advantages and faces specific challenges, particularly concerning catalyst requirements, operational conditions, and scalability, as described in Table 1 [33]. AWE, the most established technology, operates in a highly alkaline liquid electrolyte (typically 20–40 wt% KOH) and relies on robust, low-cost materials such as steel or Ni-based electrodes. Its simplicity and maturity have made it a staple in industrial hydrogen production; however, AWE suffers from low current densities (0.2–0.5 A cm^{-2}), limited dynamic response to intermittent renewable energy inputs, and challenges in achieving high-purity hydrogen due to gas crossover through the porous diaphragm. Moreover, the maximum operating geometric current density of AWE is less than 0.4 A cm^{-2}, and the power consumption for H_2 production is approximately 4.5–5.5 kWh Nm^{-3} with an efficiency of approximately 60 % [34]. These limitations necessitate advancements in catalyst design and system efficiency to meet modern energy demands. In contrast, PEMWE employs a solid polymer electrolyte (e.g., Nafion) and operates under acidic conditions, enabling high current densities (1–2 A cm^{-2}), compact designs, and rapid response to

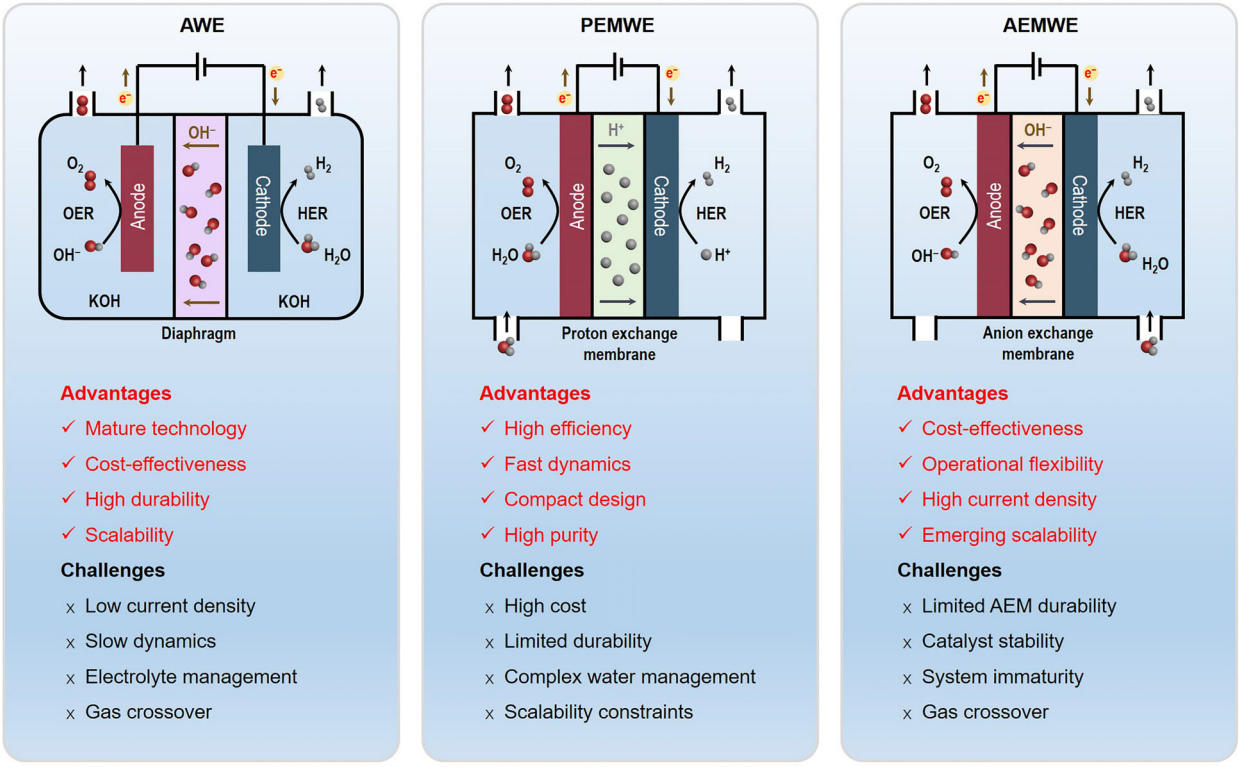

FIGURE 3 | Comparison of different water electrolyzers from the perspective of technological and economic feasibility.

TABLE 1 | Technical characteristics of typical water electrolysis technologies.

Electrolyzer	AWE	PEMWE	AEMWE
Electrolyte	20%–30% KOH	Pure water	1.0 M KOH or Pure water
Separator	Zirfon	Nafion	Fumatech
Electrode/Catalyst (Hydrogen side)	Nickel-coated perforated stainless steel	Platinum carbon	Nickel
Electrode/Catalyst (Oxygen side)	Nickel-coated perforated stainless steel	Iridium oxide	Nickel or NiFeCo alloys
Gas diffusion layer	Nickel mesh	Titanium mesh/carbon cloth	Nickel foam/carbon cloth
Bipolar plates	Stainless steel/Nickel-coated stainless steel	Platinum/Gold-coated titanium or titanium	Stainless steel/Nickel-coated stainless steel
Nominal current density	0.2–0.8 A cm^{-2}	1–2 A cm^{-2}	0.2–2 A cm^{-2}
Voltage range (limits)	1.4–3 V	1.4–2.5 V	1.4–2.0 V
Operating temperature	70–90°C	50–80°C	40–60°C
Cell pressure	<30 bar	<70 bar	<35 bar
H_2 purity	99.5%–99.9998%	99.9%–99.9999%	99.9%–99.9999%
Efficiency	50%–78%	50%–83%	57%–59%
Lifetime (stack)	5–10 years	50 000–80 000 h	>20 000 h
Development status	Mature	Commercialized	Laboratory
Electrode area	10 000–30 000 cm^2	1500 cm^2	~300 cm^2
Capital costs (stack) minimum 1 MW	USD 270/kW	USD 400/kW	Unknown
Capital costs (stack) minimum 10 MW	USD 500–1000/kW	USD 700–1400/kW	Unknown
Energy input	4.5–5.3 kWh Nm^{-3} H_2	4.3–5.0 kWh Nm^{-3} H_2	4.2–4.8 kWh Nm^{-3} H_2

fluctuating power inputs, which are attributes ideal for integration with renewable energy sources. Meanwhile, benefiting from the low internal resistance and high mass-transport efficiency of PEMWE systems, the power consumption for H_2 production is approximately 4.3–5.0 kWh Nm^{-3}. However, PEMWE's reliance on scarce and expensive precious-metal catalysts (e.g., Pt for HER and Ir/Ru oxides for OER) and costly proton-conducting membranes significantly escalates capital costs, hindering widespread adoption. Additionally, the acidic environment imposes stringent stability requirements on catalysts, further limiting material options.

AEMWE combines the strengths of AWE and PEMWE by utilizing a solid AEM in an alkaline medium, facilitating the use of non-precious-metal catalysts while achieving higher current densities (>1 A cm^{-2}) than AWE and improved gas separation compared to traditional alkaline systems [35, 36]. The alkaline environment of AEMWE mitigates the harsh acidic conditions of PEMWE, broadening the range of viable catalyst materials, including transition metals like Ni, Co, and Fe. Additionally, its power consumption for H_2 production decreases to 4.2–4.8 kWh Nm^{-3}. Despite these advantages, AEMWE remains in a developmental stage, with challenges such as membrane durability, ionic conductivity, and catalyst optimization under high-current-density conditions yet to be fully resolved. The HER in AEMWE, while less demanding than the OER, requires catalysts that can efficiently manage the Volmer step (water dissociation) in alkaline media, a process where Ni-based materials exhibit considerable promise. This comparative analysis demonstrates the strategic position of AEMWE as a cost-effective, scalable technology that leverages the alkaline HER environment to reduce reliance on precious metals. The development of high-performance, durable Ni-based catalysts is thus critical to unlocking AEMWE's full potential and addressing the limitations of existing electrolysis systems.

2.2 | Potential of Ni-Based HER Catalysts for AEMWE

Ni-based catalysts stand out as prime candidates for the HER in AEMWE due to their unique combination of cost-effectiveness, electrochemical activity, and stability in alkaline conditions [37]. Unlike Pt, which excels in acidic media due to its optimal hydrogen binding energy (HBE), Ni exhibits moderate HBE and exceptional water dissociation capabilities in alkaline environments, which are key attributes for the Volmer step of the HER mechanism. This intrinsic activity, coupled with Ni's abundance and low cost, positions it as a sustainable alternative for large-scale hydrogen production. The versatility of Ni-based catalysts further enhances their potential. Pure metal, alloys (e.g., Ni-Mo, Ni-Fe), and compounds (e.g., Ni_3N, NiS_2, Ni_2P) have demonstrated competitive HER performance in alkaline media, often approaching or surpassing Pt at high current densities when optimized. For instance, Ni-Mo alloys have achieved overpotentials as low as 50 mV at 10 mA cm^{-2}, attributed to synergistic electronic effects that enhance H* adsorption and OH^- desorption [24, 38–40]. Similarly, phosphides exhibit improved conductivity and stability, making them suitable for prolonged operation in AEMWE devices [41–43]. These advancements highlight Ni's adaptability to various structural and compositional modifications, enabling tailored catalytic properties for specific operational needs. Moreover, Ni-based catalysts offer practical advantages for AEMWE integration. Their compatibility with alkaline conditions aligns with the system's use of low-cost membranes and stainless-steel components, reducing overall system costs compared to PEMWE. Recent studies have also demonstrated Ni-based catalysts' resilience under industrially relevant conditions (e.g., current densities >0.5 A cm^{-2}), a critical requirement for commercial-scale hydrogen production. However, challenges remain, including surface oxidation during extended operation, limited active site density, and insufficient mechanistic understanding of Ni's role in alkaline HER. Addressing these issues through advanced synthesis, doping, and interface engineering could elevate Ni-based catalysts to rival or exceed Pt-based benchmarks. The growing body of research on Ni-based HER catalysts reflects their rising prominence, with efforts increasingly focused on their application in AEMWE stacks rather than laboratory-scale setups [44, 45]. This shift demonstrates the urgent need for systematic studies to refine their design, elucidate degradation mechanisms, and validate their performance in real-world systems. By capitalizing on Ni's inherent strengths, AEMWE could emerge as a cornerstone of the hydrogen economy, provided that Ni-based catalysts are optimized to meet the demands of efficiency, durability, and scalability.

3 | Design Principles for Ni-Based Catalysts

The development of Ni-based catalysts for the HER in alkaline AEMWE hinges on a deep understanding of their reaction mechanisms and performance-limiting factors [46, 42]. Unlike acidic environments, where HER kinetics are relatively straightforward, the alkaline medium introduces additional complexity, necessitating tailored catalyst design strategies Ni-based materials, with their inherent electrocatalytic properties and versatility, offer a robust platform for addressing these challenges. This section explores the fundamental design principles underpinning Ni-based HER catalysts, focusing on the reaction mechanism in alkaline conditions and the key descriptors, including activity, conductivity, and stability, that govern their performance.

3.1 | Reaction Mechanism

The HER in alkaline media proceeds through a multi-step process distinct from its acidic counterpart due to the absence of free protons, relying instead on the dissociation of water molecules as the hydrogen source [47]. The generally accepted mechanism involves two primary pathways: the Volmer-Tafel and Volmer-Heyrovsky routes, each characterized by the following steps:

Volmer step (Water dissociation):

$$H_2O + e^- + * \rightarrow H* + OH^- \quad (1)$$

This initial step entails the adsorption of a water molecule onto an active site (H_2O*), followed by its reduction and cleavage to form an adsorbed hydrogen intermediate (H*) and a hydroxide ion (OH^-) [48]. The energy barrier for water dissociation is a

critical bottleneck in alkaline HER, distinguishing it from acidic HER where H* reduction is more facile.

Heyrovsky step (Electrochemical desorption):

$$H_2O + H* + e^- \rightarrow H_2 + OH^- + * \quad (2)$$

Here, a second water molecule reacts with the adsorbed H* to produce H_2, releasing OH^- and regenerating the active site. This step competes with the Tafel pathway depending on catalyst properties and reaction conditions.

Tafel step (Chemical recombination):

$$2H* \rightarrow H_2 + 2* \quad (3)$$

In this alternative, two adsorbed H* intermediates combine to form H_2, bypassing additional electron transfer. The dominance of this step is determined by the HBE and surface coverage of H*.

For Ni-based catalysts, the HER mechanism is heavily influenced by their ability to facilitate the Volmer step, as Ni exhibits a moderate HBE (typically −0.2 to −0.3 eV) and a notable capacity to weaken the H-O bond in water. Density functional theory (DFT) studies suggest that Ni's d-band electrons interact favorably with water's oxygen lone pairs, lowering the energy barrier for H_2O dissociation compared to other transition metals like Fe or Co [49]. However, pure Ni often suffers from sluggish OH^- desorption and suboptimal H* recombination, leading to higher overpotentials than Pt (−0.1 eV of HBE). Modifications such as alloying, interfacing, or heteroatom doping can tune the electronic structure, enhancing OH^- release and shifting the HBE closer to the ideal value (~0 eV), as depicted in the Sabatier principle-based volcano plot.

The reaction pathway for the HER, whether following the Volmer–Tafel or Volmer–Heyrovsky mechanism, depends strongly on the catalyst's composition and morphology. For instance, Ni-Mo alloys favor the Tafel step due to optimized H* coverage, while Ni phosphides promote the Heyrovsky step because of enhanced charge transfer [50]. Understanding these mechanistic details is vital for designing Ni-based catalysts that reduce kinetic barriers and enhance HER efficiency in AEMWE. However, the HER mechanism in practical reactions proves far more intricate than these simplified pathways suggest. Recent research has introduced theories, such as water dissociation theory, HBE theory, and interfacial water/anion transfer theory, to clarify the HER process. Correspondingly, several strategies have been summarized to regulate the reaction intermediates involved in alkaline HER, as shown in Figure 4. For example, to accelerate the Tafel process, strategies such as tuning the metal-oxygen interaction strength, adjusting the electronic structure of active sites, controlling surface hydroxyl coverage, and optimizing the local environment can be employed. For the Heyrovsky/Tafel process, precise control over the hydrogen adsorption free energy (ΔG_{H^*}), through methods like alloying, doping, or strain engineering, can be implemented, as well as the construction of complementary dual-sites or heterogeneous interfaces, and the introduction of low-loading precious metal promoters. The effectiveness of these strategies, however, varies depending on the specific operational conditions. For instance, alloying introduces electronic modulation that weakens H* adsorption and enhances water dissociation, thereby accelerating the Volmer step and favoring a faster Volmer-Heyrovsky pathway [51]. Research on Ni-M (M = Ti, V, and 10 other metals) bimetallic alloys has found that NiCu alloy exhibits nearly optimal ΔG_{H^*}, attributed to its suitable d-band center [51]. Additionally, nitridation, phosphidation, and sulfidation can create metal-nonmetal bonds, increasing electron density around surface Ni sites, which further lowers the kinetic barrier for water dissociation. This often shifts the rate-determining step from being Volmer-limited to Heyrovsky-limited [52–54]. For example, Ni_2P and $Ni_{12}P_5$ form a synergistic effect through strong interfacial coupling [55]. $Ni_{12}P_5$ accelerates H_2O dissociation, while Ni_2P optimizes H adsorption. Ultimately, the catalyst exhibits excellent HER performance across the full pH range. Furthermore, defect engineering and high-entropy designs could modify the d-band center and optimize both H_2O adsorption and H binding energies, potentially enabling Tafel-like recombination step to become more significant [56–59]. For instance, low-coordinated Ru atom arrays confined in Mn oxides (i.e., $Li_4Mn_5O_{12}$) enable the formation of adjacent Ru atom arrays [59]. Both electrochemical and theoretical results uncover that the array-like structure allows the activation of two water molecules on two adjacent Ru atoms for enabling direct H*–H* recombination via the Tafel step, while isolated Ru atoms can only activate water one by one for recombining H* via the sluggish Heyrovsky step.

In the water dissociation theory, the role of HO* in alkaline HER remains unclear, with some studies indicating that HO* may not participate in the Volmer step or significantly affect HER activity. Conversely, the widely accepted HBE theory asserts that catalytic activity in HER hinges on the binding strength between active sites and adsorbed hydrogen, typically assessed through hydrogen adsorption free energy [60]. Based on the Sabatier principle, an optimal HER electrocatalyst exhibits moderate binding affinity for key reaction intermediates like H*, avoiding extremes of too strong or too weak to enable both activation and release (Figure 5a,b), thus lowering the reaction overpotential and accelerating kinetic efficiency. Therefore, effective alkaline HER catalysts must consider the adsorption behavior of multiple intermediates to achieve thorough optimization of catalytic activity.

To date, there are primarily three main strategies for designing electrocatalysts for hydrogen evolution in alkaline/neutral media. A general overview of these regulation strategies is provided below.

3.1.1 | Multi-Site Electrocatalyst Construction

In alkaline HER, efficient catalysts play a central role in boosting reaction efficiency and supporting large-scale applications, requiring fulfillment of several key conditions. From a kinetic standpoint, water dissociation initiates HER, demanding catalysts with low energy barriers for splitting water to swiftly convert H_2O into H* and OH^-. For example, catalysts featuring specific metal oxides or distinct structures can optimize H_2O adsorption and activation, reducing the energy needed for water dissociation. Equally important are the HBE and hydroxyl

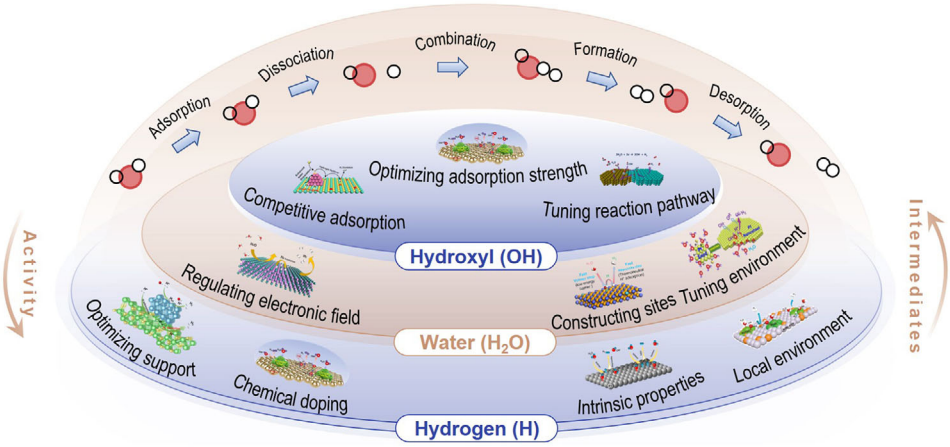

FIGURE 4 | Schematic illustration of various efficient synthesis strategies based on the active intermediates for the preparation of alkaline HER catalysts.

binding energy (OHBE) [61, 62]. An ideal catalyst maintains an HBE near the optimal value for H_2 evolution to facilitate H-H bond formation, while ensuring an appropriate OHBE to allow timely desorption of OH species, preventing active site blockage and maintaining reaction progress. Additionally, alkaline HER encompasses multiple elementary steps, necessitating catalysts that coordinate water dissociation, OH transfer, and H-H bond formation effectively. In composite catalysts, different components can capitalize on their unique strengths, collaborating to improve the overall reaction. Consequently, designing well-constructed composite catalysts offers a promising approach to developing high-performance HER catalysts. For instance, Li et al. synthesized a Ni_3Sn_2-$NiSnO_x$ nanocomposite electrocatalyst for efficient alkaline HER [63]. DFT calculations (Figure 5c–f) showed that Ni_3Sn_2 provides ideal hydrogen adsorption and low hydroxyl affinity, while $NiSnO_x$ supports water dissociation and hydroxyl transfer. At the Ni_3Sn_2-$NiSnO_x$ heterointerface, water dissociates and adsorbs, with H* preferentially binding to Ni sites on the Ni_3Sn_2 side and OH* attaching to modified Ni sites in $NiSnO_x$. Subsequently, H* desorbs electrochemically from Ni_3Sn_2's active Ni sites to produce H_2 rapidly, while OH* transfers efficiently within $NiSnO_x$ for further reaction, resulting in highly effective alkaline HER. The experimentally optimized Ni_3Sn_2-$NiSnO_x$-2 catalyst exhibited outstanding performance in 1 M KOH, achieving overpotentials of 14 and 165 mV at current densities of 10 and 1000 mA cm^{-2}, respectively, with excellent stability.

3.1.2 | Local pH Manipulation

Since the HER in acidic conditions has been reported to be about two orders of magnitude faster than in neutral and alkaline conditions, tailoring the local environment around the catalyst from neutral to acidic has proven to be an effective strategy to enhance neutral HER performance. In conventional alkaline conditions, the low concentration of H^+ leads to a slow HER process. However, in a locally acidic microenvironment, the increased concentration of H_3O^+ can effectively accelerate the hydrogen evolution rate. For example, Peng et al. anchored Ru single atoms onto low-crystallinity nickel hydroxide [64]. Due to the activation effect of the metal-support interaction, the reconstruction of the interfacial ion distribution balance, and the low oxidation state of Ru single atoms (average oxidation state +0.46), the accumulation of HO^+ was induced, creating a locally acidic microenvironment in an alkaline medium. This strategy broke the pH dependence of HER activity. To achieve rapid hydrogen evolution in neutral environments, Wang et al. found that hydrogen in the HER process combines with WO_3 on the catalyst to form H_xWO_3, which in turn creates a local acidic microenvironment around the active sites [65]. Combined with in situ characterization and DFT calculations (Figure 5g), they confirmed that the activated lattice hydrogen species at the interface efficiently couple with the surface-adsorbed hydrogen on Ir via a thermodynamically favorable Volmer–Tafel step (Figure 5h). This allowed the catalyst to exhibit acid-like HER activity in neutral media, achieving a 10 mA cm^{-2} current density with an overpotential of only 20 mV and a Tafel slope as low as 28 mV dec^{-1}.

3.1.3 | Interfacial Water Organization

Although neutral HER follows the same mechanism as alkaline HER, the kinetics are much slower. This slower kinetics can be attributed to the difference in the mass transfer of reaction intermediates, specifically the inward transport of H_2O and the outward transport of OH^- through the water layer. For example, nickel sulfide has become a research focus for AEMWE catalysts due to its low cost, high conductivity, and good stability. However, it faces issues such as low adsorption coverage of OH^- on the anode and poor proton supply rates. Traditional modification strategies (e.g., morphology control, vacancy creation, and heteroatom doping) focus primarily on increasing the number of active sites and enhancing charge transfer rates, often neglecting the critical role of interfacial water structure at the solid-liquid interface in determining HER performance. To address this, Pan et al. combined experimental and theoretical studies and found that the W_1O motif can induce a local electric field, leading to the accumulation of free water at the inner Helmholtz plane

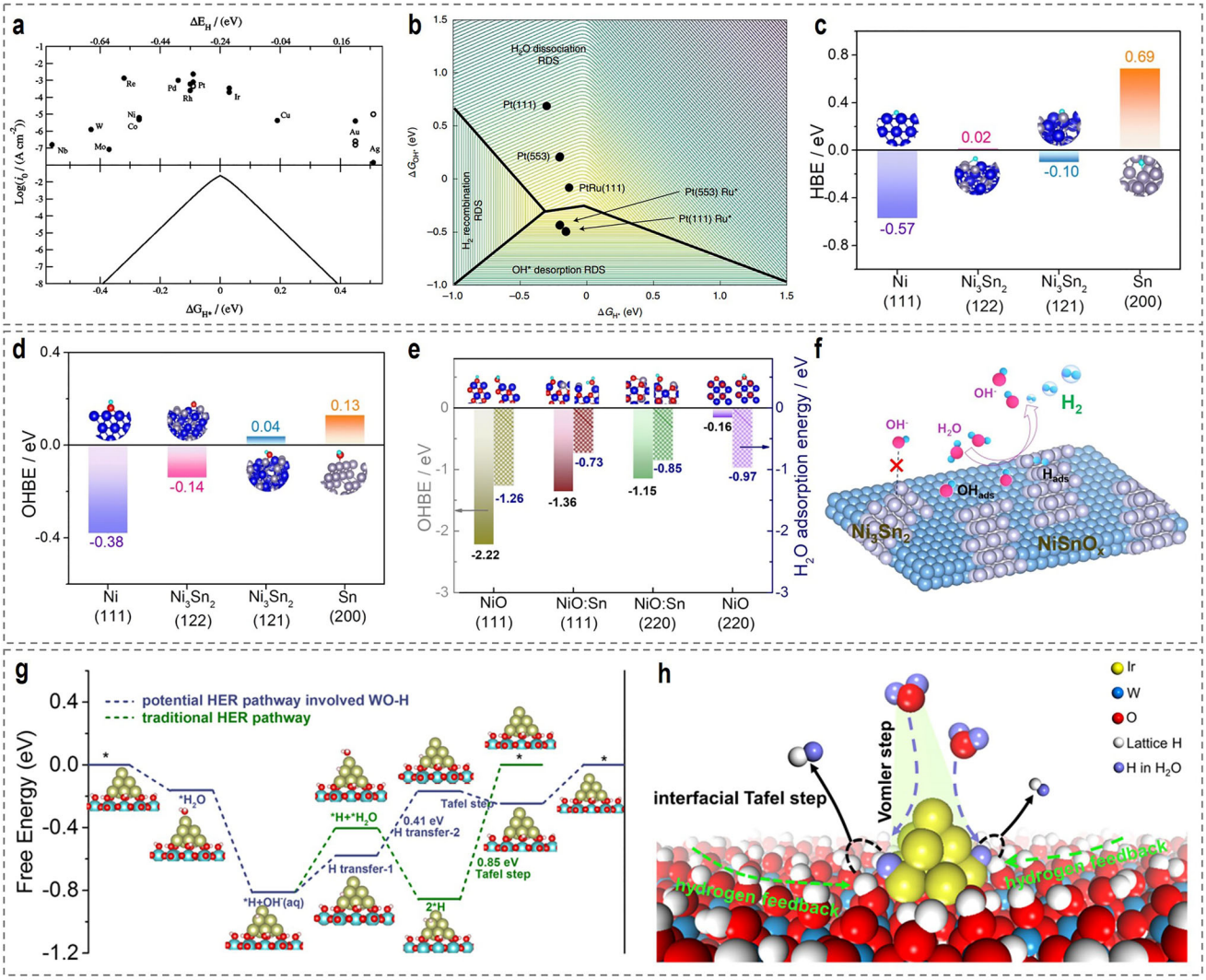

FIGURE 5 | (a) lgj0 plotted versus of ΔGH* of adsorbed atomic hydrogen. Reproduced with permission [50]. Copyright 2005, IOP Publishing. (b) 3D HER activity volcano between H* and OH* for catalyst design. Reproduced with permission [68]. Copyright 2020, Nature Publishing. (c) Calculated H-binding energies (HBEs, ΔEH) and (d) OH-binding energies (OHBEs, ΔEOH) for model surfaces. (e) Calculated OHBEs and H2O adsorption energies on different surfaces of metal oxides. Blue, red, gray, and small sky-blue spheres represent Ni, O, Sn, and H atoms, respectively. (f) Predicted schematic diagram of alkaline HER process on synergistic Ni_3Sn_2-$NiSnO_x$ electrocatalyst. Reproduced with permission [63]. Copyright 2023, Wiley-VCH. (g) Free energy profiles for HER over Ir10-HxWO3 via different reaction pathways. (h) Schematic illustrating the proposed reaction mechanism on Ir-HxWO3. Reproduced with permission [65]. Copyright 2023, Nature Publishing.

(IHP) [66]. This reorders the interfacial water molecules into an "H-down" configuration, lowering the energy barrier of the Volmer step from 2.41 eV to 1.02 eV. The catalyst demonstrated excellent performance in 1 M KOH, with overpotentials of only 67 mV at 10 mA cm^{-2} and 236 mV at 1000 mA cm^{-2}, and it maintained 98% of its activity after 300 h of stable operation at 200 mA cm^{-2}, outperforming most nickel-based HER catalysts. In neutral conditions, the OH^- concentration is extremely low, and unlike in alkaline systems, it cannot effectively promote intermediate transport. This leads to difficulty in the penetration of the H_2O*/OH* (reaction intermediates) through the rigid water layer at the electrode/electrolyte interface, hindering the regeneration of active sites. To address this, Chen et al. discovered that the rigid interfacial water layer in neutral media inhibits the transport of H_2O*/OH* on Ru single-atom (RuNC) surfaces, while ruthenium selenide clusters ($RuSe_x$) can break the hydrogen-bond network of the interfacial water and increase its disorder, thus accelerating the transport of H_2O*/OH* and increasing the available number of H_2O* on the RuNC surface [67]. The synergistic $RuSe_x$-RuNC catalyst demonstrated excellent performance in neutral HER, with an overpotential of only 29 mV at 10 mA cm^{-2}.

3.2 | Relationship Between AEMWE Interfacial Transport Mechanisms and HER Kinetics

Unlike the simple HER surface reaction behavior in traditional AWE systems, in AEMWE, the OH^- transport behavior and the interfacial microenvironment of the catalyst layer/anion-exchange ionomer/membrane (CL/AEI/AEM) are key variables that regulate the HER performance of Ni-based catalysts. This

distinction represents the core difference between AEMWE and traditional alkaline electrolysis systems. The following sections will elaborate on the mechanisms by which the interfacial microenvironment in AEMWE influences HER performance.

3.2.1 | OH^- Transport and the Uniqueness of the Interfacial Environment

Traditional alkaline HER mechanisms focus solely on the macroscopic mass transfer of OH^- from the electrolyte phase to the catalyst surface. In contrast, the HER rate in AEMWE is primarily determined by the precise transport efficiency of OH^- at the CL/AEI/AEM interface and the dynamic response of active sites on the Ni-based catalyst surface. This coupled relationship is what distinguishes the mechanism of AEMWE. Therefore, the OH^- transport capacity and the local environment at the CL/AEI/AEM interface are crucial for hydrogen evolution performance in AEMWE. Given that the alkaline environment in AEMs is provided by the fixed cationic functional groups, it is believed that an AEI with a high ion exchange capacity (IEC) may induce a localized environment with a higher pH, thereby influencing electrode kinetics. To investigate the effect of ionomer IEC on the local pH environment, Thiele et al. coated a Pt RDE with a Nafion proton-exchange ionomer (PEI) or an Aemion AEI and monitored changes to the HOR/HER reversible potential in different electrolyte solutions [69]. Under these conditions, the pH of the electrode was found to be primarily dependent on the external solution, rather than the expected pH within the ionomer coating. The pH of the local environment is also defined by the local rate of OH^- consumption (at the anode) or production (at the cathode) due to Faradaic reactions. Fortin et al. reported that when the pH in Aemion AEM was monitored by doping with thymolphthalein, no color change was observed at the anode (where OH^- is consumed), even when maximum conductivity was reached [70].

In AEMs, the competition between OH^- and CO_3^{2-} for transport can reduce the effective OH^- concentration, and low KOH concentrations can also lead to localized pH fluctuations in the catalyst layer [71]. These fluctuations significantly affect the water dissociation rate of Ni-based catalysts. Previous discussions have focused on HER performance in various electrochemical cells, highlighting the relationship between catalyst structure, composition, and alkaline electrolytes [72, 73]. In pure-water-fed AEMs, the cations involved are primarily those from the anion-conducting ionomer phase, such as quaternary ammonium groups. The impact of these large, less mobile cations on interfacial water structure and local transport remains unclear [74–77]. In these systems, pH distribution at the active surface is influenced by factors like current, electrode treatments, and ionomer properties. Similar to PEM systems, OH^- transport in water is slower than proton transport, leading to significant pH gradients between the anode and cathode. Understanding these pH variations and their impact on HER kinetics is essential for optimizing AEMWE systems. Electrocatalysts resilient to local pH changes can reduce concentration polarization, enhancing reaction rates, device efficiency, and durability. Further research on interfacial behavior and operational conditions is crucial for improving performance and scaling practical applications.

3.2.2 | Relationship Between OH^- Transport and Electrolyte Composition

Electrolytes used in AEMWEs can be classified into three main types: hydroxide solutions, carbonate solutions, and pure water combined with a solid electrolyte. One of the key advantages of a water-only feed is the absence of OH^-, which allows for operation at higher temperatures without compromising the mechanical stability of the AEM [78]. The ionic conductivity of the AEM typically exceeds 0.08 S cm^{-1}, which, in theory, is sufficient to facilitate the transport of OH^- from the cathode to the anode. However, using pure water in combination with the AEI as the electrolyte presents several challenges. A primary hurdle is the need to develop stable AEIs with high ionic conductivity under neutral and mildly alkaline conditions, which remains an ongoing area of research. Additionally, the overall resistance of the cell is higher when pure water and AEI are used compared to systems utilizing thin AEMs and liquid alkaline electrolytes. Diluted KOH solutions, typically ranging from 3% to 10% by weight, are often preferred in these systems to mitigate the nucleophilic attack of OH^- on the AEM and AEI. However, while milder alkaline electrolytes help reduce these detrimental effects, they are less effective in promoting efficient OH^- transport within the catalyst layer. For example, the conductivity of KOH decreases by nearly an order of magnitude from 0.178 to 0.02 S cm^{-1}, when the concentration is reduced from 5% to 0.5% [79]. This significant drop in conductivity can hinder OH^- transport, which is crucial for efficient HER kinetics. In cases of low electrolyte concentrations, the absence of a buffering effect may lead to rapid and undesired pH changes within both the AEM and catalyst layers. Furthermore, even small concentrations of CO_2 dissolved in the electrolyte can increase the cell voltage (E_{cell}) due to the formation of carbonic acid, which can further complicate performance. The effects of water and various alkaline electrolyte concentrations on E_{cell}-j performance, as well as the high-frequency resistance (HFR) of single MEA cells, have been well-documented in the literature [80]. As shown in Figure 6a–c, higher KOH concentrations help reduce the E_{cell} value, primarily by lowering resistance, as reflected in the HFR. This reduction in resistance also benefits from an increase in the effective electrochemical surface area of the catalysts when using liquid alkali electrolyte feeds. The catalytic kinetics and stability are highly sensitive to the pH conditions in the system. Depending on the reaction order of the catalyst with respect to pH, both the HER kinetics and the catalyst stability can be significantly enhanced or altered by variations in pH [81, 82]. This makes understanding and controlling pH variations crucial for optimizing AEMWE performance. Tailoring the electrolyte composition and pH to the specific needs of the catalyst can lead to improvements in both reaction rate and long-term stability, which are essential for the commercial viability of AEMWE systems.

3.2.3 | The Role of AEM in OH^- Transfer

Traditional AEMs have low IEC (~1.5 meq·g^{-1}) and ammonium ion concentrations (~0.1 M), which are insufficient to provide the high pH environment (>13) necessary for efficient HER and OER processes. Additionally, many AEMs contain aromatic groups in the polymer backbone, which, under high OER voltages (>1.5 V),

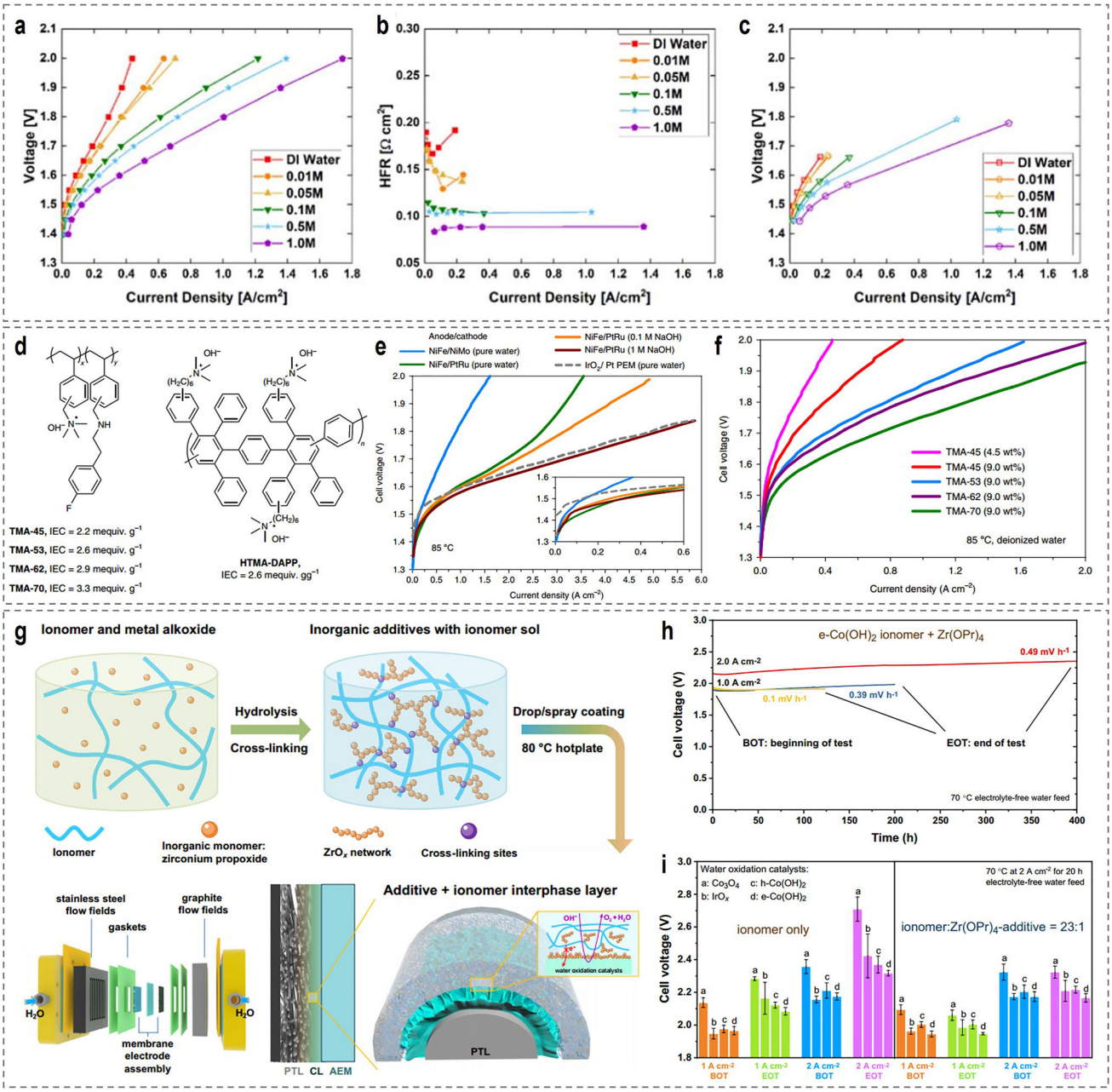

FIGURE 6 | (a) Voltage (Ecell) and (b) HFR versus j curves. (c) AEM electrolyzer performance with HFR compensated as a function of KOH concentration. Reproduced with permission [80]. Copyright 2021, IOP Publishing. (d) The chemical structure of the polymeric materials about trimethyl ammonium functionalized polystyrenes. (e) AEM electrolyzer performance catalyzed by a PGM-free anode. (f) The performance of MEAs employing the TMA ionomers. Reproduced with permission [78]. Copyright 2020, Nature Publishing. (g) Illustration of the engineering of a solid–electrolyte interphase in AEMWE devices. (h) Chronopotentiometry stability test using e-$Co(OH)_2$ anodes coated with additive-ionomers. (i) BOT and EOT cell voltages at 1.0 and 2.0 A cm^{-2} for different anode catalysts. Reproduced with permission [71]. Copyright 2025, Nature Publishing.

can undergo oxidation to form acidic phenols (p*K*a = 9.6). These phenols neutralize the OH^- ions in the membrane, leading to a significant drop in local pH. For example, when 25% of the phenyl groups in 1.6 M TMAOH were oxidized, the pH dropped from 14.2 to 11.4. This creates challenges in maintaining the desired high-pH conditions for optimal reaction kinetics. To address this issue, Li et al. designed and synthesized a high-quaternary ammonium poly(phenylene) AEM (TMA-x series, IEC 2.2–3.3 meq·g^{-1}) that eliminates the phenyl groups in the polymer backbone to prevent the formation of acidic phenols and maintain a stable high pH (Figure 6d) [78]. When combined with NiFe nanoflake OER catalysts, this AEM demonstrated excellent performance in a non-corrosive alkaline environment, achieving a current density of 2.7 A·cm^{-2} at 85°C and 1.8 V, approaching the performance of commercial PEMWE systems (Figure 6e). They also found that increasing the ionomer content from 4.5% to 9% enhanced the activity by 1.8 times (Figure 6f). Furthermore, at higher IEC, the current density increased, confirming that higher ammonium ion concentrations help maintain a high pH and promote the reaction.

However, as IEC increases, the hydrophilicity of the ionomer also increases, leading to swelling in pure water, reduced adhesion, and the loss of catalyst particles due to water flow, which causes rapid deactivation. Kang et al. employed a surface-coating strategy with anion exchange ionomers containing quaternary ammonium groups to engineer the membrane-electrode interface [83]. This ionomer coating extended the diffusion distance of OH^- towards the electrode, creating a local alkaline environment. Stability tests showed that Ni dissolution was significantly reduced, and measurements of local current density with segmented cells confirmed that the stability of the coated ionomer (ICNF) was six times greater than that of uncoated samples (NF). In situ Raman spectroscopy and XPS analysis also revealed that the ionomer coating effectively suppressed Ni oxidation, preventing the transformation to Ni^{3+}. This approach successfully addressed the catalyst dissolution issue under neutral pH conditions in AEMWE. The ionomer, which is chemically similar to the AEM, filled the porous structure of the NF, extending the OH^- diffusion distance and creating a local alkaline environment at the membrane-electrode interface, which prevents Ni dissolution under neutral pH. Additionally, the ionomer enhances the continuity of the membrane-electrode interface, reduces electrode resistance, and minimizes catalyst corrosion by inhibiting Ni oxidation. While this method helps mitigate the local dissolution of metals, it does not fully resolve the underlying challenge. In subsequent research, Hou et al. proposed an interface engineering strategy involving inorganic additives such as zirconium alkoxides [71]. These inorganic additives, when co-assembled with the ionomer, form a crosslinked interface layer rich in Zr–OH and Zr–O oligomers, as depicted in Figure 6g. This crosslinked layer improves the performance of pure water electrolysis cells, reducing the degradation rate to <0.5 mV h^{-1} at 2.0 A cm^{-2} under 70°C, representing an over 20-fold improvement compared to traditional systems (Figure 6h,i). The chemical crosslinking between the $Zr(OPr)_4$ hydrolyzed oligomers and the ionomer prevents direct oxidation of the ionomer by the catalyst, thanks to the oxidation resistance of ZrO_x. Additionally, the hydrophilicity of ZrO_x drives the assembly of OH^- transport channels, improving ion conductivity by 12% compared to pure ionomers (conductivity: 190 mS cm^{-1} vs. 170 mS cm^{-1}). This strategy provides a molecular-level balance between electron-blocking and ion-conducting capabilities, enabling better structural order and enhanced performance. Furthermore, the compatibility of this approach with a variety of catalysts (e.g., Co_3O_4, IrO_x) and ionomers demonstrates its potential for low-cost hydrogen production in AEMWEs. While significant progress has been made, challenges such as maintaining long-term stability and preventing catalyst deactivation under neutral pH conditions still persist. Future research should focus on optimizing the interaction between ionomers, catalysts, and the electrolyte, as well as enhancing the mechanical integrity and stability of AEMs.

3.3 | Catalyst Performance Descriptors

Electrocatalysts of Ni-based catalysts with excellent catalytic performance require high intrinsic activity, good electronic conductivity, and outstanding stability. Performance descriptors are a key tool to understand and optimize these properties. These descriptors, as summarized in Figure 7, derived from DFT calculations, can offer valuable insights into the electronic structural characteristics related to catalytic reactions, and also provide guidance for the design and synthesis of efficient electrocatalysts.

3.3.1 | Activity

Activity descriptors are central to decoding the catalytic mechanisms of Ni-based electrocatalysts, shedding light on the nature of active sites and their interactions with reaction intermediates. These descriptors encompass metrics that characterize bonding strengths, adsorption/desorption energetics, and electronic properties, enabling a detailed exploration of how structural and compositional features influence catalytic efficiency [84, 85]. For Ni-based catalysts, optimizing activity is particularly critical in reactions like the HER, where the kinetics of intermediate formation and product release dictate overall performance. A thorough investigation of activity descriptors facilitates the establishment of precise structure-performance relationships, providing a foundation for the strategic design and refinement of catalysts with enhanced intrinsic activity.

3.3.1.1 | Adsorption Energy. Adsorption energy, typically quantified as the Gibbs free energy of adsorption (ΔG), serves as a fundamental descriptor for evaluating the interaction strength between reaction intermediates and the catalyst surface. For HER, the ΔG_{H^*} holds particular significance, reflecting the balance between H* adsorption and its subsequent desorption as molecular H_2. According to the Sabatier principle, an optimal ΔG_{H^*} value close to 0 eV represents an ideal compromise, where the binding strength avoids being too weak to limit adsorption or too strong to restrict desorption. For Ni-based catalysts, this descriptor proves essential in determining their effectiveness for HER, especially in alkaline media, where the energy required for water dissociation (ΔG_{H2O}) introduces additional complexity. This energy governs the initial splitting of H_2O into H* and OH^-, often a rate-limiting step in alkaline conditions [86, 87]. DFT calculations demonstrate that adsorption energies depend heavily on the electronic environment of Ni sites, which can be tailored through compositional adjustments or structural modifications. By optimizing ΔG_{H^*} and ΔG_{H2O}, this descriptor directs the design of Ni-based catalysts with enhanced reaction kinetics and lower overpotentials, bridging theoretical insights with practical performance improvements.

For example, to systematically investigate the catalytic performance of non-precious metal materials and their integration with effective nanostructures, researchers aim to clarify the relationship between HER activity and key descriptors. Kim et al. explored the impact of incorporating oxygen-affinitive transition metals (Fe, Cr, Ti) into Ni films on HER activity [88]. To assess the effect of doping with these oxygen-affinitive transition metals on alkaline HER activity, the study constructed specific DFT calculation models. Using a (3×3) Ni (111) surface as the base, one surface Ni atom was substituted with a Ti, Cr, or Fe atom to represent the doped system (Figure 8a). For this system, the binding energies of H and OH at six distinct adsorption sites were calculated, revealing that the threefold hollow site provided the most stable adsorption for both species. The results indicated that doping Ni with Ti, Cr, or Fe increased the surface's ΔG_H and ΔG_{OH} values. This suggests that the introduction of oxygen-affinitive metals strengthens the catalyst surface's binding affinity

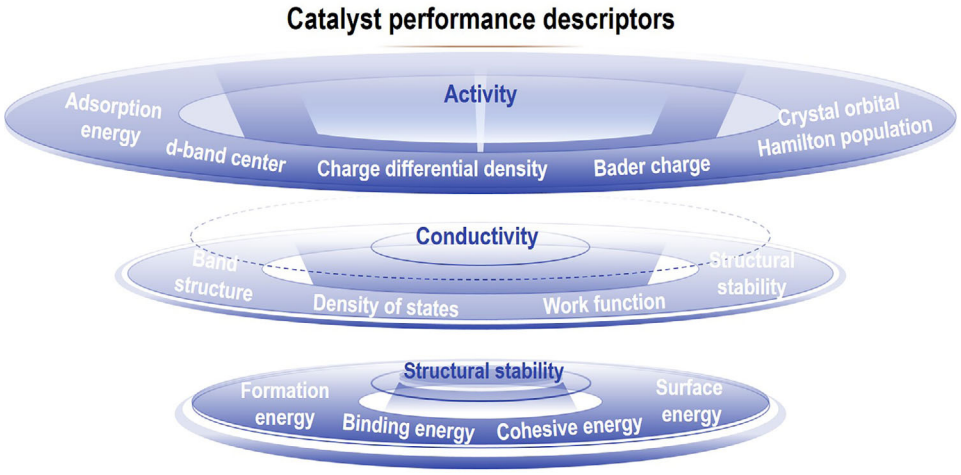

FIGURE 7 | Overview contents of the catalyst performance descriptors for electrocatalysis.

for H and OH. The data showed significant changes in binding energy, providing a quantitative foundation for subsequent analysis. By calculating the Gibbs free energy profile for HER, researchers found that the water dissociation activation energy on a Cr-Ni surface dropped considerably from 0.78 eV to 0.43 eV compared to a pure Ni surface (Figure 8b). Although Cr doping somewhat hindered hydrogen desorption, the Brønsted-Evans-Polanyi principle suggests that enhanced adsorption of H and OH lowers the water dissociation activation energy, making water molecule dissociation energetically more favorable and thus accelerating overall HER kinetics. Correlating experimentally measured alkaline HER activity (including overpotential and Tafel slope) with calculated ΔG_{OH} values revealed a volcano-type relationship (Figure 8c). This relationship aligns with the Sabatier principle, indicating that an active catalyst's affinity for reaction intermediates must strike a balance between being neither too strong nor too weak. Specifically, Ni and Fe-Ni catalysts exhibited relatively weak OH adsorption, struggling to effectively drive water dissociation, while Ti-Ni catalysts showed excessively strong OH adsorption, blocking active sites and limiting water molecule adsorption for alkaline HER. In contrast, the Cr-Ni catalyst demonstrated an optimal combination, with a suitable OH binding energy that balanced the promotion of water dissociation and the prevention of active site poisoning, explaining its superior performance among the M-Ni catalysts considered. Thus, DFT studies of ΔG_H and ΔG_{OH} elucidated the influence of oxygen-affinitive transition metal doping on alkaline HER activity.

3.3.1.2 | d-Band Center. The d-band center (ε_d), defined as the energy centroid of the d-orbitals relative to the Fermi level, stands as a critical electronic descriptor influencing a catalyst's interaction with adsorbates. Grounded in the d-band model, this parameter governs the strength of adsorbate-surface interactions: a higher (less negative) d-band center strengthens binding by enhancing the overlap between d-orbitals and adsorbate states, whereas a lower (more negative) position diminishes it [89, 90]. For Ni-based catalysts, the d-band center's position significantly shapes their catalytic activity, particularly in the HER, where it regulates the binding affinity of H* and OH* intermediates. DFT studies reveal that the d-band center of pristine Ni, typically located near the Fermi level, can shift through electronic perturbations caused by alloying, doping, or strain. These adjustments modify the filling of antibonding states during adsorption, directly affecting ΔG_{H^*} and reaction barriers. Consequently, the d-band center emerges as a powerful tool for tuning the electronic structure of Ni-based catalysts, establishing a predictive connection between electronic properties and catalytic performance that facilitates systematic optimization.

The d-band center theory closely ties to hydrogen adsorption strength and offers a means to predict the adsorption energies of reactants and intermediates on metal and metal compound surfaces, making it a valuable descriptor for HER [91]. Electrons from adsorbed hydrogen on transition metal electrocatalyst surfaces interact strongly with d-band electrons, forming chemical bonds whose strength depends on the d-orbital states of the electrocatalyst. Hybridization between the d-orbital electrons of the transition metal and the electrons of adsorbed hydrogen generates a fully occupied bonding orbital and a partially filled antibonding orbital. Variations in the energy levels of antibonding orbitals across different metals lead to differences in M-H bond strength, directly influencing electrocatalytic performance. Thus, an appropriately positioned d-band center can yield exceptional HER catalytic activity. In practical applications, however, traditional d-band theory struggles to accurately describe adsorption energies at hollow sites in multi-element alloys, as it simplifies real systems by treating elements separately. To address this, Chou et al. investigated ΔG_{H^*} on a series of Ni-M (M representing various metals) bimetallic alloy surfaces and proposed an improved d-band model with the formula $\varepsilon_d = A\varepsilon_{Ni} + (1\text{-}A)\varepsilon_M$, which accounts for hollow site adsorption [51]. DFT calculations demonstrated a linear relationship between ΔG_{H^*} and the refined d-band center, with NiCu exhibiting a ΔG_{H^*} value near the optimum (Figrue 8d,e). Introducing O atoms to the NiM surface accelerated water dissociation (Figrue 8f), and the resulting O-NiCu catalyst excelled in alkaline HER, achieving an overpotential of just 23 mV at 10 mA cm^{-2}, a Tafel slope of 34.1 mV dec^{-1}, and excellent stability over 100 h, surpassing most reported HER catalysts.

3.3.1.3 | Charge Differential Density and Bader Charge. Charge differential density and Bader charge analysis offer complementary perspectives on the electronic interactions occurring

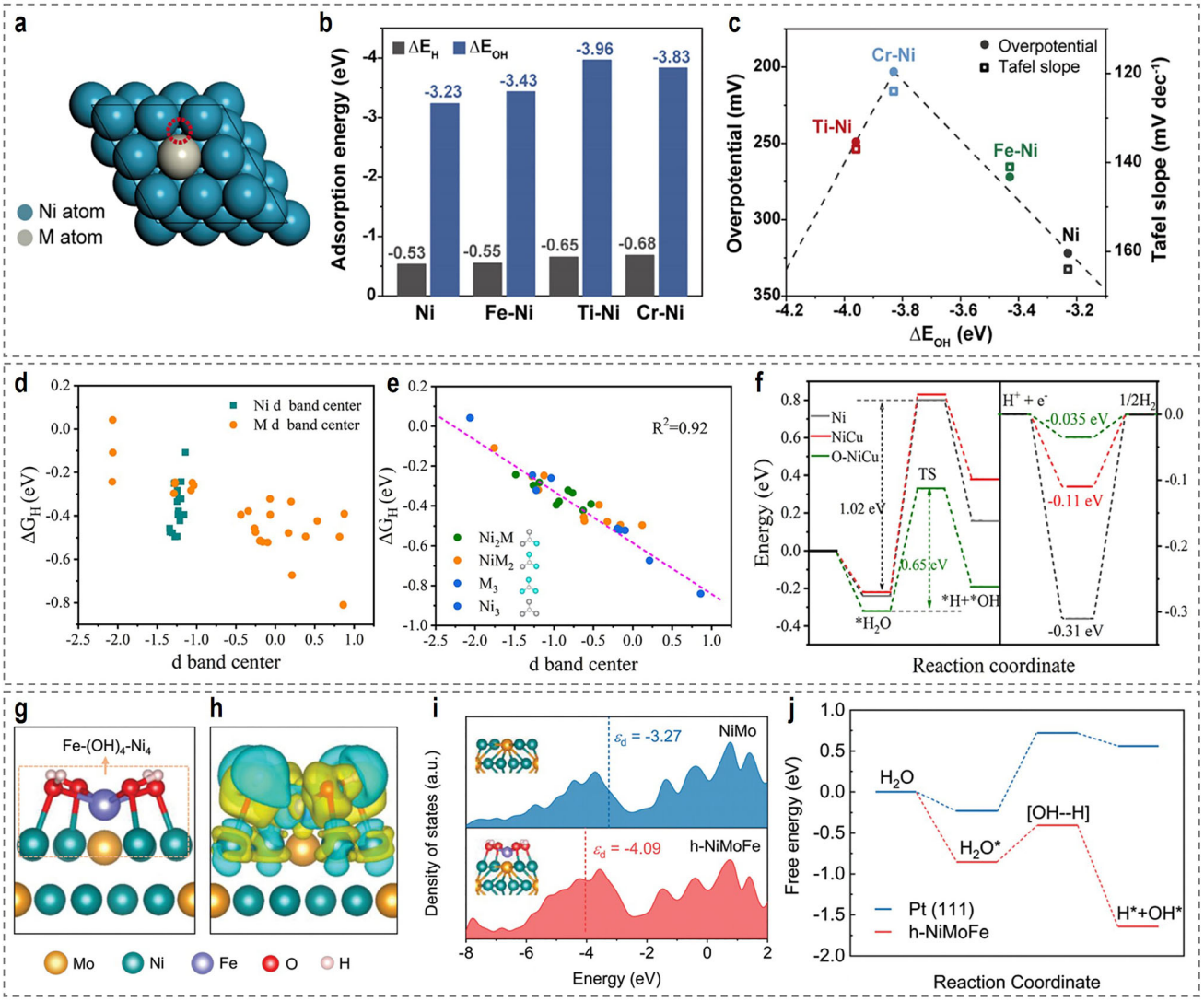

FIGURE 8 | Theoretical calculation of H- and OH-binding energies for Ni and M-Ni surfaces. (a) DFT model of Ni(111) surface in which a Ni atom is replaced with a M atom. The most stable adsorption site, the 3-fold hollow site, is marked by red dotted-line circle. (b) Calculated ΔEH and ΔEOH for Ni(111) and M-Ni(111) surfaces. (c) Volcano plot of overpotentials at 10 mA cm^{-2} and Tafel slopes as a function of the ΔEOH for M-Ni and Ni catalysts. Reproduced with permission [88]. Copyright 2021, American Chemical Society. (d) Dependence of ΔGH on the traditional d-band center of Ni and M atoms. (e) Dependence of ΔGH on the improved d-band center. (f) Corresponding energy differences for the water dissociation process and the diagram of ΔGH for Ni, NiCu, and O-NiCu. Reproduced with permission [51]. Copyright 2022, Wiley-VCH. (g) Calculated relaxed configuration of an Fe-$(OH)_4$-Ni_4 motif on a Ni_4Mo(002) slab and (h) the corresponding charge density difference in this configuration. (i) Calculated PDOS of Ni in the NiMo slab (top) and the h-NiMoFe slab (bottom). (j) Adsorption energies for dissociated H_2O on h-NiMoFe and Pt (111). Reproduced with permission [96]. Copyright 2021, Royal Society of Chemistry.

at the catalyst surface [92, 93]. Charge differential density visualizes the spatial redistribution of electrons upon adsorption, pinpointing areas of electron accumulation or depletion that affect reactivity. Bader charge analysis, in contrast, quantifies the net charge transfer between atoms, providing a precise assessment of electronic perturbations at active sites. For Ni-based catalysts, these descriptors clarify how charge redistribution influences the stabilization of reaction intermediates and the activation of critical reaction steps [94, 95]. In the HER, electron donation or withdrawal at Ni sites alters the binding strength of H* or OH^-, directly affecting adsorption energies and reaction kinetics. DFT calculations indicate that charge transfer often stems from the introduction of heteroatoms or the creation of interfaces, generating localized electronic environments that enhance catalysis.

By linking charge dynamics to catalytic activity, these descriptors deepen the understanding of electronic factors driving performance, informing the design of Ni-based catalysts with optimized charge distributions for improved reactivity. For instance, Liu et al. synthesized FeO_x-modified Ni_4Mo nanoparticles supported on MoO_2 nanosheets, denoted as h-NiMoFe [96]. This h-NiMoFe catalyst exhibited exceptional performance in 1.0 M KOH solution. Computational results revealed that a Fe-$(OH)_4$-Ni_4 motif, where one Fe atom connects to four hydroxylated Ni sites, forms on the Ni_4Mo surface (Figure 8g). Through Fe-OH-Ni bonds, electrons are withdrawn from Ni atoms, resulting in an increase in unoccupied states at Ni sites. Charge density difference maps, with yellow and cyan regions representing electron accumulation and depletion, respectively, clearly illustrate electron transfer

from Ni atoms to other regions (Figure 8h). This finding aligns with X-ray absorption spectroscopy results, which confirmed significant changes in the charge distribution at Ni sites upon iron incorporation, further validating the presence of charge transfer. The altered electronic structure of Ni sites in h-NiMoFe positively impacts its HER performance in multiple ways. First, the increased unoccupied states at Ni sites enhance the catalyst's bonding behavior with hydrogen. Analysis of the partial density of states (PDOS) and d-band center position shows that the d-band center energy of Ni in h-NiMoFe is more negative than in the iron-free NiMo catalyst (Figure 8i), bringing the ΔG_{H^*} close to 0 eV. This near-optimal value greatly facilitates the adsorption and desorption of hydrogen, accelerating the hydrogen adsorption/desorption steps in HER. Second, this electronic adjustment promotes water dissociation. Compared to the conventional Pt (111) catalyst, h-NiMoFe exhibits a lower energy barrier and faster reaction kinetics for water splitting (Figure 8j), creating more favorable conditions for water dissociation and markedly boosting HER activity in alkaline media.

3.3.1.4 | Crystal Orbital Hamilton Population. The Crystal Orbital Hamilton Population (COHP) serves as an advanced descriptor that dissects the bonding interactions between a catalyst and adsorbates by analyzing the electronic band structure. COHP separates these interactions into bonding and antibonding components, with the integrated COHP (ICOHP) offering a quantitative measure of bond strength, where a more negative ICOHP signifies stronger bonding [97]. For Ni-based catalysts, COHP proves especially useful in evaluating the interactions of Ni sites with H* or OH^- intermediates during the HER. DFT-derived COHP results illustrate how the electronic overlap between Ni d-orbitals and adsorbate orbitals determines the stability of reaction intermediates, affecting both adsorption energies and reaction barriers. Differences in ICOHP across various Ni-based systems highlight the influence of structural or compositional changes on bonding characteristics, establishing a direct connection to catalytic activity. This descriptor thus emerges as a robust tool for precisely adjusting the strength of catalyst-adsorbate interactions, facilitating the optimization of Ni-based catalysts through a detailed understanding of orbital-level contributions to performance. Yang et al. developed a bimetallic nitride heterostructure electrode (WN-NiN/CFP) with excellent lattice matching and high conductivity for alkaline water electrolysis to produce hydrogen [98]. To uncover the origins of the high HER activity in the Ni_3N-WN heterostructure, the study employed ICOHP to thoroughly investigate the orbital interactions of H-W (Figure 9a) and O-W (Figure 9b). The analysis revealed that the Ni_3N-WN heterostructure exhibits weaker adsorption of H and O compared to standalone WN, attributed to its integrated ICOHP values being closer to the Fermi level (ICOHP of 3.77 eV for H and 5.9 eV for O). Further examination showed that the key orbital interactions between H 1s and W 5d on the Ni_3N-WN and WN surfaces primarily stem from the W $5d_{yz}$ orbital (52.26% contribution, integrated ICOHP of 2.09 eV) and W $5d_{xz}$ orbital (49.83% contribution, integrated ICOHP of 1.88 eV), respectively, while the O 2p and W 5d interactions on both surfaces are predominantly driven by the W $5d_{xz}$ orbital. These findings indicate that the unique electronic structure of the Ni_3N-WN heterostructure effectively modulates O-W and H-W interactions through interfacial charge escape and capture behaviors, thereby enhancing the HER process. The strength of ICOHP lies in its ability to provide quantitative insights into atomic orbital interactions from an electronic structure perspective, offering a microscopic view of a material's chemical properties and reactivity. Its results are intuitive and straightforward, facilitating comparative analyses of orbital interaction differences across systems. However, its limitations include reliance on precise theoretical models and computational methods, which can render the process complex. In handling intricate multiphase systems, COHP may face constraints from model simplifications and computational accuracy, necessitating a comprehensive interpretation that accounts for multiple factors.

Understanding the collective interactions between these descriptors is vital for achieving a comprehensive understanding of the catalyst's performance. However, the relationships between them are complex and still not fully unified, especially when considering the Ni electronic configuration and its effect on HER activity. Current research suggests that while d-band theory and ΔG_{H^*} are useful for guiding catalyst design, other descriptors, such as charge density and orbital interactions, also play an important role in modulating the adsorption strength and the kinetics of intermediate states. A unified theoretical framework that connects these descriptors to Ni's electronic structure and HER performance remains an open challenge. Bridging this gap could lead to the development of scaling relations that more accurately predict the catalyst's intrinsic activity, considering all contributing factors simultaneously. Future work is needed to develop a more holistic understanding of how these descriptors interact and influence one another, potentially using advanced computational models or machine learning techniques. This could ultimately lead to the creation of more efficient and predictable electrocatalysts for the HER, with the ability to rationalize catalyst performance across a range of structural and compositional modifications.

3.3.2 | Conductivity

Electrical conductivity is a critical attribute of Ni-based electrocatalysts, underpinning their ability to facilitate rapid electron transfer between the catalyst surface, reactants, and reaction intermediates. Efficient electron transport accelerates charge redistribution and transition processes at active sites, directly enhancing reaction rates and overall catalytic performance [99, 100]. This is particularly vital in electrochemical reactions such as the HER, where the timely delivery of electrons dictates the kinetics of intermediate formation and product release. Conductivity in Ni-based catalysts is governed by their electronic structure, which can be systematically probed using descriptors derived from DFT calculations [101]. A deep understanding of these conductivity descriptors elucidates the mechanisms driving electron transfer, offering valuable insights into how structural and compositional modifications can optimize charge transport properties. Such knowledge is essential for designing Ni-based electrocatalysts with enhanced efficiency and applicability in energy conversion systems.

3.3.2.1 | Band Structure/Density of States. The band structure and density of states (DOS) are foundational descriptors of a catalyst's electronic conductivity, providing a comprehensive view of the energy distribution and availability of electronic states

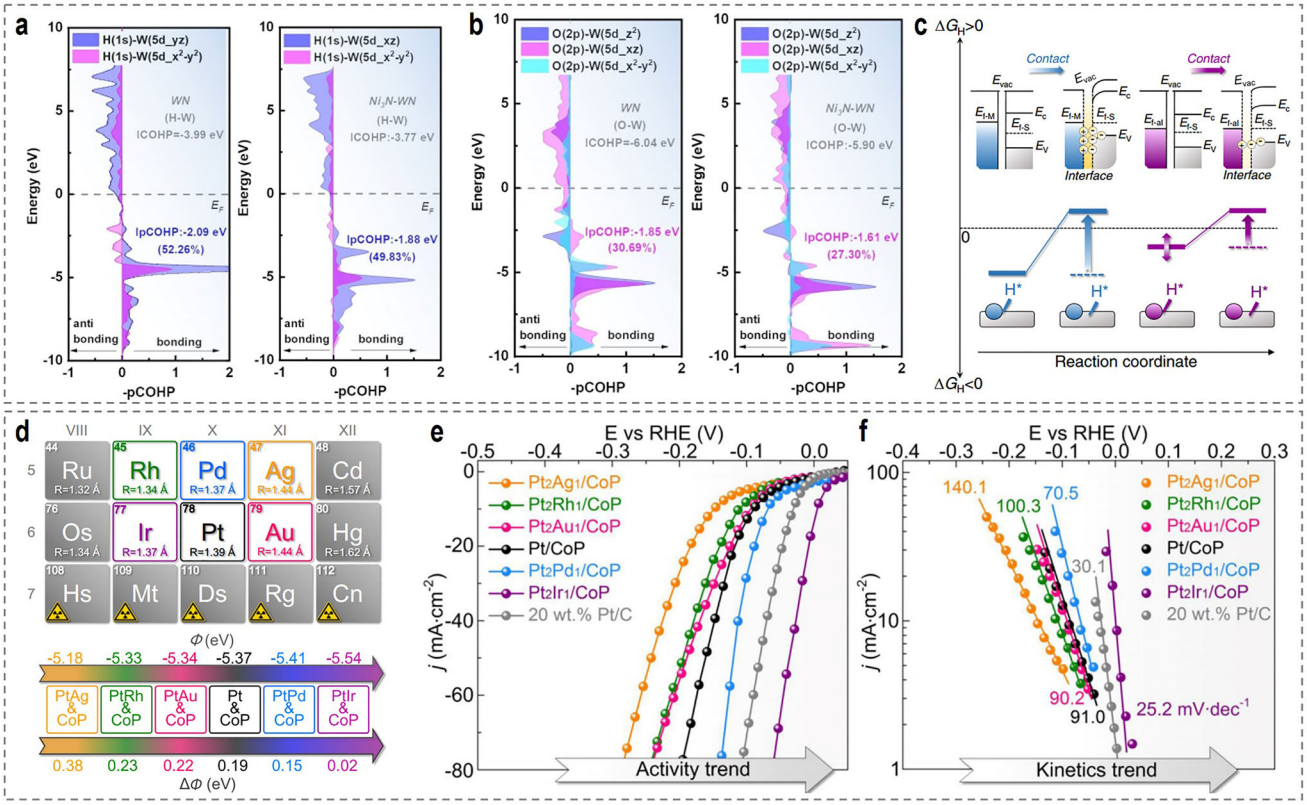

FIGURE 9 | The projected crystal orbital Hamilton population (pCOHP) of H (from H*) (a) and O (from OH*) (b) with W orbitals of WN and Ni3N-WN. Reproduced with permission [98]. Copyright 2025, Wiley-VCH. (c) Schematic illustrations of the interfacial electronic configurations and hydrogen spillover phenomenon in hydrogen spillover-based binary (HSBB) catalysts. (d) Design of PtM/CoP model catalysts with the controllable ΔΦ. (e) LSV curves of various Pt2M1/CoP and Pt/CoP catalysts (1.0 wt%) and Pt/C (20 wt%) benchmarks. (f) LSV-derived Tafel plots for various catalysts. Reproduced with permission [106]. Copyright 2021, Nature Publishing.

[102]. The band structure delineates the allowed energy levels for electrons within the catalyst's lattice, distinguishing between metallic, semiconducting, or insulating behavior. For Ni-based catalysts, a metallic band structure, characterized by the absence of a bandgap and a continuous distribution of states across the Fermi level, is often desirable, as it ensures high electron mobility and efficient charge transport. The DOS, which quantifies the number of electronic states per energy interval, further refines this picture by revealing the density of states available for electron occupation or excitation near the Fermi level (E_F). A high DOS at E_F correlates with enhanced conductivity, as it facilitates rapid electron transfer to or from adsorbates during catalytic reactions [103]. With respect to Ni-based catalysts, DFT calculations of the band structure and DOS reveal how electronic properties are influenced by the catalyst's composition and structure. For instance, the introduction of heteroatoms or defects can narrow or eliminate bandgaps, shifting the material toward metallic behavior and increasing the DOS at E_F. This enhancement in state availability reduces charge transfer resistance, accelerating reaction kinetics. Moreover, the hybridization between Ni d-orbitals and states from dopants or substrates can broaden the conduction band, further boosting electron delocalization. The band structure and DOS thus serve as critical tools for predicting and optimizing conductivity, linking electronic characteristics to catalytic performance and guiding the design of Ni-based catalysts with superior electron transport capabilities. Li et al. synthesized the single-atom nickel (Ni SA) encapsulated in nanosheet-coiled rGO-cetyltrimethyl ammonium bromide (CTAB)-MoS_2 nanoflowers and used for HER [104]. In-depth research was conducted on materials such as pristine MoS_2, rGO-CTAB-MoS_2, and Ni SA/rGO-CTAB-MoS_2. By calculating the PDOS of these materials, it was found that, compared with pristine MoS_2, Ni SA/rGO-CTAB-MoS_2 exhibits a higher density of electronic states near the Fermi level. This result indicates that in the Ni SA/rGO-CTAB-MoS_2, the distribution state of electrons is more conducive to their movement within the material, which is directly reflected in the enhanced electrical conductivity of the material. This analysis method based on DOS clearly reveals the close relationship between the microscopic electronic structure and the macroscopic electrical conductivity of the material, providing a microscopic basis for a deeper understanding of the electrical properties of the materials.

3.3.2.2 | Work Function. The work function (Φ), defined as the minimum energy needed to extract an electron from the Fermi level to the vacuum level, serves as a crucial descriptor of a catalyst's surface electronic properties and its capacity for electron transfer [105]. A lower work function reflects a greater ability to donate electrons, easing the transfer of electrons from the catalyst to reaction intermediates, whereas a higher work function implies stronger electron affinity, which may assist in stabilizing electron-deficient species. For Ni-based catalysts, the work function closely relates to their conductivity and catalytic efficiency, as it determines the energy barrier for electron

exchange at the catalyst-electrolyte interface. In electrochemical processes like the HER, an optimal work function ensures effective charge injection into adsorbed intermediates, reducing energy losses and boosting reaction rates. DFT calculations show that the work function of Ni-based catalysts responds sensitively to surface modifications and changes in electronic structure [106]. Elements such as surface orientation, doping, or the creation of heterointerfaces can adjust Φ by modifying the surface dipole or redistributing electron density near the Fermi level. For instance, electron-rich dopants may decrease the work function by elevating surface electron density, enhancing electron transfer to reactants. In contrast, electron-withdrawing species can increase Φ, potentially improving the catalyst's ability to accept electrons from intermediates. The relationship between the work function and the DOS at the E_F holds particular importance, as a high DOS often corresponds to a lower Φ, enhancing conductivity [107]. This descriptor thus offers a direct assessment of the catalyst's electron transfer efficiency, paving the way for tailoring Ni-based catalysts to achieve superior charge transport and catalytic performance through surface and electronic engineering.

Ma et al. explored the influence of the work function difference ($\Delta\Phi$) in metal-support systems on HER performance, identifying its critical role in the hydrogen spillover phenomenon [106]. As illustrated in Figure 9c, a large work function difference between the metal and the support leads to charge accumulation at the interface, causing strong proton adsorption and creating a high energy barrier for hydrogen transfer, which impedes hydrogen spillover from the metal to the support and reduces HER activity. Conversely, a smaller $\Delta\Phi$ induces charge dilution and redistribution at the interface, weakening proton adsorption and facilitating hydrogen spillover, thereby enhancing HER performance. To test this hypothesis, the researchers meticulously designed and synthesized a series of Pt alloy-CoP catalysts with the controllable $\Delta\Phi$ (Figure 9d). By precisely tuning the alloy composition, they effectively controlled $\Delta\Phi$. The experimental results proved striking, with Pt_2Ir_1/CoP emerging as the standout performer among the catalysts, exhibiting a $\Delta\Phi$ of just 0.02 eV and exceptional HER performance (Figure 9e,f). At a current density of 20 $mA{\cdot}cm^{-2}$, this catalyst achieved an overpotential of only 7 mV, a Tafel slope of 25.2 $mV{\cdot}dec^{-1}$, and a mass activity of 110 $A{\cdot}mg_{Pt}^{-1}$ at −50 mV vs. RHE, far surpassing commercial benchmark catalysts and most reported advanced HER electrocatalysts. These findings demonstrate that the $\Delta\Phi$ serves as a pivotal criterion for designing binary HER electrocatalysts based on hydrogen spillover. Besides the regulation of hydrogen spillover, by constructing a built-in electric field (BEF) strategy, a catalyst system with a heterojunction structure and a large $\Delta\Phi$ was prepared, which can also effectively enhance the alkaline HER activity. For example, Zhao et al. constructed a Ni_2P-CoCH/CFP nanowire array for use as a HER catalyst [108]. Constructing a BEF in Ni_2P-CoCH can promote the asymmetrical distribution of charges, causing electrons to transfer from CoCH to Ni_2P, forming an electron-enriched Ni_2P region and an electron-deficient CoCH region. This is beneficial for optimizing the adsorption of hydrogen/oxygen intermediates. In the HER process, the electron-enriched side of Ni_2P optimizes the adsorption of H*, promotes the hydrogen adsorption kinetics, and improves the catalytic activity.

3.3.3 | Structural Stability

Structural stability is a cornerstone of Ni-based electrocatalysts, directly influencing their efficiency, operational lifespan, and selectivity in catalytic reactions. Catalysts lacking stability are susceptible to degradation mechanisms such as deactivation, dissolution, or agglomeration, which compromise catalytic activity and often lead to undesirable by-product formation. These instabilities can arise from harsh electrochemical environments, including corrosive electrolytes or fluctuating potentials, making long-term durability a critical design parameter. For Ni-based catalysts, achieving robust stability is essential not only to maintain high performance over extended periods but also to ensure economic viability in applications like water electrolysis. Stability descriptors, derived from DFT calculations, provide a quantitative lens through which to assess and enhance the structural integrity of these materials. By probing the energetic and thermodynamic factors governing stability, these descriptors offer critical insights into degradation pathways and guide the development of Ni-based catalysts with improved resistance to structural breakdown, laying the foundation for electrocatalytic systems.

3.3.3.1 | Formation Energy. Formation energy acts as a key descriptor that quantifies the thermodynamic stability of a catalyst by measuring the energy change linked to its formation from constituent elements in their standard states [109]. A more negative formation energy signifies higher stability, indicating a stronger energetic favorability for the catalyst's structure compared to its dissociated components. For Ni-based catalysts, formation energy provides a critical measure of phase stability, revealing whether a specific composition or crystal structure can endure the challenges of synthesis and operational environments. DFT calculations show that formation energy depends heavily on factors like lattice composition, coordination environment, and defect incorporation, all of which affect the material's resistance to decomposition or phase changes. In electrocatalytic settings, a stable formation energy ensures that the catalyst withstands dissolution into ionic species under applied potentials or in harsh electrolytes, a frequent degradation mechanism for Ni-based materials [110]. Additionally, formation energy indicates the likelihood of preserving catalytically active phases during extended operation, preventing shifts to less active or amorphous forms. By refining formation energy through compositional adjustments or structural engineering, this descriptor offers a predictive approach to bolstering the inherent stability of Ni-based catalysts, ensuring their durability and effectiveness in applications.

For instance, Yang et al. reported a Ni_3Mo integrated electrode with edge dislocation strain enhancement (D-Ni_3Mo/NF) [111]. Using DFT calculations, they constructed Ni_3Mo models under varying strain conditions to study Mo atom dissolution. The dissolution of Mo atoms is tied closely to the energy required to form vacancies on the alloy surface, known as the vacancy formation energy of Mo. When compressive strain is applied to the Ni_3Mo alloy, the bond lengths of Mo-M (where M represents Ni or Mo) shorten, and the bond energy strengthens. Computational data revealed that the vacancy formation energy of Mo rises significantly from 0.63 eV to 0.96 eV under this strain. This increase implies that, during alkaline HER, Mo atoms face greater difficulty detaching from the alloy surface to

form vacancies, as they must overcome a higher energy barrier, effectively suppressing Mo dissolution. These theoretical findings provide a quantitative basis for understanding the stability of Mo atoms under different strain conditions.

3.3.3.2 | Binding Energy and Cohesive Energy. Binding energy and cohesive energy are closely related descriptors that assess the strength of atomic interactions within the catalyst, offering insights into its resistance to structural disintegration. Binding energy typically refers to the energy required to dissociate a specific bond or adsorbate from the catalyst surface, reflecting the stability of surface-active sites under reaction conditions. Cohesive energy, on the other hand, measures the total energy required to separate all atoms in the bulk material into isolated gaseous atoms, providing a holistic view of lattice stability [112]. For Ni-based catalysts, both descriptors are critical for understanding how the material withstands mechanical stresses, thermal fluctuations, or chemical attacks that could lead to agglomeration or fracturing. DFT calculations demonstrate that high binding and cohesive energies correlate with enhanced structural integrity, as they indicate strong interatomic forces that resist atomic displacement or leaching. In electrocatalysis, binding energy is particularly relevant for surface stability, where weak interactions may result in the loss of active sites through dissolution or reconstruction. Cohesive energy complements this by ensuring the bulk framework remains intact, preventing pulverization or phase segregation [113, 114]. The interplay between these energies is influenced by factors such as lattice strain, heteroatom incorporation, or interfacial effects, which can either reinforce or destabilize the structure. By leveraging these descriptors, researchers can design Ni-based catalysts with robust atomic cohesion and surface resilience, mitigating degradation and extending operational lifetimes.

3.3.3.3 | Surface Energy. Surface energy quantifies the excess energy associated with the catalyst's surface relative to its bulk, serving as a key descriptor of surface stability and resistance to morphological changes. A lower surface energy indicates a more stable surface, less prone to reconstruction, dissolution, or agglomeration, while a higher surface energy suggests greater thermodynamic instability, driving processes like sintering or facet reformation [115]. For Ni-based catalysts, surface energy is a critical determinant of long-term performance, as the surface is the primary interface for catalytic reactions and is directly exposed to the electrolyte environment. DFT calculations of surface energy provide a means to evaluate how surface termination, orientation, and chemical composition influence stability under operational stresses. In electrocatalytic systems, surface energy governs the susceptibility of Ni-based catalysts to degradation mechanisms such as corrosion or Ostwald ripening, where atoms migrate from high-energy surfaces to lower-energy regions, leading to particle growth and activity loss. The descriptor also reflects the energetic cost of maintaining catalytically active facets, which may reconstruct into less active configurations if surface energy is unfavorable [116]. Modifications such as doping, alloying, or the creation of protective overlayers can modulate surface energy, stabilizing high-activity surfaces against degradation. By optimizing surface energy, this descriptor enables the design of Ni-based catalysts with durable surface structures, ensuring sustained performance and selectivity over extended reaction cycles. Typically, NiMo-based catalysts show promise in alkaline HER due to their nanorod array structure and elemental properties, yet the poor stability stemming from Mo's susceptibility to dissolution remains a challenge. Wang et al. developed an interstitial B-doped Ni_4Mo nanoarray catalyst ($B_{4.7}$-Ni_4Mo/NF) [117]. The strong interaction between B and Mo enhances Mo's stability within $B_{4.7}$-Ni_4Mo/NF, elevating the detachment energy of Mo from 1.72 eV to 1.97 eV, thereby increasing the energy barrier for Mo dissolution. This effectively curbs Mo dissolution in alkaline solutions, mitigating catalyst deactivation caused by Mo loss and consequently improving the catalyst's overall stability.

3.4 | Catalyst Preparation Strategies

With the continuous advancement of nanotechnology, a wide variety of strategies for synthesizing electrocatalysts have emerged, enabling the tailored design of catalysts with specific morphologies, compositions, and physicochemical properties [118, 119]. These developments have enabled the fabrication of highly efficient Ni-based catalysts for HER. Researchers have been able to fine-tune various synthesis parameters to control factors such as particle size, surface area, and structural stability. These strategies have proven effective in laboratory-scale studies, leading to significant advances in catalyst design and performance. However, it is important to highlight that most of the synthesis methods developed in laboratory settings are currently limited to producing catalysts at the gram scale, with challenges in scaling up production for commercial applications [120–122]. Consequently, there are three promising catalyst preparation strategies that show great potential for industrial-scale production, which could meet the growing demands of AEMWE commercialization. These strategies, namely electrodeposition, solvothermal synthesis, and thermal treatment calcination, have demonstrated success in laboratory-scale synthesis and, with further optimization, could be adapted for large-scale production [123–125]. The following sections provide a brief overview of these three strategies, highlighting their advantages, challenges, and potential for scalability when used for AEMWE, as depicted in Figure 10.

3.4.1 | Electrodeposition

Electrodeposition involves the redox electrochemical reaction of metal ions under an applied potential to yield the desired electrocatalyst. Precise control over reaction parameters such as current density, potential, duration, additives, pH, and temperature enables the production of electrocatalysts with varying sizes, morphologies, and physicochemical properties. For instance, Xu et al. employed a one-step electrodeposition method to fabricate ND-Ni catalysts on nickel foam (NF) (Figure 11a). The three-dimensional dendritic structure of ND-Ni, composed of ultrafine nickel grain chains, offers a high specific surface area, facilitating the exposure of active sites and increasing the reaction contact area [126]. The orderly assembly of grains forms smooth internal electron transport channels, reducing resistance and enhancing electron conduction efficiency. In 1.0 M KOH, the ND-Ni catalyst exhibits outstanding HER performance, surpassing commercial Raney Ni catalysts. However, the scalability of electrodeposition remains limited by significant constraints, including

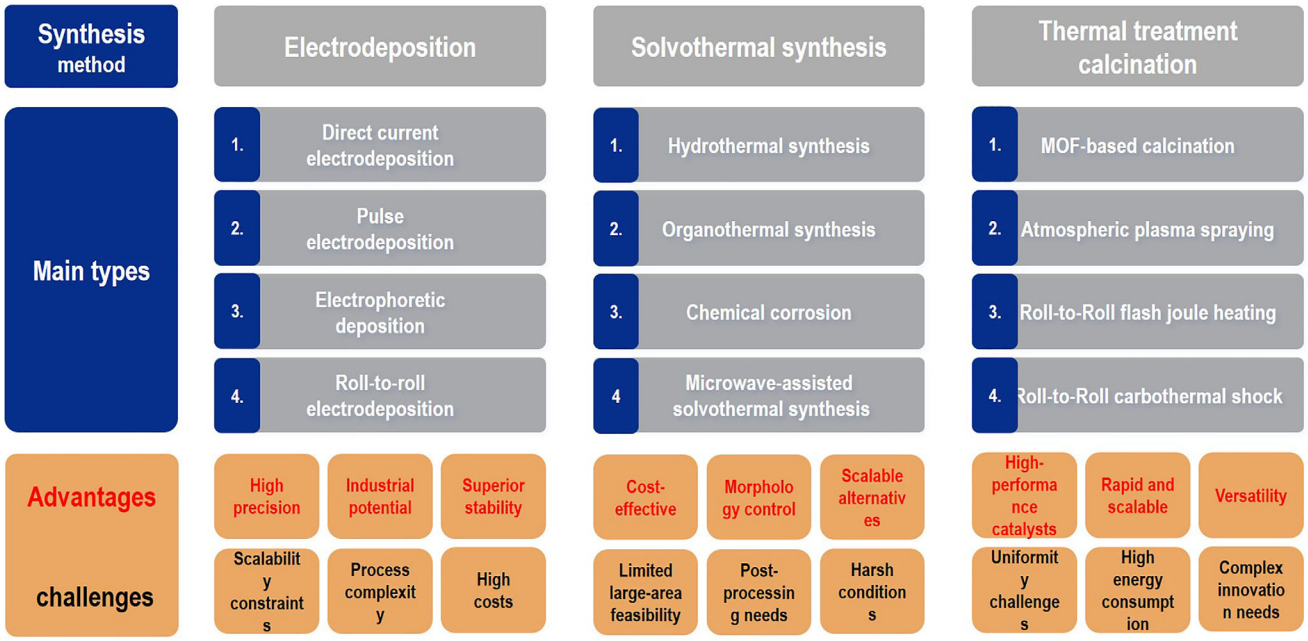

FIGURE 10 | A comparison between different catalyst synthesis methods.

non-uniform current distribution, mass transport limitation, and difficulty in controlling microstructure at scale, particularly for preparing large-area electrodes [127]. For example, Luo et al. investigated the effect of electrodeposition conditions on the uniformity and profiles of electroplated individual Ni microstructures, showing significant dependence on the plating current density and temperature [128]. Meanwhile, Yeh et al. studied the effects of pulse parameters, including pulse on-time, pulse off-time, and peak-current density, on the grain size, surface morphology, and crystal orientation of electrodeposited NiFe alloy [129]. Their study found that current density is a key parameter influencing the microstructure and performance of electrodeposited NiFe coatings. As current density increases, the grain size of the coating significantly refines, microhardness improves, hydrogen content decreases, and current efficiency increases. These studies highlight the complexity of achieving uniform coatings on large-scale electrodes.

Of course, recent research efforts have also been dedicated to addressing these challenges, with a focus on developing strategies for fabricating large-area electrodes via electrodeposition. For instance, Yang et al. fabricated pure nickel nano-pyramid arrays (NNAs) with high-density crystal facet steps as electrodes for the HER by leveraging spiral dislocation-dominated growth kinetics induced by an electrodeposition process [130]. In 1.0 M KOH electrolyte, the NNA electrode exhibited an overpotential as low as 469 mV at a current density of 5000 mA cm^{-2} and maintained stable operation for 7000 h at 1000 mA cm^{-2}, outperforming most reported catalysts and commercial platinum catalysts. To evaluate the feasibility of large-scale NNA electrode production, they developed a pilot-scale roll-to-roll electrodeposition system capable of processing films up to 300 mm in width (Figure 11b), demonstrating potential for industrial applications. Using this system, large-area NNA electrodes measuring 20 × 100 cm were successfully fabricated on commercial NF. These NNA electrodes, with a geometric area of 161 cm^2, were integrated as cathodes in a commercial hydrogen generator (HFH-300). After 60 days of testing, the HER activity of the NNA electrodes showed negligible changes in polarization curves, whereas the HER activity of commercial Pt/Ti electrodes significantly deteriorated, highlighting the superior stability of NNAs under high current densities.

3.4.2 | Solvothermal Synthesis

Solvothermal synthesis refers to chemical reactions conducted in a sealed system above the solvent's boiling point, typically generating high temperatures and pressures. Compared to other preparation methods, solvothermal synthesis produces materials with small particle sizes, uniform distribution, controllable morphologies, and low costs. Among solvothermal techniques, hydrothermal synthesis stands out as the most widely applied. Over the past few decades, hydrothermal reactions have been extensively utilized in materials chemistry and science to develop advanced inorganic materials and functional ceramics, particularly for preparing transition metal hydroxides and oxides. These synthesized materials can undergo subsequent processing to yield Ni-based catalysts with diverse phase structures or compositions, thereby enhancing catalytic activity. Despite its unique advantages in tailoring catalyst micro- and nano-morphologies, solvothermal synthesis faces certain challenges that require attention. The fabrication of large-area electrodes using hydrothermal techniques remains highly challenging. As an alternative to hydrothermal growth, chemical corrosion at room temperature offers an effective strategy for the rapid preparation of large-area electrodes. Zou et al. reported a rapid sulfidation method to transform stainless steel mesh into highly efficient OER electrodes at room temperature [131]. By reacting stainless steel mesh in a solution containing $FeCl_3$ and $Na_2S_2O_3$, electrodes with NiFeCr multimetallic sulfide surfaces (MS/SS) were produced (Figure 11c), enabling scalable fabrication of electrodes on the

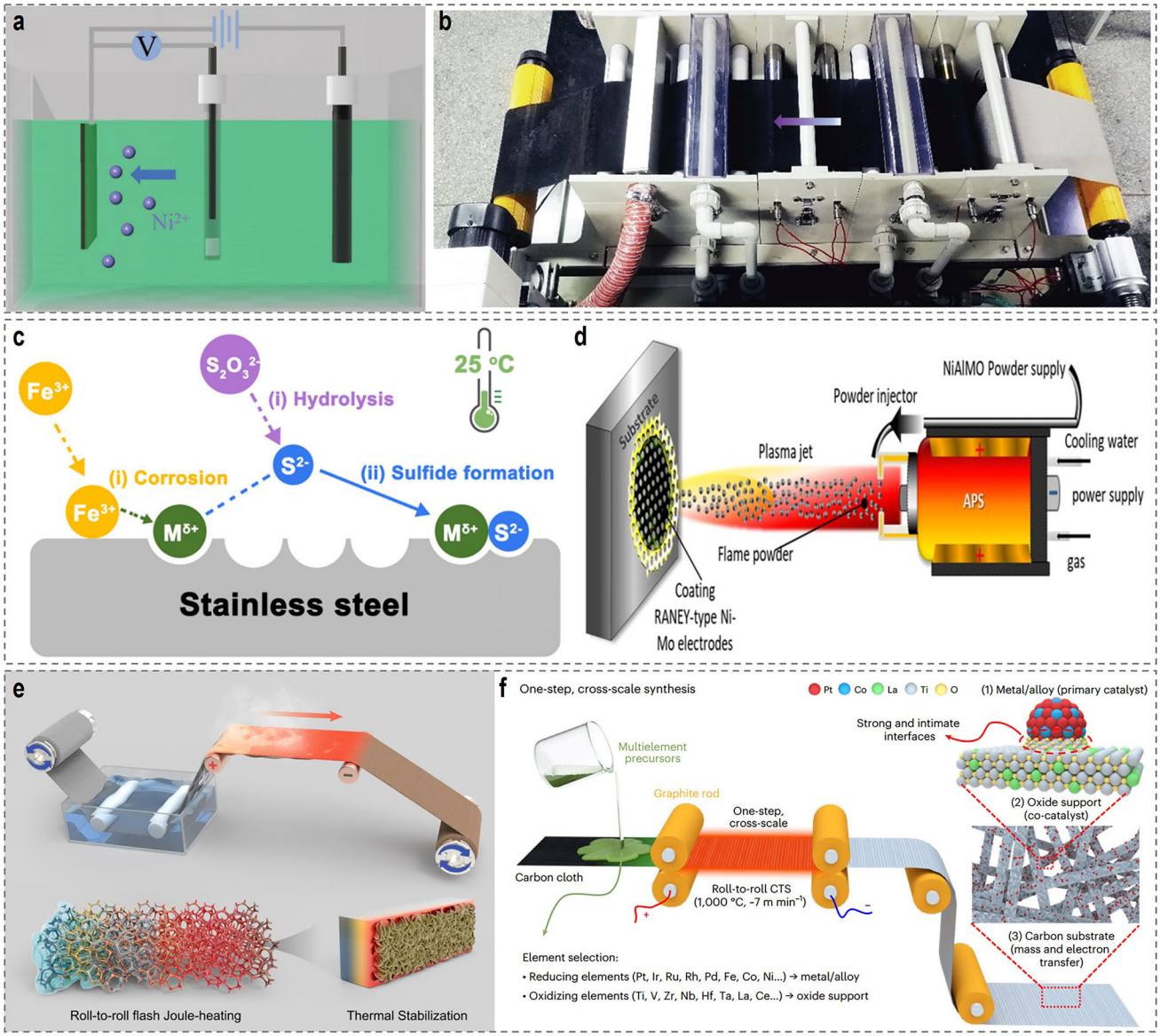

FIGURE 11 | (a) Schematic illustration of electrodepositing ND-Ni catalyst on NF substrate. Reproduced with permission [126]. Copyright 2024, Wiley-VCH. (b) Photographic image of a lab-designed roll-to-roll electrodeposition setup for nickel nanopyramid arrays electrode. Reproduced with permission [130]. Copyright 2023, Wiley-VCH. (c) Schematic illustration of the formation of the MS phase on the SS surface at ambient temperature. Reproduced with permission [131]. Copyright 2022, Elsevier. (d) Schematic illustration of APS coating of Raney-type Ni-Mo electrode on perforated nickel sheet. Reproduced with permission [133]. Copyright 2020, Nature Publishing. (e) Schematic of the home-made R2R-FJH synthetic system, consisting of precursor deposition, flash Joule heating, and rolled-up collection. Reproduced with permission [134]. Copyright 2025, American Chemical Society. (f) Schematic synthesis of metal@oxide heterostructured catalysts by the roll-to-roll method. Reproduced with permission [135]. Copyright 2025, Nature Publishing.

square-meter scale. In a standard three-electrode system, the MS/SS electrodes exhibited OER activity 7.2 times higher than that of pristine stainless steel and maintained stable catalysis for over 1000 h at current densities of 100–200 mA cm^{-2}. When integrated as anodes in industrial alkaline electrolyzers operating in 30% KOH at 80°C, the MS/SS electrodes demonstrated superior catalytic activity compared to commercial Raney nickel electrodes, achieving stable operation for over 120 h at approximately 300 mA cm^{-2}. The in situ formation of γ-(Fe,Ni)OOH was identified as the active phase for electrocatalysis. However, it is noteworthy that materials prepared via chemical corrosion strategies are predominantly metal hydroxides. To enhance their suitability for alkaline HER performance, a potential approach involves post-treatment of these electrodes to convert them into alloy or composite catalyst systems.

3.4.3 | Thermal Treatment Calcination

Thermal treatment calcination typically involves high-temperature roasting of metal salt precursors and organic matter to produce metal-based catalyst systems. The most widely reported approach within this category uses metal-organic frameworks (MOFs) as precursors, which, upon

high-temperature calcination, yield pure metal-based or metal-carbon composite catalysts. Such catalysts allow precise control over particle size and leverage synergistic effects between components to significantly enhance the hydrogen evolution performance of Ni-based catalysts. A notable challenge remains in achieving large-scale catalyst production while maintaining performance, revealing the need for innovative synthesis techniques. For example, Wang et al. pioneered a solvent-free microwave reduction method to successfully synthesize a series of noble metal-doped ultrasmall M-Ni/NiO@CNT nanocatalysts [132]. This approach offers rapid synthesis (60 s), simplicity, surfactant-free conditions, scalability (>1 g), and high yield (82.7%). The 15 wt% Ir-Ni/NiO@CNT catalyst demonstrates excellent HER activity and stability under alkaline conditions, providing a novel pathway for the large-scale production of high-performance Ni-based HER electrocatalysts.

The fabrication of large-area, self-supported electrode structures using thermal treatment calcination techniques remains a formidable challenge, primarily due to the need for uniform heating and phase transformation across expansive surfaces while maintaining structural integrity and mechanical stability. To address these challenges, innovative fabrication strategies have been developed, building upon thermal treatment approaches to enable scalable and high-performance electrode production. For instance, atmospheric plasma spraying (APS) has been employed to deposit spherical NiAlMo atomized powders onto perforated nickel sheets (Figure 11d), producing Raney-type Ni-Mo electrodes [133]. Prior to spraying, the electrodes undergo activation in a 30 wt% KOH and K-Na-tartrate-tetrahydrate solution at 80°C for 24 h to enhance their specific surface area. Increasing plasma gas flow and input power elevates the velocity and momentum of powder particles during flight, resulting in finer electrode structures with increased and more uniformly distributed porosity. However, excessively high velocities and temperatures can cause molten metal particles to form splashes and fragments, leading to large spherical pores (1–10 μm) in the electrode structure. Wu et al. introduced a roll-to-roll flash Joule heating (R2R-FJH) strategy, which involves sequential precursor deposition, flash Joule heating, and winding collection on flexible conductive NF substrates to fabricate high-performance water electrolysis electrodes (Figure 11e) [134]. The resulting MoNiFe-LDH and PtNi catalysts exhibited exceptional performance in oxygen evolution reaction (OER) and HER, with overpotentials as low as 246 mV and 31 mV, respectively. The assembled AWE achieved a cell voltage of 1.66 V at a current density of 0.5 A cm^{-2} and demonstrated remarkable durability, operating stably for 800 h. Furthermore, a prototype roll-to-roll hydrogen production device was developed, capable of continuously generating high-purity hydrogen, revealing the practicality and scalability of the R2R-FJH strategy for industrial water electrolysis electrode manufacturing. More recently, Yao et al. proposed a roll-to-roll carbothermal shock (CTS) technique, utilizing the oxidation potential difference between metal and carbon ($\Delta G^{M-C}{}_{Temp}$) as a thermodynamic descriptor to achieve one-step synthesis and continuous manufacturing of multielement heterostructure catalysts (Figure 11f) [135]. This method enables the production of diverse catalysts with precisely controlled elemental distributions. For alkaline HER, the PtCo@La-TiO_2 catalyst, rapidly screened using this approach, exhibited an overpotential of only 15 mV at 10 mA cm^{-2} in 1.0 M KOH electrolyte and demonstrated superior performance in AEMWE, highlighting its broad applicability in multistep catalytic reactions. Notably, the roll-to-roll CTS technique enables one-step synthesis and continuous manufacturing with a short preparation time (~0.5 s) and high production speed (up to 7 m min^{-1}), allowing for the continuous fabrication of large-area electrodes (e.g., 10 × 100 cm^2) at a high production efficiency (~116.69 cm^2 s^{-1}). In contrast, conventional methods typically involve multiple steps and struggle to meet large-scale production demands. The CTS technique can synthesize a wide range of catalysts, from single-element to high-entropy alloys, oxides, and their heterostructures, leveraging the alloying capabilities of high-temperature CTS and guidance from elemental oxidation potentials. Unlike traditional methods, which often produce catalysts with poorly defined interfaces and limited accessibility to active sites, catalysts prepared via roll-to-roll CTS exhibit robust and intimate interfaces with more uniform elemental distributions, significantly enhancing their catalytic performance.

As discussed in the above research progress, each of these synthesis methods possesses distinct advantages and limitations, highlighting the need for further development of preparation techniques suitable for commercial applications. Beyond these approaches, methods such as vapor deposition, chemical deposition, and ball milling have also been employed for electrocatalyst synthesis [136–138]. However, due to various constraints, their application remains relatively limited at present.

4 | Regulation Approaches for Ni-based Catalysts

The optimization of Ni-based catalysts for the HER in alkaline AEMWE requires precise regulation strategies to enhance their activity, conductivity, and stability under industrially relevant conditions [139]. Building on the fundamental design principles, various approaches have been developed to tailor the electronic structure, surface properties, and interfacial interactions of Ni-based catalysts. These efforts aim to overcome inherent limitations such as sluggish water dissociation kinetics and surface degradation in alkaline media [140]. This section reviews the key regulation approaches, emphasizing surface and interface engineering as pivotal strategies to advance Ni-based HER catalysts toward commercial scalability.

4.1 | Design Principles for Catalysts

To develop high-performance Ni-based catalysts tailored for hydrogen production via AEMWE, several critical design principles must be addressed to meet the unique demands of alkaline environments [91]. First, the catalyst surface requires abundant active sites. In the electrocatalytic process of AEMWE, effective contact between the electrolyte and water molecules drives the HER, making the exposure of electrochemically active sites essential. Dispersing Ni-based catalysts on high-surface-area substrates, such as NF or carbon-based materials, minimizes aggregation and enhances active site utilization [141]. Furthermore, optimizing synthesis methods to reduce catalyst particle size to the nanoscale or even achieving single-atom catalysts can increase surface area and significantly boost efficiency. Studies demonstrate that chemical doping or compositional tuning alters

the physicochemical properties of catalysts, optimizing active site performance, while introducing electrochemically active dopants further increases surface active sites. Second, enhancing the intrinsic catalytic activity stands as a key consideration in catalyst design. Intrinsic activity directly governs the performance of Ni-based catalysts in HER. Strategies such as optimizing catalyst composition, constructing heterostructures, incorporating heteroatom dopants, modulating crystal phases, or introducing defects effectively tune the electronic structure. Such adjustments often center on the d-band center and DOS, which provide critical insights into electron transfer and the adsorption behavior of reactants (e.g., *H, *OH, H_2O*) at active sites. Properly optimized electronic structures achieve moderate adsorption strengths for reactants and intermediates, markedly improving intrinsic activity. Third, excellent conductivity proves vital to catalyst performance. In the electrochemical process of AEMWE, efficient electron transfer reduces interfacial impedance and accelerates reaction kinetics. Conductivity correlates closely with electron density near the Fermi level, which serves as the driving force for electron transfer and can be optimized through compositional adjustments, cation doping, or heterostructure design [142]. Loading Ni-based catalysts onto conductive supports like NF, carbon paper, or carbon nanotubes, while reducing particle size, enhances both overall electrode conductivity and electron transport efficiency. Finally, long-term durability and stability are indispensable for sustained hydrogen production. In alkaline electrolytes, Ni-based catalysts must resist electrochemical corrosion and detachment to maintain performance. Compositional tuning, nanostructure design, and heterostructure engineering enhance chemical and mechanical stability under harsh conditions. Additionally, techniques such as electrodeposition or hydrothermal synthesis enable direct loading of active materials onto porous conductive substrates, forming binder-free, self-supported electrodes. This approach not only improves stability but also eliminates electrochemical hindrances potentially introduced by traditional binders. These design principles collectively ensure that Ni-based catalysts for AEMWE exhibit high activity, excellent conductivity, and superior stability, laying a solid foundation for their industrial application.

4.2 | Activity Regulation Strategies

For alkaline HER, the Brønsted-Evans-Polanyi relationship has suggested that a low activation energy for water dissociation requires strong enough H/OH binding strength on the catalyst surface, whereas the strong adsorption of H/OH prohibits the desorption of products [143]. Therefore, from the thermodynamic perspective, the key point of designing high-performance alkaline HER catalysts is to delicately balance the following three parameters: (i) the energy barrier for the water dissociation process to be overcome; (ii) the ΔG_{H^*} value; (iii) the effect of OH* (Figure 12) [144, 145]. Roughly speaking, if a catalyst is good at breaking down water, efforts should focus on adjusting the H/OH binding strength to make it easier for products to detach. On the other hand, if a catalyst struggles to attract oxygen-containing species, the priority is lowering the energy barrier for water splitting. In general, two main strategies are used to develop better electrocatalysts for alkaline HER: creating catalysts with dual functionality and modifying their electronic properties. This section reviews progress on Ni-based HER catalysts, focusing on surface and interface design, to provide insights for future catalyst development. Surface design includes three key approaches: introducing defects, shaping surface structures, and adjusting crystal properties. Interface design, meanwhile, centers on building heterostructures. Each approach improves catalyst performance through unique mechanisms, which are assessed based on preparation methods, benefits, and drawbacks, with examples provided to illustrate their impact.

4.2.1 | Defect Engineering

Defect engineering can be categorized into three types, including vacancies, elemental doping, and amorphization. This subsection introduces the design strategies for these catalysts, explains how they enhance catalytic activity, and highlights typical Ni-based catalyst systems.

4.2.1.1 | Elemental Doping. Elemental doping represents an effective strategy for tuning the electrocatalytic performance of transition metal compounds, encompassing cationic and anionic doping approaches [146]. Cationic doping leverages the vacant d-orbitals of transition metals, introducing metal elements as dopants into the host material structure to optimize the adsorption and activation of key intermediates in electrocatalysis. For instance, in Ni-based catalysts, doping Fe into Ni_3S_2 elevates the valence state of Ni, shifting its d-band center upward and optimizing the binding energy between the Ni_3S_2 surface and HER intermediates, thereby markedly enhancing catalytic activity [147]. Anionic doping involves incorporating non-metal elements such as C, N, O, S, and P into anion sites, altering the physicochemical properties of the materials. This doping also modifies the catalyst's conductivity, electronic band structure, and local charge distribution. Miao et al. employed DFT calculations to elucidate the regulatory mechanisms of non-metal doping (B, N, O, F) on the adsorption energies and electronic structure of Ni_3S_4 [148]. The adsorption energies of H_2O and OH correlate directly with the ε_d of the transition metal Ni (Figure 13a). As the electronegativity of dopants increases from B to F, ε_d shifts, influencing the adsorption of H_2O and OH on the catalyst surface. Specifically, F doping elevates ε_d, strengthening Ni-O interactions and reducing ΔG_{H2O} and ΔG_{OH}, which facilitates water dissociation and OH adsorption, laying the groundwork for subsequent reactions (Figure 13b). The adsorption energy of adsorbed hydrogen atoms exhibits a linear relationship with the p-band center (ε_p) of non-metal S. As dopant electronegativity rises, ε_p shifts toward the Fermi level, decreasing ΔG_H and easing hydrogen adsorption (Figure 13c). Among the doped samples, F-Ni_3S_4 achieves the most suitable ε_p adjustment, with ΔG_H approaching an optimal value that favors hydrogen adsorption and desorption, thus boosting HER efficiency. Experimental results confirm that elemental doping significantly enhances the HER catalytic activity of Ni_3S_4, with F-Ni_3S_4 outperforming others, requiring an overpotential of only 29 mV to achieve a current density of 10 mA cm^{-2}, surpassing B-Ni_3S_4, N-Ni_3S_4, and commercial Pt/C catalysts.

Ni-based catalysts attract attention due to their high abundance and low cost, yet their unfavorable d-band energy levels hinder efficient HER kinetics. Introducing heteroatoms offers an effective means to modulate the d-band structure, though achieving

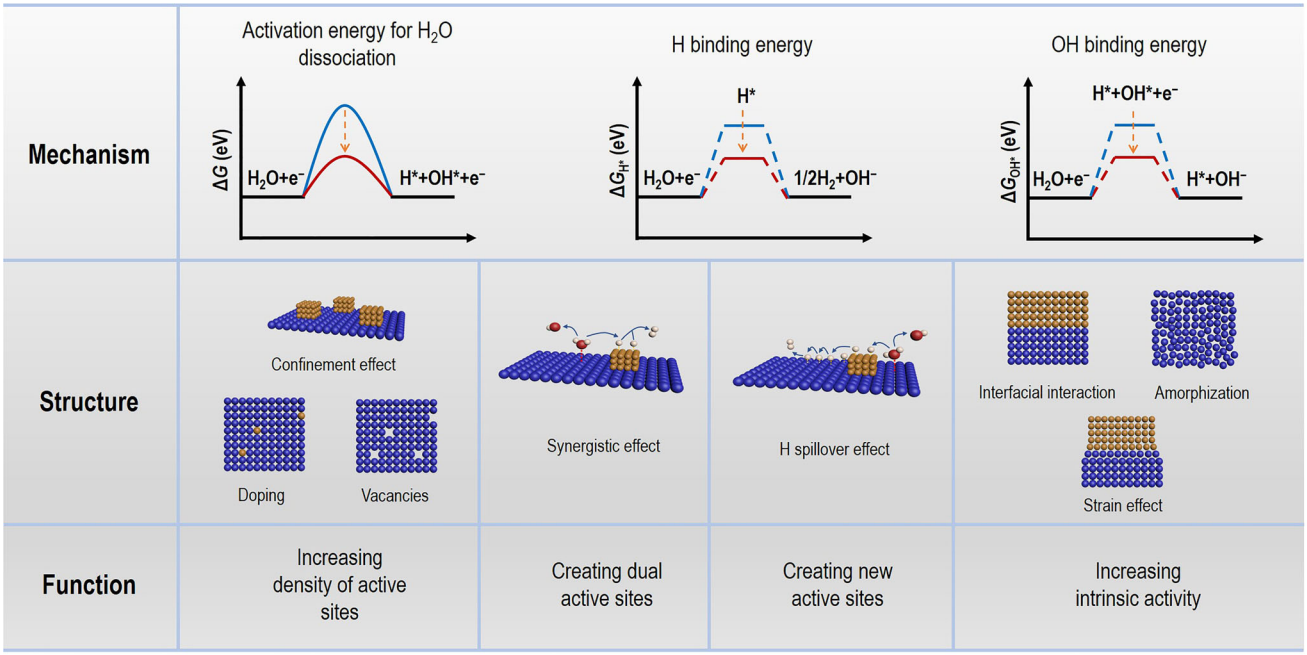

FIGURE 12 | Illustration of the electrocatalyst design strategies toward alkaline HER.

precise control remains challenging due to the limited tunability of current methods. Song et al. developed a single iodine atom-structured I-Ni@C catalyst for alkaline HER using a simplified gas-assisted diffusion method [149]. XRD and TEM confirmed the successful synthesis of I-Ni@C, with iodine atoms uniformly dispersed on the surface of carbon-coated Ni nanoparticles. XPS, and XANES results suggest that the carbon shell weakens the interaction between I and Ni, potentially influencing Ni's E_d. Resonant inelastic X-ray scattering (RIXS) measurements combined with DFT calculations indicate that the introduction of single iodine atoms and the carbon shell effectively tunes Ni's E_d, positioning the d-band center of I-Ni@C at an intermediate level. DFT calculations reveal that iodine atoms act as a bridge, enhancing electron exchange between Ni and the carbon layer, forming an interlayer electric field that promotes H_2O decomposition at Ni sites and lowers the energy barrier of the rate-determining Volmer step, resulting in more favorable reaction kinetics. At a current density of 10 mA cm^{-2}, I-Ni@C exhibits an overpotential of just 78 mV, a Tafel slope of 60 mV dec^{-1}, and low charge transfer resistance, revealing its superior kinetic performance.

In some examples, doping and vacancy engineering synergistically enhance HER catalytic activity. Wang et al. proposed an innovative strategy to regulate the electronic distribution of Ni_2P through cationic doping and vacancy engineering [150]. For HER, Fe-Ni_2P_v demonstrates exceptional performance, requiring an overpotential of only 289 mV to achieve a current density of 3.0 A cm^{-2}, comparable to commercial Pt/C catalysts. In-depth mechanistic studies reveal that Fe doping and P vacancies play pivotal roles in boosting catalyst performance. During HER, the presence of Fe atoms optimizes the ΔG_{H^*}, facilitating the adsorption and desorption of hydrogen atoms on the catalyst surface and thereby improving reaction efficiency. Furthermore, the study identifies the true active sites in Fe-Ni_2P_v, with Ni atoms serving as the catalytic centers for the OER and Fe atoms acting as the primary active sites for HER. The presence of P vacancies significantly enhances the catalyst's conductivity, providing more efficient pathways for electron transport.

4.2.1.2 | Vacancies. Vacancies constitute a vital aspect of defect engineering, playing a significant role in electrocatalysts. Introducing vacancies into transition metal compounds markedly alters their electronic structure and surface properties, thereby enhancing catalytic activity. Two-dimensional transition metal compounds serve as an example, with most internal atoms exposed on the surface, creating favorable conditions for vacancy incorporation. Doping with non-equivalent dopants introduces extrinsic vacancies into the material matrix, and precise control over vacancy concentration becomes achievable by adjusting synthesis conditions, substrate type, ionic radius, dopant valence, and doping level. Zhang et al. utilized multivalent Ni-based sulfides (e.g., NiS_2, α-NiS, β-NiS, and Ni_3S_4) as model catalysts, combining in situ Raman spectra, XAS, and theoretical calculations to uncover their atomic-scale evolution during HER [151]. The study revealed that sulfur vacancies critically influence surface reconstruction and phase transformation in these catalysts. For NiS_2, the diffusion and accumulation of surface sulfur vacancies during HER prompt spontaneous reconstruction into a Ni_3S_2 layer, which drives subsequent catalytic reactions. This dynamic reconstruction from surface to bulk phases is mediated by sulfur vacancies. Partial Fe substitution accelerates this process by modifying the electronic structure, shifting the S 3p band center closer to the Fermi level and lowering the energy barrier for sulfur vacancy formation, thus increasing vacancy concentration (Figure 13d–f). Compared to NiS_2, $Ni_{0.8}Fe_{0.2}S_2$ exhibits a higher sulfur vacancy density, facilitating sulfur removal from the surface and promoting interdiffusion of constituent atoms, which reduces the applied potential threshold for phase transformation and enhances HER performance. Performance tests demonstrated that $Ni_{0.8}Fe_{0.2}S_2$ achieves a significantly lower overpotential than NiS_2, with a reduced Tafel slope, decreased charge

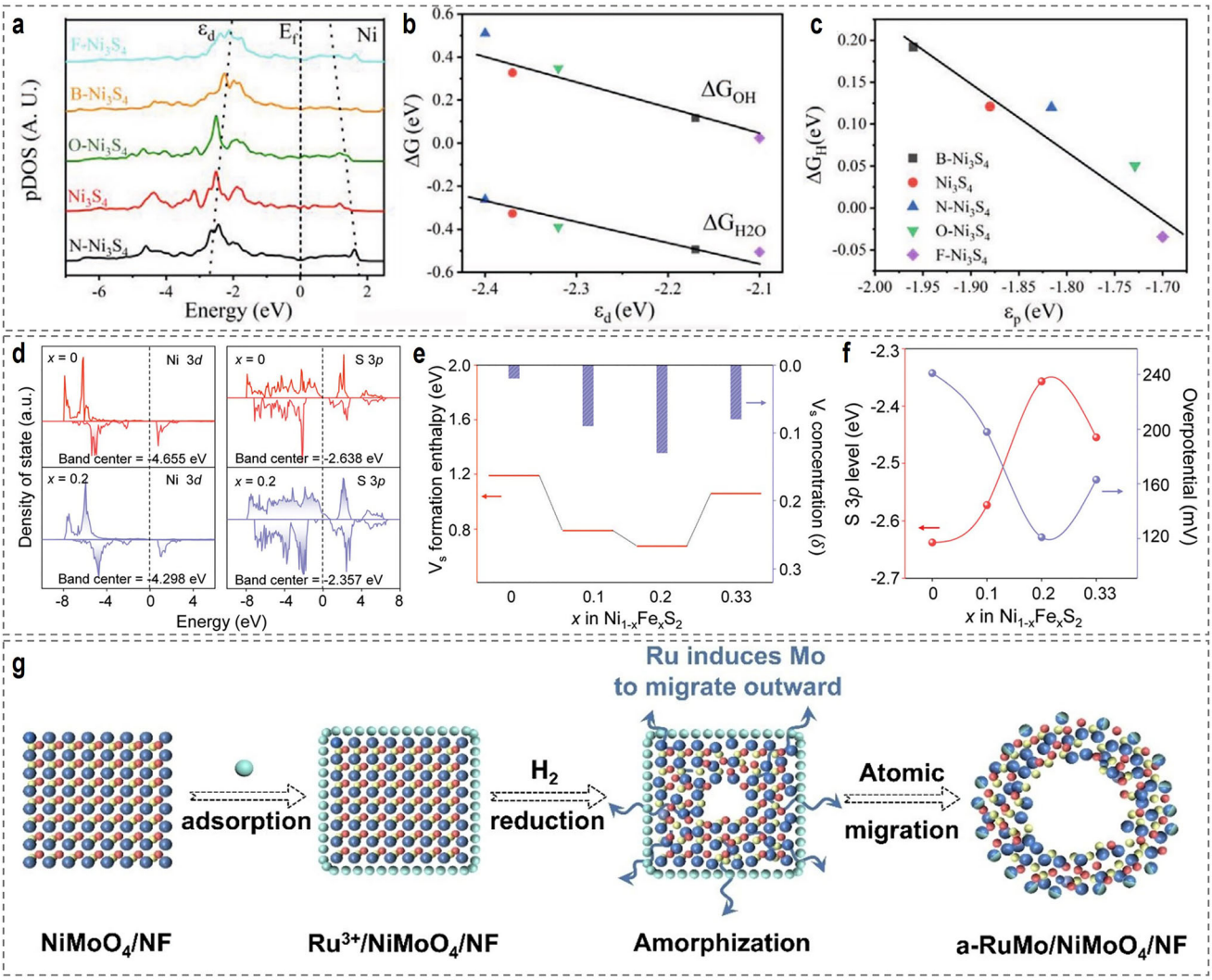

FIGURE 13 | (a) The PDOS of pristine, B-, N-, O-, and F-doped Ni3S4 for the transition metal Ni atom. (b) Dependence of ΔGH2O and ΔGOH on the d-band center of the Ni atom. (c) Dependence of ΔGH on the p-band center of the S atom. Reproduced with permission [148]. Copyright 2021, Wiley-VCH. (d) Computed Ni 3d, S 3p PDOS of Ni1-xFexS2 (x = 0.0, 0.2). (e) Calculated sulphur vacancy (VS) formation enthalpy and sulphur vacancy concentration (δ) of the samples for Ni1-xFexS2 (x = 0.0, 0.1, 0.2, 0.33). (f) Computed S 3p PDOS related to the overpotential of Ni1-xFexS2 (x = 0.0, 0.1, 0.2, 0.33) @10 mA cm−2. Reproduced with permission [151]. Copyright 2022, Royal Society of Chemistry. (g) Schematic diagram of the formation mechanism of a-RuMo/NiMoO4/NF. Reproduced with permission [166]. Copyright 2025, Wiley-VCH.

transfer resistance, increased electrochemically active surface area, and substantially higher turnover frequency, collectively revealing the positive impact of sulfur vacancies on hydrogen evolution performance.

4.2.1.3 | Amorphization. Amorphization represents a distinctive defect engineering strategy, endowing electrocatalysts with unique structural and performance advantages. Unlike crystalline materials, amorphous materials feature disordered atomic arrangements, abundant unsaturated bonds, and defect sites, providing a wealth of active sites for electrocatalytic reactions [152, 153]. In Ni-based catalyst systems, amorphization demonstrates promising potential. Han et al. synthesized a porous flower-like nanohybrid structure, Ni_2P/V-Pi/CC, comprising Ni_2P nanocrystals supported on amorphous V-doped nickel phosphate (V-Pi) nanosheets [154]. XRD, Raman, and FT-IR analyses confirmed the presence of Ni_2P and amorphous V-Pi, along with their strong coupling. The HER overpotential at 10 mA cm^{-2} reached 80.8 mV. XPS indicated robust electronic coupling between amorphous V-Pi and crystalline Ni_2P, with electrons transferring from V-Pi to Ni_2P, rendering Ni_2P an electron-rich proton acceptor and V-Pi an electron-deficient hydride acceptor, thereby facilitating the HER process. At the amorphous NiS/NiS_2 interface, conversion of intermediate NiS_2 species into NiS enables rapid electron transfer [155]. This electrocatalyst requires an ultralow overpotential of 248 mV at a current density of 100 mA cm^{-2}. Experimental results confirmed that NiS's strong affinity for adsorbed hydrogen surpasses that of Ni_3S_2 nanoparticles in activity.

In addition, the amorphous structure effectively reduces interfacial energy and charge transfer resistance, thereby enhancing electrocatalytic reactions [156]. The underlying mechanism involves several key factors. Amorphization disrupts the long-range order of the crystalline structure, leading to an

increase in surface atomic disorder [157, 158]. This results in a higher density of unsaturated coordination sites on the catalyst surface, which are more reactive and can better interact with reactants, thus facilitating the adsorption and activation of H*. These sites play a critical role in improving charge transfer kinetics and enhancing overall catalytic performance. Zhao et al. confirmed through in situ liquid electrochemical TEM techniques that during the HER process, Ru-doped $NiPS_3$ at the edges undergoes gradual amorphization, forming a stable amorphous layer about 7.5 nm thick after 16 h [159]. This amorphous layer causes the rate-determining step of the HER to shift from the Volmer step (water splitting) to the H desorption step, significantly lowering the activation energy. The amorphous structure also influences the electronic structure of the catalyst, leading to an optimized d-band center [160–162]. The disorder introduced by amorphization leads to a more delocalized electron density, reducing the energy required for H* adsorption, thus improving the catalytic efficiency. In particular, amorphous catalysts have been shown to exhibit a more favorable ΔG_{H^*}, which is a key factor in determining the catalytic activity of HER electrocatalysts. For instance, Zhang et al. in situ constructed amorphous-crystalline $NiCo(OH)_2$ nanosheet electrodes (ac-$NiCo(OH)_2$/NF) on the surface of nickel foam using $NaBH_4$ treatment [163]. Amorphization enhanced the electron density of the metal sites and formed stretched Ni-O bonds, causing the d-band center of low-coordination, unsaturated Ni sites to shift down to the Fermi level. This optimized the adsorption/desorption energies of intermediates and significantly lowered the reaction energy barrier. The HER overpotential at 1000 mA·cm^{-2} was 510 mV, with excellent stability. When used in AEMWE, the cell voltage required was only 1.68 V at 10 mA·cm^{-2}. During the HER process, the amorphous structure disrupts the network of interfacial water layers, inducing the directional conversion of 4-coordinated hydrogen-bonded water (4-HBW) into free interfacial water. This transformation of water into a more accessible form accelerates the Volmer step, the rate-limiting step in alkaline HER, and significantly boosts the overall reaction efficiency [164, 165]. The presence of free interfacial water acts as a co-catalyst, further enhancing the catalytic activity. For example, Liu et al. demonstrated the beneficial effects of amorphization by exploiting Mo atom migration in $NiMoO_4$ under a reducing atmosphere during annealing [166]. This process was influenced by the presence of Ru atoms, which disrupted the original crystalline structure and induced disorder, forming amorphous $NiMoO_4$. The migrated Mo atoms entered the Ru lattice, perturbing the ordered arrangement of Ru atoms and leading to the formation of amorphous RuMo alloy nanoclusters (Figure 13g). The resulting a-RuMo/$NiMoO_4$/NF heterostructure exhibited significantly improved catalytic performance. In HER tests, this catalyst exhibits exceptional performance, requiring an overpotential of only 13 mV to achieve 10 mA cm^{-2} and 129 mV at 1000 mA cm^{-2}, outperforming many reported catalysts. During the reaction, the amorphous structure effectively disrupts the network of interfacial water layers, inducing directional conversion of 4-HBW into free interfacial water, as proved by in situ Raman spectra. Theoretical calculations further reveal that the amorphous structure and RuMo alloy formation promote electron transfer from RuMo nanoclusters to the $NiMoO_4$ framework, optimizing the d-band center position. This adjustment reduces the ΔG_{H^*} from 1.29 eV to 0.06 eV, substantially enhancing the HER process.

It is worth noting that the beneficial effects described above primarily arise from moderate and dynamic amorphization under operational conditions, which enhances charge transfer and creates more active sites without compromising structural integrity. However, excessive amorphization, particularly at extremely high current densities, can lead to irreversible structural collapse, loss of long-range order, and eventual catalyst deactivation [167, 168]. This detrimental process is distinct from the beneficial dynamic amorphization and highlights the importance of controlled amorphization in maintaining long-term stability.

4.2.2 | Crystal Facets and Phase Structures

Different crystal facets exhibit distinct atomic arrangements and electronic structures, leading to variations in their adsorption capacities for reactants and intermediates, as well as their catalytic activities. Tailoring crystal facets optimizes catalyst performance [169, 170]. In certain Ni-based catalysts, exposing specific facets enhances the adsorption of water molecules or OH^-, accelerating reaction kinetics. Studies indicate that particular facets of Ni-based catalysts in alkaline HER exhibit lower energy barriers for water dissociation, facilitating active hydrogen formation and boosting hydrogen evolution rates. Guo et al. synthesized face-centered cubic (fcc) RuNi nanoparticles, achieving an overpotential of only 16 mV at a current density of 10 mA cm^{-2} [171]. The exceptional HER performance of fcc-RuNi nanoparticles arises from several factors. First, phase engineering reveals that the fcc phase, compared to the hexagonal close-packed (hcp) phase, offers more active sites and an optimized electronic structure, influencing the adsorption behavior of reactants and intermediates. DFT calculations demonstrate a lower water dissociation energy barrier and more favorable H/OH adsorption. Second, Ru-Ni alloying enhances HER performance through electronic coupling and bond length adjustments. Third, the core-shell structure, with Ru enriched on the surface, promotes HER, while the smaller Ni lattice induces compressive stress in the Ru shell, affecting intermediate adsorption/desorption kinetics. Peng et al. utilized annealing and acid etching to prepare porous Ni phosphide ultrafine particles, achieving precise control over porosity and crystal phases by adjusting the Ni and Ni_2P nanoparticle ratios, ultimately yielding Ni_3P porous superparticles with specific crystal phases [172]. High-resolution transmission electron microscopy (HRTEM) and DFT calculations elucidated the catalytic activities of different facets in HER. Results show that the predominantly exposed (110) facet of Ni_3P porous superparticles exhibits a lower ΔG_H compared to the (101) and (321) facets, rendering the (110) facet more active in HER, with the rate-determining step being H desorption. Shi et al. fabricated a hierarchical electrocatalyst ($NiWO_4$-Ni_3S_2@NiO/NF) comprising $NiWO_4$-coupled Ni_3S_2 nanofibers and a secondary NiO layer [173]. The study found that $NiWO_4$ induces a shift in the exposed facets of Ni_3S_2 from the relatively low-index (112) to the high-index (123). This facet regulation significantly enhances performance, as the high-index (123) facet provides more abundant active sites for HER. DFT calculations further indicate that the (123) facet optimizes Ni_3S_2's ΔG_{H^*}, strengthening Ni-H interactions. In performance tests, the optimized $NiWO_4$-Ni_3S_2@NiO/NF-3 electrode excels in 1 M KOH, requiring only 89 mV overpotential to achieve 10 mA cm^{-2}.

Phase structure alterations profoundly influence a catalyst's electronic properties, crystal structure, and surface active site distribution, thereby affecting catalytic performance. In Ni-based catalyst systems, common phase regulation strategies include modifying metal oxidation states, introducing impurity elements, or altering crystal structure types. For instance, doping or adjusting synthesis conditions can transform Ni-based catalysts from cubic to orthorhombic phases, modifying the coordination environment of metal ions and electron cloud distribution, optimizing adsorption and desorption energies of reaction intermediates, and enhancing catalytic activity. Phase regulation also impacts conductivity and stability, ensuring efficient and durable electrocatalytic reactions. Wang et al. discovered that trace cobalt doping induces a phase transition in nickel selenide from hexagonal (H-NiSe) to rhombohedral (R-NiSe), forming an H-NiSe/R-NiSe heterostructure [174]. Structurally, Ni atoms in R-NiSe adopt a five-coordinate configuration, compared to six-coordinate in H-NiSe, resulting in smaller crystal field splitting energy. This shift encourages electrons to occupy e_g orbitals, leaving more unoccupied states in t_{2g} orbitals, providing additional channels for electron transfer and greatly enhancing reaction kinetics, as depicted in Figure 14a. XPS and Raman spectra confirm that cobalt doping redistributes electrons, altering the chemical states of Ni and Se. DFT calculations reveal that R-NiSe's d-band center lies higher than H-NiSe's, enhancing its adsorption capacity for reaction intermediates and favoring HER (Figure 14b). Additionally, R-NiSe's density of states near the Fermi level appears more continuous, exhibiting metallic characteristics that improve electron transport efficiency and catalytic performance.

In practice, combining crystal facet and phase structure regulation strategies often maximizes Ni-based catalyst performance. Yang et al. employed electrodeposition and millisecond laser direct writing in liquid nitrogen (MLDW-LN) to fabricate a Ni_3Mo integrated electrode with high-density edge dislocations (D-Ni_3Mo/NF) [111]. Edge dislocations subject Mo atoms to compressive strain and Ni atoms to tensile strain. Compressive strain strengthens Mo–M bond energy, increasing Mo's vacancy formation energy and suppressing dissolution, while tensile strain shifts Ni's d-band center upward, enhancing H_2O adsorption and dissociation. Conversely, compressive strain lowers Mo's d-band center, weakening H* adsorption, optimizing intermediate adsorption energies, and promoting HER activity and stability. In 1 M KOH, this electrode excels, requiring overpotentials of only 15 mV and 232 mV to achieve 10 mA cm^{-2} and 1000 mA cm^{-2}, respectively, and maintaining stability for 200 h at 500 mA cm^{-2}, outperforming most reported NiMo-based catalysts.

4.2.3 | Heterointerface Structures

Constructing heterojunction interfaces significantly enhances electrocatalyst performance, particularly in the HER, by integrating distinct active centers at the atomic scale, creating unique active sites that accelerate multistep hydrogen evolution kinetics [175]. Heterointerfaces composed of different components generate synergistic effects that promote the HER process. Thoughtful design and construction of heterointerface structures effectively tune the catalyst's electronic structure, increase the number of active sites, and facilitate charge transfer, markedly improving HER catalytic performance. Poudel et al. reported a Mo_3Se_4-NiSe core-shell nanowire array heterostructure catalyst prepared via a one-step in situ hydrothermal method on NF [176]. This heterostructure exhibits exceptional performance, requiring an overpotential of only 84.4 mV to achieve 10 mA cm^{-2} in alkaline media. DFT calculations indicate that the Mo_3Se_4-NiSe heterostructure possesses high electron density near the Fermi level, reflecting strong interfacial interactions between NiSe and Mo_3Se_4. The adsorption free energy of the active Se site (ΔG_{H^*}) reaches 0.207 eV, close to zero, greatly enhancing HER catalytic activity. In another example, the Pt_3Ni/NiS_x heterostructure with a tunable interface demonstrates that NiS_x at the heterointerface promotes water molecule dissociation, while Pt_3Ni efficiently reduces protons to hydrogen [177]. This synergy between the two components at the heterointerface boosts different steps of alkaline HER, resulting in significantly enhanced electrocatalytic activity. Liu et al. employed a multi-interface engineering strategy, using graphene-wrapped NF as a template, to prepare a graphene-crosslinked triphasic nickel sulfide (NiS-NiS_2-Ni_3S_4) polymorphic foam (G-NNNF) via hydrothermal sulfidation for HER in alkaline media [178]. This catalyst displays outstanding activity, requiring an overpotential of only 68 mV to achieve 10 mA cm^{-2}, outperforming most reported metal sulfide catalysts. DFT calculations further elucidate the intrinsic mechanism behind the enhanced hydrogen evolution activity at heterojunction interfaces. In G-NNNF, the Ni_3S_4@G interface exhibits a ΔG_{H^*} of just 0.111 eV, far lower than other comparative interfaces, favoring H* adsorption kinetics for HER. Additionally, interactions between heterojunction interfaces drive electron transfer from Ni_3S_4/NiS_2 to NiS, leading to electron accumulation on NiS that optimizes H* adsorption energy, while hole accumulation on Ni_3S_4 enhances H_2O adsorption, collectively advancing the hydrogen evolution process. Moreover, the heterointerface between nickel sulfides and graphene improves material conductivity, facilitating electron transport during catalysis and further elevating HER activity.

As a critical component of heterointerface catalyst systems, metal–support interactions also serve as an effective means to enhance hydrogen evolution activity. Wang et al. developed a heterostructure-induced strategy to optimize metal-support interactions (MSI) and improve the electrochemical HER performance of Ru-Ni_3N/NiO [179]. DFT calculations predict that the Ni_3N/NiO heterostructure optimizes structural stability, electron distribution, and orbital coupling, reducing reaction energy barriers and enhancing electrocatalytic activity. Experimentally, a Ru-Ni_3N/NiO catalyst was successfully synthesized, featuring two-dimensional Ni_3N/NiO heterostructure nanosheet arrays, uniformly dispersed Ru nanoparticles, and strong MSI. The Ni_3N/NiO heterostructure enhances performance by optimizing the electronic structure, with electron-rich interfaces aiding electron transfer and strengthened orbital coupling, improving inter-site electron transport. Adjusting the d-band centers of Ru and Ni sites promotes water dissociation and proton binding, lowering reaction energy barriers for both HER and OER. For HER, water dissociation energy barriers for Ru-Ni_3N, Ru-NiO, and Ru-Ni_3N/NiO measure 0.83 eV, 0.73 eV, and 0.60 eV, respectively, with Ru-Ni_3N/NiO exhibiting the lowest barrier, facilitating the reaction. In HER performance, Ru-Ni_3N/NiO excels at low potentials, achieving low overpotentials across

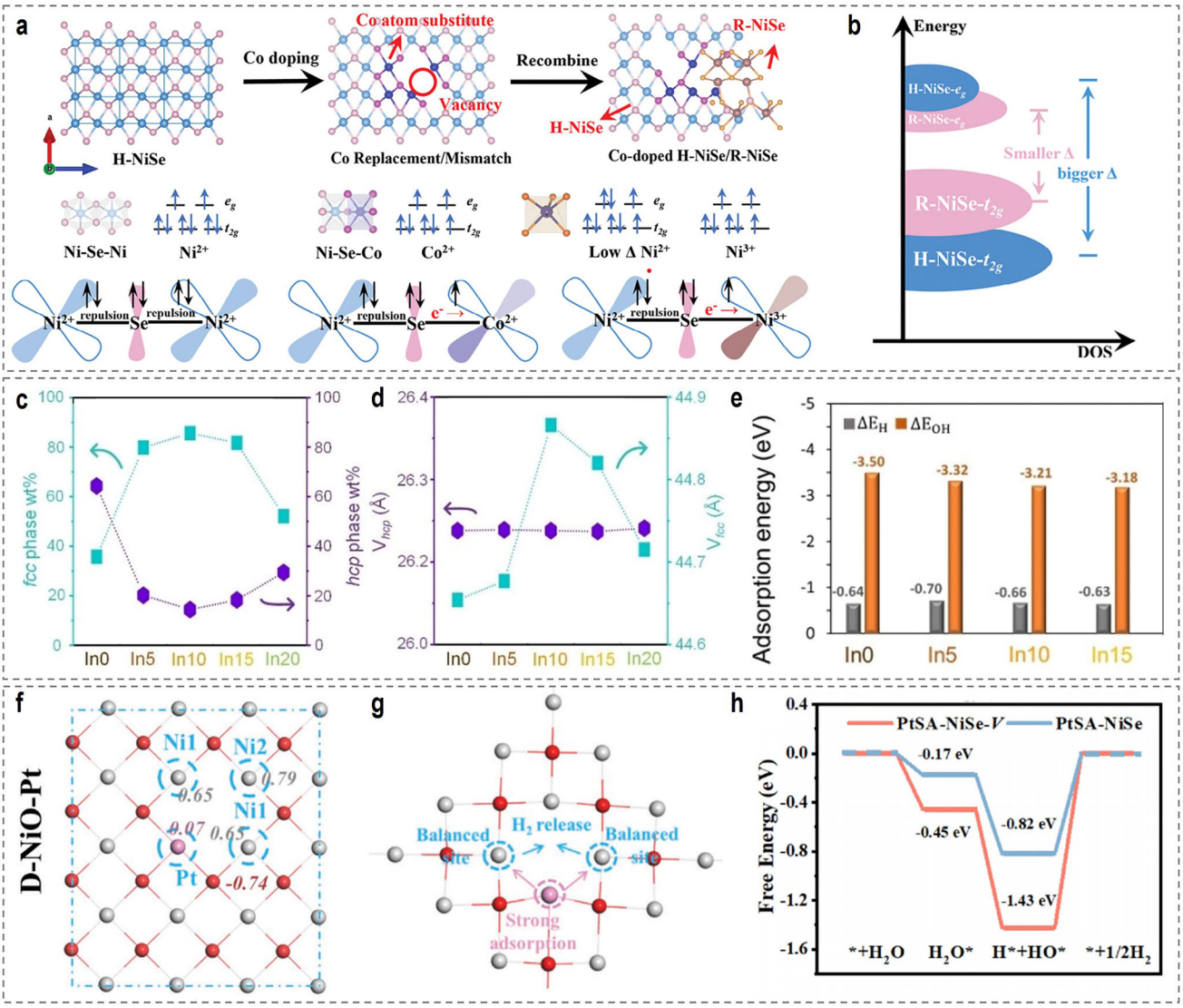

FIGURE 14 | (a) The schematic diagram of the electron transfer process in the lattice. (b) The schematic diagram of the band structure according to the calculations. Reproduced with permission [174]. Copyright 2024, Wiley-VCH. (c) The relative weight fraction of the fcc and hcp phases as a function of In at% in the Ni-In heterogeneous alloys. (d) The variation of unit cell volume of fcc and hcp phases of the Ni–In heterogeneous alloys, as a function of In at%. (e) Adsorption energy of ΔEH and ΔEOH for In0, In5, In10, and In15. Reproduced with permission [180]. Copyright 2023, Wiley-VCH. (f) The atomic models and corresponding Mulliken charge analysis of the D-NiO-Pt. (g) The illustration of the proton adsorption transfer path for D-NiO-Pt (Volmer-Tafel mechanism). Reproduced with permission [182]. Copyright 2022, Wiley-VCH. (h) The free energy diagram for HER in alkaline solution for PtSA-NiSe-V and PtSA-NiSe. Reproduced with permission [183]. Copyright 2023, Wiley-VCH.

various current densities, such as 190 mV at 1000 mA cm^{-2}, with a mass activity 40.3 times higher than commercial Pt/C catalysts.

Beyond conventional heterointerface systems, lattice mismatch, which readily forms at heterointerfaces, also significantly impacts catalytic performance. In Ni-based catalyst systems, lattice mismatch at heterointerfaces alters the lattice parameters of metals or metal compounds, adjusts surface electron density, optimizes adsorption and desorption of HER intermediates, and enhances hydrogen evolution activity. For example, in nickel-indium (NiIn) multiphase alloys, leveraging lattice mismatch to regulate alloy structure markedly improves alkaline HER performance [180]. A series of NiIn multiphase alloys with varying In content were prepared via a non-hydrothermal temperature-programmed colloidal reduction method. The lattice mismatch between tetragonal In and fcc Ni (14.9%) is much lower than that with hcp Ni (49.8%), leading to selective In incorporation into the fcc Ni phase (Figure 14c,d). This incorporation significantly alters the alloy's phase composition. Without In, 18–20 nm Ni particles contain only 36 wt% fcc phase, but with In doping, the fcc phase in the In5 sample rises to approximately 80%, increasing further to 86% and 82% in In10 and In15, respectively. Performance-wise, the In5 sample with 5 at% In exhibits superior HER activity, requiring an overpotential of only 67 mV at 10 mA cm^{-2} in 1 M KOH electrolyte. Mechanistic studies reveal that In doping transfers charge from In to Ni, stabilizing the Ni^0 state, while partially positively charged In enhances *OH adsorption. DFT calculations show that In5 excels in water adsorption and dissociation, with higher water adsorption energy, a lower activation energy barrier for water splitting (0.46 eV compared to

0.72 eV, 0.96 eV, and 1.04 eV for In0, In10, and In15) (Figure 14e), and a more negative ΔE_{OH}, facilitating water dissociation and preventing catalyst poisoning, thus significantly boosting HER activity. Strain engineering via lattice mismatch effectively can also tune the catalyst's electronic structure to enhance performance. Combining structurally distinct $MoSe_2$ and Ni_3Se_4 leverages lattice mismatch to improve HER performance, so Cai et al. used $NiMoO_4$ nanorods as precursors to prepare a Ni_3Se_4-$MoSe_2$ nano-heterostructure catalyst (MN-Ni_3Se_4/$MoSe_2$) with abundant interfaces via hydrothermal selenization [181]. MN-Ni_3Se_4/$MoSe_2$ outperforms UN-Ni_3Se_4/$MoSe_2$ (lacking abundant interfaces) in alkaline HER, demonstrating that constructing heterostructures with rich interfaces and utilizing lattice mismatch-induced strain effectively enhances catalyst performance.

Broadly, interfacial confinement structures fall within the realm of heterointerface structures. Employing confinement synthesis strategies enables precise control over electrocatalyst structure, morphology, and electrocatalytic properties, playing a pivotal role in performance enhancement [16]. Nanospatial confinement stands out as a highly effective approach, restricting or encapsulating active species, such as single atoms or diatoms, within nano- or sub-nanoscale spaces. This unique spatial environment creates a specialized microenvironment, fostering favorable conditions for regulating chemical reactions and balancing transition states. Within these (sub)nanoscale confined spaces, reactants are efficiently accommodated, while the physical constraints limit nanocatalyst formation, enabling the precise synthesis of uniform nanoscale metal clusters, nanoparticles, or nanosheets. This approach prevents aggregation of active species, ensuring high dispersibility and stability. At such nanoscale single-atom or cluster-support interfaces, unique metal-support interactions emerge, altering the electronic structure of active species and potentially inducing strong interfacial synergistic catalysis. In HER, this synergy optimizes reaction pathways, lowers activation energies, and promotes water dissociation, hydrogen adsorption, and desorption, significantly enhancing catalytic activity and efficiency. In Ni-based catalyst studies, researchers have ingeniously designed nanospatial confinement structures, precisely confining single atoms or clusters within specific Ni-based support nanomaterials, successfully synthesizing electrocatalysts with superior hydrogen evolution performance. Experimental results show that, compared to conventional Ni-based catalysts, those based on nanospatial confinement exhibit significantly lower overpotentials and substantially higher current densities under identical conditions, demonstrating exceptional electrocatalytic activity and stability. For instance, Qi et al. filled Pt atoms into Ni vacancies (Ni_v) of dual-defect NiO to obtain the D-NiO-Pt catalyst [182]. Results indicate uniform Pt atom incorporation into Niv, with oxygen vacancies (O_v) stably present. D-NiO-Pt performs exceptionally, requiring only 20 mV overpotential to achieve 10 mA cm^{-2}, surpassing commercial Pt/C catalysts. Theoretical calculations reveal the intrinsic mechanisms behind this performance. The synergy between O_v and Pt optimizes the electronic structure of surrounding Ni sites, bringing the ΔG_{H^*} closer to zero, facilitating HER. Specifically, Pt acts as an electron acceptor, altering the Mulliken charges of nearby Ni and O, while O_v increases electron cloud density at Ni sites (Figure 14f), enhancing hydrogen adsorption and reactivity. This synergy markedly improves HER kinetics, shifting the rate-determining step from the Volmer step in the Volmer-Heyrovsky mechanism to the Tafel step in the Volmer-Tafel mechanism, greatly accelerating reaction rates (Figure 14g). This strategy proves effective for other Ni-based compounds (e.g., Ni_2P, $Ni_{0.96}S$, $NiSe_2$), offering a new avenue for developing high-performance catalysts. Chen et al. prepared a vacancy-rich nickel selenide-supported Pt single-atom catalyst (PtSA-NiSe-V) via a hydrothermal-impregnation stepwise method [183]. This approach cleverly exploits low-electron-density regions of the substrate to capture and confine high-electron-density metal atoms. Multiple characterization techniques, including AC-STEM and HAADF-STEM, confirm uniform Pt single-atom distribution at cationic vacancies in nickel selenide with a loading of 3.2 wt%. XPS, XANES, and EXAFS analyses reveal that Pt atoms form PtSe bonds with highly electronegative Se, acting as a bridge for rapid electron transfer between single atoms and the substrate. In 1 M KOH, this catalyst achieves an ultralow overpotential of 45 mV at 10 mA cm^{-2} during HER. Calculations indicate that Pt atoms preferentially anchor at vacancies in NiSe-V, forming a stable structure that optimizes H_2O adsorption and H* dissociation, significantly lowering the reaction energy barrier for water splitting and accelerating alkaline HER kinetics. The suitable d-band center position of Pt atoms in PtSA-NiSe-V weakens Pt-H bond strength (Figure 14h), further enhancing electrocatalytic activity. These findings validate the immense potential of nanospatial confinement strategies in optimizing electrocatalyst performance, providing fresh insights and directions for designing and developing high-performance electrocatalysts.

Surface morphology engineering enhances catalyst surface area and active site exposure by constructing specific nanostructures such as nanosheets, nanowires, or porous forms, employing methods like templating, solvothermal synthesis, and electrochemical deposition [184]. This optimized morphology yields multifaceted performance improvements. Porous structures significantly enhance mass transfer efficiency, providing more pathways for electrolyte transport, enabling water molecules to reach active sites more rapidly while allowing generated hydrogen gas to detach quickly, reducing transport resistance and accelerating reaction kinetics. Tailoring surface morphology, by reducing catalyst particles to ultrasmall nanoscale dimensions, designing multidimensional structures, or creating porous, rough surfaces, effectively promotes electron transfer and mass diffusion, increases active site exposure and utilization, and enhances reaction kinetics and mechanical stability, enabling superior performance at high current densities. Fan et al. utilized a simple one-step wet chemical deposition under an external magnetic field to combine ultrasmall amorphous NiFe hydroxide nanoparticles (<5 nm) with crystalline NiFe alloy on NF, producing the Ni_xFe_{1-x}–AHNAs catalyst for efficient water splitting [185]. HRTEM images confirmed that the crystalline NiFe alloy core is encapsulated by an ultrathin amorphous nanolayer (1–5 nm). Compared to oxides prepared via conventional electrodeposition, hydrothermal, or wet chemical methods, these amorphous NiFe oxide nanodomains are much smaller, reducing electron transfer resistance while increasing surface area and active catalytic sites. Consequently, this self-supported hybrid catalyst exhibits exceptional activity, particularly at high current densities. With an optimized Ni:Fe atomic ratio of 0.8:0.2, $Ni_{0.8}Fe_{0.2}$-AHNAs drives current densities of 500 and 1000 mA cm^{-2} at 248 and 258 mV, respectively. When paired with $Ni_{0.8}Fe_{0.2}$-AHNAs as the anode and nickel nanowires (Fe-free) as the cathode in an alkaline

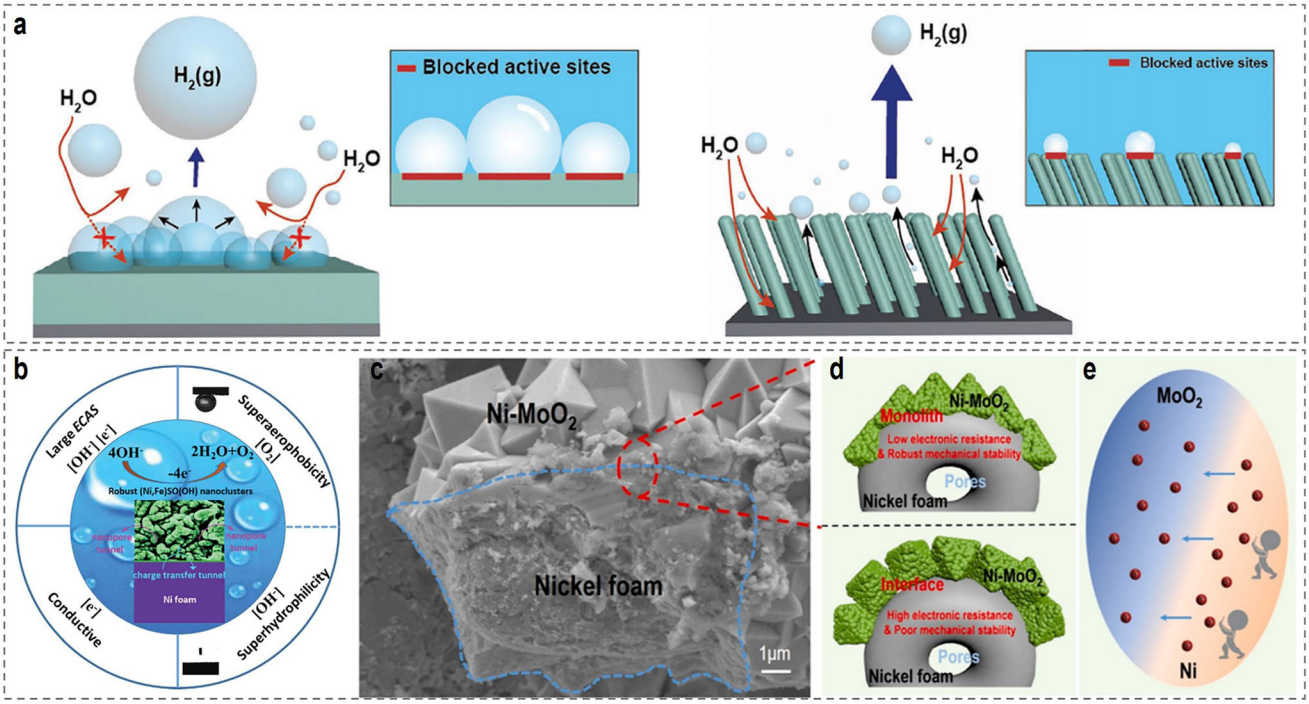

FIGURE 15 | (a) Schematic illustrations of the H2 bubble-release behavior of the Ni film and the Ni-80 catalysts. The enhanced HER performance of the Ni-80 catalyst can be attributed to its superaerophobic surface that facilitates H2 bubble release. Reproduced with permission [187]. Copyright 2023, Wiley-VCH. (b) The influence factors for designing large current-density OER catalysts inspired by the intrinsic OER equation. Reproduced with permission [189]. Copyright 2019, Royal Society of Chemistry. (c) Cross-sectional SEM image of Ni-MoO2/NF. (d) Schematic illustration of the comparison between the monolith electrode (up) and the directly grown electrode (down). (e) Illustration of interface electron transfer from Ni to MoO2 in Ni-MoO2/NF. Reproduced with permission [191]. Copyright 2022, Elsevier.

electrolyzer, cell voltages of only 1.55, 1.7, and 1.76 V achieve 100, 500, and 1000 mA cm^{-2}, respectively. These voltages are notably lower than those of standard Ni and stainless steel electrode pairs used in industrial electrolyzers at equivalent current densities. Remarkably, the Faraday efficiency (FE) for hydrogen and oxygen production in the $Ni_{0.8}Fe_{0.2}$-AHNAs electrolyzer approaches 100%. Calculations based on measured cell voltages indicate that this electrolyzer saves 11.16 kWh kg^{-1} of hydrogen produced compared to a simulated industrial electrolyzer, highlighting its substantial commercial potential. Zong et al. prepared $Ni_3N/Ni@W_2N_3$ with a unique nanoarray structure, conferring superhydrophilicity and superaerophobicity [186]. The water contact angle nears 0°, ensuring excellent electrolyte wetting, while the H_2 bubble contact angle reaches 145.5°, with a bubble adhesion force of only 5.4 μN, far lower than the 212.5 μN of Ni/Ni_3N. These properties enable efficient detachment of generated H_2 bubbles from the electrode surface, minimizing their adverse effects on the reaction and enhancing catalyst efficiency and stability. Kim et al. employed oblique angle deposition to fabricate Ni nanorod array catalysts with controllable surface porosity on substrates like Ti foil, investigating their impact on H_2 bubble release behavior and performance in alkaline HER [187]. Increasing porosity enhances aerophobicity and hydrophilicity, with the Ni-80 catalyst (approximately 52% porosity) exhibiting superaerophobicity. This property, combined with effective open channels, accelerates H_2 bubble release, significantly improving geometric activity, intrinsic activity (specific and mass activity), and stability, particularly at high current densities (Figure 15a). Thus, constructing suitable nanoarrays with porous structures proves critical for rapid bubble detachment, reducing reaction hindrance, and boosting efficiency [188]. Adjusting porosity and roughness also controls electrode surface wettability. Superhydrophilic surfaces (liquid contact angle <5° or 10° in air) markedly enhance electrolyte permeability, ensuring access to most active sites. Conversely, underwater bubble contact angles exceeding 150° indicate superaerophobicity, allowing gas bubbles to detach smoothly. Due to the interfacial energy balance, superhydrophilic catalysts inherently exhibit superaerophobicity. At high current densities, such superhydrophilic/superaerophobic catalysts prevent severe bubble accumulation, enhancing active site utilization and delivering superior activity and stability. Ding et al. reported a porous nanocatalyst, (Ni,Fe)SO(OH), loaded on NF via a simple one-step wet chemical method [189]. The rough, porous surface of (Ni,Fe)SO(OH)/NF imparts superhydrophilicity and superaerophobicity, improving electrolyte penetration, exposing more accessible active sites, and enhancing bubble release, as depicted in Figure 15b. In 1 M KOH, this catalyst achieves an OER current density of 1 A cm^{-2} at an overpotential of 260 mV. Constructing porous/rough nanostructures also enhances water-splitting activity under high current density conditions by increasing specific surface area and electrochemical active sites. For instance, Qiu et al. coupled mesoporous NiFe-LDH nanosheets with a 3D MXene framework on NF, efficiently driving 500 mA cm^{-2} at low voltage in 1.0 M KOH [190].

Additionally, unique morphological structures enhance mechanical stability by improving catalyst-substrate bonding, reducing detachment at high current densities, and ensuring long-term

stability during electrocatalytic reactions. Yuan et al. prepared a monolithic Ni-MoO_2/NF catalyst via hydrothermal corrosion growth and thermal reduction, growing nanoscale Ni-MoO_2 heterojunctions directly on NF [191]. This structure minimizes interfacial resistance between the catalyst and substrate, enabling efficient charge transfer, and strengthens bonding through robust covalent connections (Figure 15c–e). In practical high-current-density scenarios, this electrode excels. In HER, Ni-MoO_2/NF sustains operation at 400 mA cm^{-2} for over 60 h with negligible current decay. This stability stems from its design: the monolithic structure prevents detachment due to weak adhesion (common in traditional electrodes) and resists hydrogen bombardment, while the heterointerface promotes charge redistribution, optimizing the electronic structure and enhancing stability at high current densities. However, preparing complex morphologies poses challenges. In practice, intricate processes often require specialized equipment and reagents, increasing costs. Moreover, the complexity may reduce production efficiency, hindering large-scale industrial application. Future research should explore simpler, cost-effective, and scalable surface morphology preparation methods to fully harness the potential of surface morphology engineering in electrocatalysis.

4.3 | Stability Regulation Strategy

The HER in AEMWE is pivotal for scalable green hydrogen production, with Ni-based electrocatalysts offering a cost-effective alternative to precious-metal catalysts. Despite significant progress in enhancing HER activity, achieving long-term stability under industrial conditions, such as 20–30 wt% KOH, 60–90°C, and current densities ≥1 A cm^{-2}, remains a critical challenge. Current Ni-based catalysts often exhibit limited durability, stabilizing primarily under milder conditions (1 M KOH, 25°C) for less than 1000 h, as documented in recent studies. Catalyst stability encompasses the physical integrity of the electrode architecture (structural stability) and the preservation of active sites' chemical and electronic properties (intrinsic stability) [192]. This chapter explores strategies to enhance both aspects, addressing industrial challenges such as bubble-induced mechanical stress, dynamic surface reconstruction, and foreign ion contamination, to enable robust, scalable, and efficient AEMWE systems.

4.3.1 | Structural Stability

Maintaining the physical integrity of Ni-based catalysts under the harsh conditions of industrial AEMWE is critical to prevent delamination, corrosion, or mechanical degradation. A primary challenge lies in the weak interfacial adhesion of traditional powder catalysts integrated onto substrates using polymer binders, which often leads to delamination under high current densities or elevated temperatures. Self-supported electrodes, where catalysts are directly grown on conductive substrates such as Ni foam or mesh, mitigate this issue by enhancing catalyst-substrate bonding, thereby improving mechanical and chemical stability. For instance, a superhydrophilic self-supported Ni/Y_2O_3 heterostructure electrocatalyst was prepared via a high-temperature selective reduction method, demonstrating exceptional performance in alkaline HER [193]. In 1 M KOH solution, this catalyst exhibited an overpotential of only 61.1 ± 3.7 mV at 10 mA cm^{-2}, with a Tafel slope of 52.8 mV dec^{-1}, and maintained stable operation for 500 h at a high current density of 1000 mA cm^{-2}. Its superior performance stems from multi-interface engineering: the Ni/Y_2O_3 heterostructure provides dual active sites that lower the water dissociation barrier and optimize ΔG_{H^*}; the self-supported structure facilitates charge transfer and prevents catalyst detachment; and the superhydrophilic surface accelerates H_2 bubble release, enhancing catalytic activity and stability at high current densities. The mechanical stability of electrodes primarily depends on the interfaces between the electrocatalyst and the substrate (electrocatalyst-substrate interface) and between the electrocatalyst and gas bubbles (electrocatalyst-bubble interface), as depicted in Figure 16a,b. At high current densities, bubble detachment generates strong adhesive forces that, if exceeding the binding strength between the electrocatalyst and substrate, can cause catalyst delamination. Common methods to enhance electrocatalyst-substrate adhesion, such as using binders like Nafion, suffer from insufficient adhesion strength, blockage of active sites, and reduced ionic conductivity. While in situ growth of electrocatalysts addresses some of these issues, most catalysts are bound to substrates via weak interactions, resulting in suboptimal stability. Additionally, Schottky barriers between semiconducting electrocatalysts and metallic substrates can impede reaction kinetics [194]. To overcome these limitations, Liu et al. developed a mechanically stable, fully metallic, and highly active $CuMo_6S_8$/Cu electrode through in situ reaction between MoS_2 and Cu [195]. This electrode features strong electrocatalyst-substrate interfacial bonding and weak electrocatalyst-bubble adhesion, enabling rapid hydrogen evolution and charge transfer kinetics (Figure 16c). It achieved a high current density of 2500 mA cm^{-2} at a low overpotential of 334 mV and operated stably for over 100 h. Yuan et al. extended this concept to Ni-based catalyst systems [191, 196, 197]. For example, a monolithic Ni-MoO_2 heterojunction catalyst supported on Ni foam (Ni-MoO_2/NF) was fabricated via hydrothermal corrosion growth followed by thermal reduction [191]. Comprehensive characterization and testing revealed that the heterostructure-induced charge redistribution, unique electrode surface properties, and monolithic structure synergistically enhanced catalytic performance. This catalyst exhibited near-platinum-like activity, high stability, and excellent Faradaic efficiency in alkaline electrolytes. When integrated into a monolithic urea oxidation-assisted water splitting electrolyzer with $NiMoO_4$/NF, the system achieved a low cell voltage of 1.53 V at 20 mA cm^{-2} and operated stably for 120 h.

Hierarchical nanostructures significantly enhance the structural stability of electrodes by increasing surface area and facilitating bubble detachment, thereby mitigating mechanical stress under high current densities conditions. For example, a self-supported electrode composed of heterostructured Ni_2P-$Ni_{12}P_5$ nanorod arrays rooted on a Ni_3S_2 film (Ni_2P-$Ni_{12}P_5$@Ni_3S_2) was fabricated on metallic NF through simultaneous corrosion and sulfidation followed by phosphidation treatment [55]. This electrode features a 3D open architecture without polymer binders, promoting efficient mass transfer of reactants, rapid release of gas bubbles, and effective diffusion of electrolyte and ionic species (Figure 16d). In the HER, rapid mass transfer ensures timely delivery of reactants to active sites and swift removal of reaction products, preventing accumulation that could compromise electrode integrity. Efficient diffusion of electrolyte and ionic species maintains internal charge balance, reducing

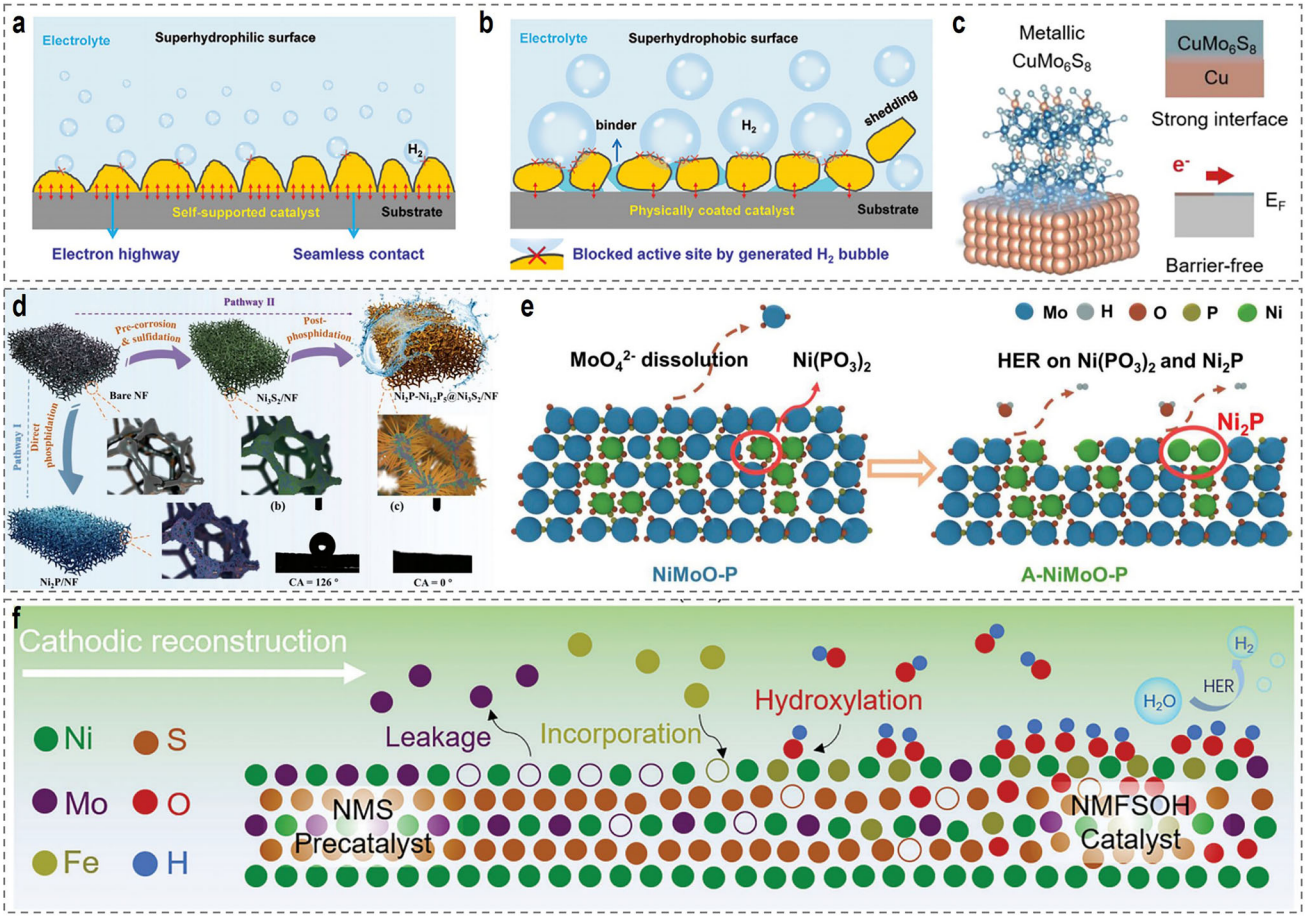

FIGURE 16 | (a) Schematic illustration of the growth of gas bubbles on superhydrophilic self-supported electrode. (b) Schematic illustration of the growth of gas bubbles on the hydrophobic physically coated electrode. Reproduced with permission [193]. Copyright 2024, Wiley-VCH. (c) A schematic showing the structural advantages of CuMo6S8/Cu electrode. Reproduced with permission [195]. Copyright 2022, Nature Publishing. (d) The schematic illustration of the synthetic procedures for different phase conversion-induced TMPs from NF. Reproduced with permission [55]. Copyright 2022, Wiley-VCH. (e) Schematic illustration of active site constructions by in situ refreshing strategy on the A-NiMoO-P for accelerating HER by water splitting. Reproduced with permission [204]. Copyright 2024, Wiley-VCH. (f) Schematic diagram of in situ cathodic reconstitution dynamics. Reproduced with permission [211]. Copyright 2023, Wiley-VCH.

structural stress caused by charge imbalances. The inherent mechanical strength of this self-supported structure enables it to withstand gas impact and mechanical stress during reactions, ensuring long-term structural integrity and stability. Conversely, gas bubble adhesion poses a significant challenge at current densities exceeding 500 mA cm^{-2}, as it restricts electron and mass transfer and induces mechanical damage through stretching forces. Nanostructured designs with superhydrophilic and aerophobic properties effectively reduce bubble adhesion. Xu et al. developed an ordered nanodendritic nickel (ND-Ni) catalyst via a one-step electrodeposition method, characterized by ultrafine nanocrystalline grains arranged in chain-like structures with interconnected 3D microporous networks [126]. This catalyst exhibited superior activity and stability in alkaline HER at high current density, outperforming commercial Raney nickel (R-Ni) catalysts. The unique structure of ND-Ni significantly enhances HER performance. Its 3D interconnected microporous structure provides a high specific surface area (198.848 m^2 g^{-1}), facilitating active site exposure and mass transfer, thus accelerating catalytic kinetics. The ordered nanocrystalline chain structure reduces electrode resistance (sheet conductivity ≈ 7.05×10^{-4} Ωm, longitudinal conductivity ≈ 6.75×10^{-2} Ωm), promoting electron transfer and improving electrocatalytic efficiency. Post-surface hydroxylation renders the electrode superhydrophilic, enhancing affinity for liquid reactants, reducing gas bubble adhesion, and facilitating gas release at high current densities, which collectively contribute to low overpotential, small Tafel slope, low charge transfer resistance, and excellent catalytic activity and stability. Surface wettability also plays a critical role in bubble dynamics, with hydrophilic surfaces reducing bubble size and contact area, thereby enhancing electrode durability [198]. Yu et al. fabricated a highly efficient and durable self-supported Ni/Ni_xS_y-PNF electrode for alkaline HER by growing Ni/Ni_xS_y heterostructures on hierarchical porous NF (PNF) through a two-step electrodeposition process [199]. This electrode leverages its hierarchical porous structure and superhydrophilic surface to accelerate mass transfer and bubble detachment at high current densities. In terms of HER performance, the Ni/Ni_xS_y-PNF heterostructure demonstrates significant advantages, achieving overpotentials of 61 mV and 121 mV at 100 and 500 mA cm^{-2}, respectively, notably lower than those of comparative Pt/C-PNF electrodes. The hierarchical porous structure provides abundant

active sites, increases the effective reaction area, and enhances mass transfer, enabling rapid delivery of reactants to active sites and timely removal of products. The superhydrophilic surface improves electrode-electrolyte contact, reduces bubble adhesion, and promotes bubble detachment, ensuring sufficient exposure of active sites. These synergistic effects collectively accelerate the HER process at high current densities, significantly enhancing electrode performance.

4.3.2 | Intrinsic Stability

Preserving the chemical and electronic properties of active sites under reductive potentials and in high-concentration alkaline electrolytes is critical for ensuring long-term HER performance [200, 201]. However, dynamic surface reconstruction presents significant challenges. While surface reconstruction during HER is less studied compared to OER catalysts, it can either enhance or impair catalytic performance depending on its control [202]. Controlled reconstruction can stabilize catalysts by forming highly active phases, thereby improving their efficiency and durability. Zhang et al. investigated the behavior of Ni_4Mo alloy in alkaline HER [203]. Tested in a three-electrode system with 1.0 M KOH electrolyte, the Ni_4Mo alloy exhibited exceptional HER performance, achieving an overpotential of only 86 mV at a current density of 100 mA cm^{-2}, surpassing commercial 20% Pt/C with equivalent mass loading. The alloy also demonstrated remarkable durability, maintaining stable operation for over 50 h with Faradaic efficiency of approximately 100%. Notably, an activation process was observed during the initial 4 h of reaction. Through comprehensive characterization, it was found that during HER, Mo oxidizes and dissolves as MoO_4^{2-}, which subsequently re-adsorbs onto the electrode surface and polymerizes into $Mo_2O_7^{2-}$. The addition of an appropriate amount of MoO_4^{2-} restored the durability of the Ni_4Mo alloy and enhanced the HER activity of single metals such as Ni, Fe, and Co. Theoretical calculations revealed that the polymerized $Mo_2O_7^{2-}$ is particularly favorable for alkaline HER, elucidating the structural transformation and activity enhancement mechanisms of the Ni_4Mo alloy. These findings provide new insights for the design of related electrocatalytic materials and highlight the potential of leveraging controlled reconstruction during HER to develop highly active catalysts. Similarly, Shi et al. utilized a hydrothermal process followed by thermal phosphidation to prepare a NiMoO-P precursor on NF using various chemical reagents, which was subsequently electrochemically activated to form the A-NiMoO-P catalyst [204]. The NiMoO-P precursor consisted of $Ni(PO_3)_2$ and an amorphous molybdenum oxide matrix. Upon electrochemical activation, as depicted in Figure 16e, the molybdenum oxide dissolved, and a portion of $Ni(PO_3)_2$ was converted into Ni_2P, resulting in A-NiMoO-P with a rougher surface and increased exposure of active sites. The A-NiMoO-P catalyst exhibited superior HER performance compared to NiMoO-P and 20% Pt/C/NF, with lower overpotential and Tafel slope. The enhanced activity stems from the gradual dissolution of the amorphous molybdenum compound matrix during HER, which exposes internal $Ni(PO_3)_2$ active sites, some of which are reduced to Ni_2P active sites. Additionally, the dissolution-deposition dynamic equilibrium of the molybdenum compound matrix ensures continuous exposure and renewal of active sites, preventing performance degradation due to site coverage or deactivation. This mechanism significantly enhances the catalyst's durability, demonstrating the effectiveness of controlled surface reconstruction in optimizing HER performance.

Compared to the well-studied reconstruction of OER catalysts in the reported studies, dynamic changes in HER catalysts have received relatively little attention [205, 206]. This is largely due to the fact that HER catalysts typically operate under reducing conditions, unlike OER catalysts, which are exposed to oxidative environments [207, 208]. As a result, HER catalysts do not generally undergo the same type of oxidation-induced reconstruction as OER catalysts. However, HER catalysts may still experience structural changes under certain conditions, such as element dissolution or leaching, particularly in high-current-density operations, but such studies remain relatively scarce [209]. Reports on designing alkaline HER catalysts tailored for industrial-scale high current densities through controlled reconstruction are particularly limited [203, 210]. Xu et al. employed a hydrothermal method to grow Ni-Mo sulfide (NMS) nanosheet arrays on NF [211]. Using NMS as a precursor, electrochemical reconstruction was performed via constant current polarization (1 A cm^{-2}) in electrolytes containing various cations, resulting in the formation of NMFSOH catalysts. At high current densities (≥500 mA cm^{-2}), NMS undergoes dynamic reconstruction characterized by Mo leakage and Ni stabilization. The incorporation of different cations promotes reconstruction, with Fe exhibiting the most pronounced effect, leading to the formation of NMFSOH. This process involves the cleavage of Mo-S bonds, leakage of Mo ions, and subsequent reconstruction with hydroxyl and Fe ions, as shown in Figure 16f. The NMFSOH catalyst retains the 3D porous structure of NMS while exhibiting a rougher surface and enhanced hydrophilicity, which facilitate electrolyte penetration and gas product release. Composed of ultrathin nanosheets, NMFSOH contains crystalline phases such as Ni_3S_2, NiFe layered double hydroxide (LDH), and MoS_2, featuring abundant crystalline-amorphous interfaces and active sites. Consequently, strategically leveraging the electrode reconstruction process offers a novel design approach to enhance the intrinsic stability of electrodes, enabling the development of high-performance HER catalysts suitable for industrial applications. It is important to note that the dynamic reconstruction of the HER process not only optimizes the local electronic structure and hydrogen evolution pathway but also provides a protective layer to prevent catalyst structural collapse. For example, Zhang et al. revealed the epitaxial growth of a catalytic layer on nickel molybdate, utilizing it as a platform to investigate the local electrochemical microenvironment regulation mechanisms at the catalyst-electrolyte interface [212]. The localized enhancement of the electric field around the dendritic epitaxial hydroxide layer increased the concentration of hydrated potassium ions within the OHP, facilitating the rearrangement of the surface hydrogen bond network and improving HER kinetics. Additionally, the dynamically structured epitaxial layer exhibited a denser structure, effectively suppressing molybdenum dissolution and providing enhanced stability against corrosive degradation during HER. Ultimately, the material achieved continuous operation for 1400 h at a current density of 0.45 A cm^{-2} in an industrial alkaline water electrolyzer.

It is important to note that while the majority of the current literature suggests that dynamic reconstruction at high current densities enhances HER performance, it should be emphasized

that such a severe catalyst structural reconstruction process, if not properly controlled, may lead to irreversible structural damage, such as structural collapse [213, 214]. This can cause a loss of active sites and a decrease in catalyst stability, ultimately resulting in a significant drop in efficiency and lifespan. Therefore, differentiating between beneficial dynamic amorphization and detrimental structural collapse requires careful monitoring of the reversibility of structural changes and the long-term stability of performance. Beneficial amorphization typically leads to temporary performance enhancement, followed by recovery to a stable state, while structural collapse is characterized by continuous performance degradation and irreversible structural damage [215]. This distinction can be achieved through the use of in situ characterization techniques, such as structural characterization and performance metrics. Future research will require further experimental work, particularly leveraging advanced characterization tools, to fully elucidate the role of dynamic amorphization in Ni-based electrocatalysts under high-current conditions.

4.4 | High Current Density Water Electrolysis Catalysts

In the field of water electrolysis, most reported nanocatalysts are synthesized as powders and subsequently coated onto current collectors using polymer binders such as Nafion or polytetrafluoroethylene. However, this approach often results in partial coverage of active sites, limiting electron transfer efficiency and impeding mass transport due to reduced active surface area and disrupted microstructures. In practical applications, binder degradation compromises film stability, diminishes operational efficiency, and elevates manufacturing costs. To enhance conductivity, carbon-based conductive additives are frequently introduced, yet their susceptibility to oxidation at high current densities or potentials can trigger electrode performance decay [4]. Consequently, developing binder-free, self-supported Ni-based catalysts has emerged as a critical research direction in AEMWE, aiming to overcome the limitations of powder catalysts and meet industrial demands under high current densities.

Compared to conventional electrodes, self-supported Ni-based catalysts grown directly on conductive, flexible substrates offer distinct advantages [13]. This design accommodates higher catalyst loadings, exposing more active sites, while eliminating the need for polymer binders and conductive additives, further improving site accessibility. Through nanostructure engineering, such as one-dimensional nanowires, two-dimensional nanosheets, or three-dimensional porous frameworks, the electrochemical surface area expands, significantly boosting charge and mass transfer efficiencies and enhancing reaction kinetics. Moreover, strong adhesion and intimate contact between the catalyst and substrate effectively prevent mechanical detachment caused by bubble impact at high current densities, ensuring long-term operational stability. Surface wettability regulation plays a pivotal role as well. Optimizing nanostructure and composition can yield superhydrophilic surfaces, promoting electrolyte infiltration and active site utilization, while imparting superaerophobic properties that enable rapid bubble detachment, mitigating interfacial impedance and site shielding. This binder-free design simplifies fabrication processes and reduces costs, positioning self-supported catalysts as highly promising for AEMWE applications.

Designing efficient self-supported Ni-based catalysts hinges on three core elements: deposited nanostructures, substrate selection, and preparation methods. The composition, structure-performance relationships, and surface reconstruction during electrocatalytic processes directly influence catalyst performance [216, 217]. The choice of conductive substrates like NF or insulating substrates shapes nanomorphology and catalytic properties, while preparation techniques such as electrodeposition or wet chemical methods determine catalyst morphology, size, and active site exposure. At high current densities, efficient charge and mass transfer become paramount. Traditional powder catalysts, constrained by binders and carbon additives, often block transport pathways and hinder bubble release, leading to catalyst detachment and performance decline. In contrast, self-supported structures ensure robust catalyst-substrate integration via chemical bonding, enhancing transfer efficiency and stability, making them an ideal choice for high-current-density hydrogen production in AEMWE.

5 | Types of Ni-Based Catalysts

Transition metal elements, owing to their unique outer electron configurations, can donate electrons and provide vacant orbitals during electrocatalytic processes, demonstrating significant catalytic potential in water-splitting reactions. Among these, Ni-based water electrolysis catalysts stand out due to their low cost, abundant reserves, excellent conductivity, structural diversity, and high activity, making them highly promising for applications in the field of water electrolysis [218, 219]. Ni-based electrocatalysts primarily encompass metallic nickel and its derivatives, including sulfides, selenides, carbides, nitrides, phosphides, hydr(oxy)oxides, as well as alloys and heterostructures (Figure 17). This subsection will summarize and discuss the HER catalytic performance of these Ni-based catalysts prepared by different methods and the typical progress of the literatures.

5.1 | Intermetallic Compounds/Alloys

The volcano plot of HER metals reveals that most transition metals exhibit either excessively strong or weak hydrogen adsorption, resulting in suboptimal intrinsic activity. To address this, researchers propose alloying multiple metals to enhance the catalytic performance of active sites. Transition metal alloys typically offer excellent conductivity, synergistic effects from multi-metal active sites, abundant unsaturated coordination environments, and dangling bonds. Adjusting composition and structure tunes the electronic structure of active sites, optimizing adsorption energies for reaction intermediates and yielding superior catalytic performance [220]. Jiang et al. synthesized ruthenium-nickel alloy nanoparticles supported on reduced graphene oxide ($Ru_{90}Ni_{10}$/rGOP) for alkaline hydrogen evolution [221]. In 1 M KOH solution, this catalyst achieves a current density of 1000 mA cm^{-2} at an overpotential of approximately 106 mV, with a Tafel slope of about 26 mV dec^{-1}, outperforming many reported Ru-based catalysts and even surpassing commercial Pt/C catalysts in certain aspects. The alloying process induces electron transfer

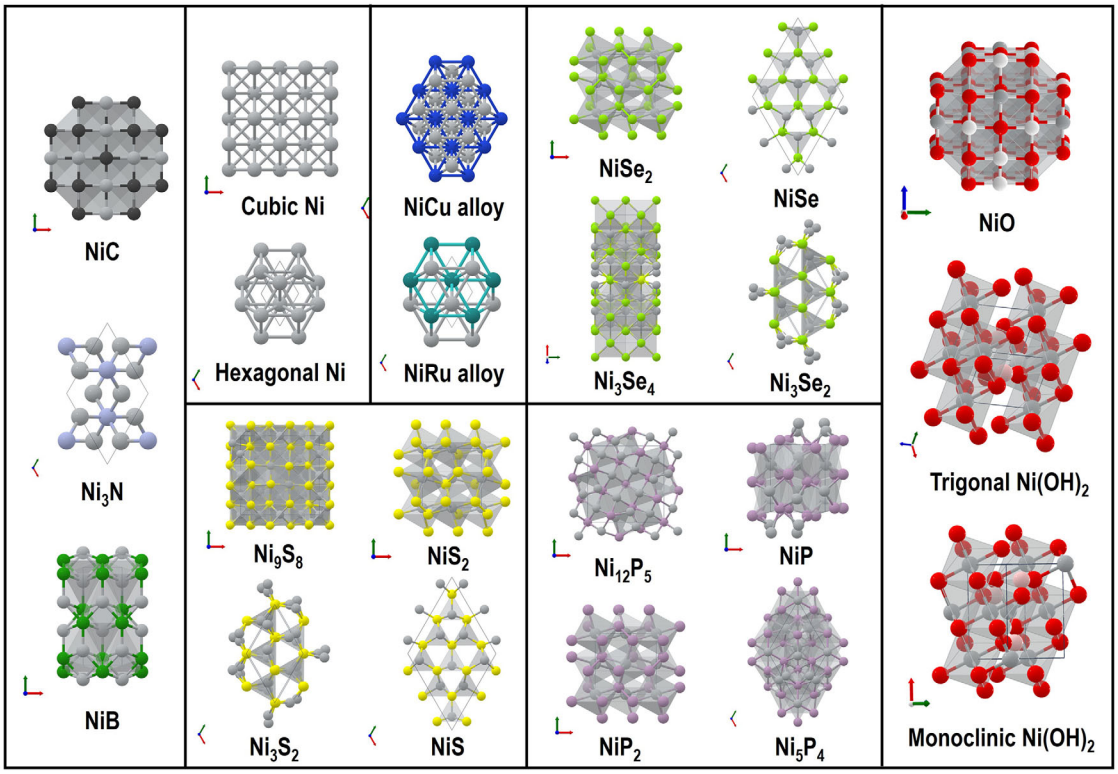

FIGURE 17 | The phase compositions and crystal structures of common Ni-based water electrolysis catalysts.

between Ru and Ni atoms, altering the catalyst's electronic structure. XPS analysis shows a slight shift in the Ru 3p peak in $Ru_{90}Ni_{10}$/rGOP compared to Ru/rGOP, indicating electron transfer from Ni to Ru, which optimizes the catalyst's adsorption and desorption capabilities for reaction intermediates, facilitating the reaction. Additionally, Ni's high oxygen affinity in alkaline media leads to hydroxylation of Ni atoms on the $Ru_{90}Ni_{10}$/rGOP electrode surface, forming a Ru-Ni(OH) multi-active-site surface. XPS and Raman spectra confirm the presence of these multi-active sites, which accelerate water dissociation. Appropriate adsorption of H and OH at Ru-Ni-Ru and Ru-Ru-Ru hollow sites promotes water splitting into active hydrogen intermediates, creating favorable conditions for subsequent hydrogen molecule formation. DFT calculations based on the RuNi (101) plane with a Ru-Ni(OH) multi-active-site surface demonstrate reduced energy barriers for water dissociation and H_2 formation (0.57 eV and 0.42 eV, respectively), significantly lower than those on a single-metal Ru (101) surface, highlighting the critical role of Ru-Ni(OH) multi-active sites in accelerating the reaction. Through suitable alloying, non-precious-metal-based Ni alloys can achieve catalytic activity comparable to Pt/C. Qian et al. prepared Mo-doped NiCoCu alloy (NiCoCu-Mo_x/CF) via solvothermal and annealing methods [222]. Theoretical calculations indicate that Mo doping induces lattice tensile strain and localized electron generation, with electrons transferring from Mo to Ni, Co, and Cu atoms, enhancing O* and H* adsorption from H_2O at Mo and Co sites and accelerating water dissociation. Experimental data confirm the alloy's exceptional performance in 1.0 M KOH electrolyte, with NiCoCu-$Mo_{0.078}$/CF requiring only 35 mV overpotential to reach 10 mA cm^{-2} and sustaining operation at −1000 mA cm^{-2} for 100 h. Zhang et al. utilized a one-step electrochemical reduction method to dope Group VIB transition metals (Cr, Mo, W) into fcc NiCo alloy, producing M-NiCo (M = Cr, Mo, W) hierarchical alloy structures [223]. W-NiCo excels in alkaline media, achieving −10 mA cm^{-2} at an overpotential of 109.2 mV with a Tafel slope of 110.3 mV dec^{-1}. Doping with different elements affects the alloy's crystal structure, electronic structure, and surface properties, leading to different hydrogen evolution kinetics. For instance, W doping expands the NiCo lattice, inducing electron coupling effects that optimize electronic configuration and enhance the overall reaction kinetics in alkaline media towards HER (Figure 18a).

For conventional binary or ternary alloys, limited elemental compositions and surface active sites restrict comprehensive optimization of all reaction intermediates in alkaline HER, capping the performance gains of such Ni-based alloy catalysts. The advent of high-entropy alloys (HEAs), with their tunability and multi-active-site advantages, offers unique potential for constructing Ni-based alloy catalysts [58, 224]. Comparing HER activities across alloys reveals that catalytic performance improves with increasing element count; for example, the six-element alloy PtPdNiCoMn outperforms quaternary and ternary alloys, as reflected by the optimized bond length on TM-H along with the increase number of metal elements (Figure 18b) [225]. Control sample tests show that medium-entropy alloys (MEAs) like PtNiCoMn, PdNiCoMn, and NiCoMn exhibit lower HER activity than the PtPdNiCoMn HEA. Electronic structure analysis of the (111)-oriented PtPdNiCoMn HEA surface during hydrogen adsorption indicates decreasing electron density of H* from Mn to Co, Ni, Pd, and Pt sites, suggesting charge transfer from H* to the catalyst surface. The density of states for Ni, Co, and Mn increases significantly at the Fermi level, facilitating electron transfer. Hydrogen adsorption shifts the d-band centers of Co and Mn toward the Fermi level (Figure 18c),

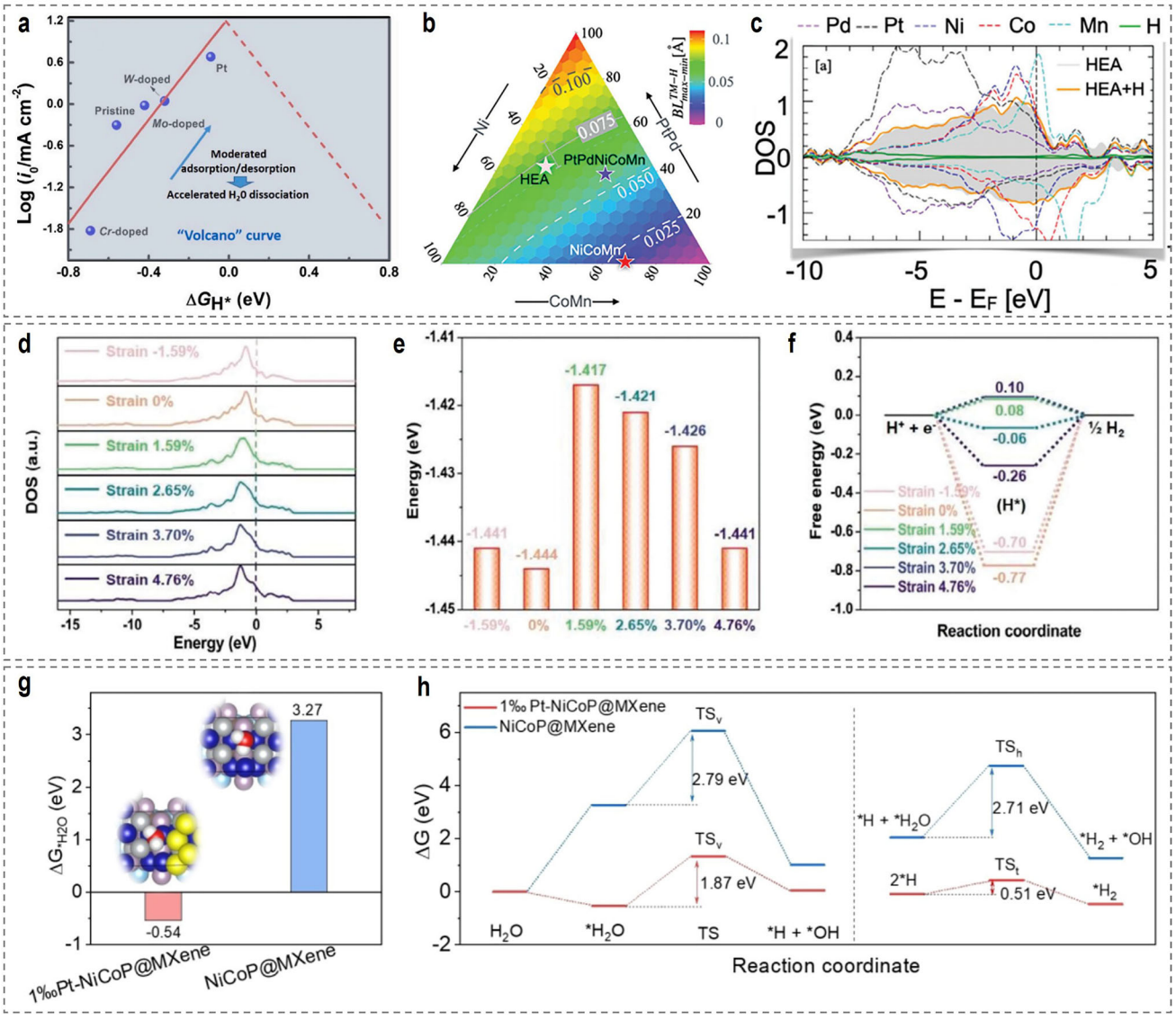

FIGURE 18 | (a) Volcano plot of the polarized exchange current density (i0) versus the ΔGH* for pristine and Cr-, Mo-, or W-doped NiCo. Reproduced with permission [223]. Copyright 2022, Elsevier. (b) A cut-through 5D composition space showing the variance in bond length on TM-H surface. (c) DFT calculated the partial density of states (states/eV-atom) for HEA both with and without hydrogen coverage. Reproduced with permission [225]. Copyright 2024, Wiley-VCH. (d) Density of states, (e) d band centers, (f) free energies for H adsorption for CoP models with different lattice strains. Reproduced with permission [231]. Copyright 2024, Wiley-VCH. (g) Comparison of adsorption energy of water molecule on two kindsofcatalysts. (h) Gibbs free energy diagram including initial state (0 eV), intermediate state (water adsorption), transition state (TSv, TSh, and TSt represent the transition states of Volmer, Heyrovsky, and Tafel step, respectively), and final state. Reproduced with permission [232]. Copyright 2024, Wiley-VCH.

strengthening TM-H interactions, while those of Pt, Pd, and Ni move away. Chen et al. synthesized a non-precious-metal HEA catalyst (NNM-HEA@CF) composed of Cu, Ni, Mo, W, and Co, achieving an overpotential of only 22 mV at 10 mA cm^{-2} for HER [226]. DFT calculations reveal significant d-orbital overlap among the metals, indicating strong electronic interactions. The Ni site exhibits a ΔG_{H^*} of −0.25 eV, close to the ideal HER value, and a ΔG_{OH} of −1.05 eV, more stable than other sites, favoring *H and *OH adsorption. Compared to Ni (111), the d-band center of Ni in NNM-HEA shifts, adjusting its electronic configuration, weakening Ni-H* binding, and enhancing *OH adsorption, thus improving H_2O adsorption and dissociation for superior HER performance. A key challenge for alloy catalysts lies in the high energy barrier of water dissociation, limiting practical applications due to their limited water dissociation sites. To address this, Li et al. developed a phase-separated NiCu/NiMn(OH)$_2$ nanocomposite (NiCuMn) via one-step electrodeposition for alkaline HER [227]. Low-electronegativity Mn induces low-valence Ni$^{\delta+}$ in NiMn(OH)$_2$, accelerating the water dissociation (Volmer step), while Cu optimizes the d-band center of the NiCu alloy, enhancing the Heyrovsky/Tafel steps. This synergy results in exceptional performance in 1 M KOH, with overpotentials of 17 mV and 62 mV at 10 and 100 mA cm^{-2}, respectively, a turnover frequency of 0.78 s^{-1} at 100 mV, and excellent durability after 10000 cyclic voltammetry cycles. Similarly, Fu et al. synthesized an efficient alkaline HER catalyst (Eu_2O_3-NiCo) by electrodepositing Eu_2O_3 with NiCo alloy [228]. Leveraging Eu_2O_3's oxygen affinity and multi-site synergy with NiCo, this

catalyst enhances water adsorption and dissociation, optimizing intermediate adsorption energies. In 1.0 M KOH, Eu_2O_3-NiCo achieves 10 mA cm^{-2} at an overpotential of just 60 mV.

5.2 | Phosphides

Electrons in metals typically move freely, endowing metals with excellent electrical and thermal conductivity. However, the strong electronegativity of P atoms in transition metal phosphides restricts electron delocalization in the metal, impacting electron transport capabilities [229]. Transition metal phosphides garner attention due to the high electronegativity of P atoms, and modulating their electronic structure through asymmetric coordination offers potential to enhance HER activity. Consequently, extensive research focuses on improving the conductivity of metal phosphides through several strategies: (i) Optimizing the metal-to-phosphorus ratio in transition metal phosphides minimizes the restriction of P on metal electron delocalization; (ii) Doping with other atoms such as oxygen or nitrogen alters the material's electronic structure, boosting conductivity; (iii) Loading metal phosphides onto highly conductive substrates like alloys, carbon cloth, or nickel mesh effectively enhances conductivity [230]. Yuan et al. reported an Fe- and Ni-co-doped CoP catalyst, achieving an overpotential of only 36 mV at 10 mA cm^{-2} in HER [231]. Through electronic structure and lattice strain engineering, Fe and Ni co-doping modifies the electronic structure and lattice strain of CoP. Electronic structure optimization positions the d-band center at a more favorable level, facilitating intermediate adsorption and reducing the HER reaction energy barrier, while tensile strain from lattice engineering optimizes hydrogen intermediate adsorption behavior, synergistically enhancing HER performance (Figure 18d–f). Beyond single phosphides, bimetallic phosphides exhibit superior catalytic activity due to synergistic effects from multiple metal active sites. Wang et al. synthesized Ru-doped Ni_2P/Ni_5P_4 catalysts featuring a multiphase structure and abundant heterointerfaces [43]. This Ru-Ni_2P/Ni_5P_4 catalyst requires an overpotential of just 128 mV to reach 1000 mA cm^{-2} in HER, with a Tafel slope of 52 mV dec^{-1}. Theoretical calculations reveal that Ru-Ni_2P/Ni_5P_4 exhibits the highest charge density near the Fermi level in its total density of states, enhancing conductivity. Its d-band center lies closer to the Fermi level, favoring intermediate adsorption and electrochemical processes during the reaction. Additionally, this catalyst displays the lowest work function, enabling electrons to spill over and exchange with reactants more readily, accelerating electrocatalytic kinetics. Zhou et al. utilized MXene to construct a Pt/NiCoP interface, preparing the Pt-NiCoP@MXene catalyst, which demonstrates exceptional performance in 1 M KOH, achieving overpotentials of 26.5 and 181.6 mV at 10 and 500 mA cm^{-2}, respectively [232]. Theoretical calculations indicate that interfacial electron transfer occurs between adjacent Pt atoms and NiCoP, lowering the valence states of Co and Ni and rendering NiCoP negatively charged. This reduces the potential required for catalyst pre-activation and repels OH^-, providing more active sites for water molecule adsorption. Furthermore, this electron transfer optimizes the adsorption energy of H_2O molecules, lowering the water dissociation energy barrier and shifting the catalytic pathway from Volmer-Heyrovsky to Volmer-Tafel steps (Figure 18g,h). It also weakens H_2 adsorption, enabling rapid H_2 release and enhancing overall catalytic performance.

Transition metal sulfides attract widespread use as catalysts due to their excellent conductivity, large specific surface area, and abundant hydrogen adsorption active sites [233, 234]. However, sulfides tend to agglomerate during preparation, leading to structural collapse during cycling and generating significant dead volume inaccessible to electrolytes, which drastically reduces catalytic efficiency and impacts electrode lifespan. This remains a critical challenge for sulfide catalysts. Combining sulfides with highly conductive current collectors such as metal foams, carbon cloth, carbon fibers, metal meshes, or metal plates effectively mitigates agglomeration during growth, enhancing catalytic activity and chemical stability. Conventionally, cationic Ni serves as the recognized HER active site in nickel sulfides. Wang et al. synthesized a NiS_2/NiS_2-NiS catalyst featuring NiS_2 nanoflowers grown on a biphasic NiS_2-NiS foam [235]. XPS and DFT calculations reveal that this unique interfacial structure induces reverse electron transfer from Ni to S, increasing electron density at S sites and rendering them more active. In HER tests conducted in 1 M KOH solution, the NiS_2/NiS_2-NiS electrode excels, requiring only 55 mV overpotential to achieve 10 mA cm^{-2}. DFT calculations further elucidate the intrinsic mechanism of interface regulation in enhancing hydrogen evolution performance. In the NiS_2/NiS_2-NiS system, the ΔG_{H^*} of S sites reach an optimal value, ΔG_{H2O} becomes more negative, and the transition state energy barrier for water dissociation minimizes. These findings indicate that interface regulation optimizes the adsorption and activation capabilities of S sites for reaction intermediates, facilitating water dissociation and hydrogen adsorption/desorption, thus accelerating HER kinetics. Nickel sulfides like Ni_3S_2, with suitable d-electron configurations and high conductivity, undergo extensive study, yet challenges such as high water dissociation energy barriers and difficulties in converting H_{ads} to H_2 persist. Introducing NiS and sulfur vacancies into Ni_3S_2 systems to construct heterostructures and defects holds research value. Yu et al. employed a hydrothermal sulfidation-acid-assisted etching strategy to prepare Mo-doped NiS/Ni_3S_2 polymorphic heterostructures rich in sulfur vacancies (Mo-NiS/Ni_3S_2-rich S_v) for alkaline HER [236]. Structural characterization confirms the formation of heterostructures and sulfur vacancies, with the catalyst exhibiting outstanding HER activity and durability in alkaline solution, requiring only 230 mV overpotential to reach 100 mA cm^{-2}. In situ Raman spectra and theoretical calculations reveal that S centers on the Ni_3S_2 side act as hydrogen evolution sites, Ni sites on the Mo-NiS side facilitate H-O-H bond cleavage, and sulfur vacancies accelerate H* conversion to H_2 (Figure 19a). This synergy between polymorphic heterostructures and elemental defects offers valuable insights for designing high-performance HER electrocatalysts. Although Ni_3S_2 shows potential, its high water dissociation energy barrier as a single component remains problematic. Shan et al. utilized a one-step hydrothermal method to fabricate MoO_2/Ni_3S_2/NF on NF [237]. Differing work functions between MoO_2 and Ni_3S_2 induce electron transfer from Ni_3S_2 to MoO_2 upon heterojunction formation. DFT calculations show that water dissociation on Ni_3S_2 alone requires a 1.49 eV energy barrier, which drops to 1.17 eV in the MoO_2/Ni_3S_2 heterostructure. MoO_2 acts as a water dissociation promoter at the interface, with OH preferentially adsorbing on Ni sites of Ni_3S_2 and H on O sites of MoO_2, synergistically lowering the water dissociation barrier and accelerating the Volmer step of HER. Ni_3S_2, abundant on Earth and inherently active, emerges as a promising HER electrocatalyst, yet strong

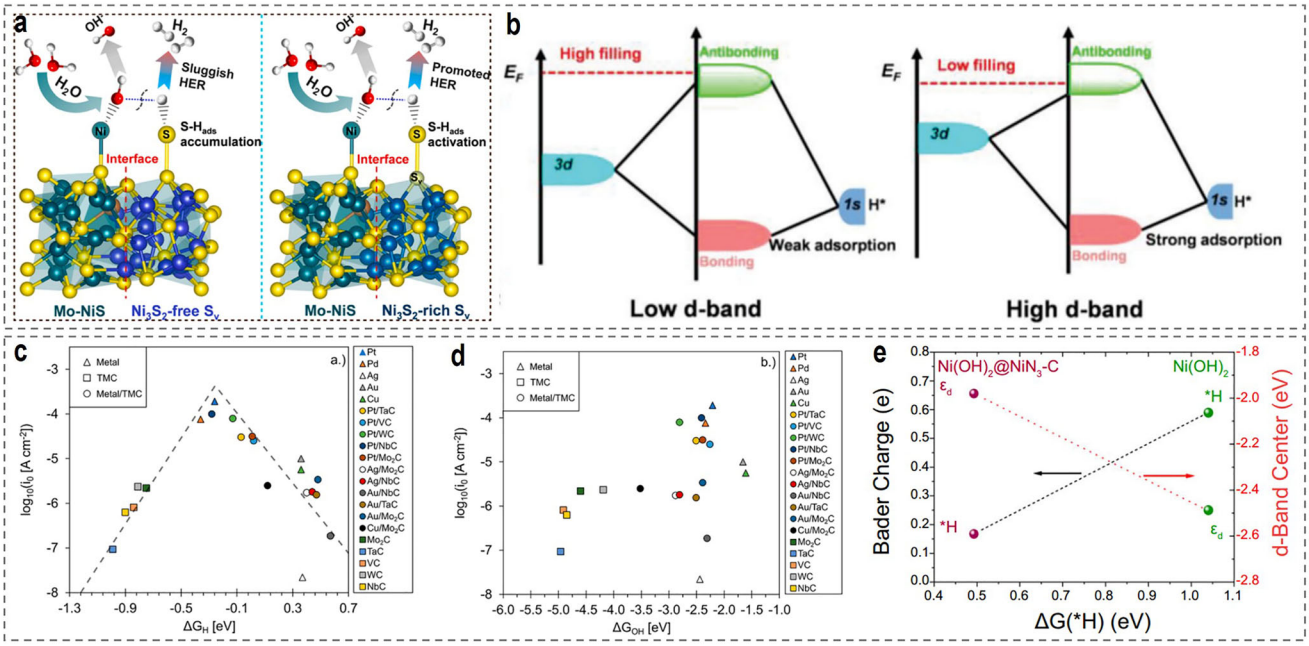

FIGURE 19 | (a) Schematic diagram illustrates the heterointerface and S-vacancy roles on the surface of the Mo-NiS/Ni3S2-free Sv (left) and rich Sv (right) electrocatalysts during the alkaline HER process. Reproduced with permission [236]. Copyright 2023, Elsevier. (b) Schematic bond interaction between the H atom and the surface active sites with different d-band electronic structures. Reproduced with permission [242]. Copyright 2024, Wiley-VCH. log10(i0) for metals, TMCs, and metal-modified TMCs as a function of ΔGH* (c) or ΔGOH (d) in 0.1 M KOH. Reproduced with permission [246]. Copyright 2019, American Chemical Society. (e) Relationship between Bader charge of *H adsorption and d-band center with the free energy of Ni(OH)2@NiN3-C and Ni(OH)2. Reproduced with permission [248]. Copyright 2023, Nature Publishing.

S-H_{ads} bonds form on its surface during HER, hindering H_{ads} desorption and reducing activity. Constructing heterointerfaces adjusts the surface electronic configuration of Ni_3S_2, optimizing H_{ads} adsorption/desorption and enhancing HER performance. Wu et al. prepared amorphous $NiWO_4$ nanoparticle-modified Ni_3S_2 electrocatalysts ($NiWO_4/Ni_3S_2$) [238]. It exhibits remarkable performance in alkaline media, with $NiWO_4/Ni_3S_2$-16 requiring overpotentials of 136 mV and 274 mV at 10 mA cm^{-2} and 100 mA cm^{-2}, respectively, a Tafel slope of 112 mV dec^{-1}, and stability over 75 h. This superior performance stems from strong electronic interactions between $NiWO_4$ and Ni_3S_2, enhancing water adsorption at Ni sites and hydrogen adsorption/desorption at S sites, offering a novel pathway for designing efficient non-precious-metal HER catalysts.

Although transition metal chalcogenides hold promise as alkaline HER electrocatalysts, controversies persist regarding reaction mechanisms and active sites. Real-time monitoring of catalytic processes and identification of active sites carry significant implications for elucidating catalytic mechanisms. Operando XAS and near-ambient pressure XPS studies of NiS in alkaline HER reveal dynamic reconstruction, with NiS transforming in situ into a mixed Ni_3S_2/NiO phase [239]. This Ni_3S_2/NiO interface generates highly active synergistic dual sites, where interfacial Ni facilitates water dissociation and OH* adsorption, and interfacial S supports H* adsorption and H_2 evolution. This mixed phase enables the NiS electrocatalyst to achieve 10 mA cm^{-2} at an overpotential of 95 ± 8 mV, highlighting the dynamic chemical nature of transition metal chalcogenides and the potential to enhance performance through precise control of operating conditions. While transition metal sulfides show promise, sulfur leaching compromises stability, making precise control of sulfur leaching critical for high-performance applications. Wang et al. utilized hydrothermal sulfidation/carbon coating to prepare CN differentiated NiCoS catalysts, with CN@NiS, CN@CoS, and NiCoS as controls [240]. The CN@NiCoS electrocatalyst achieves enhanced activity and stability through a unique structural design. The Ni_3S_2/Co_9S_8 heterostructure promotes sulfur migration, forming sulfur vacancies that accelerate electron transfer and boost HER activity, while the nitrogen-doped carbon shell (CN) captures migrating sulfur atoms via strong C-S bonds, preventing sulfide dissolution and enhancing stability. Additionally, dynamically formed sulfur-doped CN shells and sulfur vacancy pair sites alter the d-band center near the Fermi level, optimizing the reaction process and further improving activity and stability.

5.3 | Selenides

Selenides exhibit high conductivity and unique electronic structures, positioning them as promising candidates for electrocatalytic water splitting [241]. Sharing the same outermost electron count as sulfur, selenium displays similar chemical properties. With an outer electron configuration of $4s24p^4$, Se readily accepts electrons from less electronegative elements to form Se^{2-}. Zheng et al. employed a hydrothermal method followed by etching to initially synthesize a $NiSe_2$ precursor, subsequently converting part of it into $Ni_{0.85}Se$ by controlling etching duration, yielding a structure rich in heterointerfaces [242]. Experimental results demonstrate that the $NiSe_2/Ni_{0.85}Se$-2 h electrocatalyst excels in HER performance in 1 M KOH electrolyte, requiring an overpotential of only 76 mV to achieve 10 mA cm^{-2}, which is

substantially lower than standalone $NiSe_2$ (202 mV) and $Ni_{0.85}Se$ (213 mV). Multiple characterization techniques and theoretical calculations unveil the intrinsic mechanisms behind the superior HER performance of the $NiSe_2/Ni_{0.85}Se$ heterostructure. The heterointerface induces strong electronic interactions between $NiSe_2$ and $Ni_{0.85}Se$, with electrons transferring from $NiSe_2$ to $Ni_{0.85}Se$, optimizing the material's electronic structure. This optimization elevates the charge state of $Ni_{0.85}Se$, facilitating electron donation to hydrogen protons and significantly accelerating H_2 molecule formation (Figure 19b). Theoretical calculations further indicate that the heterointerface modulates the electronic structure, optimizing the adsorption energy of intermediate H and lowering reaction energy barriers, thereby markedly enhancing HER catalytic activity. Nickel selenides, with their high conductivity and low bandgap, emerge as potential electrocatalysts, with HER performance closely tied to the Se-to-Ni ratio. Tuning the phase composition of biphasic nickel selenides offers a pathway to improve catalytic performance. Tan et al. precisely controlled the charge state of nickel, phase composition, and electrocatalytic properties by adjusting the initial selenium powder mass [243]. Among the variants, $NiSe_2/Ni_3Se_4$/NF-4 exhibits exceptional alkaline HER performance. In 1.0 M KOH electrolyte, this catalyst achieves 10 mA cm^{-2} at an overpotential of just 145 mV, outperforming single-component catalysts. Structural and electronic analyses reveal that the higher $NiSe_2$ phase content and relatively lower nickel charge state in $NiSe_2/Ni_3Se_4$/NF-4 confer distinct advantages in alkaline HER. XPS analysis shows a higher presence of $Se^{\delta-}$ and fewer oxidized nickel species. Calculations indicate that the ΔG_{H^*} value for Ni sites in the $NiSe_2/Ni_3Se_4$ reaches −0.372 eV, closer to 0 eV than other catalysts, suggesting superior H* adsorption and desorption efficiency, which benefits HER. Charge density difference and Bader charge analyses reveal electron transfer from Ni_3Se_4 to $NiSe_2$ at the interface, enhancing electron accumulation on the $NiSe_2$ side, promoting H* adsorption, and improving conductivity, thus optimizing overall hydrogen evolution performance.

Bimetallic selenide systems also effectively enhance hydrogen evolution activity. Cheng et al. utilized a meticulous multistep wet chemical approach to construct 3D copper-nickel selenide (CuNi@NiSe) nanodendrites with abundant heterointerfaces, composed of $Cu_{2-x}Se$-Ni_3Se_4 interfaces [244]. In 1 M KOH solution, this material achieves 10 mA cm^{-2} at an overpotential of only 41 mV, outperforming many comparative catalysts. Calculations reveal that Cu defects on the $Cu_{2-x}Se$ surface at the $Cu_{2-x}Se/Ni_3Se_4$ interface facilitate electron transfer between Cu atoms and Se atoms of Ni_3Se_4. This electron transfer substantially lowers the reaction barrier of the rate-determining HER step, reducing it from 1.73 eV on Ni_3Se_4 and 2.28 eV on $Cu_{2-x}Se$ to 0.94 eV at the $Cu_{2-x}Se/Ni_3Se_4$ interface. Additionally, the ΔG_{H^*} at this interface measures 0.21 eV, significantly lower than 0.41 eV for Ni_3Se_4 and 0.71 eV for $Cu_{2-x}Se$, enabling easier H* adsorption on Se surfaces, promoting water dissociation, and accelerating the hydrogen evolution rate.

5.4 | Carbides

Hybridization between the d-band of transition metals and the s- and p-orbitals of carbon in transition metal carbides (TMCs) narrows the metal d-band, resulting in a d-band structure resembling that of Pt [245]. Formed by carbon atoms occupying interstitial sites within metal lattices, TMCs exhibit a combination of metallic, ionic, and covalent bonding characteristics. Their metallic nature confers excellent charge transfer capabilities, while covalent bonds contribute to high hardness and brittleness. Ionic interactions between metal and carbon atoms narrow the d-band, endowing TMCs with properties akin to precious metals. Zhang et al. found that the HBE of metal-modified TMCs correlates with HER activity in both acidic and alkaline environments, following a volcano-type relationship, making it an effective descriptor of HER activity [246]. Optimal HER activity occurs when ΔG_{H^*} approaches a suitable value, as excessively strong or weak hydrogen adsorption hinders the reaction (Figure 19c). In contrast, the OHBE shows a weaker correlation with alkaline HER activity (Figure 19d), suggesting it is not a robust descriptor for alkaline HER and implying that adsorbed hydroxyl groups may not directly influence the rate-determining step in alkaline HER kinetics. Beyond forming carbides, incorporating carbon into the Ni lattice also enhances activity. Chen et al. pyrolytically reduced a $Ni_3(BTC)_2$ precursor to synthesize nickel catalysts with varying lattice carbon (LC) content [247]. As LC content increases, the electronic structure of nickel transitions from a Ni_3C-like configuration to a quasi-Ni structure. XRD analysis of the crystal structure reveals that higher hydrogen concentrations improve catalyst crystallinity, with LC content influencing structural order. XPS and XAS probe the electronic structure, with shifts in the position and intensity of the Ni $2p_{3/2}$ peak in XPS reflecting the presence of carbon-nickel bonds and LC content variations. XANES spectra from XAS indicate changes in Ni's average valence state, while EXAFS spectra confirm Ni-C coordination, establishing the relationship between LC content and electronic structure. DFT calculations on Ni(111) models with varying LC doping levels show that LC incorporation shifts the Ni d-band center downward, weakening HBE and OHBE. For C_{less}-Ni, HBE decreases from 0.56 eV in pure Ni to 0.37 eV, and OHBE drops from 0.32 eV to 0.27 eV. Reaction energy barrier calculations reveal that C_{less}-Ni exhibits the lowest Volmer step barrier (1.08 eV) compared to 1.49 eV for pure Ni, indicating that moderate LC doping optimizes HBE and OHBE, enhancing catalytic activity. Zhao et al. utilized NF, solvothermal reaction, and thermal annealing to fabricate an electrode with nano-heterointerfaces, where Ni-N/Ni-C phases, as key components, synergize significantly with the $Ni(OH)_2$ phase [248]. This synergy markedly boosts the electrode's hydrogen evolution activity in alkaline media. Compared to single-phase $Ni(OH)_2$ catalysts, the $Ni(OH)_2$@Ni-N/Ni-C electrode demonstrates superior performance, reducing overpotentials by 102 mV and 113 mV at 10 mA cm^{-2} and 100 mA cm^{-2}, respectively. Tafel slopes measure 43.9 mV dec^{-1} at low current densities and 95.8 mV dec^{-1} at high current densities, reflecting significantly accelerated reaction kinetics. Mechanistic insights highlight the pivotal role of carbides. The presence of carbides optimizes the electronic structure, shifting the Ni d-band center upward and increasing the Ni d-state density at the Fermi level (Figure 19e). This reduces antibonding state energy and facilitates reaction intermediate adsorption, creating favorable conditions for hydrogen evolution. Additionally, the Ni-N/Ni-C phase enhances interphase charge transfer, accelerating *H adsorption-desorption and *OH desorption, enabling more efficient hydrogen evolution. This structure also optimizes *H and *OH adsorption energies, promoting

their co-adsorption and further enhancing hydrogen evolution performance.

5.5 | Nitrides

Transition metal nitrides, classified as interstitial compounds, benefit from the small size of nitrogen atoms, which readily embed into lattice interstices, fostering a compact atomic arrangement and conferring excellent electron conduction properties [249]. The presence of nitrogen in these nitrides modulates the electronic structure of adjacent metal atoms, contracting the d-band near the Fermi level. This results in an overall electronic structure resembling that of metals, exhibiting pronounced metallic behavior. Ni_3N stands as the most utilized Ni-based nitride material; however, its ΔG_{H^*} value is notably negative, indicating excessively strong interactions between H_{ads} and Ni. This impedes hydrogen desorption, leading to suboptimal HER activity. Sun et al. addressed this by first electrodepositing Ni nanoparticles onto NF, followed by thermal nitridation, successfully synthesizing a catalyst rich in Ni_3N/Ni interface sites [250]. Experimental results reveal that in 1.0 M KOH, this catalyst achieves a current density of −10 mA cm^{-2} with an overpotential of only 12 mV, rivaling the performance of Pt/C catalysts supported on NF. DFT calculations further demonstrate that the ΔG_{H^*} at the Ni_3N/Ni interface approaches 0 eV, accompanied by high water adsorption energy and a low water dissociation energy barrier, enabling effective promotion of alkaline HER. Zong et al. employed a nitridation process to fabricate a triphasic heterointerface nanoarray electrode, Ni_3N/Ni@W_2N_3, for alkaline HER [186]. The Ni_3N/Ni@W_2N_3 triphasic heterojunction interface facilitates electron redistribution. XPS analysis indicates electron transfer from Ni_3N to surrounding W_2N_3 and metallic Ni, establishing Ni_3N as an electron-hole center. This electronic restructuring weakens Ni-H bonds and optimizes ΔG_{H^*}. Calculations show that the ΔG_{H^*} of Ni_3N/Ni@W_2N_3 decreases to −0.41 eV, enhancing hydrogen adsorption kinetics and boosting HER catalytic activity. The overpotential required to drive 10 mA cm^{-2} measures just 66 mV, comparable to commercial Pt/C. Zhang et al. prepared a series of $Cu_xIn_{1-x}NNi_3$ catalysts by partially substituting A-site atoms (A = Cu or In) in $ANNi_3$ [251]. Experimental findings highlight $Cu_{0.4}In_{0.6}NNi_3$ as the top performer, achieving 10 mA cm^{-2} in 1.0 M KOH with an overpotential of only 42 mV and a low Tafel slope of 51 mV dec^{-1}, indicative of high intrinsic catalytic activity. In stability tests, this catalyst sustains operation at 100 mA cm^{-2} for 60 h with a mere 7 mV increase in overpotential, significantly outperforming commercial Pt/C. Theoretical calculations reveal that partial substitution lowers the water dissociation kinetic barrier in $Cu_xIn_{1-x}NNi_3$ and optimizes the ΔG_{H^*}. For instance, $Cu_{0.5}In_{0.5}NNi_3$ exhibits a water dissociation barrier of 1.49 eV, lower than that of unsubstituted InNNi (2.09 eV), and a ΔG_{H^*} of 0.09 eV, near the optimal value for HER, facilitating the reaction progression.

5.6 | Borides

In borides where metals serve as active centers, the small atomic radius and electronegativity of boron contribute to a diverse range of structures. Unlike other non-metal elements, boron can transfer electrons back to adjacent metal atoms, enriching the electron density at metal sites and enhancing water electrolysis capabilities. Zhou et al. demonstrated that metal-boron electronic interactions significantly influence surface hydrogen adsorption and catalytic activity [252]. In intermetallic compounds formed by transition metals (TMs) and boron, strong hybridization occurs between the d-orbitals of TMs and the sp-orbitals of boron, altering the metal's electronic structure and consequently affecting surface hydrogen adsorption and catalytic performance. Comparing the DOS and PDOS of Ru and RuB reveals that the d-band center of RuB shifts downward, away from the Fermi level. According to d-band theory, this shift lowers the energy of antibonding states and increases their occupancy. Since hydrogen adsorption correlates with antibonding states, this change weakens hydrogen adsorption. Specifically, under crystal field theory (Figure 20a–c), Ru atoms coordinate with six neighboring B atoms in an octahedral field with D3h symmetry, splitting the five 4d orbitals of Ru into three groups. The d_{xz} and d_{yz} orbitals strongly hybridize with the sp-orbitals of B, exhibiting the lowest energy; the d_{x2-y2} and d_{xy} orbitals possess moderate energy; and the d_{z2} orbital, due to symmetry mismatch, hybridizes weakly with B atoms. This orbital hybridization contrasts with the degenerate energy of the five 4d orbitals in metallic Ru, fundamentally driving the altered d-band properties in RuB and resulting in weaker hydrogen adsorption on the RuB surface compared to Ru. Catalytic activity closely ties to surface hydrogen adsorption, with the ΔG_{H^*} serving as a key metric for evaluating HER performance. An efficient HER catalyst ideally exhibits a ΔG_{H^*} value near zero at its catalytic sites. Theoretical calculations indicate that the weakened hydrogen adsorption due to metal-boron electronic interactions endows certain TM borides (e.g., PdB, RuB, ReB) with favorable ΔG_{H^*} values. These compounds are thus predicted to possess high HER catalytic activity. Experimental validation confirms that among seven synthesized TM borides, RuB exhibits exceptional performance, requiring an overpotential of only 22 mV to achieve 10 mA cm^{-2}, approaching the catalytic efficiency of Pt. Shen et al. prepared a novel monolithic 3D hollow foam electrode, Ni-Mo-B HF, using an electroless plating-calcination strategy [253]. This electrode has a large electrochemical surface area, high electrical conductivity, high mechanical strength, and low gas mass transfer resistance. It exhibits excellent catalytic activity and long-term stability towards the HER at high current densities. For example, in the HER, a current density of 50 mA cm^{-2} can be achieved at an overpotential of 68 mV. In the HER reaction, the addition of Mo rearranges the atomic distribution in Ni-B, increases the bonds between Ni and B, enables more electrons to transfer from B to Ni, and thus enhances the HER rate. Preliminary DFT calculations show that Ni-Mo-B has a more efficient ΔG_{H^*}. At the same time, the introduction of Mo atoms causes lattice distortion, resulting in solid-solution strengthening or dispersion strengthening, which improves the mechanical properties of the electrode.

5.7 | Hydr(oxy)Oxides

Transition metal hydr(oxy)oxides attract significant attention in catalytic reactions due to their low cost, straightforward synthesis, good chemical stability, and excellent synthetic controllability. However, their poor conductivity and intrinsic catalytic activity limit further advancement. Nickel hydr(oxy)oxides, in particular,

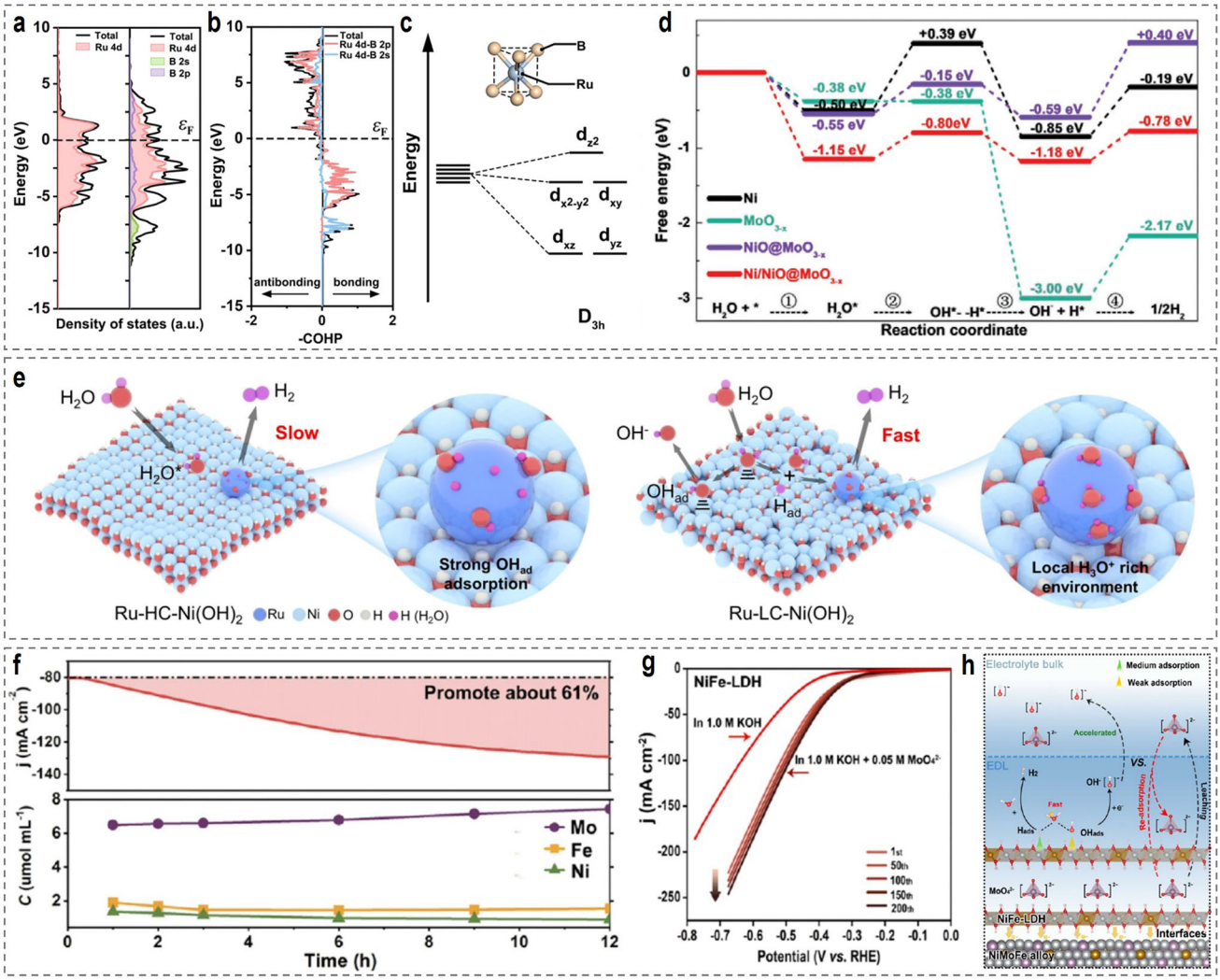

FIGURE 20 | (a) Calculated DOS and pDOS of Ru (0001) surface and RuB (001) surface. (b) COHP of the Ru-B bond in RuB. (c) The occupation of electrons in Ru 4d orbitals under the crystal field of RuB. Reproduced with permission [252]. Copyright 2020, Wiley-VCH. (d) Calculated adsorption free energy diagram of alkaline HER for the Ni, MoO3-x, NiO@MoO3-x, and Ni/NiO@MoO3-x. Reproduced with permission [188]. Copyright 2022, Wiley-VCH. (e) Schematic diagram of microenvironmental changes on Ru-LC-Ni(OH)2 and Ru-HC-Ni(OH)2. Reproduced with permission [64]. Copyright 2024, Wiley-VCH. (f) Current density-time curve under a certain potential (at −275 mV vs. RHE) and dependence of the leached Ni, Mo, and Fe molar concentrations on time. (g) LSVcurves of NiFe-LDH in 1.0 M KOH, adding 0.05 M Na2MoO4. (h) Schematic diagram of the dynamic changes of species in the EDL near the surface of NiMoFe HI during the alkaline HER process. Reproduced with permission [255]. Copyright 2024, American Chemical Society.

exhibit notable water dissociation capabilities. Strategies such as heteroatom doping and morphological modification effectively enhance the catalytic activity of oxides. Combining oxides with structures exhibiting strong hydrogen adsorption compensates for their deficiencies in hydrogen evolution, enabling the development of bifunctional catalysts. This synergy simultaneously promotes water molecule dissociation and the adsorption of hydrogen and hydroxide species, improving the energy conversion efficiency of overall water splitting. Wang et al. employed a one-step electrodeposition method to deposit Mn-Ni/CoP onto pretreated nickel mesh, followed by 100 cycles of CV in 1 M KOH for surface reconstruction, yielding the r-Mn-Ni/CoP catalyst [254]. TEM and XRD analyses reveal the presence of crystalline CoP and NiP phases alongside amorphous regions, forming abundant heterointerfaces. XPS analysis confirms successful Mn doping into Ni/CoP, with doping and heterostructure formation inducing electron transfer and valence state changes. Post-reconstruction, the r-Mn-Ni/CoP surface develops hydrophilic $Co(OH)_2$-rich nanosheets, with contact angle tests verifying significantly improved hydrophilicity. Consequently, this reconstructed catalyst achieves an overpotential of only 134 mV at 100 mA cm^{-2} and maintains nearly constant potential over 1250 h at 10 mA cm^{-2}, surpassing Pt/C catalysts. To develop Ni-based composites with superior performance at high current densities, Zhao et al. utilized a wet chemical method followed by moderate reduction to prepare Ni/NiO@MoO_{3-x} composite nanoarrays [188]. Characterization results indicate that these nanoarrays consist of surface Ni/NiO nanocrystals and amorphous MoO_{3-x} nanorods. DFT calculations highlight the exceptional energy profiles of Ni/NiO@MoO_{3-x} for H_2O adsorption, dissociation, and hydrogen generation or desorption (Figure 20d). The catalyst exhibits a H_2O adsorption energy of −1.15 eV, outperforming

comparative catalysts, attributed to charge transfer between Ni and MoO_{3-X}. The H_2O dissociation energy barrier measures only 0.35 eV, with a reaction energy of −0.03 eV, facilitating dissociation. For hydrogen generation or desorption, the energy cost stands at 0.40 eV, indicating suitable H* adsorption strength. These energy dynamics demonstrate that the composite nanoarray synergistically optimizes reaction barriers, enhancing HER progression. At 100 mA cm^{-2} and 200 mA cm^{-2}, Ni/NiO@MoO_{3-x} achieves overpotentials of 75 mV and 112 mV, respectively, far lower than most comparative catalysts.

Transition metal hydroxides (TMHs) actively participate in alkaline HER, significantly influencing reaction pathways and activity. Surface metal sites serve as reaction centers, directly engaging in water adsorption and dissociation. In low-crystallinity $Ni(OH)_2$ supports, unsaturated Ni sites exhibit substantial negative adsorption energy for H_2O, promoting preferential adsorption and subsequent dissociation. Additionally, interactions between TMH supports and active metal atoms modify the electronic structure of the metal, altering the adsorption and desorption energies of reaction intermediates, optimizing reaction pathways, and enhancing HER activity. Peng et al. loaded Ru single atoms onto low- and high-crystallinity nickel hydroxides, finding that Ru-LC-$Ni(OH)_2$ activates the support via metal dangling bonds, restructures interfacial ion distribution, and forms a local acidic microenvironment in alkaline media, breaking pH-dependent HER activity limitations [64]. In 1.0 M KOH, this catalyst requires overpotentials of just 9 and 136 mV at 10 and 1000 mA cm^{-2}, respectively. DFT calculations of H migration pathways and energies reveal lower H migration energy for Ru-LC-$Ni(OH)_2$, facilitating H accumulation and local acidic environment formation, as depicted in Figure 20e. Bader charge analysis indicates high charge density on Ru single atoms, aiding acidic microenvironment development. Analysis of the d-band center shows a shift to lower energy, optimizing H* adsorption energy and improving adsorption-desorption processes. Calculations of water dissociation barriers and H* binding energies highlight the role of low-crystallinity supports in accelerating the Volmer step and reducing reaction barriers, providing a theoretical basis for the observed HER performance enhancement. Li et al. synthesized a NiMoFe heterostructure (NiMoFe HI) catalyst comprising NiMoFe alloy and MoO_4^{2-}-intercalated NiFe-LDH for HER in alkaline media [255]. NiMoFe HI excels in HER, achieving 10 mA cm^{-2} at an overpotential of 73 mV with a Tafel slope of 121 mV dec^{-1}. The constant potential test was performed to examine the catalytic stability by tracking the change in the current density versus time (Figure 20f). Over 12 h, the current density increased by 61% compared to the original value, demonstrating that NiMoFe HI can continually activate and boost activity during electrolysis. Following the initial hour of constant potential testing, the dissolved concentration of Mo (6.5 μM) was notably higher than that of Ni (1.9 μM) and Fe (2.1 μM) and exhibited a continued increase with the electrolysis time (Figure 20f). In addition, LSV of NiFe-LDH show that the activity of NiFe-LDH is increased significantly only after the addition of MoO_4^{2-} to the KOH solution, and the activity is further improved with several CV cycles (Figure 20g). Therefore, the activity enhancement mechanism of NiMoFe HI during HER was depicted in Figure 20h. During HER, MoO_4^{2-} leaching and readsorption optimize the electronic structure of NiFe-LDH, enhancing H_2O adsorption and dissociation. Its accumulation in the double layer drives OH^- migration via charge repulsion, promoting *OH desorption from active sites, and boosting HER activity.

6 | Ni-Based AEMWE Performance

The integration of water electrolysis with renewable energy sources is widely regarded as the most promising approach for sustainable green hydrogen production. Among the diverse electrolyzer technologies, AEMWE has garnered increasing interest due to its ability to produce high-purity hydrogen under mild alkaline conditions, typically at operating temperatures below 80°C, while utilizing cost-effective, earth-abundant materials. Unlike PEMWE, which depends on scarce and expensive noble metal catalysts like Pt and Ir, AEMWE combines the cost advantages of traditional AWE with the operational efficiency and compactness of membrane-based systems [30]. This makes AEMWE highly adaptable to variable renewable energy inputs, offering benefits such as scalability, rapid response, and reduced capital costs. At the heart of AEMWE's potential are Ni-based catalysts, which excel in the HER in alkaline media due to their abundance, affordability, and versatile electrocatalytic properties. In this section, we provide an in-depth examination of the operational principles and key components of an AEMWE device, emphasizing the pivotal role of Ni-based catalysts. We also present representative examples to show recent advancements in this field, covering topics such as electrode materials, AEM properties, catalyst design, and system engineering. The goal is to offer a thorough overview of the current state-of-the-art in Ni-based AEMWE technology, while identifying critical challenges and opportunities for further advancement toward widespread adoption.

6.1 | Operational Principle and Fundamental Components of AEMWE

A schematic overview of AEMWEs integrated with upstream renewable electricity sources is presented in Figure 21a [256]. Renewable electricity, following conversion via transformer and rectifier units, directly drives the electrolyzer stack. Electrolyte is delivered to the anode through a gas-liquid separator, circulated via a pump, thermally conditioned by a heat exchanger, and purified through an ion-exchange unit. The evolved oxygen, entrained in the recirculating electrolyte, is separated and collected for downstream applications. On the cathode side, the generated hydrogen dissolves in the electrolyte and is similarly routed to a cathodic gas-liquid separator. After deoxygenation and drying, the purified hydrogen is ready for utilization. A representative stack configuration is shown in Figure 21b, while Figure 21c depicts the architecture of an individual cell. At the heart of the device is the membrane-electrode assembly (MEA, Figure 21e,f), comprising an AEM, an anode catalyst layer for the OER, and a cathode catalyst layer for the HER [257]. The AEM, typically based on quaternary ammonium-functionalized polymers, facilitates OH^- transport from cathode to anode, which is distinct from the PEMWE [76]. MEAs are commonly fabricated using either the catalyst-coated membrane (CCM) or the catalyst-coated substrate (CCS) approach (Figure 21d) [258]. Ni-based catalysts, integral to HER under alkaline conditions, are deposited on the cathode via

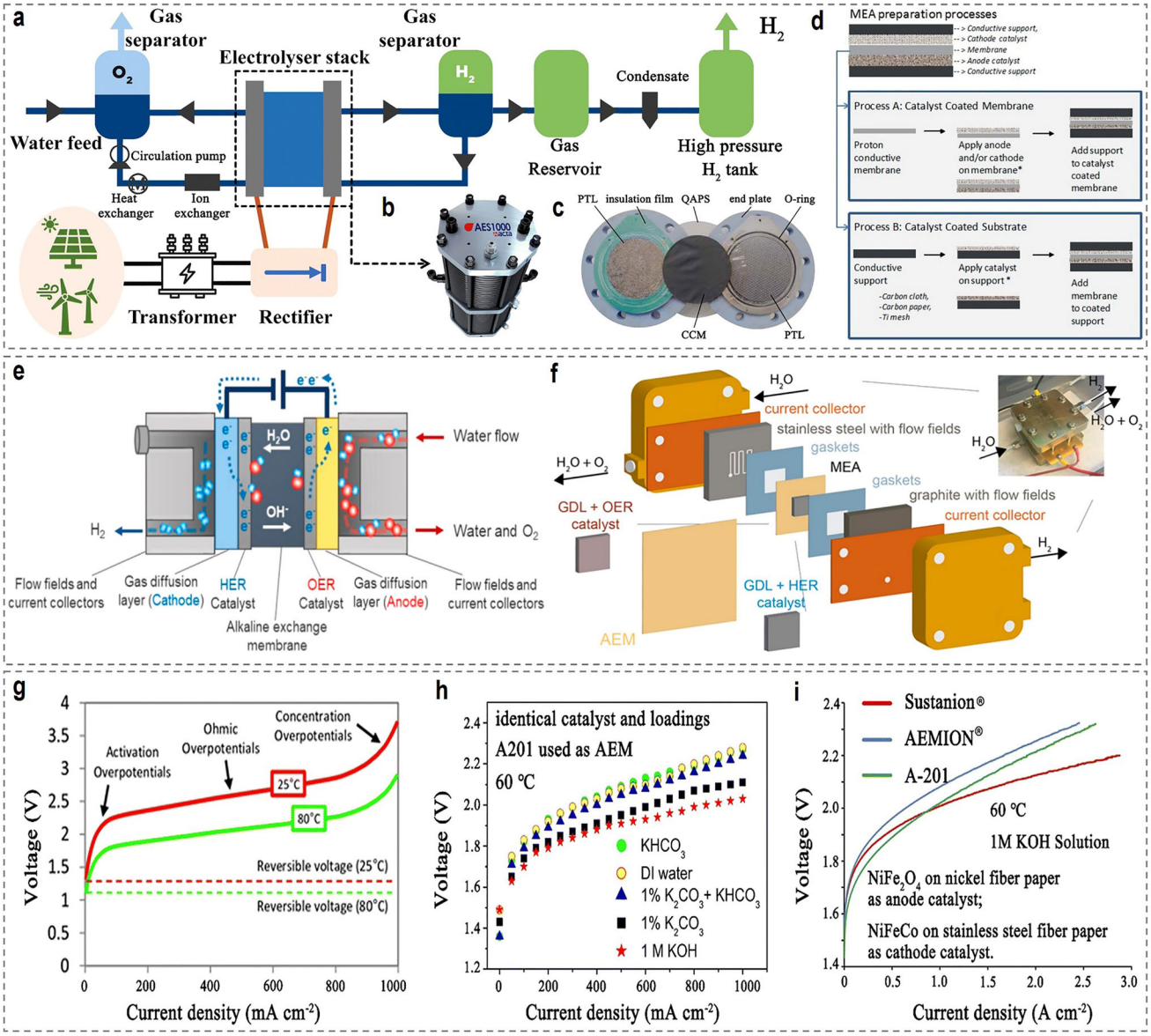

FIGURE 21 | (a) Overview of the basic components of AEM water electrolyzers at the system level. (b, c) Images of a normal water electrolyzer stack and the components inside. Reproduced with permission [256]. Copyright 2022, Royal Society of Chemistry. (d) Schematic of CCS and CCM processes. Reproduced with permission [258]. Copyright 2022, Wiley-VCH. (e) Schematic cross section of an AEM water electrolysis system. (f) AEM electrolyzer components. Reproduced with permission [257]. Copyright 2019, American Chemical Society.Working polarization curves of AEM water electrolyzers impacted by (g) temperature. Reproduced with permission [259]. Copyright 2017, De Gruyter Brill. (h) Different electrolytes. Reproduced with permission [261]. Copyright 2017, Elsevier. (i) Different membranes. Reproduced with permission [265]. Copyright 2020, Elsevier.

techniques such as spraying, electrodeposition, or hot pressing to form a mechanically stable and electrochemically active layer. Bipolar plates, which serve as both electrical interconnects and thermal conduits, are positioned between adjacent cells. The performance of AEMWEs at industrially relevant current densities is governed by the integrated behavior of the AEM, catalytic layers, porous transport layers (PTLs), and bipolar plates. The cathodic PTL, typically referred to as the gas diffusion layer (GDL), and the anodic PTL, referred to as the liquid-gas diffusion layer (LGDL), enable efficient mass transport of gases and electrolyte. Materials such as NF, stainless steel mesh, or carbon cloth are routinely employed to optimize conductivity and gas diffusion. Structural integrity and sealing are maintained by endplates, while engineered flow fields ensure uniform water delivery and effective gas evacuation.

During operation of AEMWEs, water or a dilute alkaline electrolyte (typically 1 M KOH) is introduced into the cathode compartment, where HER is catalyzed by Ni-based electrodes [35]. The resulting hydrogen gas is liberated, while OH^-, generated concurrently, traverses the AEM toward the anode, where OER occurs. This electrochemical sequence exploits the favorable interaction between Ni surfaces and water molecules, facilitating hydrogen intermediate formation in alkaline environments. However, the requirement for an additional water dissociation step (Volmer step) imposes kinetic limitations relative to

hydrogen evolution in acidic media. System-level performance is governed by a combination of ohmic losses, primarily arising from AEM resistance and interfacial contact resistances, kinetic overpotentials, typically evaluated via Tafel analysis, and mass transport constraints such as gas bubble accumulation. Integration of Ni-based catalysts with conductive supports (e.g., Ni foam) has been shown to mitigate these losses by promoting efficient electron transport and improving the accessibility of active sites. Nevertheless, internal resistance, particularly from membrane and electrode interfacial contributions, continues to represent a principal source of energy inefficiency.

The *I–V* characteristics of AEMWEs provide critical insight into single-cell electrochemical behaviour, particularly when evaluated as a function of temperature, electrolyte composition, and membrane selection. Representative polarization curves at 25°C and 80°C are shown in Figure 21g [259]. The overall cell overpotential can be deconvoluted into three principal components: the activation overpotential (V_{act}), arising from sluggish electrode kinetics; the ohmic overpotential (V_{ohm}), reflecting ionic and electronic resistance within the cell; and the concentration overpotential (V_{con}), associated with mass transport limitations under high current densities. With increasing temperature, the reversible voltage (U_{rev}) for water electrolysis decreases, and U_{rev} is calculated to be 1.167 V at 100°C, which explains the lower U_{rev} at 80°C compared to 25°C. Elevated temperatures also enhance ionic conductivity and accelerate reaction kinetics, thereby reducing both V_{act} and V_{ohm} [260]. However, thermal acceleration of membrane degradation constrains long-term performance. As such, a practical operational window of 40–70°C is typically adopted to balance energy efficiency and durability. Electrolyte composition constitutes a second major factor influencing AEMWE performance. Common feedstocks include dilute alkaline solutions such as 1 M KOH, Na_2CO_3, and $NaHCO_3$, as well as deionized water. Optimal electrolytes must ensure efficient ion transport while minimizing ohmic losses and preserving membrane stability. Comparative polarization studies reveal a performance trend of 1 M KOH > 1% K_2CO_3> 1% K_2CO_3 + $KHCO_3$> $KHCO_3$> deionized water (Figure 21h) [261]. This ordering reflects the superior OH^- conductivity of 1 M KOH, which lowers internal resistance and enhances overall performance [262]. However, further increases in KOH concentration elevate the risk of CO_2 ingress and membrane degradation, in addition to incurring a higher cost. By contrast, carbonate- and bicarbonate-based electrolytes offer improved chemical compatibility with AEMs but suffer from reduced reaction kinetics and ionic conductivity [263, 264]. While deionized water is the most economical and abundant option, its limited ionic conductivity and the associated need for advanced bipolar plate designs remain obstacles to practical implementation. Finally, membrane properties are crucial determinants of cell performance. As shown in Figure 21i, MEAs constructed from commercial AEMs, such as Sustainion (Dioxide Materials, USA), A-201 (Tokuyama, Japan), and AEMION (Ionomr, Canada), exhibited distinct electrochemical behaviors under identical conditions [265]. A-201 demonstrated superior performance at lower current densities (<~0.8 A cm^{-2}), whereas Sustainion outperformed at higher current densities (>~0.8 A cm^{-2}), highlighting the influence of membrane properties such as hydroxide conductivity, water uptake, and mechanical thickness. These intrinsic parameters govern ion transport, interfacial resistance, and water management, and their optimization remains central to advancing AEMWE technology. The key underlying factors and associated challenges are summarized herein and will be discussed in detail in the following section.

Gas bubble dynamics represent a critical, yet often underappreciated, bottleneck in the performance of AEMWE [266]. During the HER and OER, H_2 and O_2 gas bubbles form at the cathode and anode, respectively. At elevated current densities (>500 mA cm^{-2}), these bubbles tend to accumulate on electrode surfaces, obstructing active sites, increasing overpotentials, and compromising catalyst adhesion. Performance degradation has been linked to factors including high bubble coverage, delayed detachment, restricted nucleation, and gas entrapment within the PTLs. Despite their significance, gas evolution and transport phenomena remain underexplored compared to the intense focus on catalyst development. Mitigation strategies have begun to emerge. Structural engineering of PTLs, such as tailoring the pore size of Ni foams, can facilitate more efficient gas removal. Surface modification of catalyst layers with superhydrophobic treatments promotes bubble detachment, while advanced flow field architectures enhance convective gas evacuation. Wang et al. recently introduced a swelling-assisted transfer strategy to fabricate high-performance MEAs for AEMWE [267]. Using ultrasonic spraying, anion-conducting ionomers were deposited directly onto porous anodic catalyst layers (ACLs) supported on Ni foil, forming a three-dimensionally interlocked ACL/AEM interface (Figure 22a). This interface enabled effective removal of the dense substrate, yielding MEAs with vertically aligned through-holes and ion-conductive pathways. Building on this approach, hierarchical $NiCo_2O_4$@FeNi LDH and NiCo@FeNi LDH ACLs were integrated with AEMs to form structurally ordered MEAs (Figure 22b,c). These systems demonstrated exceptional performance, achieving 3.61 A cm^{-2} at 2.0 V in pure-water-fed operation, and sustained 1.0 A cm^{-2} for over 700 h. The performance gains stem from: (i) enhanced exposure of catalytic active sites and improved gas-liquid mass transport via hierarchical ACL architectures; (ii) vertically aligned ionomer pathways that facilitate rapid OH^- conduction in low-conductivity media; and (iii) a 3D interlocked ACL/AEM interface that minimizes interfacial resistance and enhances ionic flux. For long-term practical implementation, a systems-level optimization of MEA architecture, PTL morphology, flow field geometry, bipolar plates, and sealing materials is imperative. Advances in AEM conductivity (e.g., novel polymer chemistries) and the durability of Ni-based catalysts are also essential to further reduce voltage losses. Continued research is urgently needed to elucidate the interplay between gas bubble evolution, electrolyte flow, and electrochemical performance, thereby enabling the rational design of bubble management strategies to unlock the full potential of AEMWE technology.

6.2 | Difference Between Laboratory Tests and AEMWE Evaluation

In recent years, extensive research has focused on developing high-performance Ni-based catalysts for the HER under laboratory conditions, primarily relying on three-electrode systems to assess activity (e.g., overpotential at 10 mA·cm^{-2}) and short-term stability (typically hours to tens of hours). However, a

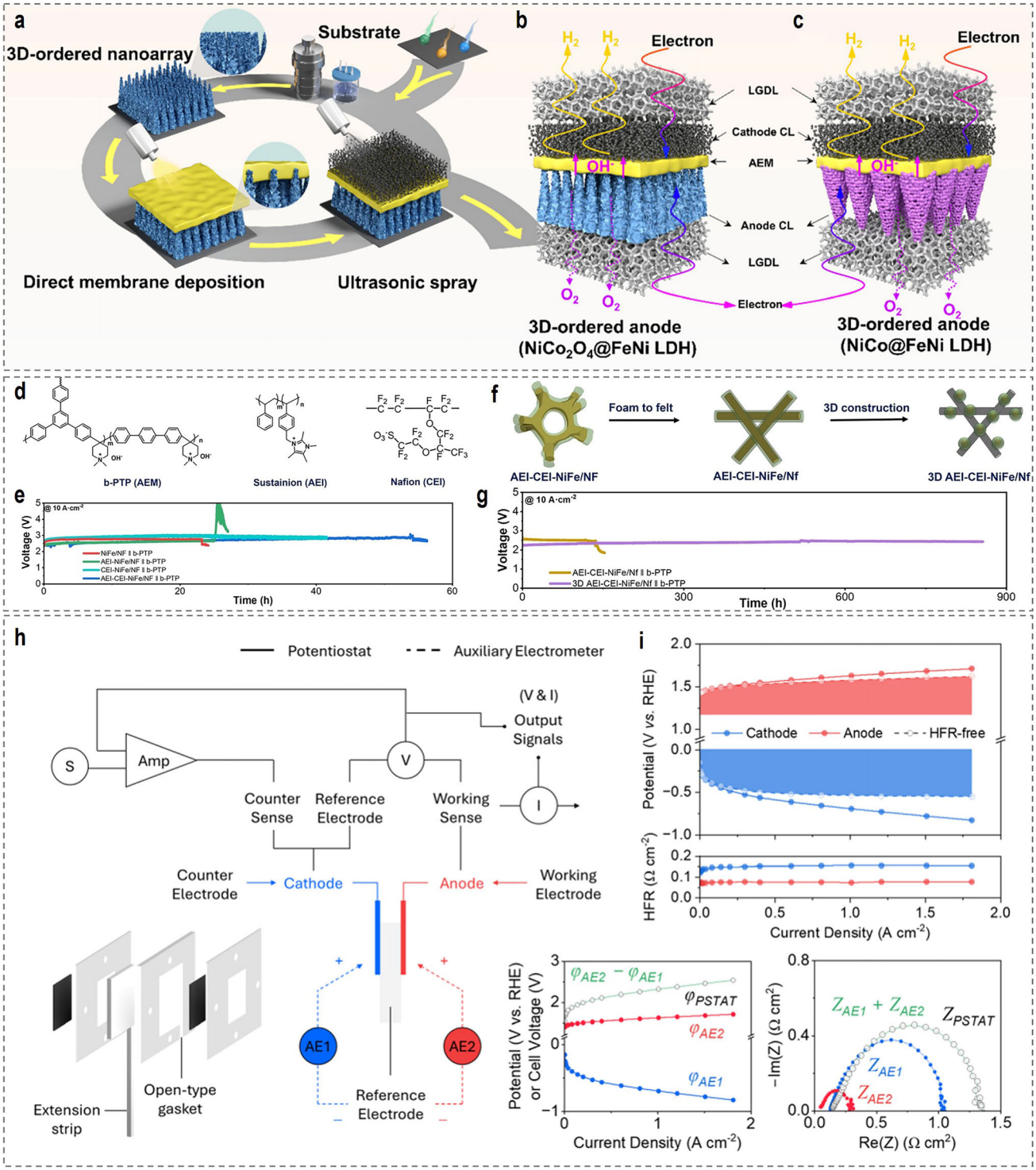

FIGURE 22 | (a) Schematic illustration of the general fabrication method of 3D-ordered ACL in MEA. (b) 3D-ordered anode based on NiCo2O4@FeNi LDH hierarchical nanoarrays. (c) 3D-ordered anode based on NiCo@FeNi LDH hierarchical foams. Reproduced with permission [267]. Copyright 2024, Royal Society of Chemistry. (d) Molecular structures of AEM: branched poly(terphenyl piperidinium) (b-PTP), AEI: Sustainion XB-7, and CEI: Nafion. (e) Stability tests upon changing membrane and ionomers at 10 A · cm−2. (f) Schematic illustration of different catalyst-PTL interfaces. (g) Stability tests upon changing catalyst-PTL interfaces at 10 A · cm−2. Reproduced with permission [270]. Copyright 2025, Wiley-VCH. (h) Schematic illustrating the sensing lead configuration of the interfaced potentiostat and auxiliary electrometer, enabling voltage, potential, and impedance measurements in galvanostatic mode. (i) Polarization curves with HFR, where the shaded regions indicate overpotential calculated from the equilibrium potential derived via cell modeling. Reproduced with permission [271]. Copyright 2025, Royal Society of Chemistry.

significant discrepancy remains between these controlled experimental setups and the practical requirements of industrial alkaline water electrolysis using AEMWEs, as the latter involves more complex operating environments, multi-component interactions, and stricter performance demands that are rarely replicated in laboratory tests [268]. Commercial AEMWEs are integrated systems composed of hundreds of electrochemical cells connected in series, with each individual cell comprising a bipolar plate, cathode/anode catalysts, GDL, an AEM, sealing gaskets, and current collectors. The total voltage across the stack equals the sum of voltages from each unit cell, and industrial evaluations typically use cell voltage at large current densities (1000–2000 $mA{\cdot}cm^{-2}$) as the core benchmark for catalyst applicability, far higher than the 10–100 $mA{\cdot}cm^{-2}$ commonly tested in three-electrode systems. Moreover, real-world AEMWE operations often involve intermittent working modes (e.g., coupling with wind/solar power), leading to frequent start-stop cycles that generate reverse currents. These reverse currents accelerate the corrosion and degradation of Ni-based catalysts: for instance, Ni active sites are prone to oxidation (forming $Ni(OH)_2$ passivation layers) or dissolution under fluctuating potentials, a phenomenon rarely captured in static laboratory stability tests that lack voltage cycling or reverse conditions.

Another critical difference lies in the operating environment. To ensure adequate ionic conductivity and reaction kinetics, industrial AEMWEs typically use low-concentration alkaline electrolytes and operate at elevated temperatures (50–70°C) with H_2 pressures up to 30 bar. In contrast, laboratory tests for Ni-based catalysts often employ dilute electrolytes (e.g., 0.1–1 M KOH) and ambient temperature/pressure, which underestimate the impact of harsh conditions on catalyst stability. For example, high electrolyte concentration in AEMWEs can exacerbate the Ostwald ripening of Ni-based nanoparticles, while elevated temperatures accelerate the leaching of heteroatoms (e.g., Mo in NiMo alloys) that are often doped to optimize HER activity, which are factors that are rarely studied in standard three-electrode evaluations.

The multi-component interaction in AEMWEs further widens the performance gap. In laboratory three-electrode systems, Ni-based catalysts are usually loaded on flat glassy carbon electrodes with minimal mass transport limitations (static electrolyte, no gas blocking). However, in AEMWEs, the catalyst layer interacts closely with the AEM and GDL, leading to two key challenges: limited mass transport and gas bubble trapping. The AEM, though thinner and more conductive than the diaphragm in AWE, still exhibits higher ionic resistance than the free electrolyte in laboratory tests, restricting the transfer of OH^- between the cathode and anode. Additionally, the violent H_2 evolution at large current densities generates numerous bubbles that accumulate on the Ni-based cathode surface, blocking active sites and disrupting the catalyst–electrolyte interface, which is an issue rarely observed in low-current laboratory tests. For example, Choi et al. found that Co_3S_4 nanosheets on Ni foam (Co_3S_4 NS/NF) exhibited a current density of only 431 $mA{\cdot}cm^{-2}$ at 2.0 V in AEMWE, far lower than its laboratory-measured HER activity, primarily due to bubble-induced mass transport resistance in AEMWE configuration [269].

Beyond reaction kinetics, system-level factors (e.g., AEM stability, GDL performance, and interfacial design) also play a decisive role in AEMWE efficiency, but these are entirely absent from three-electrode catalyst evaluations. As demonstrated by Hu et al., AEM degradation and increased mass transport resistance are primary factors limiting long-term AEMWE operation at ultrahigh current densities (e.g., 10 $A{\cdot}cm^{-2}$) [270]. By selecting more stable AEMs, efficient ionomers, and advanced catalysts, and by engineering the interface between catalyst and PTL, they significantly improved gas, liquid, and ion transport at the electrode interface. Their optimized system maintained stable operation for over 800 h at 10 A cm^{-2}. The first improvement involved replacing the commercial Sustainion membrane with the Branion b-PTP AEM from NovaMea (Figure 22d). This change extended the device lifetime from 6 s to 23 h at 10 A cm^{-2}, representing a 13 800-fold enhancement (Figure 22e). The lower ionic loss observed for b-PTP after extended operation indicated its superior chemical stability under extreme conditions. Second, substituting Ni foam with Ni felt as the PTL further increased operational stability from 50 h to over 140 h (Figure 22f,g), while maintaining a similar cell voltage of approximately 2.54 V. This result suggested that electrochemical surface area was not the limiting factor in this setup. Finally, they constructed a three-dimensional anode by spray-casting a mixture of NiFe powders and ionomers onto the Ni felt, forming a percolating structure that promoted both charge and mass transport. This 3D electrode enabled operation at 10 A cm^{-2} with a reduced cell voltage of around 2.3 V, which was 0.24 V lower than the non-3D reference system (Figure 22g). This highlights that even if a Ni-based cathode exhibits excellent HER activity in the laboratory, its performance in AEMWE will be compromised if other components (e.g., AEM, GDL) fail to match, as multi-component synergy directly affects ion transport, gas management, and overall cell efficiency.

A major unresolved challenge is the inability to accurately measure single-electrode kinetics in AEMWEs, which hinders the identification of whether performance losses originate from the Ni-based cathode or other components (e.g., anode OER, AEM resistance). In three-electrode systems, a reference electrode (e.g., Hg/HgO) directly monitors the cathode potential, enabling precise analysis of HER kinetics (e.g., Tafel slope, exchange current density). However, integrating a reference electrode into AEMWEs is technically difficult due to the sealed cell structure, electrolyte flow, and gas cross-contamination. While inspiration can be drawn from AWE: Noh et al. developed a minimally invasive single-cell configuration with a reference electrode via diaphragm extension, enabling real-time monitoring of anode/cathode potentials (Figure 22h,i) [271]. This approach has not yet been widely adapted for AEMWEs, leaving the intrinsic HER kinetics of Ni-based catalysts in practical devices largely uncharacterized. Notably, even when kinetic analysis is feasible, the reaction mechanism of Ni-based catalysts in AEMWEs differs from that in laboratory tests. Arrhenius-type analysis reveals that localized electric fields induced by AEM-catalyst-GDL interactions shift Ni-based HER kinetics from classical Butler-Volmer behavior (dominant in dilute electrolytes) toward a Marcus-like regime, where interfacial molecular dynamics (e.g., water structure rearrangement) and bimolecular charge transfer dominate [271]. This means that descriptors optimized for laboratory conditions (e.g., ΔG_{H^*} from DFT) may not accurately predict Ni-based catalyst performance in AEMWEs, as they fail to account for the influence of the AEM's microenvironment (e.g., confined water structure, anion adsorption) on reaction pathways.

In summary, bridging the gap between laboratory tests and AEMWE evaluations of Ni-based catalysts requires not only optimizing the catalysts themselves (e.g., enhancing water dissociation ability via heterostructure design) but also: (1) simulating industrial operating conditions (large current densities, concentrated electrolytes, intermittent modes) in laboratory setups; (2) developing standardized AEMWE testing protocols (e.g., unified catalyst loading, electrolyte concentration, and cell configuration) for consistent performance comparison; (3) adapting in-situ/operando characterization techniques (e.g., operando XAS, Raman) to AEMWEs to capture dynamic Ni-based catalyst evolution (e.g., phase transformation, active site reconstruction) under gas bubbling and high current densities; and (4) integrating reference electrode systems to decouple cathode HER kinetics from system-level losses. Only through a holistic approach that considers both catalyst performance and AEMWE system integration can the true potential of Ni-based catalysts in industrial hydrogen production be realized.

6.3 | Critical Role of AEM in AEMWE

In AEMWE, the AEM plays a critical role in determining overall device performance. It governs ion transport, catalyst compatibility, and system stability across multiple dimensions. From the perspective of ion transport, the AEM is responsible for conducting OH^-, and its ionic conductivity directly influences both the reaction kinetics and the overall electrolysis efficiency. High OH^- conductivity is essential to minimize ion transport resistance and reduce overpotential losses. In contrast, insufficient ion conduction hinders OH^- migration through the membrane, limiting reactant availability at the electrode interface. This transport bottleneck affects both the HER and OER, thereby compromising the performance of the entire system. To develop high-performance AEMs, various polymer backbones have been explored, including poly(arylene ether) [272], poly(norbornene) [273], poly(benzimidazole) [274], and ether-free polyarylenes [36]. These backbones are often functionalized with diverse cationic groups such as ammonium [275], imidazolium [276], phosphonium and metallocene [277], and so on [278, 279]. These structural designs aim to optimize both ion transport and chemical stability under alkaline operating conditions.

Catalyst compatibility is another crucial factor. The interaction between the AEM and electrode catalysts can profoundly influence electrochemical performance. For instance, anion exchange polymers based on aryl piperidinium (PAP) with bicarbonate counterions have been shown to significantly suppress the HER activity of Ni-Mo/C catalysts, leading to a pronounced decrease in cathodic specific current [280]. In contrast, the use of halide-stabilized PAP ionomers restores the catalytic activity, highlighting the sensitivity of membrane–catalyst interactions to the chemical structure of the membrane. An incompatible membrane-catalyst pairing can severely inhibit performance, while a well-matched combination can preserve or even enhance catalytic activity. The stability of the AEM is equally vital for long-term operation. Under alkaline conditions and electric fields generated during electrolysis, the membrane must retain both structural integrity and functional performance. Membranes that lack chemical or mechanical robustness are prone to degradation, swelling, or even rupture, leading to reduced ion conductivity and eventual device failure. Therefore, the long-term durability of AEMs under realistic operating conditions is essential for reliable and efficient hydrogen production. To address stability challenges, a quinuclidinium-based cation, 1-methyl-3,3-diphenyl quinuclidinium (DPQui), was synthesized and systematically evaluated [22]. Compared to the commonly used 1,1-dimethyl-4,4-diphenyl piperidinium (DPPip), DPQui exhibited significantly improved alkaline stability. Building on this insight, ultra-stable quinuclidinium rings were incorporated into a branched, ether-free polyaromatic backbone using superacid-catalyzed polycondensation followed by quaternization. The resulting polymer, designated as poly(aryl quinuclidinium) (PAQ-x), was processed into membranes for AEMWE applications (Figure 23a). Among the tested variants, the PAQ-5 membrane delivered superior performance. Under identical thickness and assembly conditions, an AEMWE cell employing PAQ-5 achieved a current density of 7.03 $A\,cm^{-2}$ at 2.0 V with a low internal resistance of 0.055 Ω at 80°C (Figure 23b). In addition, a PGM-free AEMWE system based on PAQ-5 sustained high current densities up to 8 $A\,cm^{-2}$ at 2.0 V and demonstrated exceptional operational stability. The membrane maintained performance over 2446 h under various test conditions, including 1600 h at 1.0 $A\,cm^{-2}$ and 26°C, 255 h at 2.0 $A\,cm^{-2}$ and 26°C, and 524 h at 4.0 $A\,cm^{-2}$ and 60°C. These results demonstrate the importance of optimizing both the intrinsic properties of the AEM and its compatibility with electrode materials. Continued progress in AEMWE technology depends on the integrated design of membranes and catalysts to enable efficient and durable hydrogen production via water electrolysis.

6.4 | Key Issues About Stability in Industrial Applications

Industrial-scale AEMWE systems encounter a set of distinct challenges that significantly affect the durability and long-term stability of the MEA. These issues become particularly pronounced under high current density conditions and during frequent operational cycling, such as repeated start-up and shutdown processes. One major concern is the occurrence of reverse current during unplanned power interruptions, which can accelerate oxidative degradation of the AEM and AEI, as well as promote interfacial delamination. In addition, the presence of foreign ions in the electrolyte, especially trace amounts of iron, can exacerbate chemical attack on functional groups and induce secondary contamination within the MEA. These operational stressors differ fundamentally from those encountered in laboratory-scale studies, where controlled environments and short-term testing often mask synergistic long-term degradation mechanisms. As a result, laboratory-optimized MEA designs may fail to meet performance and stability requirements under industrial conditions. To address these limitations, both material selection and system engineering must be adapted to accommodate the realities of large-scale electrolysis. This includes the development of robust AEM and AEI materials with enhanced alkaline and mechanical stability, as well as mitigation strategies for hydration management and impurity control. The following section examines these critical degradation pathways in greater detail and outlines potential solutions for improving the industrial viability of MEAs in AEMWE systems.

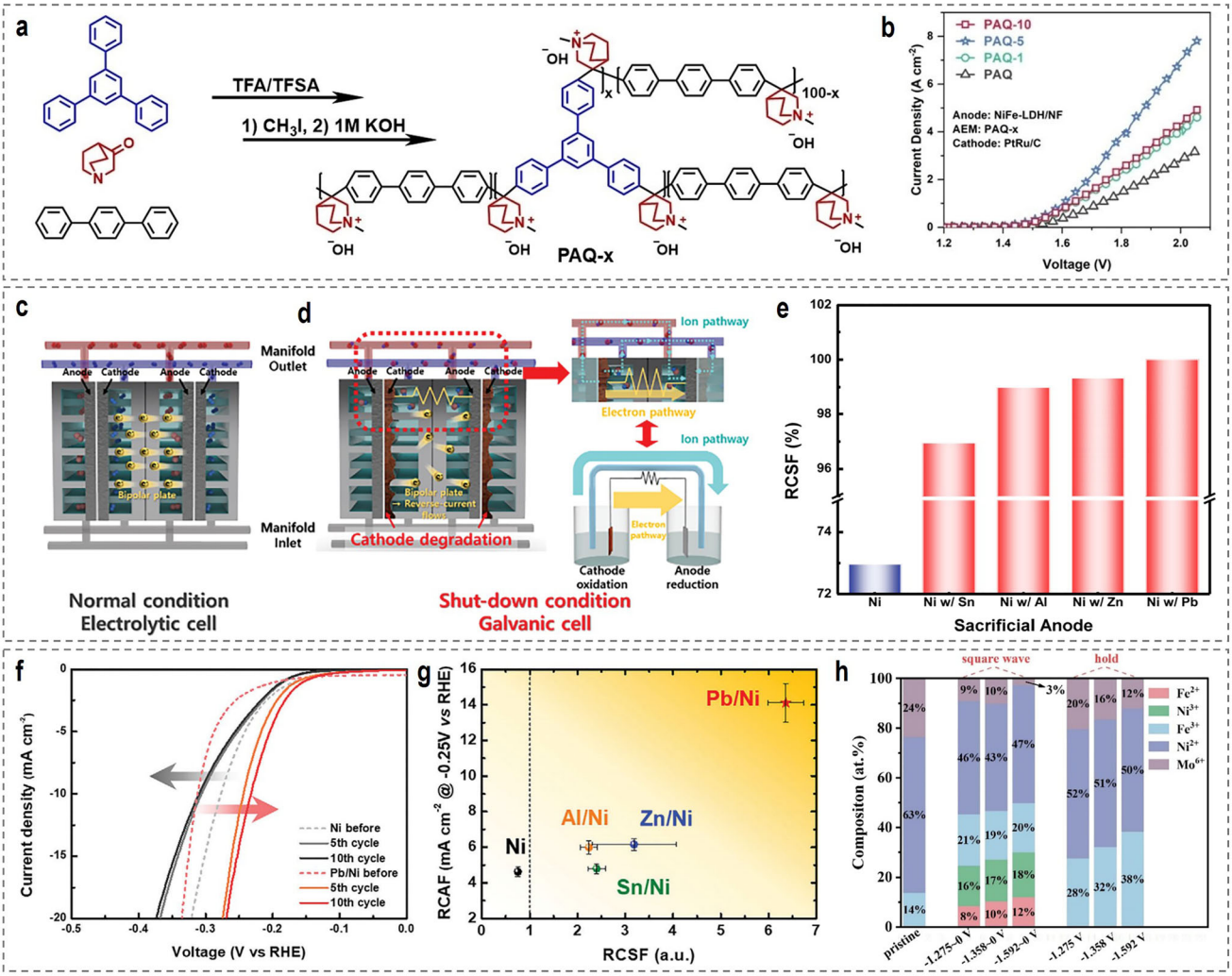

FIGURE 23 | (a) Synthetic routine of PAQ-x polymers, and x is the molar ratio of the 1,3,5-triphenylbenzene (TPB) in copolymer. (b) *V*–I spectra of AEMWEs with PAQ-x at 80°C under 1 M KOH feed. Reproduced with permission [22]. Copyright 2024, Wiley-VCH. Ni electrode degradation by reverse-current flow after the shutdown of the alkaline electrolyzer. (c) A schematic of the reverse-current flow between the cathode and anode, separated by a bipolar plate, after the shutdown process in the alkaline water-electrolyzer cell. (d) A detailed mechanism of the reverse-current phenomenon after the shutdown process. Reproduced with permission [283]. Copyright 2024, Wiley-VCH. (e) Comparison of the reverse-current stability factor (RCSF). Reproduced with permission [285]. Copyright 2022, American Chemical Society. Measurement of the Ni and Pb/Ni catalysts under RC conditions. (f) The LSV curves for Ni and Pb/Ni before and after the fifth and 10th cycles of HER-RC indicate the degradation of the HER activity of Ni and the enhancement of that of Pb/Ni during repeated RC cycles, simulating a start-up/shutdown (SU/SD) event in an alkaline water electrolyzer. (g) The RCSFη and RCAFη values for Ni and M/Ni (M = Sn, Zn, Al, and Pb) before and after the 10th RC cycle. Reproduced with permission [283]. Copyright 2024, Wiley-VCH. (h) XPS results for surface chemical analysis of FeNiMo-LDH@NiMo/SS. Reproduced with permission [288]. Copyright 2024, MDPI.

6.4.1 | Reverse-Current

Industrial AEMWE systems, which are engineered to accommodate the intermittent nature of renewable energy sources, frequently undergo power cycling that imposes considerable stress on catalyst durability [281, 282]. In these systems, the MEA typically incorporates Ni-based cathodes and anodes separated by an AEM, forming a compact and integrated electrochemical cell. Under normal operation, the cell functions as a closed circuit; however, when external power is interrupted, residual potential differences between the electrodes establish a galvanic cell that induces a reverse-current, flowing contrary to the direction of standard electrolysis (Figure 23c) [283]. This reverse-current oxidizes the cathode, frequently generating electrochemically inactive $Ni(OH)_2$ phases, and concurrently reduces the anode, leading to catalyst degradation and enhanced electrode corrosion (Figure 23d). This phenomenon is particularly severe in AEMWE systems due to the thin membrane structure and heightened susceptibility of the MEA to potential perturbations, which exacerbate cathode deterioration in comparison to alkaline water electrolysis systems that employ thicker separators. The resulting redox imbalance promotes degradation of the electrocatalyst surface, often culminating in the partial detachment of active materials from the substrate, thus diminishing catalytic performance and reducing electrode longevity. Experimental and theoretical investigations revealed that electrode potentials shift dynamically during shutdown in response to reverse charge accumulation, with pronounced reverse-currents observed at intermediate

bipolar plates [284]. The magnitude of this current is influenced more strongly by temperature and electrolyte flow conditions during shutdown than by the operational electrolysis current. Importantly, the reverse-current originates from intrinsic redox processes of the electrode materials rather than from reactions involving dissolved gases. Furthermore, selecting compatible cathode and anode materials can extend the operational lifespan of AEMWE systems, highlighting the importance of material design in mitigating reverse-current-induced degradation.

Experimental investigations have elucidated the detrimental effects of reverse-current on Ni-based cathodes in AEMWE systems. Post-shutdown analysis of Ni-based electrodes revealed that the cathode surface is prone to forming electrochemically inactive hydroxide layers, substantially diminishing HER activity, whereas the anode remains relatively unaffected [285]. To further probe this behavior, Guruprasad et al. employed a dual platinum wire reference electrode system to evaluate the performance of different cathode catalysts under both steady-state and intermittent operating conditions [286]. During normal electrolysis, the catalytic activity followed the order PtRu/C > Pt/C > NiMo/C. Under reverse-current conditions, all tested cathodes exhibited marked degradation, with NiMo/C showing the most severe performance loss, followed by PtRu/C and Pt/C. The anodes, by contrast, maintained structural and functional stability throughout. Mechanistic insights revealed distinct degradation pathways for each material. PtRu/C experienced a substantial performance decline, evidenced by a 200 mV potential drop at 1.5 A cm^{-2}, which was attributed to Ru leaching into soluble ruthenate species and carbon corrosion at elevated potentials. These processes resulted in the loss of active sites and deterioration of electronic conductivity. Pt/C demonstrated comparatively moderate degradation, with a potential drop of approximately 50 mV at 1.5 A cm^{-2}. This stability was linked to the formation of relatively inert PtO and PtO_2 surface layers at high anodic potentials, which confer partial resistance to corrosion. In contrast, NiMo/C suffered the most pronounced degradation, with the cell potential increasing by nearly 1.7 V at 1.5 A cm^{-2}. This was primarily ascribed to molybdenum dissolution and structural collapse of the catalyst under open-circuit and anodic conditions. Additional degradation of the ionomer at elevated oxidative potentials likely contributed to a decline in ionic conductivity. To counteract cathode deterioration, Kim et al. proposed a strategy based on cathodic protection by employing sacrificial anodes [285]. Through systematic screening, metals such as Pb, Zn, Sn, and Al were evaluated for their protective efficacy under simulated reverse-current conditions. Among them, Pb emerged as a promising candidate owing to its low dissolution rate, chemical stability, and cost-effectiveness, although its toxicity necessitates cautious implementation (Figure 23e). Beyond material considerations, operational parameters also play a critical role. Elevated electrolyte temperatures and increased ionic conductivity within the MEA were found to intensify reverse-current, thereby accelerating electrode degradation [287]. Mitigation approaches such as reducing electrolyte temperature or halting circulation during shutdown periods can diminish reverse-current magnitude but introduce engineering complexity and elevate system costs. The incorporation of polarization rectifiers to suppress reverse-current has also been explored, though such solutions increase capital investment and may reduce energy efficiency [287]. While both sacrificial anodes and system-level interventions can offer protection against reverse-current-induced degradation, their integration must be balanced against overall system cost and long-term operational viability. Developing cost-effective, efficient mitigation strategies remains essential for enhancing the durability of industrial AEMWE systems.

Catalyst engineering presents a viable approach to mitigate reverse-current effects in AEMWE. Modification of Ni cathodes with Pb enhances tolerance to reverse-current conditions, as demonstrated in laboratory-scale tests using a two-cell AEMWE stack [283]. These tests indicate sustained stability under start/stop cycling. Experimental data reveal that Pb/Ni catalysts exhibit superior HER activity after multiple reverse-current cycles, achieving a reverse-current stability factor of 6.35 and an activity factor of 14.11 mA cm^{-2}, markedly outperforming unmodified Ni catalysts (Figure 23f,g). The mechanism for this enhanced tolerance involves Pb/Ni oxidation, which increases cathode potential, thereby reducing the electromotive force of the galvanic cell and suppressing reverse-current flow. Additionally, water activation and ligand effects facilitate water dissociation and proton desorption, synergistically enhancing HER activity in alkaline media. In AWE stack tests, Pb/Ni catalysts retained 97.3% of their current density after 30 start/stop cycles, compared to 89.5% for unmodified Ni, confirming their superior reverse-current tolerance and potential for practical applications. Fluctuating power inputs from renewable energy sources further challenge AEMWE performance. Although Ni-based HER catalysts are valued for their cost-effectiveness and stability, their evaluation under stable power conditions predominates, with limited studies addressing fluctuating inputs. Such fluctuations significantly influence HER electrode performance, necessitating a deeper understanding of their effects on electrode degradation and HER activity to enable effective integration with renewable energy for green hydrogen production. Zou et al. explored the impact of three waveform types (square, step, and triangle), simulating renewable energy inputs, and their amplitudes on Ni-based electrode degradation and HER performance [288]. Their findings indicate that fluctuating power initially enhances, then diminishes, HER performance of planar Ni cathodes, with square waveforms exerting the greatest effect, peaking at 12 h. Increased square waveform amplitude accelerated degradation of FeNiMo-LDH@NiMo/SS cathodes, reducing HER performance. Surface analysis revealed that higher amplitudes reduced flower-like spherical structures, caused uneven element distribution, increased Ni^{3+} and Fe^{2+} content, and decreased Mo^{6+}, confirming exacerbated electrode degradation under larger amplitudes (Figure 23h).

When AEMWE is coupled with intermittent power sources such as solar or wind energy, fluctuations in current density can lead to frequent bubble formation and disappearance at the electrodes. This imposes nonlinear mechanical stresses on the MEA, which can trigger catalyst leaching, membrane degradation, and performance decay. However, the durability of commercial AEMs and ionomers (e.g., Sustainion), has not yet met the requirements for such dynamic operating conditions. To address this issue, Narayanaru et al. investigated the durability of a trimethylammonium-modified poly-(fluorene-alt-tetrafluorophenylene) (PFT-C10-TMA)-based membrane and ionomer under dynamic operation to assess its suitability for

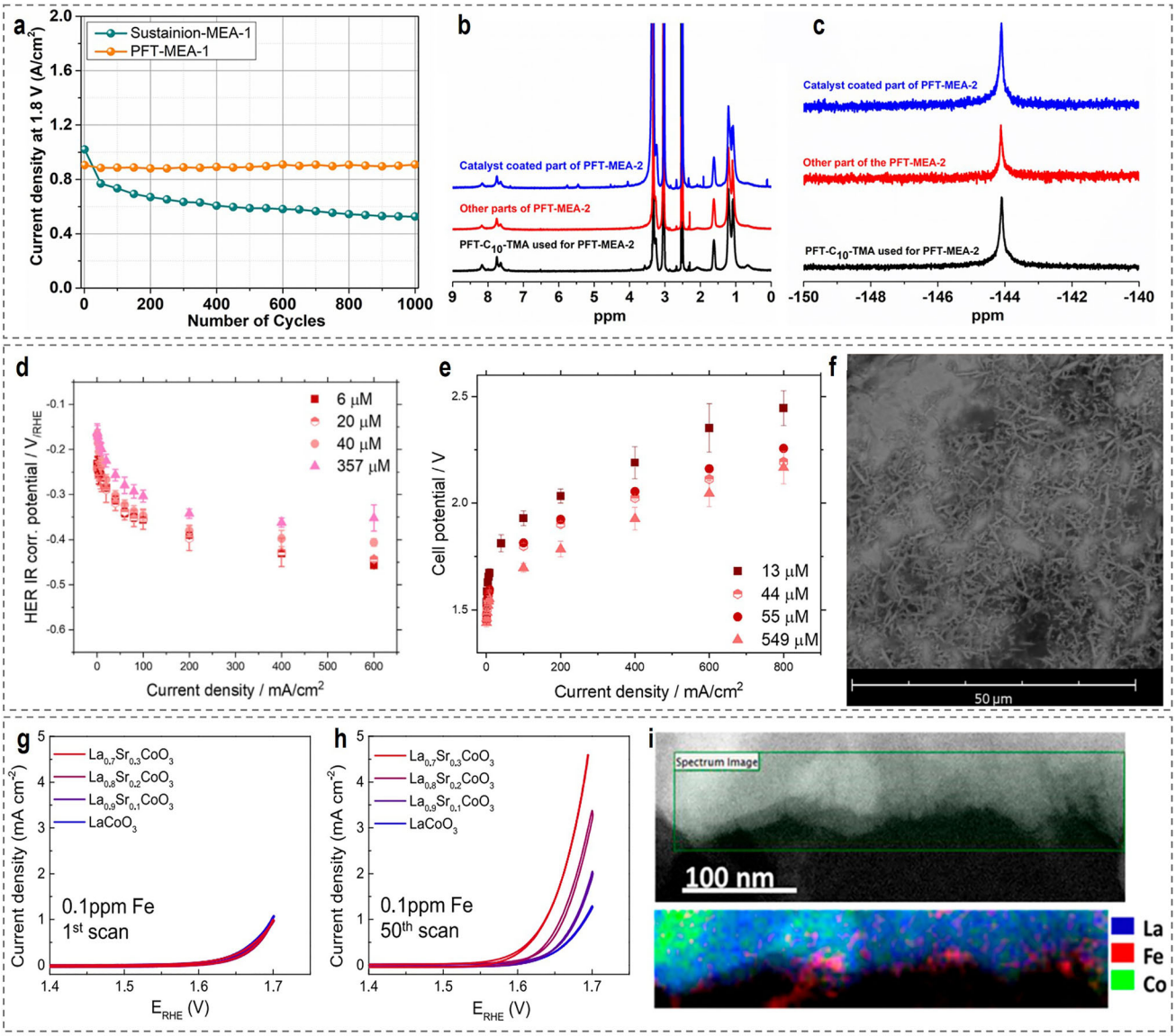

FIGURE 24 | (a) Changes in the current density values of the MEAs at 1.8 V against the number of start-stop cycles. (b) 1H- and (c) 19F-NMR spectra of the PFT-MEA-2 (black) before and after (blue and red) the 1000 start-stop cycles between 0.1 and 2.0 V at 80°C. Reproduced with permission [289]. Copyright 2023, American Chemical Society. (d) *I–V* curves for internal resistance corrected HER potential for Fe electrolyte concentrations of 6, 20, 40, and 357 mM. (e) *I–V* curves determined from chronopotentiometry in a flow cell with different Fe electrolyte concentrations. (f) SEM image of Fe deposited dendrite structures on the cathode's surface postelectrolysis with 55 mM of electrolyte Fe. Reproduced with permission [295]. Copyright 2024, Elsevier. (g) First OER polarization curve for LSCO-0, 10%, 20%, and 30% Sr content in A-sites and (h) after 50 potential cycles up to 1.7 V in 0.1 mol L^{-1} KOH deliberately containing 0.1 ppm of Fe(aq). (i) EDS mapping of LSCO-30 surface after the extensive cycling with the presence of Fe(aq). Reproduced with permission [304]. Copyright 2021, American Chemical Society.

coupling with intermittent power sources [289]. The durability of the MEAs prepared with these polymer membranes and ionomers was evaluated by performing 1000 start-stop voltage cycles in a 1 M KOH solution at 80°C while varying the applied cell voltage. The electrochemical performance of the MEAs and electrodes was evaluated using an electrolyzer with reference electrodes, and the chemical structure of the polymer was analyzed before and after the durability test using NMR techniques. The results showed that the MEA based on the commercial Sustainion XB-7 ionomer and X37-50 RT AEMs exhibited catalyst leaching during the start-stop cycles, leading to reduced cell performance (Figure 24a). In contrast, the MEAs incorporating the PFT-C10-TMA membrane and ionomer demonstrated excellent chemical and mechanical durability under dynamic start-stop operation (Figure 24b,c). The core advantages of PFT-C10-TMA lie in three synergistic structural and performance factors: (1) High molecular weight (240 000 g/mol) and chain entanglement provide the MEA with high mechanical strength, enabling it to resist the nonlinear stresses induced by bubble formation and disappearance; (2) Low swelling, with only 34% swelling in 80°C, 1 M KOH (compared to 156% for Sustainion XB-7), preventing excessive swelling of the ionomer and catalyst detachment; (3) Chemical stability, with an all-aromatic backbone free of easily broken ether bonds and quaternary ammonium groups protected

by the polymer chain, making it resistant to OH^- attack (NMR confirmed no significant degradation after cycling). Therefore, future research should focus on developing alternative dopants or protective coatings to enhance reverse-current tolerance while maintaining HER activity [290]. Optimizing membrane electrode assembly designs to minimize potential differences during shut-downs could further mitigate reverse-current effects, enhancing the durability of industrial AEMWE systems. These combined strategies in catalyst engineering and system optimization are critical for improving the robustness and efficiency of AEMWE under intermittent renewable energy inputs.

6.4.2 | Foreign Ion Contamination

Foreign ions, particularly Fe ions, in AEMWE electrolytes profoundly affect the activity and stability of Ni-based HER catalysts. Unlike traditional alkaline water electrolysis, which utilizes highly concentrated electrolytes such as 30 wt% KOH, AEMWE systems typically employ less concentrated solutions, including 1 M KOH or pure water. Nevertheless, Fe ion contamination, originating from electrolyte impurities, membrane electrode assembly components, or corrosion of system piping, persists as a significant challenge, with concentrations ranging from 0.03 to 3 ppm [291, 292]. Fe ions are known to enhance OER activity on Ni-based anodes by improving conductivity and providing active sites. However, their influence on HER cathodes is multifaceted, affecting surface morphology, electronic properties, and long-term stability [293]. In alkaline electrolytes, Fe impurities augment OER performance on Ni-based anodes, sustainably increasing catalytic activity. Yet, critical mechanistic questions, including the identity of the primary active site (Ni or Fe) and the oxidation state of Fe during OER, remain unresolved, particularly under industrial conditions. The long-term impact of Fe on cathode performance remains controversial, with some studies suggesting that it may cause catalyst deactivation or other detrimental effects, while others report contradictory findings. Therefore, further research is essential to elucidate the precise role of Fe in catalyst stability and performance under realistic operating conditions [31, 294].

The deposition of Fe ions on Ni-based HER cathodes in AEMWE systems can yield both beneficial and detrimental effects, depending on the operating conditions and Fe concentration. Experiments under industrial-relevant conditions (1 M KOH, 40–80°C, 0.03–3 ppm Fe) demonstrate that Fe deposition initially suppresses HER activity through surface coverage, followed by recovery as dendritic Fe structures increase surface area [295]. In three-electrode setups, elevating Fe concentration from 6 μM to 357 μM reduced IR-corrected HER overpotential across all tested temperatures (Figure 24d). At high current density, higher Fe concentrations lowered HER overpotential by at least 100 mV. This phenomenon, despite Fe's lower intrinsic HER catalytic activity compared to Ni, arises from the formation of NiFe mixed species that inhibit inactive NiH_x phase formation, thus preventing Ni deactivation. Additionally, increased surface area from Fe deposition provides more active sites, further reducing overpotential. Flow cell experiments corroborated these findings, with Fe concentrations increasing from 13 μM to 549 μM reducing zero-gap flow cell overpotential by 200 mV (Figure 24e). SEM/EDX and XPS analyses confirmed that Fe deposits form dendritic structures on the cathode surface during HER. Higher Fe concentrations in the electrolyte increase deposited Fe, elevating the Fe-to-Ni ratio. These dendritic structures, appearing as black needle-like crystals several millimeters in size, result from reductive Fe deposition, with thickness scaling with Fe concentration, as shown on SEM image (Figure 24f). Such structures suppress inactive NiH_x phase formation, reducing HER overpotential by up to 100 mV at 250 mA cm^{-2}. However, at low Fe concentrations (0.5 ppm), HER activity declines due to active site blocking by Fe deposits. In industrial AEMWE systems, where Fe concentrations may exceed several ppm due to component corrosion, these conflicting effects demonstrate Fe's complex role in cathode performance. The impact of Fe deposition likely varies with the baseline catalytic activity of the cathode, with high-activity catalysts more prone to adverse effects from Fe coverage. These findings highlight the need for a detailed understanding of Fe's role in Ni-based HER cathodes to optimize catalyst design and ensure long-term stability in industrial AEMWE applications.

Fe ions compromise the stability of AEMs in AEMWE systems, particularly due to the thin, ion-conductive membranes utilized. Fe^{2+}/Fe^{3+} ions can bind to positively charged functional groups, such as quaternary ammonium, within the AEM, competing with OH^- conduction and triggering chemical degradation through mechanisms like Hofmann elimination, especially at elevated temperatures of 60–90°C [296]. The oxidative properties of Fe^{3+} further degrade the polymer backbone, diminishing the membrane's ion exchange capacity. Additionally, Fe hydroxide precipitates obstruct ion channels, increasing membrane resistance and inducing mechanical stress or micro-cracks. These effects are intensified in AEMWE systems, which employ dilute electrolytes and thin membranes (50–100 μm), lacking the buffering capacity of thicker separators used in conventional alkaline water electrolysis [297]. Beyond Fe ions, other cationic impurities significantly influence AEMWE performance, originating from exogenous sources, such as electrolyte impurities, or endogenous sources, including corrosion of system components. Smith et al. reported that certain cations, such as Fe^{3+} and Ni^{2+}, adsorb onto catalysts in AEMWE, enhancing catalytic activity for both OER and HER [298]. Conversely, cations like Zn^{2+}, Cd^{2+}, and Pb^{2+}, which lack catalytic activity for OER or HER, impair electrode performance upon adsorption. Furthermore, Ca^{2+} and Mg^{2+} may form precipitates under high pH conditions, blocking access to catalytic sites and further reducing performance.

NiFe-based catalysts are widely recognized as highly active OER catalysts in both alkaline and neutral media; however, their practical application is severely hindered by poor stability arising from pronounced Fe leaching, which introduces additional Fe contamination into the AEMWE system [299, 300]. Typically, the dynamic Fe dissolution-redeposition process results in the formation of an FeOOH phase, ultimately leading to catalyst deactivation [301]. To mitigate Fe species dissolution, several strategies have been proposed. For instance, coating the catalyst/electrolyte interface with a nonpolar tetraphenylporphyrin layer has been shown to modulate the polarity of the electric double layer, thereby effectively suppressing Fe leaching [302]. Meanwhile, emerging studies highlight the existence of dynamically stable Fe active sites that can be engineered by tailoring either the electrode or electrolyte composition, resulting in significantly enhanced OER performance [303]. A representative example

is the observation that trace-level Fe in the electrolyte confers approximately a 10-fold improvement in stability against Co dissolution in perovskite oxides (Figure 24g,h) [304]. This enhanced OER activity is attributed to a few-nanometer-thick Co hydr(oxy)oxide surface layer that interacts with trace aqueous Fe(aq) (Figure 24i), generating dynamically stable active sites. In summary, the role of Fe contamination in AEMWE systems is inherently dual-natured: it may induce catalyst deactivation under certain conditions, yet it can also give rise to highly active and stable sites when properly controlled. Therefore, further in-depth investigations are essential to fully elucidate its complex influence.

6.4.3 | Degradation of MEA

In AEMWE, the MEA, constructed by integrating the electrocatalyst, GDL, PTL, and AEM, serves as the core component enabling efficient production of high-purity hydrogen. The electrocatalyst can be deposited either onto the substrate via the CCS approach or directly onto the membrane using the CCM technique. As the heart of an AEMWE system, the performance attenuation and structural degradation of the MEA directly govern the overall lifespan and operational stability of the electrolyzer. This issue becomes particularly acute in pure-water-fed AEMWE systems, where pronounced synergistic degradation occurs among the key components, including the AEM, ionomer, electrocatalysts, and their interfaces. The underlying degradation mechanisms and failure modes exhibit strong system-specific characteristics, necessitating systematic and in-depth investigation.

6.4.3.1 | Degradation of AEMs. The AEM serves as the ionic transport backbone of the MEA, and its degradation manifests as the simultaneous loss of chemical stability and physical integrity. Common cationic moieties (e.g., quaternary ammonium, piperidinium) are highly susceptible to degradation under high pH and anodic potentials. Alkyl-tethered trimethylammonium groups primarily undergo S_N2-mediated demethylation (Figure 25a), whereas benzylic trimethylammonium is prone to S_N2 attack at the benzylic carbon [305]. Quaternary ammoniums bearing β-hydrogens may also experience Hofmann elimination, yielding tertiary amines and loss of ion conductivity. Cyclic ammoniums (e.g., piperidinium), despite superior alkaline stability, remain vulnerable to OH^- nucleophilic attack at the α-carbon or Hofmann elimination-induced ring opening under low hydration conditions (particularly cathode dehydration), resulting in a sharp decline in ion-exchange capacity [22, 306]. Strategic molecular design, such as increasing steric hindrance, incorporating electron-donating substituents, and minimizing β-hydrogens, can effectively decelerate these degradation kinetics, thereby enhancing the alkaline resilience of cationic groups. Meanwhile, aryl ether and aromatic moieties in common backbones (e.g., poly(arylene ether)s, polysulfones) are readily oxidized by reactive oxygen species generated during the OER, leading to chain scission, molecular weight reduction, and uncontrolled swelling [307]. In pure-water-fed AEMWE systems, severe hydration fluctuations, driven by cathode dehydration and anode water accumulation, induce cyclic swelling-shrinking stresses. Prolonged operation ultimately results in membrane embrittlement, delamination, and pinhole defects. Pinhole formation dramatically exacerbates hydrogen/oxygen crossover, reducing Faradaic efficiency and potentially triggering localized H_2/O_2 recombination hotspots that accelerate thermal-oxidative degradation. As illustrated in Figure 25b–d, such mechanical stresses caused significant membrane deformation and increased MEA voltage from 1.59 V to 2.12 V after only 12 h of chronopotentiometry at 0.5 A cm^{-2} [308]. Current approaches primarily involve organic/inorganic composite membranes or polymer blending to improve mechanical robustness and alkaline stability [309]. For instance, Hager et al. blended polystyrene with polybenzimidazole, yielding AEMs with markedly enhanced mechanical and chemical durability [310]. When tested in an AEMWE at 70°C in 1 M KOH, this blended membrane achieved 2.0 A·cm^{-2} below 1.8 V with an exceptionally low initial degradation rate, outperforming the commercial Aemion$^+$ membrane.

6.4.3.2 | Degradation of AEI. AEI serve dual roles in the catalyst layer as ionic conduction pathways and catalyst binders, making their degradation a critical bottleneck for MEA performance decay, primarily manifesting as oxidative scission in the anode catalyst layer [311]. Under high OER potentials, the pendant cationic groups (e.g., quaternary ammonium) of AEI are preferentially oxidized, while the backbone C-C and C-O bonds are attacked by ·OH radicals, resulting in chain fragmentation and the formation of small molecules such as aldehydes or carboxyl groups. This degradation mode is particularly pronounced in quaternized poly(p-phenylene oxide)-based AEI, occurring in both neutral and alkaline media [312, 313]. Studies show that AEI with fully sp^3-carbon backbones (e.g., polyolefin-based) exhibit over 30% improved oxidative resistance compared to aromatic-containing counterparts, albeit often at the expense of ionic conductivity, highlighting a trade-off between stability and performance [314, 315]. In pure-water-fed systems, a mismatch between the hydration properties of AEI and the porous structure of the catalyst layer further exacerbates interfacial delamination. High IEC AEI undergoes excessive swelling in pure water, weakening van der Waals forces and hydrogen bonding with catalyst particles, ultimately leading to catalyst detachment. Conversely, low-IEC AEI suffers from insufficient hydration, resulting in increased brittleness and catalyst layer spalling under the mechanical stress of gas evolution, thereby sharply reducing the number of exposed active sites [308]. Regulation of water uptake is typically achieved by tuning ion content, enhancing hydrophobicity, or incorporating hydrophobic additives. High-ion-content ionomers have been shown to poorly retain catalyst particles during prolonged operation due to excessive swelling-induced detachment [78]. Increasing ionomer hydrophobicity is commonly accomplished by integrating hydrophobic segments or additives. For instance, in AEMWE employing hexamethyl-p-terphenyl poly(benzimidazolium) (HMT-PMBI) ionomer, hydrophobic benzylation to reduce swelling extended cell lifetime by approximately fourfold [316]. Incorporation of fluorinated segments [317], or ethylene tetrafluoroethylene backbones [318], similarly suppresses swelling. The addition of hydrophobic agents such as polytetrafluoroethylene or polydopamine has also proven effective in mitigating swelling without substantially compromising ionomer conductivity [319, 320]. In summary, careful balancing of ion content with the incorporation of hydrophobic segments or additives can significantly suppress AEI swelling, thereby enhancing interfacial stability and extending MEA durability.

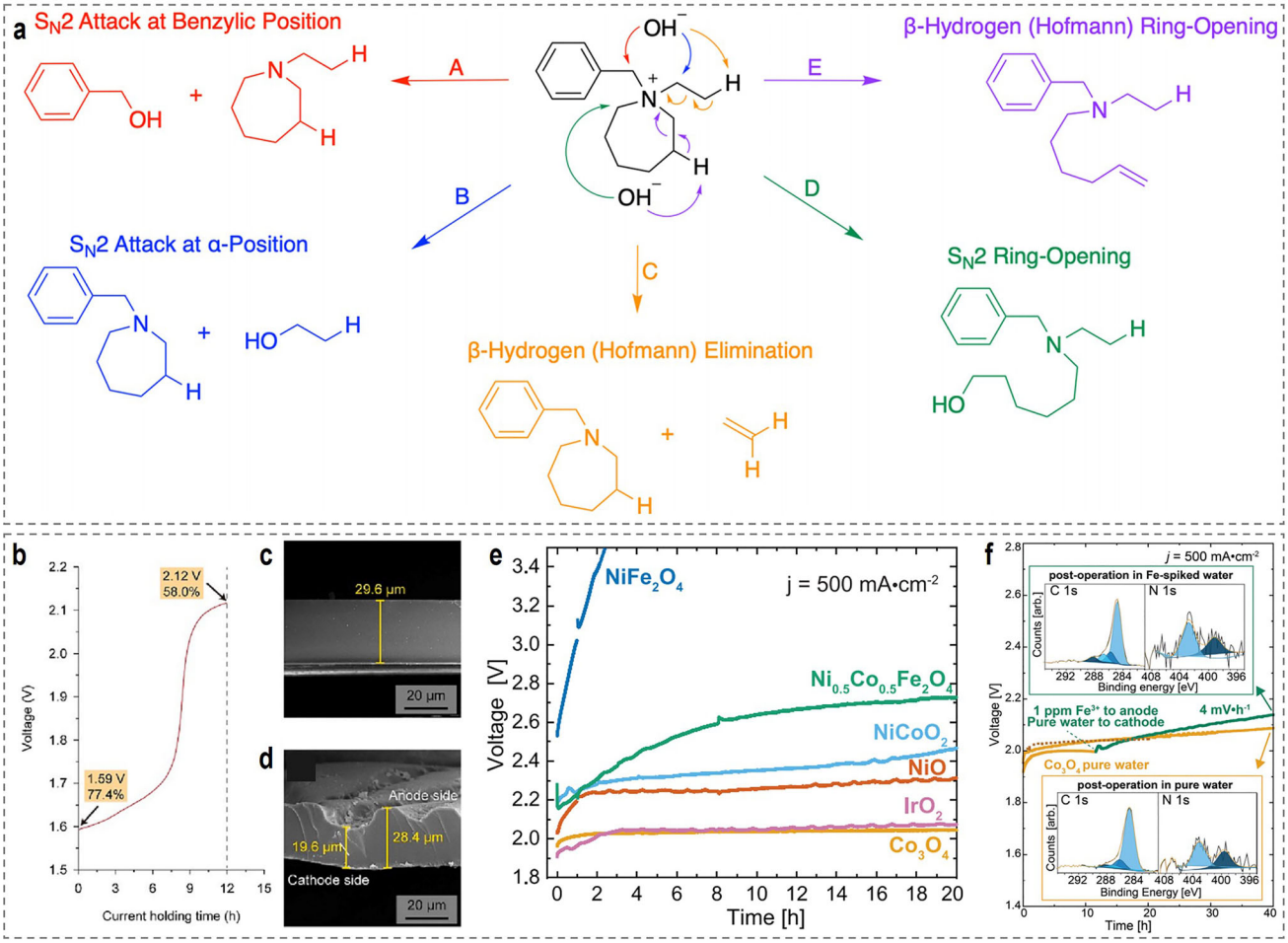

FIGURE 25 | (a) Observed degradation pathways for quaternary ammonium cations. Reproduced with permission [305]. Copyright 2022, American Chemical Society. (b) Voltage profile of the MEA during the 12 h operation at 0.5 A cm^{-2}. Comparison of SEM images of the membrane before (c) and after (d) the 12 h operation. Reproduced with permission [308]. Copyright 2023, Elsevier. (e) Durability testing for each catalyst. (f) Effect of soluble Fe on AEM durability. Reproduced with permission [299]. Copyright 2022, Wiley-VCH.

6.4.3.3 | Degradation of Electrocatalysts and Interfacial Failure. A key advantage of AEMWE lies in the utilization of non-precious metals (e.g., Ni, Fe, Co, Mo) as electrocatalysts, dramatically reducing system cost. Nevertheless, these catalysts suffer severe degradation under practical operating conditions [122, 321]. The primary deactivation pathways can be classified into loss of active sites and decline in intrinsic activity, encompassing dissolution, element segregation, structural reconstruction, particle aggregation, and site blockage [322–324]. These mechanisms are modulated by multiple factors (pH, temperature, electrolyte composition, and inherent material stability) and strongly interplay, with detailed discussions available in prior reviews [325].

Critically, catalyst degradation extends beyond intrinsic activity loss and significantly exacerbates overall MEA failure through interfacial interactions. In low-ionic-strength pure-water systems, precious-metal benchmarks (anodic IrO_2 and cathodic Pt/C) experience distorted electrical double layers, impairing HER/OER kinetics. IrO_2 undergoes lattice oxygen evolution and particle agglomeration under high anodic potentials, whereas Pt/C suffers active-site blockage due to strong OH^- adsorption [326, 327]. For state-of-the-art non-precious OER catalysts (e.g., NiFe LDH), continuous Fe dissolution forms anionic complexes under alkaline conditions that cannot migrate across the membrane and thus redeposit locally at the anode, markedly increasing surface Fe/Ni ratios (e.g., from 0.54 to 1.1 on $NiFe_2O_4$) and generating low-activity FeOOH phases, as reflected by the durability tests (Figure 25e) [299]. Such reconstruction disrupts physical contact at the catalyst-ionomer interface, elevates ion-transport resistance, and blocks active sites. Moreover, redeposited Fe species exhibit strong oxidizing capability, catalyzing radical chain reactions between OER intermediates (e.g., ·OOH) and the ionomer, accelerating backbone scission and quaternary ammonium degradation (XPS evidence: disappearance of N 1s signal and enhanced oxidized C 1s features in the presence of Fe) (Figure 25f) [299]. More severely, dissolved Fe^{3+} can generate ·OH radicals via Fenton-like processes, further intensifying ionomer oxidation and ultimately collapsing ionic conduction pathways, resulting in rapid voltage escalation [328]. Another critical challenge is carbonation, which elevates the area-specific resistance while simultaneously impairing water uptake and permeability of the membrane; these changes, in turn, exacerbate the degradation of the ionomer. Moreover, cationic degradation by-products

derived from the ionomer can react to form carbonate salts, imposing additional adverse effects on the overall performance of the electrolyzer device [329]. During electrolysis in K_2CO_3 electrolyte, the ionomer is also prone to oxidative fragmentation, which accelerates the premature failure of the AEMWE [330].

The degradation of the MEA is not the independent attenuation of a single component, but rather the synergistic failure of all functional units. For instance, the degradation of cationic groups in the AEM reduces the membrane's ionic conductivity, forcing the electrolyzer to increase its operating voltage to maintain a targeted current density. In turn, the elevated voltage exacerbates the oxidative decomposition of the anode-side AEI and the dissolution of electrocatalysts, ultimately forming a vicious cycle of "degradation–voltage rise–further degradation." In summary, the degradation of MEA in AEMWE is a complex process driven by the coupling of multiple factors, and its core technical bottleneck lies in balancing the ionic transport requirements of pure water systems with the chemical stability of each component. Moving forward, it is necessary to adopt an integrated strategy encompassing "molecular design of materials–regulation of interfacial structures–optimization of operating protocols" to achieve precise suppression of MEA degradation, thereby accelerating the commercialization of AEMWE technology.

6.5 | The Development and Bottlenecks of Ni-Based Catalysts in AEMWE

Obviously, numerous articles have reported the design of high-performance alkaline HER electrocatalysts using various activation strategies in laboratory settings. However, only a small fraction of these catalysts have been further developed and applied in industry-oriented AEMWE systems. Based on the performance data summarized in Table 2, Ni-based catalysts for HER have shown significant progress. For instance, NiMo alloy catalysts achieve a cell voltage of ~1.70 V at 1 $A{\cdot}cm^{-2}$ in AEMWE applications, performing similarly to low-loading noble metal systems [117]. Additionally, Ni-based heterostructures, such as Ru-MoO_2-Ni_4Mo/NF and Ir-Ni/Mo_5N_6, have demonstrated optimized water dissociation kinetics and H* adsorption energy, thus narrowing the activity gap with commercial Pt/C catalysts in laboratory-scale AEMWE tests [331, 332]. Despite these advancements, Ni-based catalysts still lag behind those in PEMWE and even mature AWE systems in critical metrics like long-term stability and degradation resistance. For example, state-of-the-art PEMWE systems with Pt-based cathodes can operate stably for over 50 000 h under industrial conditions, while most Ni-based AEMWE systems exhibit significant performance decay after just 1000 to 4000 h of operation [122, 216]. Even the most stable Ni-based catalysts, such as self-supported NiMo-based electrodes, show a degradation rate of approximately 23 μV h^{-1} after 3000 h at 1 $A{\cdot}cm^{-2}$, far surpassing the degradation rate of PEMWEs (~1 μV h^{-1}) [19]. This significant gap reveals the need for substantial improvements in Ni-based catalysts to meet industrial demands. The slow progress in this area is primarily due to three key challenges: insufficient activity under practical conditions, poor stability in harsh AEMWE environments, and unresolved cost-performance trade-offs.

6.5.1 | Activity Limitations

The intrinsic activity of Ni-based catalysts is limited by the complex reaction mechanisms involved in alkaline HER and the harsh operating conditions in AEMWEs. This results in a mismatch between the laboratory performance of these catalysts and their industrial requirements. In laboratory three-electrode systems, Ni-based catalysts (e.g., NiMo, Ni_2P) exhibit promising HER activity, with overpotentials of 20–50 mV at 10 $mA{\cdot}cm^{-2}$ in 1 M KOH. This is achieved by optimizing the electronic structure (e.g., d-band center regulation) or constructing heterojunctions to enhance water dissociation. However, AEMWEs operate under vastly different conditions, including high current densities (1000–2000 $mA{\cdot}cm^{-2}$), low electrolyte concentrations (1.0 M KOH or pure water), and elevated temperatures (50–70°C), which expose the insufficient kinetic adaptability of Ni-based catalysts. For example, the rate-limiting Volmer step (water dissociation) in alkaline HER becomes slower under high current densities because Ni-based active sites struggle to adsorb H_2O molecules while simultaneously releasing OH^- byproducts. In contrast to Pt, which has near-optimal H* adsorption free energy ($\Delta G_{H^*} \approx 0$ eV) and efficient water activation ability, pure Ni exhibits too negative ΔG_{H^*} values (strong H* binding), hindering H_2 release. Even after doping with Mo, Cu, or P, the synergistic effect between Ni and these modifiers is difficult to precisely control, as heteroatoms may aggregate under high currents, reducing the number of active sites, or the modified structure may collapse under thermal stress, leading to activity degradation.

Another important limitation is the multi-component interactions present in AEMWEs, which are absent in laboratory tests. Ni-based catalysts in AEMWEs rely on the AEM for ion transport and the GDL for gas management. However, the ionic resistance of the AEM and the mass transport limitations introduced by the GDL (e.g., gas bubble blocking) further suppress catalyst activity. These unavoidable factors limit the overall activity of HER electrocatalysts in AEMWE. Moreover, violent gas bubble formation under high currents blocks active sites and disrupts the catalyst-electrolyte interface. To mitigate these negative effects, one possible solution is to directly deposit metals on Ni foam or carbon paper, which have good conductivity and a porous structure. For example, Jiang et al. developed the Fe-modulated Raney-Ni electrode (NFA-CA), which was fabricated using atmospheric plasma spraying combined with chemical etching to form a NiFe nanocrystal core and NiFe hydroxide shell structure supported by a stable NiAl alloy framework (Figure 26a,b) [333]. This electrode demonstrated outstanding HER and OER performance, achieving overpotentials of only 27 mV for HER and 169 mV for OER at 10 $mA{\cdot}cm^{-2}$ while maintaining stability for over 1000 h. In an AEMWE setup, the NFA-CA electrode exhibited exceptional performance at 60°C with 1 M KOH, requiring only 1.56 V at 1 $A{\cdot}cm^{-2}$ and 1.79 V at 2 $A{\cdot}cm^{-2}$, surpassing the U.S. Department of Energy's targets and showing excellent durability of 1000 h (Figure 26c,d). This performance improvement was attributed to enhanced conductivity and rapid gas release facilitated by the Ni foam support, which has a superhydrophilic surface and excellent gas bubble detachment properties that reduce bubble coverage on active sites.

Additionally, AEMWE testing involves numerous parameters, unlike laboratory three-electrode systems. We call for the estab-

TABLE 2 | Summary of the AEMWE performance of the reported electrocatalysts.

Anode, catalyst loading ($mg\ cm^{-2}$)	Cathode, catalyst loading ($mg\ cm^{-2}$)	AEI loading (wt%) anode/cathode	MEA architecture	Membrane, thickness (μm)	$IEC_{membrane}$ ($mmol\ g^{-1}$ or $meq\ g^{-1}$)	Operation conditions	Activity	Stability	Degradation rate ($\mu V\ h^{-1}$)	Refs.
$Li_{0.21}Co_{2.79}O_4$, 2.5	Ni, 2.5	QPDTB-OH	CCM	Not mentioned	Not mentioned	H_2O (45°C)	0.3 A cm^{-2} at 2.05 V	11 h at 0.3 A cm^{-2}	22300	[340]
$Pb_2Ru_2O_{6.5}$, 2.5	Pt black, 2.5	PSF-TMA^+, 30	CCS	PSF-TMA+, 50	1.8	H_2O (50°C)	0.2 A cm^{-2} at 1.60 V	6 h at 0.2 A cm^{-2}	145	[341]
IrO_2, 2.6	Pt black, 2.4	A-Radel, 22/27	CCM	A-201 Tokuyama, 28	2.0	H_2O (50°C)	0.4 A cm^{-2} at 1.8 V	535 h at 0.2 A cm^{-2}	747	[342]
IrO_2, 2.3–2.8	Pt black, 2.3–2.8	PiperION (TP-85), 10	CCS	PiperION (TP-85), 50	2.02	H_2O (55°C)	1.0 A cm^{-2} at 1.9 V	175 h at 0.5 A cm^{-2}	670	[343]
Ir black, 2.7	Pt/C, 2.7	Sustainion XA-9, 5	CCS	Sustainion 37–50, 50	1.1	H_2O (60°C)	0.5 A cm^{-2} at 1.9 V	170 h at 0.5 A cm^{-2}	705	[75]
FeNi LDH/NF	Pt/C, 1.5	QAPPT	CCS	QAPPT, 2	2.7	H_2O (60°C)	1.2 A cm^{-2} at 1.8 V	175 h at 0.5 A cm^{-2}	242	[77]
VCoP, 2	VCoP, 2	no AEI	Self-supported electrode	Poly(alkylterphenyl piperidinium), 14	2.7	H_2O (60°C)	3.1 A cm^{-2} at 2.0 V	600 h at 1.0 A cm^{-2}	100	[344]
IrO_x, 10	PtNi, 8	GT32, 25 GT69, 20	CCS	XIONTM Composite-72-10CL, 30	Not mentioned	H_2O (60°C)	1.0 A cm^{-2} at ~2.0 V	500 h at 1.0 A cm^{-2}	93	[345]
FeNi Foam	Pt/C	no AEI	3D-self-supported MEA	XION Composite-72-10CL, 30	Not mentioned	H_2O (60°C)	2 A cm^{-2} at 1.87 V	1000 h at 0.5 A cm^{-2}	<0.1 μg h^{-1}	[346]

(Continues)

TABLE 2 | (Continued)

Anode, catalyst loading (mg cm^{-2})	Cathode, catalyst loading (mg cm^{-2})	AEI loading (wt%) anode/cathode	MEA architecture	Membrane, thickness (μm)	$IEC_{membrane}$ (mmol g^{-1} or meq g^{-1})	Operation conditions	Activity	Stability	Degradation rate (μV h^{-1})	Refs.
NiFe/NF	NiMo/NF	Not mentioned	CCS	xQAPS, 70	Not mentioned	H_2O (70°C)	0.4 A cm^{-2} at ~1.8 V	8 h at 0.4 A cm^{-2}	5	[347]
e-$Co(OH)_2$, 3	Pt black, 1.5	PiperION-A5, 10–20	CCS	PiperION-A40-HCO_3^-, 40	1.3	H_2O (70°C)	2.0 A cm^{-2} at 2.17 V	400 h at 2.0 A cm^{-2}	490	[71]
IrO_2, 3	Pt black, 3	F-PAE, 2.5/2.5	CCS	ATM-PP	1.7/(2.7 for F-PAE)	H_2O (80°C)	0.2 A cm^{-2} at 1.9 V	2000 h at 0.2 A cm^{-2}	350	[348]
Fe_xNi_yOOH-20F, 4.8	Pt/C, 0.94	PAP-TP-85	Self-supported electrode	PAP-TP-85, 30	2.4	H_2O (80°C)	0.2 A cm^{-2} at 1.63 V	150 h at 0.2 A cm^{-2}	560	[349]
IrO_2, 1.2	Pt/C, 0.3	PFOTFPh-TMA-C8, 25	CCM	PFOTFPh-TMA-C8, 23	2.7	H_2O (80°C)	0.2 A cm^{-2} at 1.9 V	120 h at 0.2 A cm^{-2}	2250	[350]
Ni_2Fe_3, 3	PtRu/C, 2	TMA-53, 20/20	CCS	HTMA-DAPP, 26	2.6	H_2O (85°C)	0.2 A cm^{-2} at 1.75 V	170 h at 0.2 A cm^{-2}	1470	[78]
NiFeCo, 5	Pt/C, 0.5	QAPPT, 15	CCS	QAPPT, 30–50	Not mentioned	0.01 M KOH (80°C)	2.0 A cm^{-2} at 1.8 V	100 h at 0.2 A cm^{-2}	<100	[351]
IrO_2, 4	PtRu/C, 2	FLN-55, ~20	CCS	HTMA-DAPP, 50	2.5	0.1 M NaOH (60°C)	2.0 A cm^{-2} at 1.80 V	24 h at 0.2 A cm^{-2}	4167	[352]
Co_3O_4/NF	Ru-MoO_2-Ni_4Mo/NF	no AEI	Self-supported electrode	PiperION, 50	1.8–2.2	0.2 M KOH (50°C)	0.86 A cm^{-2} at 1.8 V	300 h at 1 A cm^{-2}	<170	[332]
$Ni_3FeN@PO_4^{3-}$/NF, 1.5	PtNi@NiMoN/NF	no AEI	Self-supported electrode	Fumasep FAB-PK-130, 130	1.3	1.0 M KOH (25°C)	1 A cm^{-2} at 2.18 V	200 h at 0.5 A cm^{-2}	<40	[353]

(Continues)

TABLE 2 | (Continued)

Anode, catalyst loading (mg cm^{-2})	Cathode, catalyst loading (mg cm^{-2})	AEI loading (wt%) anode/cathode	MEA architecture	Membrane, thickness (μm)	$IEC_{membrane}$ (mmol g^{-1} or meq g^{-1})	Operation conditions	Activity	Stability	Degradation rate (μV h^{-1})	Refs.
Ni/Mo-Ni/NF, 2.5	Ni/Mo-Ni/NF, 2.5	no AEI	Self-supported electrode	FAB-3-pk-130, 130	1.5–2.0	1.0 M KOH (25°C)	0.4 A cm^{-2} at 1.87 V	87 h at 0.1 A cm^{-2}	<100	[354]
$NiFeO_xH_y$/NF	PtSACs-$NiCrO_3$/NF	no AEI	Self-supported electrode	Sustainion X37-50 Grade 60, 60	1.6–2.0	1.0 M KOH (25°C)	0.1 A cm^{-2} at 1.51 V	100 h at 0.1 A cm^{-2}	500	[355]
Raney Ni	NiW/NM	no AEI	Self-supported electrode	Fumasep FAA-3-PK-130, 130	1.7–2.0	1.0 M KOH (25°C)	0.5 A cm^{-2} at 1.78 V	200 h at 0.5 A cm^{-2}	400	[356]
CAPist-L1, 3.1	NiMo/Int/NF, 16.43	no AEI	Self-supported electrode	PAP-TP-85, 85	2.0–2.3	1.0 M KOH (25°C)	1 A cm^{-2} at 1.78 V	3000 h at 1 A cm^{-2}	22.8	[19]
NiFe-LDH@NF	Pt/WN@CP	no AEI	Self-supported electrode	FuMA-Tech FAA-3-50, 50	1.8–2.2	1.0 M KOH (25°C)	0.5 A cm^{-2} at 1.97 V	120 h at 0.5 A cm^{-2}	667	[357]
NiFe-LDH/NF	RuNi-MoO_2/NF	no AEI	Self-supported electrode	Fumasep FAAM-40, 40	1.8–2.1	1.0 M KOH (25°C)	1 A cm^{-2} at 1.71 V	1000 h at 1 A cm^{-2}	10	[18]
IrO_2/SS	$NiMoO_4$-550/Ni	no AEI	Self-supported electrode	Fumasep FAA-3-30, 26–34	1.6–2.0	1.0 M KOH (25°C)	1 A cm^{-2} at 2.2 V	100 h at 2.0 V	<80	[358]
NiFeSe/NF	$MoNi_4/MoO_2$/NF	no AEI	Self-supported electrode	PAP-TP-85, 45.3	2.7	1.0 M KOH (25°C)	1.0 A cm^{-2} at 1.65 V	2400 h at 1.0 A cm^{-2}	~0	[359]
z-NiFe/NF	$MoNi_4/MoO_2$/NF	no AEI	Self-supported electrode	PAP-TP-85, 40	Not mentioned	1.0 M KOH (25°C)	1.0 A cm^{-2} at 1.76 V	14000 h at 1.0 A cm^{-2}	12.3	[360]
NiFe-LDH/NF	Ni_4Mo/MoO_2/NF	no AEI	Self-supported electrode	PAQ-5, 40	2.66	1.0 M KOH (26°C)	1.0 A cm^{-2} at 1.82 V	2446 h at 1.0 A cm^{-2}	56	[22]

(Continues)

TABLE 2 | (Continued)

Anode, catalyst loading (mg cm^{-2})	Cathode, catalyst loading (mg cm^{-2})	AEI loading (wt%) anode/cathode	MEA architecture	Membrane, thickness (μm)	$IEC_{membrane}$ (mmol g^{-1} or meq g^{-1})	Operation conditions	Activity	Stability	Degradation rate (μV h^{-1})	Refs.
NiFe/NF	NiMo/NF	no AEI	Self-supported electrode	PFTP-26, 30	Not mentioned	1.0 M KOH (40°C)	2.0 A cm^{-2} at 2 V	650 h at 2.0 A cm^{-2}	650	[361]
Co_3O_4/NF	aPt/pNi-NOM	no AEI	Self-supported electrode	X37-50 Grade T, 50	1.8–2.2	1.0 M KOH (45°C)	0.5 A cm^{-2} at 1.8 V	210 h at 0.5 A cm^{-2}	360	[362]
CuCoO/NF	NiCoO-NiCo/C	Nafion, 20	CCS	X37-50 Grade T, 50	1.8–2.2	1.0 M KOH (50°C)	0.504 A cm^{-2} at 1.85 V	10 h at 0.44 A cm^{-2}	46	[25]
CuCoO/NF	NiCoO-NiCo/C	Nafion, 20	CCS	X37-50 Grade T, 50	1.8–2.2	1.0 M KOH (50°C), 5-cell	0.74 A cm^{-2} at 1.85 V	150 h at 0.44 A cm^{-2}	40	[25]
Ir black, 2	$Co_{0.5}Mo_{0.5}S_x$, 3.4-3.9	Sustainion XB-7, 3	CCS	Sustainion X37-50 grade RT, 50	1.8	0.1 M KOH (50°C)	1.22 A cm^{-2} at 2 V	40 h at 1.22 A cm^{-2}	140	[363]
VCoP, 2	VCoP, 2	no AEI	Self-supported electrode	Poly(alkylterphenyl piperidinium), 14	2.7	1.0 M KOH (60°C)	4.2 A cm^{-2} at 2.0 V	200 h at 1.0 A cm^{-2}	200	[344]
IrO_2, 2	Pt/C, 0.5	PFTP, 10/PFBP, 25	CCS	PFTP-13 AEM, ~30	2.82	1 M KOH (60°C)	0.5 A cm^{-2} at 1.6 V	1100 h at 0.5 A cm^{-2}	455	[364]
NiAl, 47.9	NiAlMo, 42.7	no AEI	CCS	HMT-PMBI, 50	2.52	1 M KOH (60°C)	2.0 A cm^{-2} at 2.086 V	145 h at 1.0 A cm^{-2}	650	[365]
Raney Ni-Fe, 20	Raney Ni-Fe, 20	no AEI	Self-supported electrode	Sustainion 37–50, 50	1.1	1 M KOH (60°C)	0.5A cm^{-2} at 1.93 V	250 h at 0.5 A cm^{-2}	1200	[364]
Ni-Mo@NF	Pt/C, 1	Nafion	CCS	T3-1.0-0.5, 40	2.79	1 M KOH (60°C)	2.0 A cm^{-2} at 1.77 V	500 h at 2.0 A cm^{-2}	77	[314]

(Continues)

TABLE 2 | (Continued)

Anode, catalyst loading (mg cm^{-2})	Cathode, catalyst loading (mg cm^{-2})	AEI loading (wt%) anode/cathode	MEA architecture	Membrane, thickness (μm)	$IEC_{membrane}$ (mmol g^{-1} or meq g^{-1})	Operation conditions	Activity	Stability	Degradation rate (μV h^{-1})	Refs.
Ni-Fe-O_x, 5	Ni-Fe-Co, 5	Sustainion XB-7	CCS	PBI-based AEM	Not mentioned	1 M KOH (60°C)	1.0 A cm^{-2} at 2.09 V	100 h at 1.0 A cm^{-2}	100	[366]
$NiFe_2O_4$, 1.8	modified Raney nickel, 14.5	Nafion	CCS	Sustainion grade Td, 50–80	1.1	1 M KOH (60°C)	1.0 A cm^{-2} at 1.82 V	1920 h at 1.0 A cm^{-2}	0.7	[367]
$NiFe_2O_4$, 1.8	modified Raney nickel, 2.7	Nafion	CCS	Sustainion X37-50, 50–80	1.1	1 M KOH (60°C)	1.0 A cm^{-2} at 1.85 V	12180 h at 1.0 A cm^{-2}	0.7	[367]
Raney Ni-Fe	Raney Ni-Fe	no AEI	Self-supported electrode	PFTP-13 AEM, ~30	2.82	1 M KOH (60°C)	0.5 A cm^{-2} at 1.5 V	1000 h at 0.5 A cm^{-2}	0	[364]
$NiFeO_x$, 2	NiFeCo, 3	Nafion	CCS	Sustainion 37–50, 50	1.1	1 M KOH (60°C)	1.0 A cm^{-2} at 1.9 V	1920 h at 1.0 A cm^{-2}	5	[368]
Fe-Modulating Raney-Ni	Fe-Modulating Raney-Ni	no AEI	Self-supported electrode	X37-50 Grade 60, 50	3.7	1.0 M KOH (60°C)	2 A cm^{-2} at 1.79 V	1000 h at 1 A cm^{-2}	<50	[333]
SW@A-NiFe	SW@A-NiFe	no AEI	Self-supported electrode	CMX-2.2-35-X, 35	2.2	1.0 M KOH (60°C)	1 A cm^{-2} at 1.815 V	1800 h at 1 A cm^{-2}	41	[369]
Fe_2P-$Ni_{12}P_5$/NF, 3	Co_2P-$Ni_{12}P_5$/NF, 3	no AEI	Self-supported electrode	FAA-3-50, 50	1.8	1.0 M KOH (60°C)	1 A cm^{-2} at 1.95 V	120 h at 0.5 A cm^{-2}	<100	[370]
$Fe_{0.2}Ni_{0.8}$-$P_{0.5}S_{0.5}$, 3.2	$Fe_{0.2}Ni_{0.8}$-$P_{0.5}S_{0.5}$, 3.2	no AEI	Self-supported electrode	FAA-3-50, 50	1.8	1.0 M KOH (60°C)	2.5 A cm^{-2} at 2.0 V	300 h at 1 A cm^{-2}	80	[371]
IrO_2/SS, 1	Ni-RuO_2/C, 1.92	Not mentioned	CCS	PiperION, 40	1.8–2.1	1.0 M KOH (60°C)	1 A cm^{-2} at 1.71 V	1000 h at 1 A cm^{-2}	50	[372]

(Continues)

TABLE 2 | (Continued)

Anode, catalyst loading ($mg\ cm^{-2}$)	Cathode, catalyst loading ($mg\ cm^{-2}$)	AEI loading (wt%) anode/cathode	MEA architecture	Membrane, thickness (μm)	$IEC_{membrane}$ ($mmol\ g^{-1}$ or $meq\ g^{-1}$)	Operation conditions	Activity	Stability	Degradation rate ($\mu V\ h^{-1}$)	Refs.
NF	MoO_2/Ni (600)	no AEI	Self-supported electrode	Fumatech FAA-3-PK-130, 130	1.7–2.0	1.0 M KOH (60°C)	0.55 A cm^{-2} at 2 V	300 h at 0.5 A cm^{-2}	750	[373]
NiFe LDH	Pt/Cr-Ni$(OH)_2$	no AEI	Self-supported electrode	Not mentioned	Not mentioned	1.0 M KOH (60°C)	1 A cm^{-2} at 1.75 V	100 h at 1 A cm^{-2}	120	[374]
PCoVO@NF, 5.5	CoN/VN@NF, 4.8	no AEI	Self-supported electrode	Fumasep FAA3-PK-130, 130	1.3	1.0 M KOH (70°C)	0.5 A cm^{-2} at 1.76 V	1000 h at 0.5 A cm^{-2}	<17	[375]
NiFe oxyhydroxide, 1	Pt-CNTS, 2	FAA-3-Br, 10	CCS	FAA-3-50, 50	1.8	1.0 M KOH (70°C)	1.48 A cm^{-2} at 2.05 V	40 h at 0.5 A cm^{-2}	<10	[376]
NiFe-LDH/Ni	PMoNiTm/Ni	no AEI	Self-supported electrode	Zirfon UTP220, 220	Not mentioned	1.0 M KOH (70°C)	1 A cm^{-2} at 2.43 V	100 h at 1 A cm^{-2}	300	[377]
Mo_5N_6/Co-450	Mo_5N_6/Ni-450	no AEI	Self-supported electrode	Fumasep FAA-3-PK-130, 130	1.7–2.0	1.0 M KOH (70°C)	0.45 A cm^{-2} at 1.8 V(70°C)	120 h at 0.45 A cm^{-2}	833	[378]
$NiFeO_x$, 1.25	UP-$RuNi_{SAs}$/C, 1.25	Not mentioned	CCS	Not mentioned	Not mentioned	1.0 M KOH (70°C)	0.5 A cm^{-2} at 1.70 V	250 h at 1 A cm^{-2}	<20	[379]
NiFeOOH	Pt/C, 0.4	Fumion, 30	CCS	FAA-3, 50	1.4	1.0 M KOH (70°C)	3.6 A cm^{-2} at 1.9 V	100 h at 0.5 A cm^{-2}	0	[136]
NiFe-LDH/NF	Ni_4Mo/MoO_2/NF	no AEI	Self-supported electrode	PAMP, 40	2.67	1.0 M KOH (80°C)	7.35 A cm^{-2} at 2.0 V	1532 h at 1.0 A cm^{-2}	31	[315]

(Continues)

TABLE 2 | (Continued)

Anode, catalyst loading (mg cm^{-2})	Cathode, catalyst loading (mg cm^{-2})	AEI loading (wt%) anode/cathode	MEA architecture	Membrane, thickness (μm)	$IEC_{membrane}$ (mmol g^{-1} or meq g^{-1})	Operation conditions	Activity	Stability	Degradation rate (μV h^{-1})	Refs.
IrO_2, 1.2	Pt/C, 0.3	PFOTFPh-TMA-C8, 25	CCS	PFOTFPh-TMA-C8, 53	2.7	1.0 M KOH (80°C)	0.2 A cm^{-2} at 1.6 V	135 h at 0.2 A cm^{-2}	370	[350]
NiFe-LDH, 0.4	Ru_3Ni-N-C, 0.4	Nafion	CCS	Not mentioned	Not mentioned	1.0 M KOH (80°C)	2.376 A cm^{-2} at 2 V	200 h at 0.5 A cm^{-2}	56.7	[380]
NiFeMo-NH_3	NiFeMo-NH_3	no AEI	Self-supported electrode	Not mentioned	Not mentioned	1.0 M KOH (80°C)	2.1254 A cm^{-2} at 2 V	1630 h at 0.5 A cm^{-2}	46.6	[381]
NiFe LDH/NF	Ru/O-CNT, 1	TP-100, 5	CCS	TP-100, 100	2.0	1.0 M KOH (80°C)	2 A cm^{-2} at 1.81V	400 h at 1 A cm^{-2}	<50	[382]
Ir-Ni/Mo_5N_6, 2.5	Ir-Ni/Mo_5N_6, 2.5	XA-9, 30	CCS	Sustainion x37-50 grade T, 50	1.7–2.0	1.0 M KOH (80°C)	2.1 A cm^{-2} at 2.0 V	30 h at 0.4 A cm^{-2}	Not mentioned	[331]
Ni foam	Ni foam	no AEI	Self-supported electrode	PSEBS-CM-DABCO, 100	0.76	1.95 M KOH (50°C)	0.3 A cm^{-2} at 2.26 V	160 h at 0.3 A cm^{-2}	20	[262]
$NiCo_2O_4$, 8	Pt, 0.3	qPPO, 90/10 (catalyst/polymer)	CCS	qPPO, TMA quaternized, 200	1.46	1.95 M KOH (70°C)	0.3 A cm^{-2} at 1.80 V	400 h at 0.3 A cm^{-2}	100	[383]
$NiCo_2O_4$, 8	Pt, 0.3	PSEBS-CM-TMA/PTFE, ~5	CCS	PSEBS-CM-TMA, 100	0.75	1.95 M KOH (70°C)	0.3 A cm^{-2} at 1.76 V	800 h at 0.3 A cm^{-2}	50	[384]
$NiCo_2O_4$, 8	Pt, 0.3	qPPO, 90/10 (catalyst/ionomer)	CCS	Dowex Marathon A and LDPE blend	2.45	1.95 M KOH (70°C)	0.3 A cm^{-2} at 1.80 V	100 h at 0.3 A cm^{-2}	200	[385]
$NiMoFeO_x$/NF	Ru NPs/TiN	no AEI	Self-supported electrode	Fumasep FAAM-20, 18–22	1.8–2.2	30 wt% KOH (80°C)	2.0 A cm^{-2} at 1.84 V	1000 h at 5 A cm^{-2}	<50	[386]

(Continues)

TABLE 2 | (Continued)

Anode, catalyst loading ($mg\ cm^{-2}$)	Cathode, catalyst loading ($mg\ cm^{-2}$)	AEI loading (wt%) anode/cathode	MEA architecture	Membrane, thickness (μm)	$IEC_{membrane}$ ($mmol\ g^{-1}$ or $meq\ g^{-1}$)	Operation conditions	Activity	Stability	Degradation rate ($\mu V\ h^{-1}$)	Refs.
CuCoO, 36	Ni/(CeO_2-La_2O_3)/C, 7.4	PTFE	CCS	A-201 Tokuyama, 28	1.8	1 wt % K_2CO_3 (43°C)	0.47 A cm^{-2} at 1.85V	1000 h at 0.47 A cm^{-2}	200	[263]
$Ni_{0.7}Co_{0.3}O_x$, 2	Pt/C (40 wt %), 1	AS-4, 5	CCS	Self-prepared APE	Not mentioned	1 wt % K_2CO_3 (50°C)	0.1 A cm^{-2} at 2.03 V	550 h at 0.1 A cm^{-2}	200	[387]
$CuCoO_x$, 30	Ni/(CeO_2-La_2O_3)/C, 7.4	Not mentioned	CCS	A-201 Tokuyama, 28	1.8	1 wt % K_2CO_3 (60°C)	0.5 A cm^{-2} at 1.98 V	200 h at 0.5 A cm^{-2}	500	[261]
$CuCoO_x$, 30	Ni/(CeO_2-La_2O_3)/C, 7.4	Not mentioned	CCS	FAA-3-PP-75	1.4	1 wt % K_2CO_3 (60°C)	0.5 A cm^{-2} at 2.05 V	200 h at 0.5 A cm^{-2}	2380	[261]

lishment of standardized operating protocols and reporting criteria for catalyst loading, test temperature, electrolyte concentration, and measured voltage to enable more accurate evaluation of HER catalyst activity in AEMWE.

6.5.2 | Stability Challenges

Stability remains the most critical bottleneck for Ni-based catalysts in AEMWEs. The harsh operating environment, characterized by low alkalinity, high current densities, and intermittent operation, induces both chemical and mechanical degradation that far exceeds what is observed in laboratory tests. Most HER electrocatalysts only exhibit stability for several hours in practical water electrolyzers, which is far from meeting the stringent requirements for AEMWE (e.g., 80 000 h). In the strong alkaline environment at the electrode-membrane interface and under high currents, Ni-based catalysts undergo significant chemical degradation. Ni active sites are prone to oxidation, forming inert $Ni(OH)_2$ or NiOOH passivation layers that block HER active sites. This phenomenon is particularly pronounced at elevated temperatures (50–70°C), where the oxidation rate of Ni increases by 2–3 orders of magnitude compared to ambient laboratory conditions. Furthermore, the chemical degradation refers to the severe reconstruction, dissolution, Ostwald ripening, or agglomeration of the catalyst under AEMWE's harsh operating conditions, which deteriorate the active centers and reduce stability. Unlike Pt, which has high thermodynamic stability in alkaline media, Ni has a lower reduction potential, making it more susceptible to dissolution (Ni^{2+} leaching) under fluctuating potentials, especially in intermittent AEMWE operation (e.g., coupled with solar power). These frequent start-stop cycles generate reverse currents, exacerbating metal dissolution. To date, no efficient strategy has been developed to address these issues. For instance, Lee et al. synthesized carbon-coated NiMo alloys ($Ni_3Mo@C_x$), where the defect carbon shell suppresses irreversible oxidation of metallic Ni to $Ni(OH)_2$ and volume expansion, thus maintaining HER activity [334]. The defective carbon shell allows for the diffusion of H_2O and OH^- to maintain HER but prevents OH^- from entering the metal lattice and triggering the transition to hydroxide. DFT calculations show that $Ni_3Mo@C_x$ has much higher OH^- adsorption energy (−2.02 eV) compared to bare Ni_3Mo (−4.01 eV), reducing the binding of OH^- and minimizing oxidation. In tests with integrated reference electrode electrolyzers, it was demonstrated that NiMo catalyst degradation was the primary cause of performance decline. However, $Ni_3Mo@C_{60}$ showed stable performance for 192 cycles (8 days) under intermittent operating conditions, with a slight voltage increase from 1.99 V to 2.13 V, which is evidently different from carbon-free Ni_3Mo (Figure 26e,f). This indicates the potential feasibility of this strategy. However, such effective catalysts are still rare and require further research.

Moreover, most Ni-based catalysts are prepared as powders and require polymer binders (e.g., Aemion ionomers) to load them onto GDLs, resulting in weak metal-support interactions. In AEMWEs, violent H_2 evolution generates large bubbles that exert mechanical stress on the catalyst layer, causing Ni-based particles to peel off the support, which leads to short-term stability loss. As discussed earlier, high currents in AEMWEs

drive the violent production of gas bubbles, which will weaken the catalyst-support interaction and cause peeling, undermining the system's stability. A viable solution could be to directly grow or deposit catalysts on conductive supports, which improves the metal-support interaction and mechanical stability. Furthermore, the porous and hydrophilic characteristics of these supported catalysts facilitate the removal of gas bubbles. For example, Yuan et al. used Ni_2P-$NiMoO_x$/NF as a self-supported cathode in an AEMWE system, achieving high current density (0.62 A·cm^{-2} at 2.0 V) and stable performance for 60 h at 400 mA·cm^{-2}, without any significant activity decline [335].

The harsh operating conditions in AEMWE, particularly the fragile AEM and ionomer components, further complicate the stability challenges. Niaz et al. found that the main cause of stability deterioration is membrane dehydration, rather than catalyst deactivation [336]. Therefore, factors other than the catalyst, such as membrane integrity, should also be considered when evaluating stability in AEMWEs. Innovations in MEA design, such as integrated catalyst layers, have been developed to address these issues. For example, Kong et al. proposed a novel method for in situ catalyst coating of the membrane (m-CCM) by cycling $NaBH_4$ reductant and Ni/Fe metal precursor solutions between the AEM and GDL to synthesize Ni_3Fe catalyst layers, avoiding anion exchange ionomer defects in traditional electrolyzer (Figure 26g) [337]. This approach significantly improves catalyst utilization, reduces interface resistance (0.017 Ω, half that of traditional methods), and enhances long-term stability. The performance of the resulting AEMWE system exceeds traditional catalyst-coated substrates, achieving an industrial current density of 1 A·cm^{-2} at only 1.79 V, with stability for 200 h at this current density. This strategy represents a promising advancement in the field.

6.5.3 | Cost Trade-Offs

The cost of electrocatalysts typically accounts for over 60% of the total electrolyzer cost. Reducing catalyst costs can significantly contribute to the commercial viability of alkaline water electrolysis systems. While Ni-based catalysts are relatively inexpensive compared to Pt/Ru, their development for AEMWEs is hindered by unresolved cost-performance trade-offs. These include high modification costs, challenges in scalability, and hidden system-level expenses. Pure Ni catalysts exhibit insufficient activity and stability for AEMWEs, necessitating complex modifications that erode their cost advantage. For example, Ir-modified Ni-based catalysts still require Ir loadings of ∼0.05 mg·cm^{-2}, adding ∼\$0.1 per cm^2 to the cathode cost, which is far higher than the target of <\$0.01 per cm^2 for industrial AEMWEs [331]. In contrast, laboratory-scale synthesis of high-performance Ni-based catalysts (e.g., single-atom catalysts, heterostructured catalysts) often involves small-scale, labor-intensive methods (e.g., electrodeposition, atomic layer deposition), which are difficult to scale up. For example, hydrothermal synthesis of NiMo nanowires yields only milligram quantities per batch, and scaling to industrial production leads to uneven doping and loss of activity [335]. Industrial-scale methods (e.g., ball milling, spray pyrolysis) reduce costs but compromise catalyst structure [338]. In contrast, Pt/C catalysts used for PEMWEs are produced via mature large-scale methods (e.g., impregnation-reduction) with consistent performance, enabling cost control despite Pt's high raw material price. Therefore, for the low-cost non-noble-metal catalysts, the current focus should still be placed on employing various methods to activate their activity by using the facile preparation method.

In addition to catalyst costs, system-level adaptations add to the expense of Ni-based AEMWEs. For example, Ni-based catalysts require thicker GDLs (e.g., Ni felt instead of Ni foam) to enhance gas diffusion and reduce bubble blocking, which increases the cost of bipolar plates [333, 339]. The poor stability of Ni-based catalysts also necessitates more frequent maintenance (e.g., catalyst replacement, membrane cleaning), leading to higher operational costs over the electrolyzer's lifetime. Moreover, the instability and high cost of AEMs further exacerbate the overall hydrogen production cost in AEMWE systems compared to PEMWE.

7 | Conclusion and Perspective

Considerable strides have been made in elucidating the intricacies of the HER in alkaline media and advancing the development of effective, robust Ni-based electrocatalysts for AEMWE. This review has comprehensively outlined various strategies to engineer high-performance Ni-based catalysts that exhibit exceptional intrinsic activity, operate efficiently at high current densities, and maintain superior long-term stability in AEMWE systems. To boost intrinsic activity, approaches such as heteroatom doping, vacancy engineering, interface design, and morphological optimization have been employed to fine-tune the electronic structure and ΔG_{H^*}. For achieving high-current-density HER, nanostructuring, alloying, single-atom configurations, and phase engineering enhance the exposure of active sites and facilitate electron transfer. Exceptional durability is realized through structural stabilization, corrosion resistance enhancement, and strengthened catalyst-support interactions. Notably, these strategies are broadly applicable to the development of other high-performance HER electrocatalysts. Despite significant progress in Ni-based catalysts for AEMWE, challenges persist, including limited compositional diversity, inadequate understanding of degradation mechanisms under operational conditions, and insufficient stability at industrially relevant current densities. Addressing these issues will require continued investigation, as highlighted in subsequent discussions (Figure 27).

7.1 | Catalyst Design and Synthesis

The development of reliable, efficient, and cost-effective Ni-based catalysts for alkaline HER requires an integrated approach that blends theoretical design with practical synthesis. Critical factors such as charge transfer, mass transport, and resistance to alkaline degradation must be carefully considered and incorporated into computational models to optimize catalytic performance. Furthermore, simplifying synthesis protocols is key to enabling scalable production without compromising electrocatalytic efficacy, ensuring industrial applicability. Current design methodologies for Ni-based catalysts still lack the precision necessary

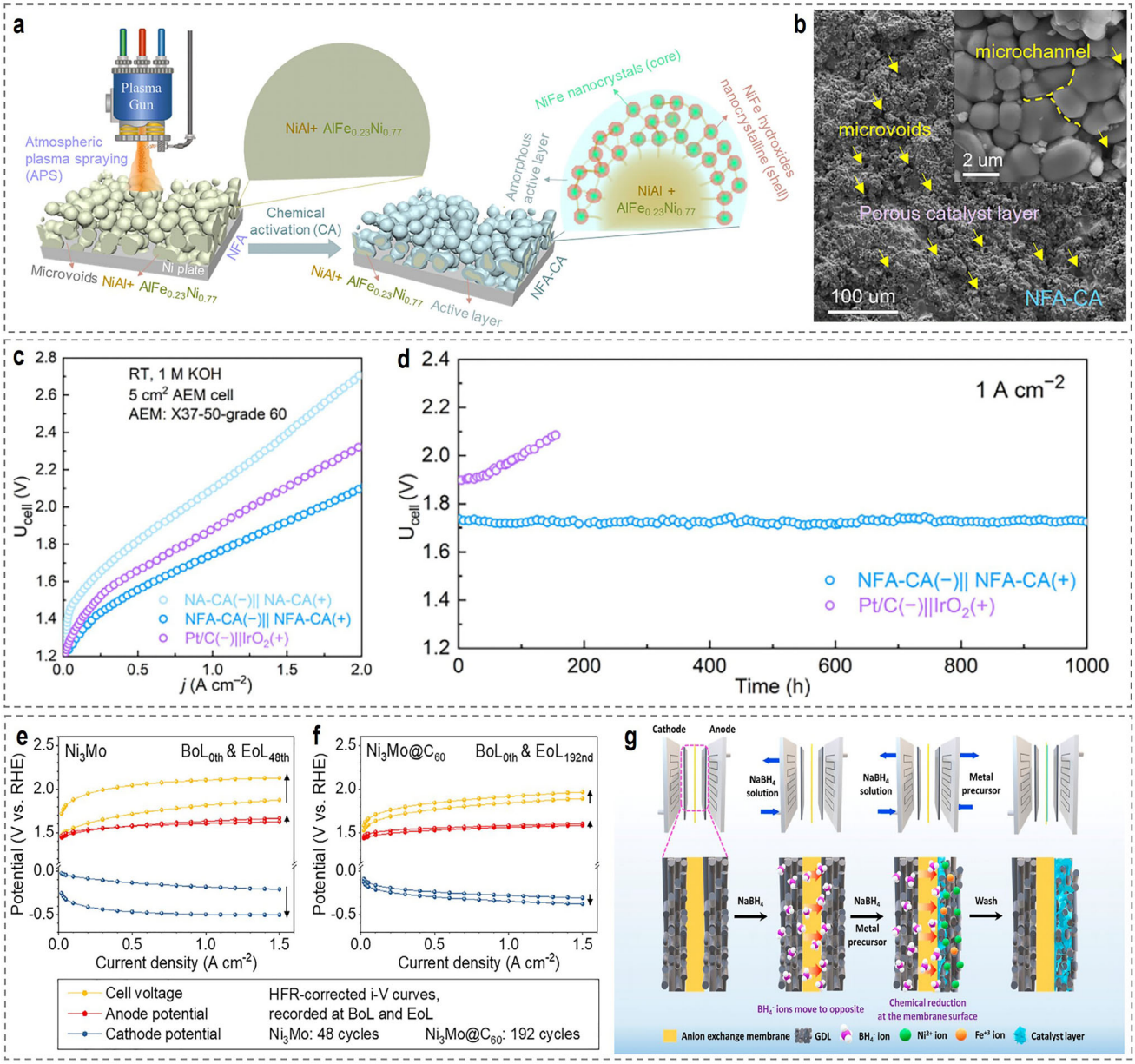

FIGURE 26 | (a) Schematic illustration of NFA-CA electrode preparation. (b) NFA-CA catalysts typical images from SEM. (c) Polarization curves for the AEMWE with various electrodes at 25°C. (d) The long-term operation stability at 1 A cm^{-2} for NFA-CA(−)||NFA-CA(+)AEMWE. Reproduced with permission [333]. Copyright 2025, Wiley-VCH. The beginning of life (BoL) and the end of life (EoL) *I–V* curves after the correction using high-frequency resistance (HFR) for MEA with (e) Ni_3Mo and (f) $Ni_3Mo@C_{60}$ cathode catalysts. Reproduced with permission [334]. Copyright 2025, Wiley-VCH. (g) Procedure for the in-situ ionomer-free m-CCM method. Reproduced with permission [337]. Copyright 2023, American Chemical Society.

to selectively target specific catalytic properties, highlighting the need for deeper insights into the underlying HER mechanisms. This gap in understanding limits the ability to fully unlock the potential of Ni-based systems. The advent of emerging tools such as machine learning and high-throughput screening offers substantial promise in accelerating the discovery of optimal Ni compositions. By leveraging descriptor-based insights and computational predictions, these tools enable a more systematic and data-driven approach to catalyst design. Advanced strategies like transition metal doping, defect engineering, and strain engineering can be employed to fine-tune the electronic structure and enhance active site accessibility. Additionally, strategies to reduce Ni content, such as single-atom catalysis or coupling Ni with non-precious supports, can lower production costs while preserving or even enhancing catalytic performance. However, significant challenges remain, particularly in achieving uniform morphology, ensuring scalability, and correlating structural features with catalytic properties. Addressing these challenges will require interdisciplinary efforts that bring together advanced synthesis techniques, state-of-the-art characterization tools, and sophisticated modeling approaches. Only through such combined efforts can we make significant strides toward realizing cost-effective, high-performance Ni-based catalysts for alkaline HER on an industrial scale.

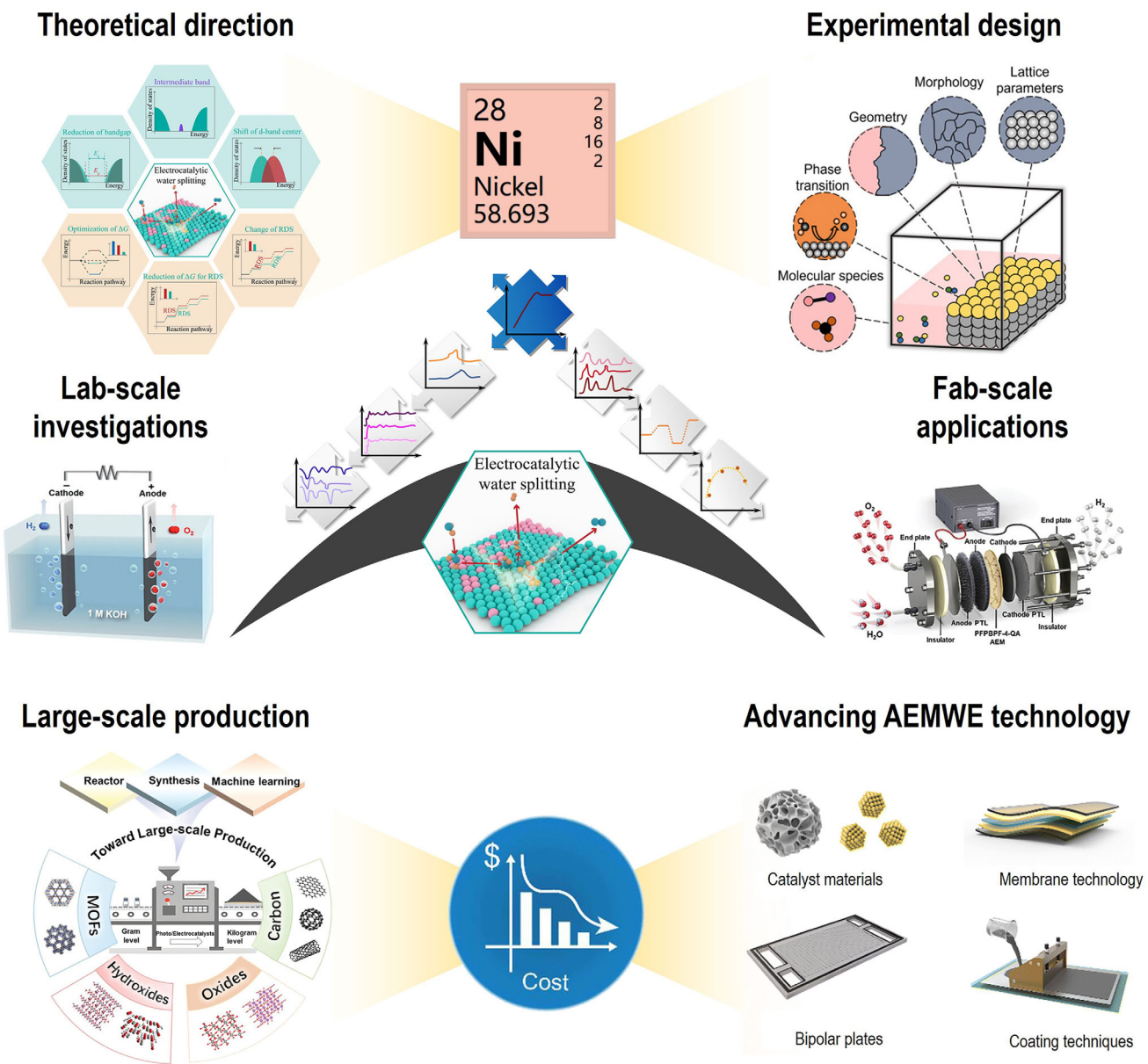

FIGURE 27 | Schematic illustration of the perspectives for the continued investigation of Ni-based HER catalysts in AEMWEs.

7.2 | Mechanism Investigation

A comprehensive understanding of the origins of HER activity is crucial for designing superior Ni-based electrocatalysts. Advanced in-situ and operando techniques such as XAS, Raman spectroscopy, and electrochemical mass spectrometry are indispensable tools for studying catalyst behavior under real-time reaction conditions. These techniques provide valuable insights into reaction pathways, the identification of key intermediates, and the determination of active sites with high spatial and temporal resolution. Such insights allow for precise control over reaction kinetics and catalyst optimization, laying the foundation for more effective catalyst design. DFT calculations complement experimental investigations by elucidating underlying reaction mechanisms and enabling the prediction of catalytic performance. However, to enhance the accuracy and relevance of DFT models, they must move beyond idealized, static structures to incorporate dynamic surface reconstructions and the effects of changing reaction environments during HER. Factors such as pH, electrolyte composition, and applied potential should be integrated into computational simulations to accurately assess energy barriers across the various steps of the HER. In recent years, the integration of machine learning (ML) into the catalyst design process has opened new avenues for high-throughput screening and the discovery of optimal catalyst compositions. ML algorithms can analyze vast datasets generated by experimental and computational studies to uncover hidden patterns in material properties and catalytic behavior. This approach enables the rapid identification of descriptors that correlate with high HER activity and helps predict new, high-performance catalysts. By combining ML with in-situ characterization and sophisticated computational models, we can gain a deeper understanding of structural evolution and reaction dynamics during HER. This integrated approach will pave the way for the rational design

of Ni-based electrocatalysts with enhanced activity, stability, and cost-effectiveness.

7.3 | Operando Spectroscopy

Operando spectroscopy holds significant promise for advancing the understanding of Ni-based hydrogen evolution catalysts in AEMWE systems. By providing real-time insights into the catalyst's behavior under operational conditions, techniques such as operando XAS, Raman spectroscopy, and infrared spectroscopy offer unparalleled resolution in monitoring dynamic changes in electronic structure, active sites, and reaction intermediates. These in-situ methods allow for the tracking of Ni oxidation states, Ni-O bond formation, and the evolution of reaction intermediates, crucial for optimizing hydrogen evolution kinetics. In particular, operando XAS can reveal the Ni redox cycles and lattice distortions under alkaline conditions, shedding light on the mechanisms that govern charge transfer and activity enhancement. Additionally, Raman spectroscopy can help visualize the surface restructuring of Ni-based catalysts during high-current-density operation, crucial for identifying pathways that lead to catalyst deactivation or performance improvement. On the scale of MEAs, operando techniques can also monitor interface interactions between the membrane, ionomer, and catalyst, which are critical for optimizing OH^- conduction and preventing performance loss due to mass transport limitations. These insights into the MEA structure can help understand the hydrophobic/hydrophilic transitions and electrolyte penetration at different stages of operation. At the electrolyzer scale, operando spectroscopy can provide information on local electrochemical activity and identify performance degradation linked to issues such as gas crossover and electrode scaling, which are crucial for scaling up AEMWE systems for industrial applications. The future of operando spectroscopy lies in its ability to provide a holistic view of the catalyst's behavior, connecting structural changes to performance metrics in real-time across different length scales, from individual catalyst sites to MEA performance and full-scale electrolyzers. Combining these techniques with machine learning and high-throughput screening will accelerate the discovery of more efficient Ni-based electrocatalysts by offering deeper insights into structure-activity relationships and guiding the design of catalysts for AEMWE systems. As these operando tools continue to evolve, they will become indispensable for developing highly stable and efficient catalysts that meet industrial requirements for scalability, cost-effectiveness, and long-term performance.

7.4 | High Current Density and Stability

Achieving both high stability and efficiency at elevated current densities (e.g., >1 A cm^{-2}) remains a significant challenge for Ni-based HER catalysts in AEMWE systems. The inherent trade-off between activity and durability complicates the development of stable high-performance catalysts under such conditions. To address this, it is crucial to identify optimal operating windows that balance these two critical parameters, which requires further in-depth investigation. To enhance stability, strategies like incorporating conductive supports and designing porous architectures have shown promise in improving the mechanical integrity and conductivity of catalysts, thus reducing the risk of catalyst corrosion and surface passivation. Additionally, the use of protective layers or coatings, such as conductive oxides, can prevent unwanted electrochemical degradation by providing an effective barrier to corrosive species, especially at high current densities. Emerging techniques like the incorporation of sacrificial agents or the application of external fields can further improve catalyst durability by enhancing the rate of charge transfer and mass transport, leading to improved reaction kinetics. These strategies, particularly in seawater electrolysis applications, hold significant potential for improving performance and longevity under challenging conditions. In addition to traditional evaluation metrics, such as overpotential and current density, new performance benchmarks should be adopted to assess long-term stability under industrially relevant conditions. These include metrics like performance retention over 1000 h, decay rates below 10%, and recyclability, which more accurately reflect the endurance and operational lifespan of Ni-based catalysts. Moreover, integrating additional metrics such as electrochemically active surface area retention and corrosion resistance indices will provide a more holistic stability assessment, guiding the design of Ni-based catalysts capable of meeting industrial requirements for both efficiency and durability.

7.5 | Industrial Advancement of AEMWE

Evaluating Ni-based HER catalysts in complete AEMWE stacks, rather than simplified three-electrode setups, is crucial for understanding real-world performance limitations and ensuring that catalysts meet the operational demands of commercial-scale applications. As AEMWE technology matures, operational targets by 2030 include achieving current densities of 1–2 A cm^{-2}, operating temperatures between 50–80°C, energy efficiencies of 70–80%, and lifetimes exceeding 50 000 h. These ambitious targets highlight the need for robust, high-performance catalysts capable of sustaining long-term operation under industrial conditions. In addition to Ni-based catalysts, key stack components, such as MEAs, GDLs, and flow field designs, must be optimized to minimize losses and ensure efficient gas evolution. To improve overall stack efficiency, it is critical to enhance mass transport, electrical conductivity, and gas product release, while mitigating ohmic resistance and fuel crossover. Innovations such as nanoporous Ni-based materials, 3D-printed bipolar plates, and advanced MEA designs can provide significant improvements in performance while also reducing system costs. Furthermore, addressing catalyst degradation mechanisms in real-world operating conditions necessitates the integration of accelerated stress testing and advanced operando imaging techniques. These techniques enable the real-time monitoring of catalyst behavior, identification of degradation pathways, and the development of more durable materials. With these tools, engineers can quickly identify weaknesses such as catalyst detachment, gas crossover, and ohmic losses, leading to more robust designs. Technoeconomic analysis will be crucial for advancing the commercial viability of AEMWE. Assessing the cost-effectiveness of Ni-based catalysts under various operational scenarios and examining lifecycle costs, including production, maintenance, and energy consumption, will be essential for identifying cost-reduction strategies and determining the economic feasibility of scaling up AEMWE systems. This analysis should include both

direct costs, such as materials and capital expenses, and indirect costs, such as maintenance and operational energy consumption over the expected 50 000 h lifetime. Conducting these analyses will provide a clearer pathway toward reducing the cost per kilogram of hydrogen, an essential metric for achieving the \$3/kg H_2 target by 2030. In conclusion, bridging the gap between fundamental research and applied engineering, combined with thorough technoeconomic assessments, will be key to optimizing Ni-based catalysts for AEMWE. This integrated approach will drive the development of highly efficient, cost-effective, and durable systems capable of meeting the stringent requirements of commercial hydrogen production at large scales.

Acknowledgements

The authors thank the support of the Strategic Priority Research Program of the Chinese Academy of Sciences (XDB0600400), the Natural Science Foundation of Liaoning Province (2025BS0139), the Science and Technology Major Project of Liaoning Province (2024JH1/11700013), and the State Key Laboratory of Catalysis (2024SKL-A-009).

Conflicts of Interest

The authors declare no conflicts of interest.

Data Availability Statement

The authors have nothing to report.

References

1. N. Dubouis, D. Aymé-Perrot, D. Degoulange, A. Grimaud, and H. Girault, "Alkaline Electrolyzers: Powering Industries and Overcoming Fundamental Challenges," *Joule* 8 (2024): 883–898, https://doi.org/10.1016/j.joule.2024.02.012.

2. L. Wan, Z. Xu, Q. Xu, et al., "Key Components and Design Strategy of the Membrane Electrode Assembly for Alkaline Water Electrolysis," *Energy & Environmental Science* 16 (2023): 1384–1430, https://doi.org/10.1039/d3ee00142c.

3. K. Yue, R. Lu, M. Gao, et al., "Polyoxometalated Metal-Organic Framework Superstructure for Stable Water Oxidation," *Science* 388 (2025): 430–436, https://doi.org/10.1126/science.ads1466.

4. Z. Li, G. Lin, L. Wang, et al., "Seed-Assisted Formation of NiFe Anode Catalysts for Anion Exchange Membrane Water Electrolysis at Industrial-Scale Current Density," *Nature Catalysis* 7 (2024): 944–952, https://doi.org/10.1038/s41929-024-01209-1.

5. L. Ji, C. Lv, Z. Chen, Z. Huang, and C. Zhang, "Nickel-Based (Photo)Electrocatalysts for Hydrogen Production," *Advanced Materials* 30 (2018): 1705653, https://doi.org/10.1002/adma.201705653.

6. L. Wu, W. Lu, W. L. Ong, et al., "Photothermal-Promoted Anion Exchange Membrane Seawater Electrolysis on a Nickel-Molybdenum-Based Catalyst," *Nature Communications* 16 (2025): 3098, https://doi.org/10.1038/s41467-025-58320-5.

7. J. Li, Z. Li, Q. Sun, et al., "Recent Advances in the Large-Scale Production of Photo/Electrocatalysts for Energy Conversion and Beyond," *Advanced Energy Materials* 14 (2024): 2402441, https://doi.org/10.1002/aenm.202402441.

8. N. Esfandiari, M. Aliofkhazraei, A. N. Colli, et al., "Metal-Based Cathodes for Hydrogen Production by Alkaline Water Electrolysis: Review of Materials, Degradation Mechanism, and Durability Tests," *Progress in Materials Science* 144 (2024): 101254, https://doi.org/10.1016/j.pmatsci.2024.101254.

9. J. Wang, F. Xu, H. Jin, Y. Chen, and Y. Wang, "Non-Noble Metal-Based Carbon Composites in Hydrogen Evolution Reaction: Fundamentals to Applications," *Advanced Materials* 29 (2017): 1605838, https://doi.org/10.1002/adma.201605838.

10. F. Liu, C. Shi, X. Guo, et al., "Rational Design of Better Hydrogen Evolution Electrocatalysts for Water Splitting: A Review," *Advanced Science* 9 (2022): 2200307, https://doi.org/10.1002/advs.202200307.

11. L. Wu, W. L. Ong, and G. W. Ho, "Advancing Seawater Electrochemical Reaction for Fuel and Chemical Production," *ACS Nano* 19 (2025): 10779–10795, https://doi.org/10.1021/acsnano.4c18818.

12. L. Huo, C. Jin, K. Jiang, Q. Bao, Z. Hu, and J. Chu, "Applications of Nickel-Based Electrocatalysts for Hydrogen Evolution Reaction," *Advanced Energy and Sustainability Research* 3 (2022): 2100189, https://doi.org/10.1002/aesr.202100189.

13. X. Zhang, C. Cao, T. Ling, C. Ye, J. Lu, and J. Shan, "Developing Practical Catalysts for High-Current-Density Water Electrolysis," *Advanced Energy Materials* 14 (2024): 2402633, https://doi.org/10.1002/aenm.202402633.

14. H. Zhang, A. W. Maijenburg, X. Li, S. L. Schweizer, and R. B. Wehrspohn, "Bifunctional Heterostructured Transition Metal Phosphides for Efficient Electrochemical Water Splitting," *Advanced Functional Materials* 30 (2020): 2003261, https://doi.org/10.1002/adfm.202003261.

15. H. Sun, Z. Yan, F. Liu, W. Xu, F. Cheng, and J. Chen, "Self-Supported Transition-Metal-Based Electrocatalysts for Hydrogen and Oxygen Evolution," *Advanced Materials* 32 (2020): 1806326, https://doi.org/10.1002/adma.201806326.

16. J. Yang, W. Li, D. Wang, and Y. Li, "Electronic Metal–Support Interaction of Single-Atom Catalysts and Applications in Electrocatalysis," *Advanced Materials* 32 (2020): 2003300, https://doi.org/10.1002/adma.202003300.

17. Z.-Y. Yu, Y. Duan, X.-Y. Feng, X. Yu, M.-R. Gao, and S.-H. Yu, "Clean and Affordable Hydrogen Fuel From Alkaline Water Splitting: Past, Recent Progress, and Future Prospects," *Advanced Materials* 33 (2021): 2007100, https://doi.org/10.1002/adma.202007100.

18. P. Guo, P. Zhang, S. Cao, et al., "Constructing RuNi-MoO_2 Heterojunction With Optimal Built-In Electrical Field for Efficient Hydrogen Production in Anion Exchange Membrane Water Electrolyzer," *Advanced Functional Materials* 35 (2025): 2415375, https://doi.org/10.1002/adfm.202415375.

19. G. Lin, A. Dong, Z. Li, et al., "An Interlayer Anchored NiMo/MoO_2 Electrocatalyst for Hydrogen Evolution Reaction in Anion Exchange Membrane Water Electrolysis at High Current Density," *Advanced Materials* 37 (2025): 2507525, https://doi.org/10.1002/adma.202507525.

20. M. Ning, Y. Wang, L. Wu, et al., "Hierarchical Interconnected NiMoN With Large Specific Surface Area and High Mechanical Strength for Efficient and Stable Alkaline Water/Seawater Hydrogen Evolution," *Nano-Micro Letters* 15 (2023): 157, https://doi.org/10.1007/s40820-023-01129-y.

21. L. Wu, M. Ning, X. Xing, et al., "Boosting Oxygen Evolution Reaction of (Fe,Ni)OOH via Defect Engineering for Anion Exchange Membrane Water Electrolysis under Industrial Conditions," *Advanced Materials* 35 (2023): 2306097, https://doi.org/10.1002/adma.202306097.

22. L. Yin, R. Ren, L. He, et al., "Stable Anion Exchange Membrane Bearing Quinuclidinium for High-Performance Water Electrolysis," *Angewandte Chemie International Edition* 63 (2024): 202400764, https://doi.org/10.1002/anie.202400764.

23. H. Huang, L. Xu, S. Zuo, et al., "Pioneering Built-In Interfacial Electric Field for Enhanced Anion Exchange Membrane Water Electrolysis," *Angewandte Chemie International Edition* 64 (2025): 202414647, https://doi.org/10.1002/anie.202414647.

24. S. H. Park, D. T. To, and N. V. Myung, "A Review of Nickel-Molybdenum Based Hydrogen Evolution Electrocatalysts From Theory to Experiment," *Applied Catalysis A: General* 651 (2023): 119013, https://doi.org/10.1016/j.apcata.2022.119013.

25. Y. S. Park, J. Jeong, Y. Noh, et al., "Commercial Anion Exchange Membrane Water Electrolyzer Stack Through Non-precious Metal Electrocatalysts," *Applied Catalysis B: Environmental* 292 (2021): 120170, https://doi.org/10.1016/j.apcatb.2021.120170.

26. N. Dubouis and A. Grimaud, "The Hydrogen Evolution Reaction: From Material to Interfacial Descriptors," *Chemical Science* 10 (2019): 9165–9181, https://doi.org/10.1039/c9sc03831k.

27. Y. Li, X. Bao, D. Chen, et al., "A Minireview on Nickel-Based Heterogeneous Electrocatalysts for Water Splitting," *Chemcatchem* 11 (2019): 5913–5928, https://doi.org/10.1002/cctc.201901682.

28. W. Yang and S. Chen, "Recent Progress in Electrode Fabrication for Electrocatalytic Hydrogen Evolution Reaction: A Mini Review," *Chemical Engineering Journal* 393 (2020): 124726, https://doi.org/10.1016/j.cej.2020.124726.

29. C. Chen, P. Y. Olu, R. Fan, and M. Shen, "Review of Ni-Based Materials for Industrial Alkaline Hydrogen Production," *Chemsuschem* 18 (2025): 202401415, https://doi.org/10.1002/cssc.202401415.

30. C. Santoro, A. Lavacchi, P. Mustarelli, et al., "What Is Next in Anion-Exchange Membrane Water Electrolyzers? Bottlenecks, Benefits, and Future," *ChemSusChem* 15 (2022): 202200027, https://doi.org/10.1002/cssc.202200027.

31. M. T. de Groot, "Alkaline Water Electrolysis: With or Without Iron in the Electrolyte?," *Current Opinion in Chemical Engineering* 42 (2023): 100981, https://doi.org/10.1016/j.coche.2023.100981.

32. H. Sun, X. Xu, H. Kim, W. Jung, W. Zhou, and Z. Shao, "Electrochemical Water Splitting: Bridging the Gaps Between Fundamental Research and Industrial Applications," *Energy & Environmental Materials* 6 (2023): 12441, https://doi.org/10.1002/eem2.12441.

33. S. S. Kumar and H. Lim, "An Overview of Water Electrolysis Technologies for Green Hydrogen Production," *Energy Reports* 8 (2022): 13793–13813, https://doi.org/10.1016/j.egyr.2022.10.127.

34. D. Hua, J. Huang, E. Fabbri, M. Rafique, and B. Song, "Development of Anion Exchange Membrane Water Electrolysis and the Associated Challenges: A Review," *ChemElectroChem* 10 (2022): 202200999, https://doi.org/10.1002/celc.202200999.

35. Y. Sugawara, S. Sankar, S. Miyanishi, et al., "Anion Exchange Membrane Water Electrolyzers: An Overview," *Journal of Chemical Engineering of Japan* 56 (2023): 2210195, https://doi.org/10.1080/00219592.2023.2210195.

36. X. Li, B. Zhang, J. Guo, et al., "High-Strength, Ultra-Thin Anion Exchange Membranes With a Branched Structure Toward Alkaline Membrane Fuel Cells," *Journal of Materials Chemistry A* 11 (2023): 10738–10747, https://doi.org/10.1039/d2ta09914d.

37. C. Hu, C. Lv, N. Zeng, et al., "Recent Advances in Ni-Based Electrocatalysts for Hydrogen Evolution Reaction," *Energy Technology* 11 (2022): 2201048, https://doi.org/10.1002/ente.202201048.

38. M. Schalenbach, F. D. Speck, M. Ledendecker, et al., "Nickel-Molybdenum Alloy Catalysts for the Hydrogen Evolution Reaction: Activity and Stability Revised," *Electrochimica Acta* 259 (2018): 1154–1161, https://doi.org/10.1016/j.electacta.2017.11.069.

39. L. Wu, F. Zhang, S. Song, et al., "Efficient Alkaline Water/Seawater Hydrogen Evolution by a Nanorod-Nanoparticle-Structured Ni-MoN Catalyst With Fast Water-Dissociation Kinetics," *Advanced Materials* 34 (2022): 2201774, https://doi.org/10.1002/adma.202201774.

40. M. Ning, Y. Wang, L. Wu, et al., "Rational Self-supported Electrode Design With Optimized Ion Migration and Gas Diffusion for Efficient Anion Exchange Membrane Water Electrolyzer," *Materials Today Physics* 50 (2025): 101611, https://doi.org/10.1016/j.mtphys.2024.101611.

41. K. Pradeep, A. A. Jeffery, A. P. Sundaresan, et al., "Impact of Catalyst Engineering on the Durability Performance of Self-Supported Catalysts in Anion Exchange Membrane Water Electrolyzers: Recent Advances and Perspectives," *Journal of Materials Chemistry A* 13 (2025): 14510–14539, https://doi.org/10.1039/d5ta00208g.

42. B. S. Salokhe, T. T. Nguyen, R. S. Rawat, H. Song, N. H. Kim, and J. H. Lee, "Unlocking Peak Efficiency in Anion-Exchange Membrane Electrolysis With Iridium-Infused Ni/Ni_2P Heterojunction Electrocatalysts," *Small* 21 (2025): 2410986, https://doi.org/10.1002/smll.202410986.

43. Y. Xia, L. Guo, J. Zhu, et al., "Manipulating Electronic Structure of Nickel Phosphide via Asymmetric Coordination Interaction for Anion-Exchange Membrane Based Seawater Electrolysis," *Applied Catalysis B: Environment and Energy* 351 (2024): 123995, https://doi.org/10.1016/j.apcatb.2024.123995.

44. D. Strmcnik, P. P. Lopes, B. Genorio, V. R. Stamenkovic, and N. M. Markovic, "Design Principles for Hydrogen Evolution Reaction Catalyst Materials," *Nano Energy* 29 (2016): 29–36, https://doi.org/10.1016/j.nanoen.2016.04.017.

45. J.-T. Ren, L. Chen, H.-Y. Wang, Y. Feng, and Z.-Y. Yuan, "Hydrogen Oxidation Electrocatalysts for Anion-Exchange Membrane Fuel Cells: Activity Descriptors, Stability Regulation, and Perspectives," *Energy & Environmental Science* 17 (2024): 3960–4009, https://doi.org/10.1039/d3ee04251k.

46. R. Subbaraman, D. Tripkovic, D. Strmcnik, et al., "Enhancing Hydrogen Evolution Activity in Water Splitting by Tailoring Li^+-$Ni(OH)_2$-Pt Interfaces," *Science* 334 (2011): 1256–1260, https://doi.org/10.1126/science.1211934.

47. W. Sheng, M. Myint, J. G. Chen, and Y. Yan, "Correlating the Hydrogen Evolution Reaction Activity in Alkaline Electrolytes With the Hydrogen Binding Energy on Monometallic Surfaces," *Energy & Environmental Science* 6 (2013): 1509, https://doi.org/10.1039/c3ee00045a.

48. F. Zhou, Y. Zhou, G.-G. Liu, C.-T. Wang, and J. Wang, "Recent Advances in Nanostructured Electrocatalysts for Hydrogen Evolution Reaction," *Rare Metals* 40 (2021): 3375–3405, https://doi.org/10.1007/s12598-021-01735-y.

49. H. Sun, Z. Yan, C. Tian, et al., "Bixbyite-type Ln_2O_3 as Promoters of Metallic Ni for Alkaline Electrocatalytic Hydrogen Evolution," *Nature Communications* 13 (2022): 3857, https://doi.org/10.1038/s41467-022-31561-4.

50. J. K. Nørskov, T. Bligaard, A. Logadottir, et al., "Trends in the Exchange Current for Hydrogen Evolution," *Journal of The Electrochemical Society* 152 (2005): J23, https://doi.org/10.1149/1.1856988.

51. J. Wang, S. Xin, Y. Xiao, et al., "Manipulating the Water Dissociation Electrocatalytic Sites of Bimetallic Nickel-Based Alloys for Highly Efficient Alkaline Hydrogen Evolution," *Angewandte Chemie International Edition* 61 (2022): 202202518, https://doi.org/10.1002/anie.202202518.

52. R. Zhang, Z. Wei, G. Ye, et al., ""d-Electron Complementation" Induced V-Co Phosphide for Efficient Overall Water Splitting," *Advanced Energy Materials* 11 (2021): 2101758, https://doi.org/10.1002/aenm.202101758.

53. S. Niu, Y. Fang, J. Zhou, et al., "Manipulating the Water Dissociation Kinetics of Ni_3N Nanosheets via in Situ Interfacial Engineering," *Journal of Materials Chemistry A* 7 (2019): 10924–10929, https://doi.org/10.1039/c9ta03249e.

54. Y. Wu, Y. Xie, S. Niu, et al., "Accelerating Water Dissociation Kinetics of Ni_3N by Tuning Interfacial Orbital Coupling," *Nano Research* 14 (2021): 3458–3465, https://doi.org/10.1007/s12274-021-3562-1.

55. H. Yang, P. Guo, R. Wang, et al., "Sequential Phase Conversion-Induced Phosphides Heteronanorod Arrays for Superior Hydrogen Evolution Performance to Pt in Wide pH Media," *Advanced Materials* 34 (2022): 2107548, https://doi.org/10.1002/adma.202107548.

56. M. Wei, Y. Sun, J. Zhang, F. Ai, S. Xi, and J. Wang, "High-Entropy Alloy Nanocrystal Assembled by Nanosheets With d–d Electron Interaction for Hydrogen Evolution Reaction," *Energy & Environmental Science* 16 (2023): 4009–4019, https://doi.org/10.1039/d3ee01929b.

57. Z. W. Chen, J. Li, P. Ou, et al., "Unusual Sabatier Principle on High Entropy Alloy Catalysts for Hydrogen Evolution Reactions," *Nature Communications* 15 (2024): 359, https://doi.org/10.1038/s41467-023-44261-4.

58. J. Hao, Z. Zhuang, K. Cao, et al., "Unraveling the Electronegativity-Dominated Intermediate Adsorption on High-Entropy Alloy Electrocatalysts," *Nature Communications* 13 (2022): 2662, https://doi.org/10.1038/s41467-022-30379-4.

59. Q. Hu, J. Cao, S. Qi, et al., "Constructing Unsaturated Ru Atom Arrays Confined in Mn Oxides to Boost Neutral Water Reduction," *Angewandte Chemie International Edition* 64 (2025): 202416402, https://doi.org/10.1002/anie.202416402.

60. J. Zhang, C. Ma, S. Jia, et al., "Electrocatalysts Design Guided by Active Intermediates of Hydrogen Evolution Reaction," *Advanced Energy Materials* 13 (2023): 2302436, https://doi.org/10.1002/aenm.202302436.

61. X. Zhang, Z. Zuo, C. Liao, F. Jia, C. Cheng, and Z. Guo, "Strategies for Designing Advanced Transition Metal-Based Electrocatalysts for Alkaline Water/Seawater Splitting at Ampere-Level Current Densities," *ACS Catalysis* 14 (2024): 18055–18071, https://doi.org/10.1021/acscatal.4c06509.

62. L. Hou, C. Li, H. Jang, et al., "Rationally Designed Mo/Ru-Based Multi-Site Heterogeneous Electrocatalyst for Accelerated Alkaline Hydrogen Evolution Reaction," *Advanced Materials* 36 (2024): 2410039, https://doi.org/10.1002/adma.202410039.

63. X. Wang, G. Long, B. Liu, et al., "Rationally Modulating the Functions of Ni_3Sn_2-$NiSnO_x$ Nanocomposite Electrocatalysts Towards Enhanced Hydrogen Evolution Reaction," *Angewandte Chemie International Edition* 62 (2023): 202301562, https://doi.org/10.1002/anie.202301562.

64. L. Wang, M. Ma, C. Zhang, et al., "Manipulating the Microenvironment of Single Atoms by Switching Support Crystallinity for Industrial Hydrogen Evolution," *Angewandte Chemie International Edition* 63 (2024): 202317220, https://doi.org/10.1002/anie.202317220.

65. X. Zheng, X. Shi, H. Ning, et al., "Tailoring a Local Acid-Like Microenvironment for Efficient Neutral Hydrogen Evolution," *Nature Communications* 14 (2023): 4209, https://doi.org/10.1038/s41467-023-39963-8.

66. W. G. Cui, X. Ren, S. Wang, et al., "Modulating the Structure of Interfacial Water via Oxygen-Coordinated Tungsten Single-Atom on Nickel Sulfide Slab to Boost Alkaline Hydrogen Evolution," *Advanced Energy Materials* 15 (2025): 03257, https://doi.org/10.1002/aenm.202503257.

67. K. Sun, X. Wu, Z. Zhuang, et al., "Interfacial Water Engineering Boosts Neutral Water Reduction," *Nature Communications* 13 (2022): 6260, https://doi.org/10.1038/s41467-022-33984-5.

68. I. T. McCrum and M. T. M. Koper, "The Role of Adsorbed Hydroxide in Hydrogen Evolution Reaction Kinetics on Modified Platinum," *Nature Energy* 5 (2020): 891–899, https://doi.org/10.1038/s41560-020-00710-8.

69. B. Mayerhöfer, K. Ehelebe, F. D. Speck, et al., "On the Effect of Anion Exchange Ionomer Binders in Bipolar Electrode Membrane Interface Water Electrolysis," *Journal of Materials Chemistry A* 9 (2021): 14285–14295, https://doi.org/10.1039/d1ta00747e.

70. P. Fortin, T. Khoza, X. Cao, S. Y. Martinsen, A. Oyarce Barnett, and S. Holdcroft, "High-performance Alkaline Water Electrolysis Using Aemion Anion Exchange Membranes," *Journal of Power Sources* 451 (2020): 227814, https://doi.org/10.1016/j.jpowsour.2020.227814.

71. S. Hou, A. Sekar, Y. Zhao, et al., "Durable, Pure Water–Fed, Anion-Exchange Membrane Electrolyzers Through Interphase Engineering," *Science* 390 (2025): 294–298, https://doi.org/10.1126/science.adw7100.

72. Y. Lee, S. Kim, Y. Shin, et al., "High-Performance Pure Water-Fed Anion Exchange Membrane Water Electrolysis With Patterned Membrane via Mechanical Stress and Hydration-Mediated Patterning Technique," *Advanced Science* 12 (2024): 2409563, https://doi.org/10.1002/advs.202409563.

73. M. S. Lemcke, R. Gockeritz, A. Muller, K. Witte-Bodnar, W. Munchgesang, and M. Bron, "Elucidating the Degradation Behavior of a 25 cm^2 Pure-Water-Fed Non-Precious Metal Anion Exchange Membrane Water Electrolyzer Cell," *Small* (2025), https://doi.org/10.1002/smll.202506262.

74. Y. Zheng, A. Serban, H. Zhang, N. Chen, F. Song, and X. Hu, "Anion Exchange Ionomers Enable Sustained Pure-Water Electrolysis Using Platinum-Group-Metal-Free Electrocatalysts," *ACS Energy Letters* 8 (2023): 5018–5024, https://doi.org/10.1021/acsenergylett.3c01866.

75. F. Razmjooei, T. Morawietz, E. Taghizadeh, et al., "Increasing the Performance of an Anion-Exchange Membrane Electrolyzer Operating in Pure Water With a Nickel-Based Microporous Layer," *Joule* 5 (2021): 1776–1799, https://doi.org/10.1016/j.joule.2021.05.006.

76. R. Vinodh, S. S. Kalanur, S. K. Natarajan, and B. G. Pollet, "Recent Advancements of Polymeric Membranes in Anion Exchange Membrane Water Electrolyzer (AEMWE): a Critical Review," *Polymers (Basel)* 15 (2023): 2144, https://doi.org/10.3390/polym15092144.

77. L. Wan, J. Liu, Z. Xu, et al., "Construction of Integrated Electrodes With Transport Highways for Pure-Water-Fed Anion Exchange Membrane Water Electrolysis," *Small* 18 (2022): 2200380, https://doi.org/10.1002/smll.202200380.

78. D. Li, E. J. Park, W. Zhu, et al., "Highly Quaternized Polystyrene Ionomers for High Performance Anion Exchange Membrane Water Electrolysers," *Nature Energy* 5 (2020): 378–385, https://doi.org/10.1038/s41560-020-0577-x.

79. H. A. Miller, K. Bouzek, J. Hnat, et al., "Green Hydrogen From Anion Exchange Membrane Water Electrolysis: A Review of Recent Developments in Critical Materials and Operating Conditions," *Sustainable Energy & Fuels* 4 (2020): 2114–2133, https://doi.org/10.1039/c9se01240k.

80. J. Liu, Z. Kang, D. Li, et al., "Elucidating the Role of Hydroxide Electrolyte on Anion-Exchange-Membrane Water Electrolyzer Performance," *Journal of The Electrochemical Society* 168 (2021): 054522, https://doi.org/10.1149/1945-7111/ac0019.

81. B. J. Trzesniewski, O. Diaz-Morales, D. A. Vermaas, et al., "In Situ Observation of Active Oxygen Species in Fe-Containing Ni-Based Oxygen Evolution Catalysts: The Effect of pH on Electrochemical Activity," *Journal of the American Chemical Society* 137 (2015): 15112–15121, https://doi.org/10.1021/jacs.5b06814.

82. L. Giordano, B. Han, M. Risch, et al., "pH Dependence of OER Activity of Oxides: Current and Future Perspectives," *Catalysis Today* 262 (2016): 2–10, https://doi.org/10.1016/j.cattod.2015.10.006.

83. S. Kang, Y. Kim, V. Wilke, et al., "Stabilizing Pure Water-Fed Anion Exchange Membrane Water Electrolyzers Through Membrane–Electrode Interface Engineering," *ACS Applied Materials & Interfaces* 16 (2024): 47387–47395, https://doi.org/10.1021/acsami.4c05327.

84. X. Zhang, L. Wang, Y. Xie, and H. Fu, "Theoretical Insights Into Performance Descriptors and Their Impact on Activity Optimization Strategies for Cobalt-Based Electrocatalysts," *Coordination Chemistry Reviews* 533 (2025): 216560, https://doi.org/10.1016/j.ccr.2025.216560.

85. L. Miao, W. Jia, X. Cao, and L. Jiao, "Computational Chemistry for Water-Splitting Electrocatalysis," *Chemical Society Reviews* 53 (2024): 2771–2807, https://doi.org/10.1039/d2cs01068b.

86. D. Adekoya, S. Qian, X. Gu, et al., "DFT-Guided Design and Fabrication of Carbon-Nitride-Based Materials for Energy Storage Devices: A Review," *Nano-Micro Letters* 13 (2020): 13, https://doi.org/10.1007/s40820-020-00522-1.

87. B. Kaduk, T. Kowalczyk, and T. Van Voorhis, "Constrained Density Functional Theory," *Chemical Reviews* 112 (2012): 321–370, https://doi.org/10.1021/cr200148b.

88. J. Kim, H. Jung, S. M. Jung, et al., "Tailoring Binding Abilities by Incorporating Oxophilic Transition Metals on 3D Nanostructured Ni Arrays for Accelerated Alkaline Hydrogen Evolution Reaction," *Journal of the American Chemical Society* 143 (2021): 1399–1408, https://doi.org/10.1021/jacs.0c10661.

89. J. Mohammed-Ibrahim and X. Sun, "Recent Progress on Earth Abundant Electrocatalysts for Hydrogen Evolution Reaction (HER) in Alkaline Medium to Achieve Efficient Water Splitting—A Review," *Journal of Energy Chemistry* 34 (2019): 111–160, https://doi.org/10.1016/j.jechem.2018.09.016.

90. H. Wang, W. Fu, X. Yang, et al., "Recent Advancements in Heterostructured Interface Engineering for Hydrogen Evolution Reaction Electrocatalysis," *Journal of Materials Chemistry A* 8 (2020): 6926–6956, https://doi.org/10.1039/c9ta11646j.

91. L. Zhang, H. Wei, R. Yuan, P. Li, and J.-T. Ren, "Interface Engineering of Transition-Metal-Based Electrocatalysts for Alkaline Water Splitting," *Coordination Chemistry Reviews* 545 (2025): 217009, https://doi.org/10.1016/j.ccr.2025.217009.

92. X. Liao, R. Lu, L. Xia, et al., "Density Functional Theory for Electrocatalysis," *Energy & Environmental Materials* 5 (2022): 157–185, https://doi.org/10.1002/eem2.12204.

93. L. Chen, J. T. Ren, and Z. Y. Yuan, "Enabling Internal Electric Fields to Enhance Energy and Environmental Catalysis," *Advanced Energy Materials* 13 (2023): 2203720, https://doi.org/10.1002/aenm.202203720.

94. V. Butera, "Density Functional Theory Methods Applied to Homogeneous and Heterogeneous Catalysis: A Short Review and a Practical User Guide," *Physical Chemistry Chemical Physics* 26 (2024): 7950–7970, https://doi.org/10.1039/D4CP00266K.

95. J. T. Ren, D. Yang, L. Chen, and Z. Y. Yuan, "Vanadium-Doped Heterointerfaced Ni_3N-MoO_x Nanosheets With Optimized H and H_2O Adsorption for Effective Alkaline Hydrogen Electrocatalysis," *Small* 20 (2024): 2406335, https://doi.org/10.1002/smll.202406335.

96. Y. Luo, Z. Zhang, F. Yang, et al., "Stabilized Hydroxide-Mediated Nickel-Based Electrocatalysts for High-Current-Density Hydrogen Evolution in Alkaline Media," *Energy & Environmental Science* 14 (2021): 4610–4619, https://doi.org/10.1039/d1ee01487k.

97. J. George, G. Petretto, A. Naik, et al., "Automated Bonding Analysis With Crystal Orbital Hamilton Populations," *ChemPlusChem* 87 (2022): 202200123, https://doi.org/10.1002/cplu.202200123.

98. L. Yang, H. Liu, Y. Li, et al., "Customizing Bonding Affinity With Multi-Intermediates via Interfacial Electron Capture to Boost Hydrogen Evolution in Alkaline Water Electrolysis," *Angewandte Chemie International Edition* 64 (2025): 202414518, https://doi.org/10.1002/anie.202414518.

99. A. Jain, Y. Shin, and K. A. Persson, "Computational Predictions of Energy Materials Using Density Functional Theory," *Nature Reviews Materials* 1 (2016): 15004, https://doi.org/10.1038/natrevmats.2015.4.

100. J.-T. Ren, L. Chen, H.-Y. Wang, et al., "Inducing Electronic Asymmetricity on Ru Clusters to Boost Key Reaction Steps in Basic Hydrogen Evolution," *Applied Catalysis B: Environmental* 327 (2023): 122466, https://doi.org/10.1016/j.apcatb.2023.122466.

101. P. Makkar and N. N. Ghosh, "A Review on the Use of DFT for the Prediction of the Properties of Nanomaterials," *RSC Advances* 11 (2021): 27897–27924, https://doi.org/10.1039/D1RA04876G.

102. A. J. Cohen, P. Mori-Sánchez, and W. Yang, "Challenges for Density Functional Theory," *Chemical Reviews* 112 (2012): 289–320, https://doi.org/10.1021/cr200107z.

103. J. Yang, P. Jia, Y. Cao, and P. Yu, "Regulating Oxygen Vacancies to Optimize the Electronic Structure and Catalytic Activity of Tungsten Oxides for Hydrogen Evolution Reaction," *International Journal of Hydrogen Energy* 92 (2024): 333–341, https://doi.org/10.1016/j.ijhydene.2024.10.287.

104. H. Liu, Q. Liu, Y. Shao, et al., "Single-Atom Nickel Encapsulated in Nanosheet-Coiled rGO-CTAB-MoS_2 Nanoflowers for High-Efficiency and Long-Term Hydrogen Evolution in Acidic Medium," *Advanced Functional Materials* 35 (2025): 2425826, https://doi.org/10.1002/adfm.202425826.

105. H. Du, S. He, B. Li, et al., "Cascade Reaction Enables Heterointerfaces-Enriched Nanoarrays for Ampere-Level Hydrogen Production," *Angewandte Chemie International Edition* 64 (2025): 202422393, https://doi.org/10.1002/anie.202422393.

106. J. Li, J. Hu, M. Zhang, et al., "A Fundamental Viewpoint on the Hydrogen Spillover Phenomenon of Electrocatalytic Hydrogen Evolution," *Nature Communications* 12 (2021): 3502, https://doi.org/10.1038/s41467-021-23750-4.

107. S. Liu, Z. Zhang, K. Dastafkan, Y. Shen, C. Zhao, and M. Wang, "Yttrium-Doped NiMo-MoO_2 Heterostructure Electrocatalysts for Hydrogen Production From Alkaline Seawater," *Nature Communications* 16 (2025): 773, https://doi.org/10.1038/s41467-025-55856-4.

108. S. Zhang, C. Tan, R. Yan, et al., "Constructing Built-in Electric Field in Heterogeneous Nanowire Arrays for Efficient Overall Water Electrolysis," *Angewandte Chemie International Edition* 62 (2023): 202302795, https://doi.org/10.1002/anie.202302795.

109. E. S. Kryachko and E. V. Ludeña, "Density Functional Theory: Foundations Reviewed," *Physics Reports* 544 (2014): 123–239, https://doi.org/10.1016/j.physrep.2014.06.002.

110. M. J. Gillan, D. Alfè, and A. Michaelides, "Perspective: How Good Is DFT for Water?," *The Journal of Chemical Physics* 144 (2016): 130901, https://doi.org/10.1063/1.4944633.

111. L. Xiao, T. Yang, C. Cheng, et al., "Coupled Compressive-Tensile Stains Boosting Both Activity and Durability of NiMo Electrode for Alkaline Water/Seawater Hydrogen Evolution at High Current Densities," *Chemical Engineering Journal* 485 (2024): 150044, https://doi.org/10.1016/j.cej.2024.150044.

112. A. Vlček and S. Záliš, "Modeling of Charge-Transfer Transitions and Excited States in d^6 Transition Metal Complexes by DFT Techniques," *Coordination Chemistry Reviews* 251 (2007): 258–287, https://doi.org/10.1016/j.ccr.2006.05.021.

113. P. Geerlings, F. De Proft, and W. Langenaeker, "Conceptual Density Functional Theory," *Chemical Reviews* 103 (2003): 1793–1874, https://doi.org/10.1021/cr990029p.

114. F. De Proft and P. Geerlings, "Conceptual and Computational DFT in the Study of Aromaticity," *Chemical Reviews* 101 (2001): 1451–1464, https://doi.org/10.1021/cr9903205.

115. H. Chermette, "Density Functional Theory," *Coordination Chemistry Reviews* 178-180 (1998): 699–721, https://doi.org/10.1016/S0010-8545(98)00179-9.

116. C. J. Cramer and D. G. Truhlar, "Density Functional Theory for Transition Metals and Transition Metal Chemistry," *Physical Chemistry Chemical Physics* 11 (2009): 10757–10816, https://doi.org/10.1039/B907148B.

117. P. Liu, Y. Shi, X. Zhang, et al., "Interstitial Boron-Doped Ni_4Mo Nanoarray Catalyst Boosts Stable Hydrogen Evolution Reaction," *Applied Catalysis B: Environmental* 341 (2024): 123332, https://doi.org/10.1016/j.apcatb.2023.123332.

118. Y. Zhu, L. Li, H. Cheng, and J. Ma, "Alkaline Hydrogen Evolution Reaction Electrocatalysts for Anion Exchange Membrane Water Electrolyzers: Progress and Perspective," *JACS Au* 4 (2024): 4639–4654, https://doi.org/10.1021/jacsau.4c00898.

119. N. Wang, S. Song, W. Wu, Z. Deng, and C. Tang, "Bridging Laboratory Electrocatalysts With Industrially Relevant Alkaline Water Electrolyzers," *Advanced Energy Materials* 14 (2024): 2303451, https://doi.org/10.1002/aenm.202303451.

120. C. Jia, Q. Sun, R. Liu, et al., "Challenges and Opportunities for Single-Atom Electrocatalysts: From Lab-Scale Research to Potential Industry-Level Applications," *Advanced Materials* 36 (2024): 2404659, https://doi.org/10.1002/adma.202404659.

121. L. He, G. Yu, Y. Cheng, N. Wang, and W. Hu, "Non-Precious Metal-Based Catalysts for Water Electrolysis to Produce H_2 Under Industrial Conditions," *Materials Chemistry Frontiers* 7 (2023): 5661–5692, https://doi.org/10.1039/d3qm00557g.

122. E. K. Volk, M. E. Kreider, S. Kwon, and S. M. Alia, "Recent Progress in Understanding the Catalyst Layer in Anion Exchange Membrane Electrolyzers—durability, Utilization, and Integration," *EES Catalysis* 2 (2024): 109–137, https://doi.org/10.1039/d3ey00193h.

123. J. Kwon, H. Han, S. Choi, et al., "Current Status of Self-Supported Catalysts for Robust and Efficient Water Splitting for Commercial Electrolyzer," *Chemcatchem* 11 (2019): 5898–5912, https://doi.org/10.1002/cctc.201901638.

124. M. B. Kale, R. A. Borse, A. Gomaa Abdelkader Mohamed, and Y. Wang, "Electrocatalysts by Electrodeposition: Recent Advances, Synthesis Methods, and Applications in Energy Conversion," *Advanced Functional Materials* 31 (2021): 2101313, https://doi.org/10.1002/adfm.202101313.

125. F. Guo, T. J. Macdonald, A. J. Sobrido, L. Liu, J. Feng, and G. He, "Recent Advances in Ultralow-Pt-Loading Electrocatalysts for the Efficient Hydrogen Evolution," *Advanced Science* 10 (2023): 2301098, https://doi.org/10.1002/advs.202301098.

126. Z. Zhu, Y. Lin, P. Fang, et al., "Orderly Nanodendritic Nickel Substitute for Raney Nickel Catalyst Improving Alkali Water Electrolyzer," *Advanced Materials* 36 (2024): 2307035, https://doi.org/10.1002/adma.202307035.

127. S. V. Chauhan, K. K. Joshi, P. M. Pataniya, and C. K. Sumesh, "Advancing Industrial Rate Current Density in Water Electrolysis for Green Hydrogen Production: Catalyst Development, Benchmarking, and Best Practices," *Sustainable Energy & Fuels* 9 (2025): 3550–3576, https://doi.org/10.1039/d5se00262a.

128. J. K. Luo, D. P. Chu, A. J. Flewitt, S. M. Spearing, N. A. Fleck, and W. I. Milne, "Uniformity Control of Ni Thin-Film Microstructures Deposited by Through-Mask Plating," *Journal of The Electrochemical Society* 152 (2005): C36, https://doi.org/10.1149/1.1833320.

129. Y.-M. Yeh, C.-S. Chen, M.-H. Tsai, Y.-C. Shyng, S.-Y. Lee, and K.-L. Ou, "Effect of Pulse-Reverse Current on Microstructure and Properties of Electroformed Nickel–Iron Mold Insert," *Japanese Journal of Applied Physics* 44 (2005): 1086, https://doi.org/10.1143/jjap.44.1086.

130. Z. Lei, P. Liu, X. Yang, et al., "Monolithic Nickel Catalyst Featured With High-Density Crystalline Steps for Stable Hydrogen Evolution at Large Current Density," *Small* 19 (2023): 2301247, https://doi.org/10.1002/smll.202301247.

131. H. Chen, J. Li, Y. Shen, et al., "Room Temperature, Fast Fabrication of Square Meter-Sized Oxygen Evolution Electrode Toward Industrial Alkaline Electrolyzer," *Applied Catalysis B: Environmental* 316 (2022): 121605, https://doi.org/10.1016/j.apcatb.2022.121605.

132. J. Liu, Z. Wang, D. Zhang, et al., "Systematic Engineering on Ni-Based Nanocatalysts Effectively Promote Hydrogen Evolution Reaction," *Small* 18 (2022): 2108072, https://doi.org/10.1002/smll.202108072.

133. F. Razmjooei, T. Liu, D. A. Azevedo, et al., "Improving Plasma Sprayed Raney-Type Nickel–Molybdenum Electrodes Towards High-Performance Hydrogen Evolution in Alkaline Medium," *Scientific Reports* 10 (2020): 10948, https://doi.org/10.1038/s41598-020-67954-y.

134. P. Du, B. Deng, X. He, et al., "Roll-to-Roll Flash Joule Heating to Stabilize Electrocatalysts Onto Meter-Scale Ni Foam for Advanced Water Splitting," *ACS Nano* 19 (2025): 1327–1339, https://doi.org/10.1021/acsnano.4c13787.

135. W. Shi, H. Liu, J. Zhang, et al., "Roll-to-Roll Synthesis of Multielement Heterostructured Catalysts," *Nature Synthesis* 4 (2025): 836–847, https://doi.org/10.1038/s44160-025-00758-y.

136. J. E. Park, S. Park, M.-J. Kim, et al., "Three-Dimensional Unified Electrode Design Using a NiFeOOH Catalyst for Superior Performance and Durable Anion-Exchange Membrane Water Electrolyzers," *ACS Catalysis* 12 (2021): 135–145, https://doi.org/10.1021/acscatal.1c04117.

137. J. M. V. Nsanzimana, L. Cai, D. Abdoulaye, et al., "Tailoring Chemical Microenvironment of Iron-Triad Electrocatalysts for Hydrogen Production by Water Electrolysis," *Advanced Energy Materials* 15 (2025): 2501686, https://doi.org/10.1002/aenm.202501686.

138. Y. Liu, Q. Song, T. Xu, et al., "Novel Large-Scale Integrated Non-precious Metal Electrodes for Efficient and Stable Oxygen Evolution Reaction at High Current Density in 2.5 kW Anion Exchange Membrane Water Electrolysis," *Applied Catalysis B: Environment and Energy* 363 (2025): 124811, https://doi.org/10.1016/j.apcatb.2024.124811.

139. X. Wang, Y. Zheng, W. Sheng, Z. J. Xu, M. Jaroniec, and S.-Z. Qiao, "Strategies for Design of Electrocatalysts for Hydrogen Evolution Under Alkaline Conditions," *Materials Today* 36 (2020): 125–138, https://doi.org/10.1016/j.mattod.2019.12.003.

140. Z. W. Seh, J. Kibsgaard, C. F. Dickens, I. Chorkendorff, J. K. Nørskov, and T. F. Jaramillo, "Combining Theory and Experiment in Electrocatalysis: Insights Into Materials Design," *Science* 355 (2017): aad4998, https://doi.org/10.1126/science.aad4998.

141. L. Ren, K. Zhang, Y.-C. Huang, et al., "Tailored Interatomic Interactions in High-Entropy Alloys for Enhanced Electrocatalytic Hydrogen Evolution Reaction in Alkaline Water," *ACS Catalysis* 15 (2025): 11022–11033, https://doi.org/10.1021/acscatal.5c02126.

142. I. O. Baibars, H. Huang, Y. Xiao, et al., "Efficient Hydrogen Evolution at Ni/CeO_x Interfaces in Anion-Exchange Membrane Water Electrolysers," *Energy & Environmental Science* 18 (2025): 6248–6259, https://doi.org/10.1039/d4ee06113f.

143. L. Chen, H. Y. Wang, W. W. Tian, et al., "Enabling Internal Electric Field in Heterogeneous Nanosheets to Significantly Accelerate Alkaline Hydrogen Electrocatalysis," *Small* 20 (2024): 2307252, https://doi.org/10.1002/smll.202307252.

144. Y.-Y. Ma, Z.-L. Lang, L.-K. Yan, et al., "Highly Efficient Hydrogen Evolution Triggered by a Multi-interfacial Ni/WC Hybrid Electrocatalyst," *Energy & Environmental Science* 11 (2018): 2114–2123, https://doi.org/10.1039/c8ee01129j.

145. J.-T. Ren, L. Chen, H.-Y. Wang, W.-W. Tian, and Z.-Y. Yuan, "Water Electrolysis for Hydrogen Production: From Hybrid Systems to Self-Powered/Catalyzed Devices," *Energy & Environmental Science* 17 (2024): 49–113, https://doi.org/10.1039/d3ee02467a.

146. B.-J. Lee, S.-M. Jung, G. Yu, et al., "Highly Active and Stable Al-Doped NiFe Self-Supported Oxygen Evolution Reaction Electrode for Alkaline Water Electrolysis," *ACS Catalysis* 15 (2025): 1123–1134, https://doi.org/10.1021/acscatal.4c04393.

147. M. Wang, L. Zhang, J. Pan, M. Huang, and H. Zhu, "A Highly Efficient Fe-Doped Ni_3S_2 Electrocatalyst for Overall Water Splitting," *Nano Research* 14 (2021): 4740–4747, https://doi.org/10.1007/s12274-021-3416-5.

148. J. Wang, Z. Zhang, H. Song, et al., "Water Dissociation Kinetic-Oriented Design of Nickel Sulfides via Tailored Dual Sites for Efficient Alkaline Hydrogen Evolution," *Advanced Functional Materials* 31 (2021): 2008578, https://doi.org/10.1002/adfm.202008578.

149. C. Liu, B. Sheng, Q. Zhou, et al., "Manipulating D-Band Center of Nickel by Single-Iodine-Atom Strategy for Boosted Alkaline Hydrogen Evolution Reaction," *Journal of the American Chemical Society* 146 (2024): 26844–26854, https://doi.org/10.1021/jacs.4c07607.

150. X. Liu, Q. Yu, X. Qu, X. Wang, J. Chi, and L. Wang, "Manipulating Electron Redistribution in Ni_2P for Enhanced Alkaline Seawater Electrolysis," *Advanced Materials* 36 (2024): 2307395, https://doi.org/10.1002/adma.202307395.

151. Y. Sun, J. Wu, Z. Zhang, et al., "Phase Reconfiguration of Multivalent Nickel Sulfides in Hydrogen Evolution," *Energy & Environmental Science* 15 (2022): 633–644, https://doi.org/10.1039/d1ee02985a.

152. J. Wu, M. Liu, J. Fan, et al., "Amorphization-Driven RhRu Bimetallene Enhances Water Dissociation Kinetics," *Advanced Functional Materials* 34 (2024): 2409825, https://doi.org/10.1002/adfm.202409825.

153. S. Anantharaj and S. Noda, "Amorphous Catalysts and Electrochemical Water Splitting: An Untold Story of Harmony," *Small* 16 (2020): 1905779, https://doi.org/10.1002/smll.201905779.

154. J. Fan, L. Wang, X. Xiang, et al., "Porous Flower-Like Nanoarchitectures Derived From Nickel Phosphide Nanocrystals Anchored on Amorphous Vanadium Phosphate Nanosheet Nanohybrids for Superior

Overall Water Splitting," *Small Methods* 8 (2024): 2301279, https://doi.org/10.1002/smtd.202301279.

155. Q. Li, D. Wang, C. Han, et al., "Construction of Amorphous Interface in an Interwoven NiS/NiS_2 Structure for Enhanced Overall Water Splitting," *Journal of Materials Chemistry A* 6 (2018): 8233–8237, https://doi.org/10.1039/C8TA01928B.

156. J.-T. Ren, L. Chen, H.-Y. Wang, et al., "Modulating Interfacial Charge Distribution of Ni_2P-$NiSe_2$ by Multiple Interface Engineering for Accelerating Water Splitting With Industry-Level Activity and Stability," *Applied Catalysis B: Environment and Energy* 347 (2024): 123817, https://doi.org/10.1016/j.apcatb.2024.123817.

157. H. Meng, Z. Chen, J. Zhu, et al., "In Situ Amorphization of Electrocatalysts," *Advanced Functional Materials* 34 (2024): 2405270, https://doi.org/10.1002/adfm.202405270.

158. Y. Zhou, W. Hao, X. Zhao, et al., "Electronegativity-Induced Charge Balancing to Boost Stability and Activity of Amorphous Electrocatalysts," *Advanced Materials* 34 (2022): 2100537, https://doi.org/10.1002/adma.202100537.

159. Q. Fu, L. W. Wong, F. Zheng, et al., "Unraveling and Leveraging In Situ Surface Amorphization for Enhanced Hydrogen Evolution Reaction in Alkaline Media," *Nature Communications* 14 (2023): 6462, https://doi.org/10.1038/s41467-023-42221-6.

160. Q. Wu, H. Li, J. Wang, et al., "Unveiling Electronic Regulation Mechanism in Amorphous Ni_3S_2/Crystalline Cu Heterointerface for Alkaline Overall Water Splitting," *Advanced Functional Materials* (2025), https://doi.org/10.1002/adfm.202515501.

161. S. Shen, Z. Wang, Z. Lin, et al., "Crystalline-Amorphous Interfaces Coupling of $CoSe_2$/CoP With Optimized d-Band Center and Boosted Electrocatalytic Hydrogen Evolution," *Advanced Materials* 34 (2022): 2110631, https://doi.org/10.1002/adma.202110631.

162. M. Xing, S. Zhu, X. Zeng, S. Wang, Z. Liu, and D. Cao, "Amorphous/Crystalline $Rh(OH)_3$/CoP Heterostructure With Hydrophilicity/Aerophobicity Feature for All-pH Hydrogen Evolution Reactions," *Advanced Energy Materials* 13 (2023): 2302376, https://doi.org/10.1002/aenm.202302376.

163. S. Ju, Y. Liu, M. Pei, et al., "Amorphization-induced Abundant Coordinatively Unsaturated Ni Active Sites in $NiCo(OH)_2$ for Boosting Catalytic OER and HER Activities at High Current Densities for Water-Electrolysis," *Journal of Colloid and Interface Science* 653 (2024): 1704–1714, https://doi.org/10.1016/j.jcis.2023.10.002.

164. T. Guo, L. Li, and Z. Wang, "Recent Development and Future Perspectives of Amorphous Transition Metal-Based Electrocatalysts for Oxygen Evolution Reaction," *Advanced Energy Materials* 12 (2022): 2200827, https://doi.org/10.1002/aenm.202200827.

165. B. Jia, G. Liu, B. Zhang, et al., "General Modification Strategy on Amorphous Materials to Boost Catalytic Performance," *Advanced Functional Materials* 34 (2024): 2405867, https://doi.org/10.1002/adfm.202405867.

166. Y. Chang, L. Kong, D. Xu, et al., "Mo Migration-Induced Crystalline to Amorphous Conversion and Formation of RuMo/$NiMoO_4$ Heterogeneous Nanoarray for Hydrazine-Assisted Water Splitting at Large Current Density," *Angewandte Chemie International Edition* 64 (2025): 202414234, https://doi.org/10.1002/anie.202414234.

167. M. Singh, D. C. Cha, T. I. Singh, et al., "A Critical Review on Amorphous–Crystalline Heterostructured Electrocatalysts for Efficient Water Splitting," *Materials Chemistry Frontiers* 7 (2023): 6254–6280, https://doi.org/10.1039/d3qm00940h.

168. T. G. Yun, Y. Sim, Y. Lim, et al., "Surface Dissolution and Amorphization of Electrocatalysts During Oxygen Evolution Reaction: Atomistic Features and Viewpoints," *Materials Today* 58 (2022): 221–237, https://doi.org/10.1016/j.mattod.2022.06.023.

169. J. T. Ren, L. Wang, L. Chen, et al., "Interface Metal Oxides Regulating Electronic State Around Nickel Species for Efficient Alkaline Hydrogen Electrocatalysis," *Small* 19 (2023): 2206196, https://doi.org/10.1002/smll.202206196.

170. L. Chen, J. T. Ren, H. Y. Wang, L. Wang, M. L. Sun, and Z. Y. Yuan, "Modulating Electronic Structures of Noble-Metal Nanoclusters via Interfacial Electron Capture in Heterojunctions for Enhanced Hydrogen Evolution in Wide-pH Region," *Nano Letters* 25 (2025): 15937–15944, https://doi.org/10.1021/acs.nanolett.5c04378.

171. K. Chen, Z. Liu, S. Zhu, et al., "Ruthenium–Nickel Nanoparticles With Unconventional Face-Centered Cubic Crystal Phase for Highly Active Electrocatalytic Hydrogen Evolution," *Advanced Functional Materials* 34 (2024): 2406259, https://doi.org/10.1002/adfm.202406259.

172. W. Xu, Y. Chen, M. Niederberger, E. Tervoort, J. Mei, and D. L. Peng, "Self-Assembled Preparation of Porous Nickel Phosphide Superparticles With Tunable Phase and Porosity for Efficient Hydrogen Evolution," *Small* 20 (2024): 2309435, https://doi.org/10.1002/smll.202309435.

173. R. Shi, J. Yang, and G. Zhou, "High-Index-Faceted and Electron Density-Optimized Ni_3S_2 in Hierarchical $NiWO_4$-Ni_3S_2@NiO/NF Nanofibers for Robust Alkaline Electrocatalytic Hydrogen Evolution," *Chemical Engineering Journal* 457 (2023): 141188, https://doi.org/10.1016/j.cej.2022.141188.

174. J. Xu, J. Ruan, Y. Jian, et al., "Cobalt-Doping Induced Formation of Five-Coordinated Nickel Selenide for Enhanced Ethanol Assisted Overall Water Splitting," *Small* 20 (2024): 2305905, https://doi.org/10.1002/smll.202305905.

175. Y. Li, A. Feng, L. Dai, et al., "Progress on the Design of Electrocatalysts for Large-Current Hydrogen Production by Tuning Thermodynamic and Kinetic Factors," *Advanced Functional Materials* 34 (2024): 2316296, https://doi.org/10.1002/adfm.202316296.

176. M. B. Poudel, N. Logeshwaran, S. Prabhakaran, A. R. Kim, D. H. Kim, and D. J. Yoo, "Low-Cost Hydrogen Production From Alkaline/Seawater Over a Single-Step Synthesis of Mo_3Se_4-NiSe Core–Shell Nanowire Arrays," *Advanced Materials* 36 (2024): 2305813, https://doi.org/10.1002/adma.202305813.

177. P. Wang, X. Zhang, J. Zhang, et al., "Precise Tuning in Platinum-Nickel/Nickel Sulfide Interface Nanowires for Synergistic Hydrogen Evolution Catalysis," *Nature Communications* 8 (2017): 14580, https://doi.org/10.1038/ncomms14580.

178. H. Wang, W. Zhang, X. Zhang, et al., "Multi-Interface Collaboration of Graphene Cross-Linked NiS-NiS_2-Ni_3S_4 Polymorph Foam Towards Robust Hydrogen Evolution in Alkaline Electrolyte," *Nano Research* 14 (2021): 4857–4864, https://doi.org/10.1007/s12274-021-3445-5.

179. R. Liu, M. Sun, X. Liu, et al., "Enhanced Metal-Support Interactions Boost the Electrocatalytic Water Splitting of Supported Ruthenium Nanoparticles on a Ni_3N/NiO Heterojunction at Industrial Current Density," *Angewandte Chemie International Edition* 62 (2023): 202312644, https://doi.org/10.1002/anie.202312644.

180. S. Mondal, S. Dutta, S. Mal, S. K. Pati, and S. Bhattacharyya, "Lattice Mismatch Guided Nickel-Indium Heterogeneous Alloy Electrocatalysts for Promoting the Alkaline Hydrogen Evolution," *Angewandte Chemie International Edition* 62 (2023): 202301269, https://doi.org/10.1002/anie.202301269.

181. X. Zheng, Y. Yang, B. Sun, R. Ning, J. Sui, and W. Cai, "$MoSe_2$ Nanoheterostructures With an Abundant Interface for Catalytic Hydrogen Evolution," *ACS Applied Nano Materials* 4 (2021): 3493–3499, https://doi.org/10.1021/acsanm.0c03480.

182. Y. Yan, J. Lin, T. Xu, et al., "Atomic-Level Platinum Filling Into Ni-Vacancies of Dual-Deficient NiO for Boosting Electrocatalytic Hydrogen Evolution," *Advanced Energy Materials* 12 (2022): 2200434, https://doi.org/10.1002/aenm.202200434.

183. Z. Chen, X. Li, J. Zhao, et al., "Stabilizing Pt Single Atoms Through Pt-Se Electron Bridges on Vacancy-Enriched Nickel Selenide for Efficient Electrocatalytic Hydrogen Evolution," *Angewandte Chemie International Edition* 62 (2023): 202308686, https://doi.org/10.1002/anie.202308686.

184. Y. Wu, Y. Liu, G.-D. Li, et al., "Efficient Electrocatalysis of Overall Water Splitting by Ultrasmall $Ni_xCo_{3-x}S_4$ Coupled Ni_3S_2 Nanosheet Arrays," *Nano Energy* 35 (2017): 161–170, https://doi.org/10.1016/j.nanoen.2017.03.024.

185. C. Liang, P. Zou, A. Nairan, et al., "Exceptional Performance of Hierarchical Ni–Fe Oxyhydroxide@NiFe Alloy Nanowire Array Electrocatalysts for Large Current Density Water Splitting," *Energy & Environmental Science* 13 (2020): 86–95, https://doi.org/10.1039/c9ee02388g.

186. H. Wang, Y. Jiao, G. Zhang, et al., "Superaerophobic Ni_3N/Ni@W_2N_3 Multi-heterointerfacial Nanoarrays for Efficient Alkaline Electrocatalytic Hydrogen Evolution Reaction," *Chemical Engineering Journal* 497 (2024): 154776, https://doi.org/10.1016/j.cej.2024.154776.

187. J. Kim, S. M. Jung, N. Lee, K. S. Kim, Y. T. Kim, and J. K. Kim, "Efficient Alkaline Hydrogen Evolution Reaction Using Superaerophobic Ni Nanoarrays With Accelerated H_2 Bubble Release," *Advanced Materials* 35 (2023): 2305844, https://doi.org/10.1002/adma.202305844.

188. J. Y. Zhang, J. Liang, B. Mei, et al., "Synthesis of Ni/NiO@MoO_{3-x} Composite Nanoarrays for High Current Density Hydrogen Evolution Reaction," *Advanced Energy Materials* 12 (2022): 2200001, https://doi.org/10.1002/aenm.202200001.

189. Y. Wang, Y. Li, L. Ding, et al., "NiFe (Sulfur)Oxyhydroxide Porous Nanoclusters/Ni Foam Composite Electrode Drives a Large-current-density Oxygen Evolution Reaction With an Ultra-low Overpotential," *Journal of Materials Chemistry A* 7 (2019): 18816–18822, https://doi.org/10.1039/c9ta04478g.

190. M. Yu, Z. Wang, J. Liu, F. Sun, P. Yang, and J. Qiu, "A Hierarchically Porous and Hydrophilic 3D Nickel–Iron/MXene Electrode for Accelerating Oxygen and Hydrogen Evolution at High Current Densities," *Nano Energy* 63 (2019): 103880, https://doi.org/10.1016/j.nanoen.2019.103880.

191. J.-T. Ren, X.-M. Wu, T. Liu, et al., "Interfacing Nickel With Molybdenum Oxides as Monolithic Catalyst to Accelerate Alkaline Hydrogen Electrocatalysis With Robust Stability," *Applied Catalysis B: Environmental* 317 (2022): 121786, https://doi.org/10.1016/j.apcatb.2022.121786.

192. J. Nie, J. Shi, L. Li, et al., "Dense Crystalline-Amorphous Nano-Interfaces Derived From Local Reconstruction for Alkaline Hydrogen Evolution," *Advanced Energy Materials* 15 (2025): 2404246, https://doi.org/10.1002/aenm.202404246.

193. H. Sun, B. Yao, Y. Han, et al., "Multi-Interface Engineering of Self-Supported Nickel/Yttrium Oxide Electrode Enables Kinetically Accelerated and Ultra-Stable Alkaline Hydrogen Evolution at Industrial-Level Current Density," *Advanced Energy Materials* 14 (2024): 2303563, https://doi.org/10.1002/aenm.202303563.

194. Q. Yu, Z. Zhang, S. Qiu, et al., "A Ta-TaS_2 Monolith Catalyst With Robust and Metallic Interface for Superior Hydrogen Evolution," *Nature Communications* 12 (2021): 6051, https://doi.org/10.1038/s41467-021-26315-7.

195. H. Liu, R. Xie, Y. Luo, et al., "Dual Interfacial Engineering of a Chevrel Phase Electrode Material for Stable Hydrogen Evolution at 2500 mA cm^{-2}," *Nature Communications* 13 (2022): 6382, https://doi.org/10.1038/s41467-022-34121-y.

196. L. Chen, L. Wang, J. T. Ren, et al., "Artificial Heterointerfaces With Regulated Charge Distribution of Ni Active Sites for Urea Oxidation Reaction," *Small Methods* 8 (2024): 2400108, https://doi.org/10.1002/smtd.202400108.

197. J.-T. Ren, Y.-S. Wang, Y.-J. Song, L. Chen, and Z.-Y. Yuan, "Interface Engineering of In–Situ Formed Nickel Hydr(Oxy)Oxides on Nickel Nitrides to Boost Alkaline Hydrogen Electrocatalysis," *Applied Catalysis B: Environmental* 309 (2022): 121279, https://doi.org/10.1016/j.apcatb.2022.121279.

198. R. Iwata, L. Zhang, K. L. Wilke, et al., "Bubble Growth and Departure Modes on Wettable/Non-Wettable Porous Foams in Alkaline Water Splitting," *Joule* 5 (2021): 887–900, https://doi.org/10.1016/j.joule.2021.02.015.

199. B. Zhong, S. Wan, P. Kuang, B. Cheng, L. Yu, and J. Yu, "Crystalline/Amorphous Ni/NixSy Supported on Hierarchical Porous Nickel Foam for High-Current-Density Hydrogen Evolution," *Applied Catalysis B: Environmental* 340 (2024): 123195, https://doi.org/10.1016/j.apcatb.2023.123195.

200. V. H. Do and J. M. Lee, "Surface Engineering for Stable Electrocatalysis," *Chemical Society Reviews* 53 (2024): 2693–2737, https://doi.org/10.1039/d3cs00292f.

201. A. Zhu, L. Qiao, K. Liu, et al., "Rational Design of Precatalysts and Controlled Evolution of Catalyst-Electrolyte Interface for Efficient Hydrogen Production," *Nature Communications* 16 (2025): 1880, https://doi.org/10.1038/s41467-025-57056-6.

202. J. Feng, X. Wang, and H. Pan, "In-Situ Reconstruction of Catalyst in Electrocatalysis," *Advanced Materials* 36 (2024): 2411688, https://doi.org/10.1002/adma.202411688.

203. W. Du, Y. Shi, W. Zhou, Y. Yu, and B. Zhang, "Unveiling the In Situ Dissolution and Polymerization of Mo in Ni_4Mo Alloy for Promoting the Hydrogen Evolution Reaction," *Angewandte Chemie International Edition* 60 (2021): 7051–7055, https://doi.org/10.1002/anie.202015723.

204. Q. Li, C. Chen, W. Luo, et al., "In Situ Active Site Refreshing of Electro-Catalytic Materials for Ultra-Durable Hydrogen Evolution at Elevated Current Density," *Advanced Energy Materials* 14 (2024): 2304099, https://doi.org/10.1002/aenm.202304099.

205. Y. Zhang, J. Pan, G. Gong, et al., "Situ Surface Reconstruction of Catalysts for Enhanced Hydrogen Evolution," *Catalysts* 13 (2023): 120, https://doi.org/10.3390/catal13010120.

206. J. Chen, H. Chen, T. Yu, et al., "Recent Advances in the Understanding of the Surface Reconstruction of Oxygen Evolution Electrocatalysts and Materials Development," *Electrochemical Energy Reviews* 4 (2021): 566–600, https://doi.org/10.1007/s41918-021-00104-8.

207. L. Gao, X. Cui, C. D. Sewell, J. Li, and Z. Lin, "Recent Advances in Activating Surface Reconstruction for the High-Efficiency Oxygen Evolution Reaction," *Chemical Society Reviews* 50 (2021): 8428–8469, https://doi.org/10.1039/d0cs00962h.

208. X. Liu, J. Meng, J. Zhu, et al., "Comprehensive Understandings Into Complete Reconstruction of Precatalysts: Synthesis, Applications, and Characterizations," *Advanced Materials* 33 (2021): 2007344, https://doi.org/10.1002/adma.202007344.

209. X. Liu, Y. Bao, L. Yuan, H. Zhao, W. Tian, and J. Ji, "From Activity to Stability: Dissolution-Mediated Surface Reconstruction and Redeposition in Transition Metal-Based Electrocatalysts," *Journal of Materials Chemistry A* 13 (2025): 35024–35053, https://doi.org/10.1039/d5ta05671c.

210. C. Yang, Z. Dai, J. Yue, G. Wang, and W. Luo, "Dynamic Surface Reconstruction Engineers Interfacial Water Structure for Efficient Alkaline Hydrogen Oxidation," *Chemical Science* 16 (2025): 5266–5274, https://doi.org/10.1039/d4sc08139k.

211. P. Fang, M. Zhu, J. Liu, Z. Zhu, J. Hu, and X. Xu, "Making Ternary-Metal Hydroxysulfide Catalyst via Cathodic Reconstruction With Ion Regulation for Industrial-Level Hydrogen Generation," *Advanced Energy Materials* 13 (2023): 2301222, https://doi.org/10.1002/aenm.202301222.

212. B. Chang, X. Liu, S. Zuo, et al., "Dynamic Construction of a Durable Epitaxial Catalytic Layer for Industrial Alkaline Water Splitting," *Nature Communications* 16 (2025): 7959, https://doi.org/10.1038/s41467-025-63361-x.

213. Y. Xie, Y. Sun, H. Tao, et al., "In Situ Investigation on Life-Time Dynamic Structure–Performance Correlation toward Electrocatalyst Service Behavior in Water Splitting," *Advanced Functional Materials* 32 (2022): 2111777, https://doi.org/10.1002/adfm.202111777.

214. K. Pang, C. Long, Y. Zhang, et al., "In Situ Time-Resolved X-Ray Absorption Spectroscopy Unveils Partial Re-Oxidation of Tellurium Cluster for Prolonged Lifespan in Hydrogen Evolution," *Journal of the American Chemical Society* 147 (2025): 14359–14368, https://doi.org/10.1021/jacs.5c00167.

215. X. Liu, R. Guo, K. Ni, et al., "Reconstruction-Determined Alkaline Water Electrolysis at Industrial Temperatures," *Advanced Materials* 32 (2020): 2001136, https://doi.org/10.1002/adma.202001136.

216. Y. Song, H. Chen, X. Wang, et al., "Engineering Ir-Based Catalysts for High Current Density Applications in Proton Exchange Membrane Water Electrolyzers," *Energy & Environmental Science* 18 (2025): 130–154, https://doi.org/10.1039/d4ee03541k.

217. W. Zhai, Y. Ma, D. Chen, J. C. Ho, Z. Dai, and Y. Qu, "Recent Progress on the Long-Term Stability of Hydrogen Evolution Reaction Electrocatalysts," *InfoMat* 4 (2022): 12357, https://doi.org/10.1002/inf2.12357.

218. L. Wu, L. Yu, F. Zhang, et al., "Heterogeneous Bimetallic Phosphide Ni_2P-Fe_2P as an Efficient Bifunctional Catalyst for Water/Seawater Splitting," *Advanced Functional Materials* 31 (2020): 2006484, https://doi.org/10.1002/adfm.202006484.

219. M. Ning, F. Zhang, L. Wu, et al., "Boosting Efficient Alkaline Fresh Water and Seawater Electrolysis via Electrochemical Reconstruction," *Energy & Environmental Science* 15 (2022): 3945–3957, https://doi.org/10.1039/d2ee01094a.

220. J. T. Ren, L. Chen, H. Y. Wang, and Z. Y. Yuan, "High-Entropy Alloys in Electrocatalysis: From Fundamentals to Applications," *Chemical Society Reviews* 52 (2023): 8319–8373, https://doi.org/10.1039/d3cs00557g.

221. Y. Liu, H. Shi, T. Y. Dai, et al., "In Situ Engineering Multifunctional Active Sites of Ruthenium-Nickel Alloys for pH-Universal Ampere-Level Current-Density Hydrogen Evolution," *Small* 20 (2024): 2311509, https://doi.org/10.1002/smll.202311509.

222. G. Qian, Y. Wang, L. Li, et al., "Strategies for Tuning Tensile Strain and Localized Electrons in a Mo-Doped NiCoCu Alloy for Enhancing Ampere-Level Current Density HER Performance," *Advanced Functional Materials* 34 (2024): 2404055, https://doi.org/10.1002/adfm.202404055.

223. D. Gao, J. Guo, H. He, P. Xiao, and Y. Zhang, "Geometric and Electronic Modulation of Fcc NiCo Alloy by Group-VI B Metal Doping to Accelerate Hydrogen Evolution Reaction in Acidic and Alkaline Media," *Chemical Engineering Journal* 430 (2022): 133110, https://doi.org/10.1016/j.cej.2021.133110.

224. Q. Gao, Z. Wang, W. Gao, and H. Yin, "NiFeCo-Based High Entropy Alloys Nanoparticles Coated With N-Doped Graphene Layers as Hydrogen Evolution Catalyst in Alkaline Solution," *Chemical Engineering Journal* 489 (2024): 151370, https://doi.org/10.1016/j.cej.2024.151370.

225. A. Chandran M, P. Dutta, P. Singh, A. K. Singh, and B. L. V. Prasad, "Design and Synthesis of PtPdNiCoMn High-Entropy Alloy Electrocatalyst for Enhanced Alkaline Hydrogen Evolution Reaction: A Theoretically Supported Predictive Design Approach," *Advanced Functional Materials* 35 (2024): 2418644, https://doi.org/10.1002/adfm.202418644.

226. S. Liu, Y. Wang, T. Jiang, et al., "Non-Noble Metal High-Entropy Alloy-Based Catalytic Electrode for Long-Life Hydrogen Gas Batteries," *ACS Nano* 18 (2024): 4229–4240, https://doi.org/10.1021/acsnano.3c09482.

227. Z. Li, S. Xin, Y. Zhang, et al., "Boosting Elementary Steps Kinetics Towards Energetic Alkaline Hydrogen Evolution via Dual Sites on Phase-Separated Ni–Cu–Mn/Hydroxide," *Chemical Engineering Journal* 451 (2023): 138540, https://doi.org/10.1016/j.cej.2022.138540.

228. Y. Zhu, X. Wu, Z. Wu, et al., "Europium Oxide Evoked Multisite Synergism to Facilitate Water Dissociation for Alkaline Hydrogen Evolution," *Advanced Functional Materials* 34 (2024): 2409324, https://doi.org/10.1002/adfm.202409324.

229. X. Yang, W. Guo, H. Xi, et al., "Engineering N—TM(Co/Fe)—P Interfacial Electron Bridge in Transition Metal Phosphide/Nitride Heterostructure Nanoarray for Highly Active and Durable Hydrogen Evolution in Large-Current Seawater Electrolysis," *Advanced Functional Materials* (2025): 2505078, https://doi.org/10.1002/adfm.202505078.

230. C. C. Weng, J. T. Ren, and Z. Y. Yuan, "Transition Metal Phosphide-Based Materials for Efficient Electrochemical Hydrogen Evolution: A Critical Review," *Chemsuschem* 13 (2020): 3357–3375, https://doi.org/10.1002/cssc.202000416.

231. H. Y. Wang, F. Yan, H. Wang, et al., "The Combination of Electronic Structure and Lattice Strain Engineering for Multi-Powered Hydrazine-Assisted Seawater Electrolysis System at High Current Densities," *Advanced Energy Materials* 14 (2024): 2402611, https://doi.org/10.1002/aenm.202402611.

232. H. J. Niu, C. Huang, T. Sun, et al., "Enhancing Ni/Co Activity by Neighboring Pt Atoms in NiCoP/MXene Electrocatalyst for Alkaline Hydrogen Evolution," *Angewandte Chemie International Edition* 63 (2024): 202401819, https://doi.org/10.1002/anie.202401819.

233. S. Wang, Z. Geng, S. Bi, et al., "Recent Advances and Future Prospects on Ni_3S_2-Based Electrocatalysts for Efficient Alkaline Water Electrolysis," *Green Energy & Environment* 9 (2024): 659–683, https://doi.org/10.1016/j.gee.2023.02.011.

234. Z. Wu, Y. Feng, Z. Qin, et al., "Bimetallic Multi-Level Layered Co-NiOOH/Ni_3S_2@NF Nanosheet for Hydrogen Evolution Reaction in Alkaline Medium," *Small* 18 (2022): 2106904, https://doi.org/10.1002/smll.202106904.

235. P. Wang, T. Wang, R. Qin, et al., "Swapping Catalytic Active Sites From Cationic Ni to Anionic S in Nickel Sulfide Enables More Efficient Alkaline Hydrogen Generation," *Advanced Energy Materials* 12 (2022): 2103359, https://doi.org/10.1002/aenm.202103359.

236. K. Zhang, Y. Duan, N. Graham, and W. Yu, "Unveiling the Synergy of Polymorph Heterointerface and Sulfur Vacancy in NiS/Ni_3S_2 Electrocatalyst to Promote Alkaline Hydrogen Evolution Reaction," *Applied Catalysis B: Environmental* 323 (2023): 122144, https://doi.org/10.1016/j.apcatb.2022.122144.

237. X. Teng, Z. Wang, Y. Wu, et al., "Enhanced Alkaline Hydrogen Evolution Reaction of MoO_2/Ni_3S_2 Nanorod Arrays by Interface Engineering," *Nano Energy* 122 (2024): 109299, https://doi.org/10.1016/j.nanoen.2024.109299.

238. S. Huang, Y. Meng, Y. Cao, et al., "Amorphous $NiWO_4$ Nanoparticles Boosting the Alkaline Hydrogen Evolution Performance of Ni_3S_2 Electrocatalysts," *Applied Catalysis B: Environmental* 274 (2020): 119120, https://doi.org/10.1016/j.apcatb.2020.119120.

239. X. Ding, D. Liu, P. Zhao, et al., "Dynamic Restructuring of Nickel Sulfides for Electrocatalytic Hydrogen Evolution Reaction," *Nature Communications* 15 (2024): 5336, https://doi.org/10.1038/s41467-024-49015-4.

240. M. Li, H. Li, H. Fan, et al., "Engineering Interfacial Sulfur Migration in Transition-metal Sulfide Enables Low Overpotential for Durable Hydrogen Evolution in Seawater," *Nature Communications* 15 (2024): 6154, https://doi.org/10.1038/s41467-024-50535-2.

241. Y. Huang, L. W. Jiang, B. Y. Shi, K. M. Ryan, and J. J. Wang, "Highly Efficient Oxygen Evolution Reaction Enabled by Phosphorus Doping of the Fe Electronic Structure in Iron–Nickel Selenide Nanosheets," *Advanced Science* 8 (2021): 2101775, https://doi.org/10.1002/advs.202101775.

242. K. Wu, C. Lyu, J. Cheng, et al., "Modulating Electronic Structure by Etching Strategy to Construct $NiSe_2$/$Ni_{0.85}Se$ Heterostructure for Urea-Assisted Hydrogen Evolution Reaction," *Small* 20 (2024): 2304390, https://doi.org/10.1002/smll.202304390.

243. L. Tan, J. Yu, H. Wang, et al., "Controllable Synthesis and Phase-Dependent Catalytic Performance of Dual-Phase Nickel Selenides on Ni Foam for Overall Water Splitting," *Applied Catalysis B: Environmental* 303 (2022): 120915, https://doi.org/10.1016/j.apcatb.2021.120915.

244. D. Cao, J. Shao, Y. Cui, L. Zhang, and D. Cheng, "Interfacial Engineering of Copper–Nickel Selenide Nanodendrites for Enhanced Overall Water Splitting in Alkali Condition," *Small* 19 (2023): 2301613, https://doi.org/10.1002/smll.202301613.

245. Q. Gao, W. Zhang, Z. Shi, L. Yang, and Y. Tang, "Structural Design and Electronic Modulation of Transition-Metal-Carbide Electrocatalysts

Toward Efficient Hydrogen Evolution," *Advanced Materials* 31 (2019): 1802880, https://doi.org/10.1002/adma.201802880.

246. Q. Zhang, Z. Jiang, B. M. Tackett, et al., "Trends and Descriptors of Metal-Modified Transition Metal Carbides for Hydrogen Evolution in Alkaline Electrolyte," *ACS Catalysis* 9 (2019): 2415–2422, https://doi.org/10.1021/acscatal.8b03990.

247. J. He, L. Luo, J. Li, et al., "Exploiting Lattice Carbon-Induced Modulation Effect in Nickel Towards Efficient Alkaline Hydrogen Oxidation," *Angewandte Chemie International Edition* 137 (2025): 202423647, https://doi.org/10.1002/anie.202423647.

248. K. Dastafkan, X. Shen, R. K. Hocking, Q. Meyer, and C. Zhao, "Monometallic Interphasic Synergy via Nano-Hetero-Interfacing for Hydrogen Evolution in Alkaline Electrolytes," *Nature Communications* 14 (2023): 547, https://doi.org/10.1038/s41467-023-36100-3.

249. N. Yao, P. Li, Z. Zhou, et al., "Synergistically Tuning Water and Hydrogen Binding Abilities over Co_4N by Cr Doping for Exceptional Alkaline Hydrogen Evolution Electrocatalysis," *Advanced Energy Materials* 9 (2019): 1902449, https://doi.org/10.1002/aenm.201902449.

250. F. Song, W. Li, J. Yang, G. Han, P. Liao, and Y. Sun, "Interfacing Nickel Nitride and Nickel Boosts Both Electrocatalytic Hydrogen Evolution and Oxidation Reactions," *Nature Communications* 9 (2018): 4531, https://doi.org/10.1038/s41467-018-06728-7.

251. J. Zhang, L. Zhang, L. Du, H. L. Xin, J. B. Goodenough, and Z. Cui, "Composition-Tunable Antiperovskite $Cu_xIn_{1-x}NNi_3$ as Superior Electrocatalysts for the Hydrogen Evolution Reaction," *Angewandte Chemie International Edition* 59 (2020): 17488–17493, https://doi.org/10.1002/anie.202007883.

252. X. Ai, X. Zou, H. Chen, et al., "Transition-Metal–Boron Intermetallics With Strong Interatomic d–sp Orbital Hybridization for High-Performance Electrocatalysis," *Angewandte Chemie International Edition* 59 (2020): 3961–3965, https://doi.org/10.1002/anie.201915663.

253. H. Liu, X. Li, L. Chen, et al., "Monolithic Ni-Mo-B Bifunctional Electrode for Large Current Water Splitting," *Advanced Functional Materials* 32 (2022): 2107308, https://doi.org/10.1002/adfm.202107308.

254. H. Xiong, C. Du, Z. Ma, et al., "Rational Design of Multiple Heterostructures With Synergistic Effect for Efficient and Stable Hydrogen Evolution Toward Industrial Alkaline Water Splitting," *Advanced Functional Materials* 34 (2024): 2402298, https://doi.org/10.1002/adfm.202402298.

255. Q. Zhang, W. Xiao, J. X. Shi, et al., "Dynamic Molybdate Oxyanion Boosts Self-Optimization and Self-Healing on the NiMoFe Heterostructure for Water Splitting in Alkaline Media," *ACS Catalysis* 14 (2024): 18003–18017, https://doi.org/10.1021/acscatal.4c05108.

256. Y. Yang, P. Li, X. Zheng, et al., "Anion-Exchange Membrane Water Electrolyzers and Fuel Cells," *Chemical Society Reviews* 51 (2022): 9620–9693, https://doi.org/10.1039/D2CS00038E.

257. D. Xu, M. B. Stevens, M. R. Cosby, et al., "Earth-Abundant Oxygen Electrocatalysts for Alkaline Anion-Exchange-Membrane Water Electrolysis: Effects of Catalyst Conductivity and Comparison With Performance in Three-Electrode Cells," *ACS Catalysis* 9 (2019): 7–15, https://doi.org/10.1021/acscatal.8b04001.

258. A. Y. Faid and S. Sunde, "Anion Exchange Membrane Water Electrolysis From Catalyst Design to the Membrane Electrode Assembly," *Energy Technology* 10 (2022): 2200506, https://doi.org/10.1002/ente.202200506.

259. E. Amores, J. Rodríguez, J. Oviedo, and A. de Lucas-Consuegra, "Development of an Operation Strategy for Hydrogen Production Using Solar PV Energy Based on Fluid Dynamic Aspects," *Open Engineering* 7 (2017): 141–152, https://doi.org/10.1515/eng-2017-0020.

260. P. M. Diéguez, A. Ursúa, P. Sanchis, C. Sopena, E. Guelbenzu, and L. M. Gandía, "Thermal Performance of a Commercial Alkaline Water Electrolyzer: Experimental Study and Mathematical Modeling," *International Journal of Hydrogen Energy* 33 (2008): 7338–7354, https://doi.org/10.1016/j.ijhydene.2008.09.051.

261. I. Vincent, A. Kruger, and D. Bessarabov, "Development of Efficient Membrane Electrode Assembly for Low Cost Hydrogen Production by Anion Exchange Membrane Electrolysis," *International Journal of Hydrogen Energy* 42 (2017): 10752–10761, https://doi.org/10.1016/j.ijhydene.2017.03.069.

262. J. Hnát, M. Plevová, J. Žitka, M. Paidar, and K. Bouzek, "Anion-Selective Materials With 1,4-diazabicyclo[2.2.2]Octane Functional Groups for Advanced Alkaline Water Electrolysis," *Electrochimica Acta* 248 (2017): 547–555, https://doi.org/10.1016/j.electacta.2017.07.165.

263. C. C. Pavel, F. Cecconi, C. Emiliani, et al., "Highly Efficient Platinum Group Metal Free Based Membrane-Electrode Assembly for Anion Exchange Membrane Water Electrolysis," *Angewandte Chemie International Edition* 53 (2014): 1378–1381, https://doi.org/10.1002/anie.201308099.

264. M. Faraj, M. Boccia, H. Miller, et al., "New LDPE Based Anion-Exchange Membranes for Alkaline Solid Polymeric Electrolyte Water Electrolysis," *International Journal of Hydrogen Energy* 37 (2012): 14992–15002, https://doi.org/10.1016/j.ijhydene.2012.08.012.

265. I. V. Pushkareva, A. S. Pushkarev, S. A. Grigoriev, P. Modisha, and D. G. Bessarabov, "Comparative Study of Anion Exchange Membranes for Low-Cost Water Electrolysis," *International Journal of Hydrogen Energy* 45 (2020): 26070–26079, https://doi.org/10.1016/j.ijhydene.2019.11.011.

266. N. Yang, H. Li, X. Lin, et al., "Catalytic Electrode Comprising a Gas Diffusion Layer and Bubble-involved Mass Transfer in Anion Exchange Membrane Water Electrolysis: a Critical Review and Perspectives," *Journal of Energy Chemistry* 105 (2025): 669–701, https://doi.org/10.1016/j.jechem.2024.12.073.

267. L. Wan, J. Liu, D. Lin, et al., "3D-Ordered Catalytic Nanoarrays Interlocked on Anion Exchange Membranes for Water Electrolysis," *Energy & Environmental Science* 17 (2024): 3396–3408, https://doi.org/10.1039/d4ee00003j.

268. R. A. Marquez, M. Espinosa, E. Kalokowski, et al., "A Guide to Electrocatalyst Stability Using Lab-Scale Alkaline Water Electrolyzers," *ACS Energy Letters* 9 (2024): 547–555, https://doi.org/10.1021/acsenergylett.3c02758.

269. Y. S. Park, J. H. Lee, M. J. Jang, et al., "Co_3S_4 Nanosheets on Ni Foam via Electrodeposition With Sulfurization as Highly Active Electrocatalysts for Anion Exchange Membrane Electrolyzer," *International Journal of Hydrogen Energy* 45 (2020): 36–45, https://doi.org/10.1016/j.ijhydene.2019.10.169.

270. Y. Zheng, W. Ma, A. Serban, A. Allushi, and X. Hu, "Anion Exchange Membrane Water Electrolysis at 10 $A{\cdot}cm^{-2}$ Over 800 h," *Angewandte Chemie International Edition* 64 (2025): 202413698, https://doi.org/10.1002/anie.202413698.

271. W. Y. Noh, S. J. Kazmouz, S.-H. Lee, J.-K. Peng, T. J. Shin, and M. Shviro, "Decoupling Electrode Kinetics to Elucidate Reaction Mechanisms in Alkaline Water Electrolysis," *Energy & Environmental Science* 18 (2025): 8679–8696, https://doi.org/10.1039/d5ee03044g.

272. K. H. Lee, D. H. Cho, Y. M. Kim, et al., "Highly Conductive and Durable Poly(Arylene Ether Sulfone) Anion Exchange Membrane With End-Group Cross-Linking," *Energy & Environmental Science* 10 (2017): 275–285, https://doi.org/10.1039/c6ee03079c.

273. T. Wang, Y. Wang, and W. You, "Dithiol Cross-Linked Polynorbornene-Based Anion-Exchange Membranes With High Hydroxide Conductivity and Alkaline Stability," *Journal of Membrane Science* 685 (2023): 121916, https://doi.org/10.1016/j.memsci.2023.121916.

274. J. Fan, S. Willdorf-Cohen, E. M. Schibli, et al., "Poly(Bis-Arylimidazoliums) Possessing High Hydroxide Ion Exchange Capacity and High Alkaline Stability," *Nature Communications* 10 (2019): 2306, https://doi.org/10.1038/s41467-019-10292-z.

275. X. Zou, G. Xu, P. Fang, et al., "Unsupervised Learning-Guided Accelerated Discovery of Alkaline Anion Exchange Membranes for Fuel Cells," *Angewandte Chemie International Edition* 62 (2023): 202300388, https://doi.org/10.1002/anie.202300388.

276. W. You, E. Padgett, S. N. MacMillan, D. A. Muller, and G. W. Coates, "Highly Conductive and Chemically Stable Alkaline Anion Exchange Membranes via ROMP of Trans-Cyclooctene Derivatives," *Proceedings of the National Academy of Sciences* 116 (2019): 9729–9734, https://doi.org/10.1073/pnas.1900988116.

277. X. Liu, N. Xie, J. Xue, et al., "Magnetic-Field-Oriented Mixed-Valence-Stabilized Ferrocenium Anion-Exchange Membranes for Fuel Cells," *Nature Energy* 7 (2022): 329–339, https://doi.org/10.1038/s41560-022-00978-y.

278. Z. Xu, Y. Liao, M. Pang, et al., "A Chemically Interlocked Bipolar Membrane Achieving Stable Water Dissociation for High Output Ammonia Electrosynthesis," *Energy & Environmental Science* 16 (2023): 3815–3824, https://doi.org/10.1039/d3ee00885a.

279. N. Chen and Y. M. Lee, "Anion Exchange Polyelectrolytes for Membranes and Ionomers," *Progress in Polymer Science* 113 (2021): 101345, https://doi.org/10.1016/j.progpolymsci.2020.101345.

280. A. Shirwalkar, M. Kaur, S. Zhong, et al., "Comparing Intrinsic Catalytic Activity and Practical Performance of Ni- and Pt-Based Alkaline Anion Exchange Membrane Water Electrolyzer Cathodes," *ACS Energy Letters* 10 (2025): 1779–1785, https://doi.org/10.1021/acsenergylett.5c00439.

281. Y. Uchino, T. Kobayashi, S. Hasegawa, et al., "Dependence of the Reverse Current on the Surface of Electrode Placed on a Bipolar Plate in an Alkaline Water Electrolyzer," *Electrochemistry* 86 (2018): 138–144, https://doi.org/10.5796/electrochemistry.17-00102.

282. Y. Uchino, T. Kobayashi, S. Hasegawa, et al., "Relationship Between the Redox Reactions on a Bipolar Plate and Reverse Current after Alkaline Water Electrolysis," *Electrocatalysis* 9 (2017): 67–74, https://doi.org/10.1007/s12678-017-0423-5.

283. S. M. Jung, Y. Kim, B. J. Lee, et al., "Reverse-Current Tolerance for Hydrogen Evolution Reaction Activity of Lead-Decorated Nickel Catalysts in Zero-Gap Alkaline Water Electrolysis Systems," *Advanced Functional Materials* 34 (2024): 2316150, https://doi.org/10.1002/adfm.202316150.

284. A. Abdel Haleem, J. Huyan, K. Nagasawa, et al., "Effects of Operation and Shutdown Parameters and Electrode Materials on the Reverse Current Phenomenon in Alkaline Water Analyzers," *Journal of Power Sources* 535 (2022): 231454, https://doi.org/10.1016/j.jpowsour.2022.231454.

285. Y. Kim, S. M. Jung, K. S. Kim, et al., "Cathodic Protection System Against a Reverse-Current After Shut-Down in Zero-Gap Alkaline Water Electrolysis," *JACS Au* 2 (2022): 2491–2500, https://doi.org/10.1021/jacsau.2c00314.

286. N. Guruprasad, J. van der Schaaf, and M. T. de Groot, "Unraveling the Impact of Reverse Currents on Electrode Stability in Anion Exchange Membrane Water Electrolysis," *Journal of Power Sources* 613 (2024): 234877, https://doi.org/10.1016/j.jpowsour.2024.234877.

287. S. Holmin, L.-Å. Näslund, Á. S. Ingason, J. Rosen, and E. Zimmerman, "Corrosion of Ruthenium Dioxide Based Cathodes in Alkaline Medium Caused by Reverse Currents," *Electrochimica Acta* 146 (2014): 30–36, https://doi.org/10.1016/j.electacta.2014.09.024.

288. C. Liu, B. Lin, H. Zhang, et al., "Influence of Power Fluctuation on Ni-Based Electrode Degradation and Hydrogen Evolution Reaction Performance in Alkaline Water Splitting: Probing the Effect of Renewable Energy on Water Electrolysis," *Catalysts* 14 (2024): 307, https://doi.org/10.3390/catal14050307.

289. S. Narayanaru, S. Miyanishi, H. Kuroki, G. M. Anilkumar, and T. Yamaguchi, "Start–Stop Cyclic Durability Analysis of Membrane–Electrode Assemblies Using Polyflourene-Based Electrolytes for an Anion-Exchange Membrane Water Electrolyzer," *ACS Sustainable Chemistry & Engineering* 11 (2023): 9295–9302, https://doi.org/10.1021/acssuschemeng.2c07387.

290. J. C. Ehlers, A. A. Feidenhans'l, K. T. Therkildsen, and G. O. Larrazábal, "Affordable Green Hydrogen From Alkaline Water Electrolysis: Key Research Needs From an Industrial Perspective," *ACS Energy Letters* 8 (2023): 1502–1509, https://doi.org/10.1021/acsenergylett.2c02897.

291. T. H. M. Pham, T. H. Shen, Y. Ko, et al., "Elucidating the Mechanism of Fe Incorporation in In Situ Synthesized Co–Fe Oxygen-Evolving Nanocatalysts," *Journal of the American Chemical Society* 145 (2023): 23691–23701, https://doi.org/10.1021/jacs.3c08099.

292. H. Li, Y. Zhang, Y. Chen, et al., "Leveraging Iron in the Electrolyte to Improve Oxygen Evolution Reaction Performance: Fundamentals, Strategies, and Perspectives," *Angewandte Chemie International Edition* 64 (2025): 202423071, https://doi.org/10.1002/anie.202423071.

293. S. Anantharaj, S. Kundu, and S. Noda, ""The Fe Effect": A Review Unveiling the Critical Roles of Fe in Enhancing OER Activity of Ni and Co Based Catalysts," *Nano Energy* 80 (2021): 105514, https://doi.org/10.1016/j.nanoen.2020.105514.

294. A. Bukowski, P.-Y. Olu, A. Gering, M. Chatenet, and A. Bonnefont, "Dissolved Iron in Alkaline Media: Techniques and Insights for Understanding Its Effects on Water-Splitting Reactions," *Current Opinion in Electrochemistry* 47 (2024): 101568, https://doi.org/10.1016/j.coelec.2024.101568.

295. M. Demnitz, Y. M. Lamas, R. L. Garcia Barros, A. de Leeuw den Bouter, and J. van der Schaaf, "Effect of Iron Addition to the Electrolyte on Alkaline Water Electrolysis Performance," *Iscience* 27 (2024): 108695, https://doi.org/10.1016/j.isci.2023.108695.

296. N. Li, S. S. Araya, X. Cui, and S. K. Kær, "The Effects of Cationic Impurities on the Performance of Proton Exchange Membrane Water Electrolyzer," *Journal of Power Sources* 473 (2020): 228617, https://doi.org/10.1016/j.jpowsour.2020.228617.

297. N. Li, S. S. Araya, and S. K. Kær, "The Effect of Fe^{3+} Contamination in Feed Water on Proton Exchange Membrane Electrolyzer Performance," *International Journal of Hydrogen Energy* 44 (2019): 12952–12957, https://doi.org/10.1016/j.ijhydene.2019.04.015.

298. H. Becker, J. Murawski, D. V. Shinde, I. E. L. Stephens, G. Hinds, and G. Smith, "Impact of Impurities on Water Electrolysis: A Review," *Sustainable Energy & Fuels* 7 (2023): 1565–1603, https://doi.org/10.1039/d2se01517j.

299. R. A. Krivina, G. A. Lindquist, S. R. Beaudoin, et al., "Anode Catalysts in Anion-Exchange-Membrane Electrolysis Without Supporting Electrolyte: Conductivity, Dynamics, and Ionomer Degradation," *Advanced Materials* 34 (2022): 2203033, https://doi.org/10.1002/adma.202203033.

300. Y. Ou, L. P. Twight, B. Samanta, et al., "Cooperative Fe Sites on Transition Metal (oxy)Hydroxides Drive High Oxygen Evolution Activity in Base," *Nature Communications* 14 (2023): 7688, https://doi.org/10.1038/s41467-023-43305-z.

301. C. Kuai, Z. Xu, C. Xi, et al., "Phase Segregation Reversibility in Mixed-metal Hydroxide Water Oxidation Catalysts," *Nature Catalysis* 3 (2020): 743–753, https://doi.org/10.1038/s41929-020-0496-z.

302. S. Kang, C. Im, I. Spanos, et al., "Durable Nickel-Iron (Oxy)Hydroxide Oxygen Evolution Electrocatalysts Through Surface Functionalization With Tetraphenylporphyrin," *Angewandte Chemie International Edition* 61 (2022): 202214541, https://doi.org/10.1002/anie.202214541.

303. D. Y. Chung, P. P. Lopes, P. Farinazzo Bergamo Dias Martins, et al., "Dynamic Stability of Active Sites in Hydr(oxy)Oxides for the Oxygen Evolution Reaction," *Nature Energy* 5 (2020): 222–230, https://doi.org/10.1038/s41560-020-0576-y.

304. P. P. Lopes, D. Y. Chung, X. Rui, et al., "Dynamically Stable Active Sites From Surface Evolution of Perovskite Materials During the Oxygen Evolution Reaction," *Journal of the American Chemical Society* 143 (2021): 2741–2750, https://doi.org/10.1021/jacs.0c08959.

305. Y. Yang, C. R. Peltier, R. Zeng, et al., "Electrocatalysis in Alkaline Media and Alkaline Membrane-Based Energy Technologies," *Chemical Reviews* 122 (2022): 6117–6321, https://doi.org/10.1021/acs.chemrev.1c00331.

306. N. Chen, Y. Jin, H. Liu, et al., "Insight Into the Alkaline Stability of N-Heterocyclic Ammonium Groups for Anion-Exchange Polyelectrolytes,"

Angewandte Chemie International Edition 60 (2021): 19272–19280, https://doi.org/10.1002/anie.202105231.

307. C. Hu, Y. Wang, and Y. M. Lee, "Ether-Free Alkaline Polyelectrolytes for Water Electrolyzers: Recent Advances and Perspectives," *Angewandte Chemie International Edition* 64 (2025): 202418324, https://doi.org/10.1002/anie.202418324.

308. J. Hyun, S. Hwan Yang, D. Wook Lee, et al., "Impact of the Binding Ability of Anion Exchange Ionomer on the Initial Performance Degradation of Anion Exchange Membrane Water Electrolyzers," *Chemical Engineering Journal* 469 (2023): 143919, https://doi.org/10.1016/j.cej.2023.143919.

309. L. Hager, M. Hegelheimer, J. Stonawski, et al., "Novel Side Chain Functionalized Polystyrene/O-PBI Blends With High Alkaline Stability for Anion Exchange Membrane Water Electrolysis (AEMWE)," *Journal of Materials Chemistry A* 11 (2023): 22347–22359, https://doi.org/10.1039/d3ta02978f.

310. N. Du, C. Roy, R. Peach, M. Turnbull, S. Thiele, and C. Bock, "Anion-Exchange Membrane Water Electrolyzers," *Chemical Reviews* 122 (2022): 11830–11895, https://doi.org/10.1021/acs.chemrev.1c00854.

311. D. Li, A. R. Motz, C. Bae, et al., "Durability of Anion Exchange Membrane Water Electrolyzers," *Energy & Environmental Science* 14 (2021): 3393–3419, https://doi.org/10.1039/d0ee04086j.

312. Z. Feng, G. Gupta, and M. Mamlouk, "Degradation of QPPO-Based Anion Polymer Electrolyte Membrane at Neutral pH," *RSC Advances* 13 (2023): 20235–20242, https://doi.org/10.1039/d3ra02889e.

313. J. Parrondo, Z. Wang, M. S. Jung, and V. Ramani, "Reactive Oxygen Species Accelerate Degradation of Anion Exchange Membranes Based on Polyphenylene Oxide in Alkaline Environments," *Physical Chemistry Chemical Physics* 18 (2016): 19705–19712, https://doi.org/10.1039/c6cp01978a.

314. T. Tang, H. Lee, Z. Wang, et al., "Bioinspired Anion Exchange Membranes With Dual Steric Cross-Linking Centers for Industrial-Scale Water Electrolysis," *Energy & Environmental Science* 17 (2024): 7816–7828, https://doi.org/10.1039/d4ee02428a.

315. L. Yin, R. Ren, L. He, et al., "Polyarylmethylpiperidinium (PAMP) for Next Generation Anion Exchange Membranes," *Angewandte Chemie International Edition* 64 (2025): 202503715, https://doi.org/10.1002/anie.202503715.

316. B. Chen, P. Mardle, and S. Holdcroft, "Probing the Effect of Ionomer Swelling on the Stability of Anion Exchange Membrane Water Electrolyzers," *Journal of Power Sources* 550 (2022): 232134, https://doi.org/10.1016/j.jpowsour.2022.232134.

317. F. Liu, K. Miyatake, M. Tanabe, et al., "High-Performance Anion Exchange Membrane Water Electrolyzers Enabled by Highly Gas Permeable and Dimensionally Stable Anion Exchange Ionomers," *Advanced Science* 11 (2024): 2402969, https://doi.org/10.1002/advs.202402969.

318. C. Hu, Y. J. Lee, J. Y. Sohn, H. Hwang, S. W. Jung, and Y. M. Lee, "ETFE-Grafting Ionomers for Anion Exchange Membrane Water Electrolyzers With a Current Density of 11.2 A cm^{-2}," *Journal of Power Sources* 599 (2024): 234228, https://doi.org/10.1016/j.jpowsour.2024.234228.

319. J. Hyun, G. Doo, E. Oh, et al., "Anode Reinforcement by Polydopamine Glue in Anion Exchange Membrane Water Electrolysis," *ACS Energy Letters* 8 (2023): 5240–5247, https://doi.org/10.1021/acsenergylett.3c02205.

320. G. Huang, M. Mandal, N. U. Hassan, et al., "Ionomer Optimization for Water Uptake and Swelling in Anion Exchange Membrane Electrolyzer: Oxygen Evolution Electrode," *Journal of The Electrochemical Society* 167 (2020): 164514, https://doi.org/10.1149/1945-7111/abcde3.

321. R. R. Raja Sulaiman, W. Y. Wong, and K. S. Loh, "Recent Developments on Transition Metal–Based Electrocatalysts for Application in Anion Exchange Membrane Water Electrolysis," *International Journal of Energy Research* 46 (2021): 2241–2276, https://doi.org/10.1002/er.7380.

322. D. Hochfilzer, I. Chorkendorff, and J. Kibsgaard, "Catalyst Stability Considerations for Electrochemical Energy Conversion With Non-Noble Metals: Do We Measure on What We Synthesized?," *ACS Energy Letters* 8 (2023): 1607–1612, https://doi.org/10.1021/acsenergylett.3c00021.

323. F.-Y. Chen, Z.-Y. Wu, Z. Adler, and H. Wang, "Stability Challenges of Electrocatalytic Oxygen Evolution Reaction: From Mechanistic Understanding to Reactor Design," *Joule* 5 (2021): 1704–1731, https://doi.org/10.1016/j.joule.2021.05.005.

324. A. J. Martín, S. Mitchell, C. Mondelli, S. Jaydev, and J. Pérez-Ramírez, "Unifying Views on Catalyst Deactivation," *Nature Catalysis* 5 (2022): 854–866, https://doi.org/10.1038/s41929-022-00842-y.

325. J. Lei, Z. Wang, Y. Zhang, et al., "Understanding and Resolving the Heterogeneous Degradation of Anion Exchange Membrane Water Electrolysis for Large-Scale Hydrogen Production," *Carbon Neutrality* 3 (2024): 25, https://doi.org/10.1007/s43979-024-00101-y.

326. J. E. Park, S. Y. Kang, S.-H. Oh, et al., "High-Performance Anion-exchange Membrane Water Electrolysis," *Electrochimica Acta* 295 (2019): 99–106, https://doi.org/10.1016/j.electacta.2018.10.143.

327. J. Hyun and H.-T. Kim, "Powering the Hydrogen Future: Current Status and Challenges of Anion Exchange Membrane Fuel Cells," *Energy & Environmental Science* 16 (2023): 5633–5662, https://doi.org/10.1039/d3ee01768k.

328. A. Konovalova, A. C. Goldman, R. Shekhar, et al., "Pathways to Electrochemical Ironmaking at Scale via the Direct Reduction of Fe_2O_3," *ACS Energy Letters* 10 (2025): 1851–1857, https://doi.org/10.1021/acsenergylett.5c00166.

329. W. E. Mustain, M. Chatenet, M. Page, and Y. S. Kim, "Durability Challenges of Anion Exchange Membrane Fuel Cells," *Energy & Environmental Science* 13 (2020): 2805–2838, https://doi.org/10.1039/d0ee01133a.

330. R. A. Krivina, C. Capuano, K. E. Ayers, and S. W. Boettcher, "Performance Degradation in Alkaline-Membrane Electrolyzers," *ECS Meeting Abstracts* MA2020-02 (2020): 2438, https://doi.org/10.1149/MA2020-02382438mtgabs.

331. H. Wang, Y. Tong, K. Li, and P. Chen, "Heterostructure Engineering of Iridium Species on Nickel/Molybdenum Nitride for Highly-Efficient Anion Exchange Membrane Water Electrolyzer," *Journal of Colloid and Interface Science* 628 (2022): 306–314, https://doi.org/10.1016/j.jcis.2022.08.056.

332. S. E. Jun, S.-W. Myeong, B.-G. Cho, et al., "Exsolved Ru-Mediated Stabilization of MoO_2-Ni_4Mo Electrocatalysts for Anion Exchange Membrane Water Electrolysis and Unbiased Solar-Driven Saline Water Splitting," *Applied Catalysis B: Environment and Energy* 358 (2024): 124364, https://doi.org/10.1016/j.apcatb.2024.124364.

333. T. Jiang, X. Jiang, C. Jiang, et al., "Novel Fe-Modulating Raney-Ni Electrodes Toward High-Efficient and Durable AEM Water Electrolyzer," *Advanced Energy Materials* 15 (2025): 2501634, https://doi.org/10.1002/aenm.202501634.

334. S. S. Jeon, Y. Choi, J. W. Lee, et al., "Degradation of NiMo Catalyst under Intermittent Operation of Anion Exchange Membrane Water Electrolyzer and Its Mitigation by Carbon Encapsulation," *Advanced Energy Materials* 15 (2025): 2501800, https://doi.org/10.1002/aenm.202501800.

335. J.-T. Ren, L. Chen, H.-Y. Wang, et al., "Synergistic Activation of Crystalline Ni_2P and Amorphous NiMoOx for Efficient Water Splitting at High Current Densities," *ACS Catalysis* 13 (2023): 9792–9805, https://doi.org/10.1021/acscatal.3c01885.

336. A. K. Niaz, A. Akhtar, J.-Y. Park, and H.-T. Lim, "Effects of the Operation Mode on the Degradation Behavior of Anion Exchange Membrane Water Electrolyzers," *Journal of Power Sources* 481 (2021): 229093, https://doi.org/10.1016/j.jpowsour.2020.229093.

337. T.-H. Kong, P. Thangavel, S. Shin, et al., "In-Situ Ionomer-Free Catalyst-Coated Membranes for Anion Exchange Membrane Water Electrolyzers," *ACS Energy Letters* 8 (2023): 4666–4673, https://doi.org/10.1021/acsenergylett.3c01418.

338. N. A. Khan, G. Rahman, T. M. Nguyen, et al., "Recent Development of Nanostructured Nickel Metal-Based Electrocatalysts for Hydrogen Evolution Reaction: A Review," *Topics in Catalysis* 66 (2022): 149–181, https://doi.org/10.1007/s11244-022-01706-2.

339. G. Lee, S. E. Jun, J. Lim, et al., "Tuning Hydrogen Binding on Ru Sites by Ni Alloying on MoO_2 Enables Efficient Alkaline Hydrogen Evolution for Anion Exchange Membrane Water Electrolysis," *Advanced Science* 12 (2025): 2414622, https://doi.org/10.1002/advs.202414622.

340. X. Wu and K. Scott, "A Li-Doped Co_3O_4 Oxygen Evolution Catalyst for Non-Precious Metal Alkaline Anion Exchange Membrane Water Electrolysers," *International Journal of Hydrogen Energy* 38 (2013): 3123–3129, https://doi.org/10.1016/j.ijhydene.2012.12.087.

341. J. Parrondo, C. G. Arges, M. Niedzwiecki, E. B. Anderson, K. E. Ayers, and V. Ramani, "Degradation of Anion Exchange Membranes Used for Hydrogen Production by Ultrapure Water Electrolysis," *RSC Advances* 4 (2014): 9875, https://doi.org/10.1039/c3ra46630b.

342. Y. Leng, G. Chen, A. J. Mendoza, T. B. Tighe, M. A. Hickner, and C. Y. Wang, "Solid-State Water Electrolysis With an Alkaline Membrane," *Journal of the American Chemical Society* 134 (2012): 9054–9057, https://doi.org/10.1021/ja302439z.

343. G. A. Lindquist, S. Z. Oener, R. Krivina, et al., "Performance and Durability of Pure-Water-Fed Anion Exchange Membrane Electrolyzers Using Baseline Materials and Operation," *ACS Applied Materials & Interfaces* 13 (2021): 51917–51924, https://doi.org/10.1021/acsami.1c06053.

344. L. Wan, Z. Xu, Q. Xu, P. Wang, and B. Wang, "Overall Design of Novel 3D-Ordered MEA With Drastically Enhanced Mass Transport for Alkaline Electrolyzers," *Energy & Environmental Science* 15 (2022): 1882–1892, https://doi.org/10.1039/d2ee00273f.

345. N. U. Hassan, Y. Zheng, P. A. Kohl, and W. E. Mustain, "KOH vs Deionized Water Operation in Anion Exchange Membrane Electrolyzers," *Journal of The Electrochemical Society* 169 (2022): 044526, https://doi.org/10.1149/1945-7111/ac5f1d.

346. T. Zhang, S. A. Lin, H. Liu, et al., "An Ionomer-Free Gapless Catalyst-Bridging Membrane Electrode Assembly for High-Performance Pure Water-Fed Anion Exchange Membrane Electrolyzer," *Advanced Materials* (2025), https://doi.org/10.1002/adma.202509805.

347. L. Xiao, S. Zhang, J. Pan, et al., "First Implementation of Alkaline Polymer Electrolyte Water Electrolysis Working Only With Pure Water," *Energy & Environmental Science* 5 (2012): 7869, https://doi.org/10.1039/c2ee22146b.

348. Y.-K. Choe, C. Fujimoto, K.-S. Lee, et al., "Alkaline Stability of Benzyl Trimethyl Ammonium Functionalized Polyaromatics: A Computational and Experimental Study," *Chemistry of Materials* 26 (2014): 5675–5682, https://doi.org/10.1021/cm502422h.

349. J. Xiao, A. M. Oliveira, L. Wang, et al., "Water-Fed Hydroxide Exchange Membrane Electrolyzer Enabled by a Fluoride-Incorporated Nickel–Iron Oxyhydroxide Oxygen Evolution Electrode," *ACS Catalysis* 11 (2020): 264–270, https://doi.org/10.1021/acscatal.0c04200.

350. R. Soni, S. Miyanishi, H. Kuroki, and T. Yamaguchi, "Pure Water Solid Alkaline Water Electrolyzer Using Fully Aromatic and High-Molecular-Weight Poly(Fluorene-Alt-Tetrafluorophenylene)-Trimethyl Ammonium Anion Exchange Membranes and Ionomers," *ACS Applied Energy Materials* 4 (2020): 1053–1058, https://doi.org/10.1021/acsaem.0c01938.

351. C. Lei, K. Yang, G. Wang, et al., "Impact of Catalyst Reconstruction on the Durability of Anion Exchange Membrane Water Electrolysis," *ACS Sustainable Chemistry & Engineering* 10 (2022): 16725–16733, https://doi.org/10.1021/acssuschemeng.2c04855.

352. K. Li, S. Yu, D. Li, et al., "Engineered Thin Diffusion Layers for Anion-Exchange Membrane Electrolyzer Cells With Outstanding Performance," *ACS Applied Materials & Interfaces* 13 (2021): 50957–50964, https://doi.org/10.1021/acsami.1c14693.

353. H. Hu, X. Wang, Z. Zhang, et al., "Engineered Nickel–Iron Nitride Electrocatalyst for Industrial-Scale Seawater Hydrogen Production," *Advanced Materials* 37 (2024): 2415421, https://doi.org/10.1002/adma.202415421.

354. H. Li, C. Cai, Q. Wang, et al., "High-Performance Alkaline Water Splitting by Ni Nanoparticle-Decorated Mo-Ni Microrods: Enhanced Ion Adsorption by the Local Electric Field," *Chemical Engineering Journal* 435 (2022): 134860, https://doi.org/10.1016/j.cej.2022.134860.

355. F. Meng, L. Zhu, R. Li, et al., "Engineering Metal-Support Interaction for Manipulate Microenvironment: Single-Atom Platinum Decorated on Nickel-Chromium Oxides Toward High-Performance Alkaline Hydrogen Evolution," *Advanced Functional Materials* 35 (2025): 2416678, https://doi.org/10.1002/adfm.202416678.

356. W. Li, Z. Ni, O. Akdim, et al., "Dual Active Site Engineering in Porous NiW Bimetallic Alloys for Enhanced Alkaline Hydrogen Evolution Reaction," *Advanced Materials* 37 (2025): 2503742, https://doi.org/10.1002/adma.202503742.

357. S. Geng, L. Chen, Y. Wu, Y. Wang, and S. Song, "Lattice-matched Metal/WN Catalyst With Highly Oxygenophilic W Sites for Hydrogen Production in Seawater Electrolyzer," *Journal of Energy Chemistry* 105 (2025): 302–311, https://doi.org/10.1016/j.jechem.2024.12.071.

358. N. Nordin, W. S. Ng, N. Azhar, S. N. A. Shaffee, N. A. Abd Samad, and R. M. Yunus, "Evaluation of Anion Exchange Membrane Water Electrolysis Performance Using Synthesised $NiMoO_4$/Ni Cathode via Solution Combustion Synthesis in Applied Thermal Reduction Approach," *International Journal of Hydrogen Energy* 104 (2025): 416–425, https://doi.org/10.1016/j.ijhydene.2024.07.050.

359. S. Ding, Z. Li, G. Lin, Y. Ding, L. Wang, and L. Sun, "Post-Selenium-Leaching Induced Fast Micro-Bubble Detachment on Nickel-Iron-Based OER Catalyst for Efficient AEM-WE," *Angewandte Chemie International Edition* (2025), https://doi.org/10.1002/anie.202517132.

360. W. Li, Y. Ding, Y. Zhao, et al., "Zwitterion-Modified NiFe OER Catalyst Achieving Ultrastable Anion Exchange Membrane Water Electrolysis via Dynamic Alkaline Microenvironment Engineering," *Angewandte Chemie International Edition* 64 (2025): 202505924, https://doi.org/10.1002/anie.202505924.

361. W. Zheng, L. He, T. Tang, et al., "Poly(Dibenzothiophene-Terphenyl Piperidinium) for High-Performance Anion Exchange Membrane Water Electrolysis," *Angewandte Chemie International Edition* 63 (2024): 202405738, https://doi.org/10.1002/anie.202405738.

362. W.-G. Lim, H. N. Truong, J.-Y. Jeong, et al., "Toward Feasible Single Atom-Based Hydrogen Evolution Electrocatalysts via Artificial Ensemble Sites for Anion Exchange Membrane Water Electrolyzer," *Applied Catalysis B: Environmental* 343 (2024): 123568, https://doi.org/10.1016/j.apcatb.2023.123568.

363. C. V. M. Inocêncio, F. Fouda-Onana, J. Rousseau, et al., "A Step Forward: Hydrogen Production on Cobalt Molybdenum Sulfide Electrocatalyst in Anion Exchange Membrane Water Electrolyzer," *ACS Applied Energy Materials* 5 (2022): 10396–10401, https://doi.org/10.1021/acsaem.2c02270.

364. N. Chen, S. Y. Paek, J. Y. Lee, J. H. Park, S. Y. Lee, and Y. M. Lee, "High-Performance Anion Exchange Membrane Water Electrolyzers With a Current Density of 7.68 A cm^{-2} and a Durability of 1000 Hours," *Energy & Environmental Science* 14 (2021): 6338–6348, https://doi.org/10.1039/d1ee02642a.

365. L. Wang, T. Weissbach, R. Reissner, et al., "High Performance Anion Exchange Membrane Electrolysis Using Plasma-Sprayed, Non-Precious-Metal Electrodes," *ACS Applied Energy Materials* 2 (2019): 7903–7912, https://doi.org/10.1021/acsaem.9b01392.

366. I. Vincent, E. C. Lee, and H. M. Kim, "Highly Cost-effective Platinum-free Anion Exchange Membrane Electrolysis for Large Scale Energy Storage and Hydrogen Production," *RSC Advances* 10 (2020): 37429–37438, https://doi.org/10.1039/d0ra07190k.

367. B. Motealleh, Z. Liu, R. I. Masel, J. P. Sculley, Z. Richard Ni, and L. Meroueh, "Next-generation Anion Exchange Membrane Water Electrolyzers Operating for Commercially Relevant Lifetimes," *International*

Journal of Hydrogen Energy 46 (2021): 3379–3386, https://doi.org/10.1016/j.ijhydene.2020.10.244.

368. J. J. Kaczur, H. Yang, Z. Liu, S. D. Sajjad, and R. I. Masel, "Carbon Dioxide and Water Electrolysis Using New Alkaline Stable Anion Membranes," *Frontiers in Chemistry* 6 (2018): 263, https://doi.org/10.3389/fchem.2018.00263.

369. S. Jang, J. Kim, and S. H. Ahn, "Scalable Fe-Rich Corroded Steel Wool Electrodes for Industrial Anion Exchange Membrane Water Electrolysis With a Two-Order-of-Magnitude Cost Reduction," *Advanced Functional Materials* 35 (2025): 2503677, https://doi.org/10.1002/adfm.202503677.

370. L. Guo, X. Liu, Z. He, et al., "Self-Supported Bimetallic Phosphide Heterojunction-Integrated Electrode Promoting High-Performance Alkaline Anion-Exchange Membrane Water Electrolysis," *ACS Sustainable Chemistry & Engineering* 10 (2022): 9956–9968, https://doi.org/10.1021/acssuschemeng.2c02520.

371. L. Wan, Z. Xu, P. Wang, P.-F. Liu, Q. Xu, and B. Wang, "Dual Regulation Both Intrinsic Activity and Mass Transport for Self-supported Electrodes Using in Anion Exchange Membrane Water Electrolysis," *Chemical Engineering Journal* 431 (2022): 133942, https://doi.org/10.1016/j.cej.2021.133942.

372. T. Liu, L. Wang, B. Chen, et al., "Modulating Built-In Electric Field Strength in Ru/RuO_2 Interfaces Through Ni Doping to Enhance Hydrogen Conversion at Ampere-level Current," *Angewandte Chemie International Edition* 64 (2025): 202421869, https://doi.org/10.1002/anie.202421869.

373. F. Bartoli, L. Capozzoli, T. Peruzzolo, et al., "Probing the Activity and Stability of MoO_2 Surface Nanorod Arrays for Hydrogen Evolution in an Anion Exchange Membrane Multi-cell Water Electrolysis Stack," *Journal of Materials Chemistry A* 11 (2023): 5789–5800, https://doi.org/10.1039/d2ta09339a.

374. Y. Yuan, X. Li, H. Wu, et al., "Enhanced Built-in Electric Field via Work Function Engineering for Efficient Anion Membrane Water Electrolysis," *ACS Energy Letters* 10 (2025): 2960–2971, https://doi.org/10.1021/acsenergylett.5c00978.

375. Z. Liang, D. Shen, Y. Wei, et al., "Modulating the Electronic Structure of Cobalt-Vanadium Bimetal Catalysts for High-Stable Anion Exchange Membrane Water Electrolyzer," *Advanced Materials* 36 (2024): 2408634, https://doi.org/10.1002/adma.202408634.

376. J. E. Park, Y.-E. Sung, and C. Choi, "Hierarchically Porous, Biaxially Woven Carbon Nanotube Sheet Arrays for next-generation Anion-exchange Membrane Water Electrolyzers," *Journal of Materials Chemistry A* 10 (2022): 20517–20524, https://doi.org/10.1039/d2ta04526e.

377. T. Zhou, S. Yu, Y. Tang, et al., "Built-in Electric Field Engineering of MoO_2-Ni Heterostructure by P3p-Mo4d-Tm4f Orbitals Hybridization for Efficient Industrial-level Hydrogen Production," *Chemical Engineering Journal* 508 (2025): 160921, https://doi.org/10.1016/j.cej.2025.160921.

378. Y. Dong, A. Wu, G. Yang, et al., "Lower-Temperature Synthesis of Nitrogen-Rich Molybdenum Nitride/Nickel (Cobalt) Heterojunctional Assembly for the Effective Water Electrolysis," *Advanced Functional Materials* 35 (2024): 2412979, https://doi.org/10.1002/adfm.202412979.

379. R. Yao, K. Sun, K. Zhang, et al., "Stable Hydrogen Evolution Reaction at High Current Densities via Designing the Ni Single Atoms and Ru Nanoparticles Linked by Carbon Bridges," *Nature Communications* 15 (2024): 2218, https://doi.org/10.1038/s41467-024-46553-9.

380. G. Xu, J. Li, Y. Zeng, et al., "Synergy of Ni Single Atom and RuNi Alloy Nanocluster Enables Boosted Hydrogen Evolution at Industrial Current Densities," *Energy & Environmental Science* 18 (2025): 6273–6282, https://doi.org/10.1039/d5ee01387a.

381. Y. Zhao, J. Li, K. Li, et al., "The Synergistic Effect of $Ni–NiMo_4N_5$ Heterointerface Construction and Fe-Doping Enables Active and Durable Alkaline Water Splitting at Industrial Current Density," *Journal of Materials Chemistry A* 13 (2025): 9184–9191, https://doi.org/10.1039/d5ta00038f.

382. H. Wang, Y. Jiao, G. Zhang, et al., "Stabilizing Electron-Deficient Ru Nanoclusters via Strong Electronic Metal-Support Interaction for Practical Anion-Exchange Membrane Electrolyzer," *Advanced Functional Materials* 35 (2024): 2418617, https://doi.org/10.1002/adfm.202418617.

383. J. Schauer, J. Hnát, L. Brožová, J. Žitka, and K. Bouzek, "Anionic Catalyst Binders Based on Trimethylamine-quaternized Poly(2,6-dimethyl-1,4-phenylene oxide) for Alkaline Electrolyzers," *Journal of Membrane Science* 473 (2015): 267–273, https://doi.org/10.1016/j.memsci.2014.09.011.

384. J. Žitka, J. Peter, B. Galajdová, et al., "Anion Exchange Membranes and Binders Based on Polystyrene-block-poly (ethylene-ran-butylene)-block-polystyrene Copolymer for Alkaline Water Electrolysis," *Desalination and Water Treatment* 142 (2019): 90–97, https://doi.org/10.5004/dwt.2019.23411.

385. J. Hnát, M. Paidar, J. Schauer, and K. Bouzek, "Polymer Anion-selective Membrane for Electrolytic Water Splitting: the Impact of a Liquid Electrolyte Composition on the Process Parameters and Long-term Stability," *International Journal of Hydrogen Energy* 39 (2014): 4779–4787, https://doi.org/10.1016/j.ijhydene.2014.01.086.

386. J. Zhao, R. Urrego-Ortiz, N. Liao, F. Calle-Vallejo, and J. Luo, "Rationally Designed Ru Catalysts Supported on TiN for Highly Efficient and Stable Hydrogen Evolution in Alkaline Conditions," *Nature Communications* 15 (2024): 6391, https://doi.org/10.1038/s41467-024-50691-5.

387. J. Chi, H. Yu, G. Li, et al., "Nickel/Cobalt Oxide as a Highly Efficient OER Electrocatalyst in an Alkaline Polymer Electrolyte Water Electrolyzer," *RSC Advances* 6 (2016): 90397–90400, https://doi.org/10.1039/c6ra19615b.